Influence of feed drives on the structural dynamics of large-scale machine tools

by

Oier Franco Dobaran

A thesis

presented to the University of Waterloo

in fulfillment of the

thesis requirement for the degree of

Doctor of Philosophy

in

Mechanical and Mechatronics Engineering

Waterloo, Ontario, Canada, 2021

© Oier Franco Dobaran 2021

Examining Committee Membership

The following served on the Examining Committee for this thesis. The decision of the Examining Committee is by majority vote.

External Examiner	Steffen Ihlenfeldt Professor, Institute of Machine Tools and Control Engineering Technical University of Dresden
Supervisor(s)	Kaan Erkorkmaz Professor, Mechanical and Mechatronics Engineering University of Waterloo
	Xavier Beudaert Adjunct Professor, Mechanical and Mechatronics Engineering University of Waterloo Researcher, Dynamics and Control department Ideko
Internal Member	Soo Jeon Associate Professor, Mechanical and Mechatronics Engineering University of Waterloo
Internal Member	Steve Lambert Professor, Mechanical and Mechatronics Engineering University of Waterloo
Internal-external Member	Sriram Narasimhan Adjunct Professor, Civil and Environmental Engineering University of Waterloo Professor, Civil and Environmental Engineering University of California, Los Angeles

Author’s Declaration

I hereby declare that I am the sole author of this thesis. This is a true copy of the thesis, including any required final revisions, as accepted by my examiners.

I understand that my thesis may be electronically available to the public.

Abstract

Milling is one of the most widely used processes in the manufacturing industry and demands machines with high productivity rates. In large machine tool applications, the cutting capability is mainly limited by the appearance of structural chatter vibrations. Chatter arises from the dynamic interaction of the machining system compliance with the cutting process. For the specific case of large-scale machine tools, the low frequency resonances have modal shapes that generate relative displacements in the machine joints. This thesis presents new approaches to minimize the appearance of chatter vibrations by targeting and understanding the machine tool compliance, in particular, from the feed drive of the machine tool. A detailed model of the double pinion and rack feed drive system and the master-slave coupling improves the large machine tools modeling. As the vibrations are measured by the axes feedback sensors, a new strategy for feed drive controller tuning allows increasing the chatter stability using a judicious selection of the servo parameters. Then, in-motion dynamic characterizations demonstrate the important influence of the nonlinear friction on the machine compliance and improve the chatter stability predictions. Finally, an operational method for characterizing both tool and workpiece side dynamics while performing a cutting operation is developed. All the contributions of the thesis have been validated experimentally and tend to consider the influence of the feed drives on the structural dynamics of large-scale machine tools.

Acknowledgements

I would like to say thank you to all those people who have helped me through these years.

First of all, I would like to express my sincere gratitude to Xavier Beudaert, whose help and encouragement are much appreciated. Without them, everything would have been much harder. Appreciation continues to Professor Kaan Erkorkmaz, for his confidence, advice and guidance throughout the course of this work. Thank you both.

I am also indebted to Danobatgroup, especially to Ideko for believing in me and giving me the chance to be part of this project and Soraluce, for the technical assistance and the support in experiments. I truly appreciate it.

I would also like to mention my colleges on both sides of the Atlantic. In Waterloo, to my PCL colleges for the infinite discussions and to all lab technicians for their endless support. In the Basque Country, to all my colleges from dynamics and control department, especially to Asier Barrios for taking the time to explain to me the control and the feed drives of machines, to Aitor Monedero for his assistance on the Finite Element simulations, and to Alex Iglesias for his assistance on the challenges in machine tool dynamics identification. Finally, I really want to thank Jokin Munoa, for the advice and for trying to make everything easier for me. Please, accept my deepest thanks.

I cannot refrain to mention the CANRIMT2 project, which has supported this thesis economically. This experience has allowed me to grow both personally and professionally.

And last but not least, I would like to express my hearty gratitude to my wife Izaskun for encouraging me to do everything I dream of. Thank you for letting everything behind and following me to Canada. Thank you for hearing me talking non-stop about this thesis, or at least pretending you did, and for expending long hours watching Netflix while I was busy.

Dedication

To my friends and family.

Table of Contents

List of Figures

List of Tables

List of Symbols

Symbol	Description	Unit
a_{p}	axial depth of cut	(mm)
a_{e}	tool radial engagement	(mm)
b	face width of the gear tooth	(mm)
c	coupling damping	$(\mathrm{Ns/m})$
c'	corrected single gear tooth pair equivalent stiffness	$(\mathrm{N/mm})/\mu\mathrm{m}$
c'_{th}	theoretical single gear tooth pair equivalent stiffness	$(\mathrm{N/mm})/\mu\mathrm{m}$
C	condition number of the excitation matrix	
$\mathbf{C}$	damping matrix	$(\mathrm{Ns/m})$
$c_{\gamma\alpha}$	gear mesh stiffness mean value	$(\mathrm{N/mm})/\mu\mathrm{m}$
$\mathbf{F}$	generalized excitation force matrix	(N)
f_{a}	anti-resonance frequency	(Hz)
$F_{\mathrm{a},j}$	axial cutting force	(N)
f_{bw}	velocity closed loop bandwidth	(Hz)
F_{mot}	motor force command	(N)
$f_{\mathrm{n},i}$	natural frequency of i modal shape	(Hz)
f_{r}	feed drive resonance frequency	(Hz)
$F_{\mathrm{r},j}$	radial cutting force	(N)
$\mathbf{F}_{\mathrm{t}}$	tool side excitation force	(N)
f_{t}	motor-locked or quenching frequency	(Hz)
$F_{\mathrm{t},j}$	tangential cutting force	(N)
$F_{\mathrm{tra},j}$	tangential, radial and axial cutting force vector	(N)
F_{tip}	external disturbance force applied in driven load	(N)
$\mathbf{F}_{\mathrm{w}}$	workpiece side excitation force	(N)
f_{Z}	feed per tooth	$(\mathrm{mm/Z})$
$\mathbf{G}$	generalized machine tool open loop dynamics	
$g(\phi)$	screen function of cutter workpiece engagement	
h	chip thickness	(mm)
h_{d}	dynamic chip thickness	(mm)
h_{s}	static chip thickness	(mm)
i_{red}	gearbox reduction factor	
I_{nom}	motor nominal current	(A)
J_{eq}	motor, gearbox and pinion joint equivalent inertia	$(\mathrm{kg/m^2})$
J_{gearbox}	gearbox equivalent inertia on motor side	$(\mathrm{kg/m^2})$
J_{motor}	motor equivalent inertia	$(\mathrm{kg/m^2})$
$\mathbf{K}$	stiffness matrix	$(\mathrm{N/m})$
$\mathbf{K}_{\mathrm{fb}}$	generalized feedback controller	
$\mathbf{K}_{\mathrm{pos}}$	generalized position controller	
$\mathbf{K}_{\mathrm{vel}}$	generalized velocity controller	
k	coupling stiffness	$(\mathrm{N/m})$
K_a	force constant of the linear motor	$(\mathrm{N/A})$

K_{ac}	specific axial force coefficient	$(\mathrm{N/mm^2})$
K_{ae}	edge axial force coefficient	$(\mathrm{N/mm})$
k_{gearbox}	gearbox torsional stiffness	$(\mathrm{Nm/rad})$
k_i	dynamic stiffness of i modal shape	$(\mathrm{N/m})$
k_{m}	master motor equivalent linear stiffness	$(\mathrm{N/m})$
k_{motor}	motor torsional stiffness	$(\mathrm{Nm/rad})$
$k_{\mathrm{p-r}}$	pinion and rack contact linear stiffness	$(\mathrm{N/m})$
K_p	proportional velocity loop gain	$(\mathrm{Ns/m})$
K_p^*	proportional velocity loop gain for optimal damping	$(\mathrm{Ns/m})$
K_r	cutting force ratio	
K_{re}	edge radial force coefficient	$(\mathrm{N/mm})$
K_{rc}	specific radial force coefficient	$(\mathrm{N/mm^2})$
k_{s}	slave motor equivalent linear stiffness	$(\mathrm{N/m})$
k_{shaft}	shaft torsional stiffness	$(\mathrm{Nm/rad})$
K_{t}	motor torque constant	$(\mathrm{Nm/A})$
K_{tc}	specific tangential force coefficient	$(\mathrm{N/mm^2})$
K_{te}	edge tangential force coefficient	$(\mathrm{N/mm})$
K_{Tm}	master motor individual weighting factor	
K_{Ts}	slave motor individual weighting factor	
K_{v}	position proportional control gain	$(\mathrm{m/min})/\mathrm{mm}$
K_v^*	proportional position gain for optimal damping	$(\mathrm{m/min})/\mathrm{mm}$
L	Padé approximation order	
$L_{\mathrm{z,m}}$	equivalent backlash of the master motor transmission	$(\mu\mathrm{m})$
$L_{\mathrm{z,s}}$	equivalent backlash of the slave power transmission	$(\mu\mathrm{m})$
$\mathbf{M}$	mass matrix	(kg)
m_2	intermediate equivalent mass	(kg)
m_{load}	driven load mass	(kg)
m_{tip}	tool tip equivalent mass	(kg)
m_{total}	rigid body equivalent mass	(kg)
m_x	mean of the Gaussian distribution	
N	spindle speed	(rpm)
O	generalized sensed output	
$\mathbf{P}$	modal force	$(\mathrm{N}/\sqrt{\mathrm{kg}})$
$\mathbf{p}$	velocity loop control signal vector	
$\mathbf{p}'$	position loop control signal vector	
PI	proportional-integral controller	$\mathrm{Nm/(rad/s)}$
PI_{master}	master motor proportional-integral controller	$\mathrm{Nm/(rad/s)}$
PI_{slave}	slave motor proportional-integral controller	$\mathrm{Nm/(rad/s)}$
PI_{preload}	torque equalization proportional-integral controller	$\mathrm{(rad/s)/Nm}$
$\mathbf{Q}$	modal vector matrix	$\left(1/\sqrt{\mathrm{kg}}\right)$
$\mathbf{q}$	velocity loop measured output vector	
$\mathbf{q}'$	position loop measured output vector	
$\mathbf{R}$	closed velocity loop machine tool dynamics	
$\mathbf{r}$	generalized vibration amplitude	(m)

$\mathbf{r}_{\mathrm{t}}$	tool side vibration amplitude	(m)
$\mathbf{r}_{\mathrm{w}}$	workpiece side vibration amplitude	(m)
s	Laplace operator	$(j\omega)$
S_{e}	tool edge length	(mm)
$\boldsymbol{S}^{\mathrm{t}}_{r,Fx}$	generalized tool side force-response spectra	(Nm)
$\boldsymbol{S}^{\mathrm{t}}_{F,Fx}$	generalized tool side force-force spectra	(N^2)
T	tooth passing period	(s)
T_{i}	integral time constant	(s)
T_i^*	integral time constant for optimal damping	(s)
$\mathbf{U}$	left singular vector of estimated FRF matrix	
$\mathbf{u}$	local normal vector	
$\mathbf{u}_k$	left singular vector of the excitation matrix	
$\mathbf{V}$	right singular vector of estimated FRF matrix	
$\mathbf{v}_k$	right singular vector of the excitation matrix	
$\mathbf{w}$	velocity loop input vector	
$\mathbf{w}'$	position loop input vector	
x_{tip}	load actual position	(mm)
x_{mot}	motor position acquired by the feedback sensor	(mm)
$\dot{x}_{\mathrm{ref}}$	CNC velocity command	$(\mathrm{mm/s})$
Z	tool teeth number	
$\mathbf{z}$	velocity loop output vector	
$\mathbf{z}'$	position loop output vector	
$\boldsymbol{\eta}$	modal displacement	$(\mathrm{m}/\sqrt{\mathrm{kg}})$
ε_{α}	Contact gear ratio	
$\gamma^2_{\mathrm{i,F_i}}$	coherence function	
κ	tool lead angle	$(°)$
$\mathcal{N}$	Normal Gaussian distribution	
ν	singular values of the excitation matrix	(N)
v_x^2	variance of the Gaussian distribution	
$\omega_{\mathrm{p},i}$	frequency of i pole	(rad)
$\omega_{\mathrm{z},i}$	frequency of i zero	(rad)
$\boldsymbol{\Phi}$	generalized Frequency Response Function	$(\mathrm{m/N})$
ϕ_{en}	cutting entry angle	(rad)
ϕ_{ex}	cutting exit angle	(rad)
ζ_i	damping ratio of i modal shape	$(\%)$
$\zeta_{\mathrm{p},i}$	Damping ratio of i pole	(rad)
$\zeta_{\mathrm{z},i}$	Damping ratio of i zero	(rad)
ϕ_j	tool immersion angle	(rad)
$\dot{\varphi}_{\mathrm{m}}$	master motor actual velocity	$(\mathrm{rad/s})$
$\dot{\varphi}_{\mathrm{s}}$	slave motor actual velocity	$(\mathrm{rad/s})$
$\boldsymbol{\Phi}_{\mathrm{tt}}$	tool side Frequency Response Function	$(\mathrm{m/N})$
$\boldsymbol{\Phi}^{\mathrm{SMFE}}_{\mathrm{tt}}$	tool side Frequency Response Function obtained by SMFE technique	$(\mathrm{m/N})$
$\boldsymbol{\Phi}_{\mathrm{tw}}$	tool-workpiece cross Frequency Response Function	$(\mathrm{m/N})$

$\mathbf{\Phi}_{\mathrm{wt}}$	workpiece-tool cross Frequency Response Function	$(\mathrm{m/N})$
$\mathbf{\Phi}_{\mathrm{ww}}$	workpiece side Frequency Response Function	$(\mathrm{m/N})$
$\mathbf{\Phi}_{\mathrm{ww}}^{\mathrm{SMFE}}$	workpiece side Frequency Response Function obtained by SMFE technique	$(\mathrm{m/N})$
σ	viscous friction	$(\mathrm{Nmin/mm})$
$\mathbf{\Sigma}$	singular values matrix	
τ	regenerative time delay	(s)
τ_{BF}	time constant of the balancing filter	(s)
τ_{cl}	closed loop associated time delay or phase lag	(s)
τ_{m}	master motor actual torque	(Nm)
τ_{net}	summation of each motor torque	(Nm)
$\tau_{\mathrm{net,max}}$	maximum achievable net torque	(Nm)
τ_{ol}	open loop associated time delay or phase lag	(s)
τ_{p}	torque bias or tension torque	(Nm)
τ_{ref}	torque reference	(Nm)
τ_{s}	slave motor actual torque	(Nm)

Chapter 1

Introduction

1.1 BACKGROUND

The current production environment demands powerful, precise, rigid and automatic machine tools. Historically, aeronautical and naval sectors have required the capabilities for machining large parts. Moreover, sectors such as renewable energy, railroad and electric power plants are currently demanding larger and more accurate parts. These machines demand precision engineering concepts to fulfill the challenging requirements of long travelling distances and high repeatability under heavy loads (Uriarte et al. [1]).

The most frequent configuration of large-scale machines are the travelling column and gantry types (Figure 1.1), in which the workpiece is usually in a fixed position. The need for large machines is increasing and, as conventional ones, they present the continuous challenge of increasing the productivity, precision and high dynamics when large travel ranges and heavy loads are involved.

Figure 1.1 Large-scale machine tool from Soraluce.

Founded in 1962, Soraluce is a worldwide leader in milling, boring and turning technologies in large machine tools. Soraluce is part of Danobatgroup, the machine tool division of Mondragon Corporation, which is one of the most prominent European holding companies. In order to respond to the required innovations to be a sector leader, Soraluce is involved in numerous R&D projects, both individually and in collaboration with other companies, technology centres and universities.

Within the same group, Ideko is a technology centre specialized in industrial production and manufacturing technologies. Among the different research lines, the Dynamics and Control department addresses the resolution of vibratory problems in all types of industrial machinery from two different and complementary approaches. On one hand, the dynamic design of machines and drives. On the other hand, the diagnosis and subsequent implementation of specific developments to suppress chatter vibrations in machining processes.

As a part of the NSERC Canadian Network for Research and Innovation in Machining Technology 2 (CANRIMT2), Danobatgroup and the Precision Controls Laboratory (PCL) from University of Waterloo have teamed up to conduct research in analyzing the influence of feed drive system dynamics on the structural response of large-scale machine tools.

1.2 THESIS OVERVIEW AND CONTRIBUTIONS

Despite the constant developments carried out by machine tool builders, self-excited vibrations still limit productivity. These vibrations are also known as chatter and it is a well known phenomena among the machine tool industry. Regardless of recent developments, the chatter problem is and will continue being a crucial problem in machine tools and hence, the development of efficient chatter avoidance techniques and accurate chatter prediction models is an interesting and necessary task for the manufacturing industry.

The design of a machine tool has become a complex process in recent years. Nowadays, machine tool designers tend to use Finite Element models to assist the design stage. However, one of the main limitations that significantly influences the accuracy of the model is the characterization of the machine joints. The machine tool builders tend to push the servo bandwidths to minimize the tracking errors. However, high gains can reduce the damping provided by the feed drives and hence affect the overall machine dynamics.

Large-scale machine tools have low natural frequencies related to the machine structure between 10 and 50Hz. In certain cases, the shapes related to these resonances can generate relative displacements at the machine joints, not only influencing the overall machine tool behaviour, but also at the most important location, the cutting point. Establishing methods to consider their effect is essential to, first, understand the behaviour and interaction with the machine structure and, second, to develop more reliable models that can predict the machine tool system dynamics accurately and hence, the process stability limits. Figure 1.2 illustrates the research contributions, which are detailed below.

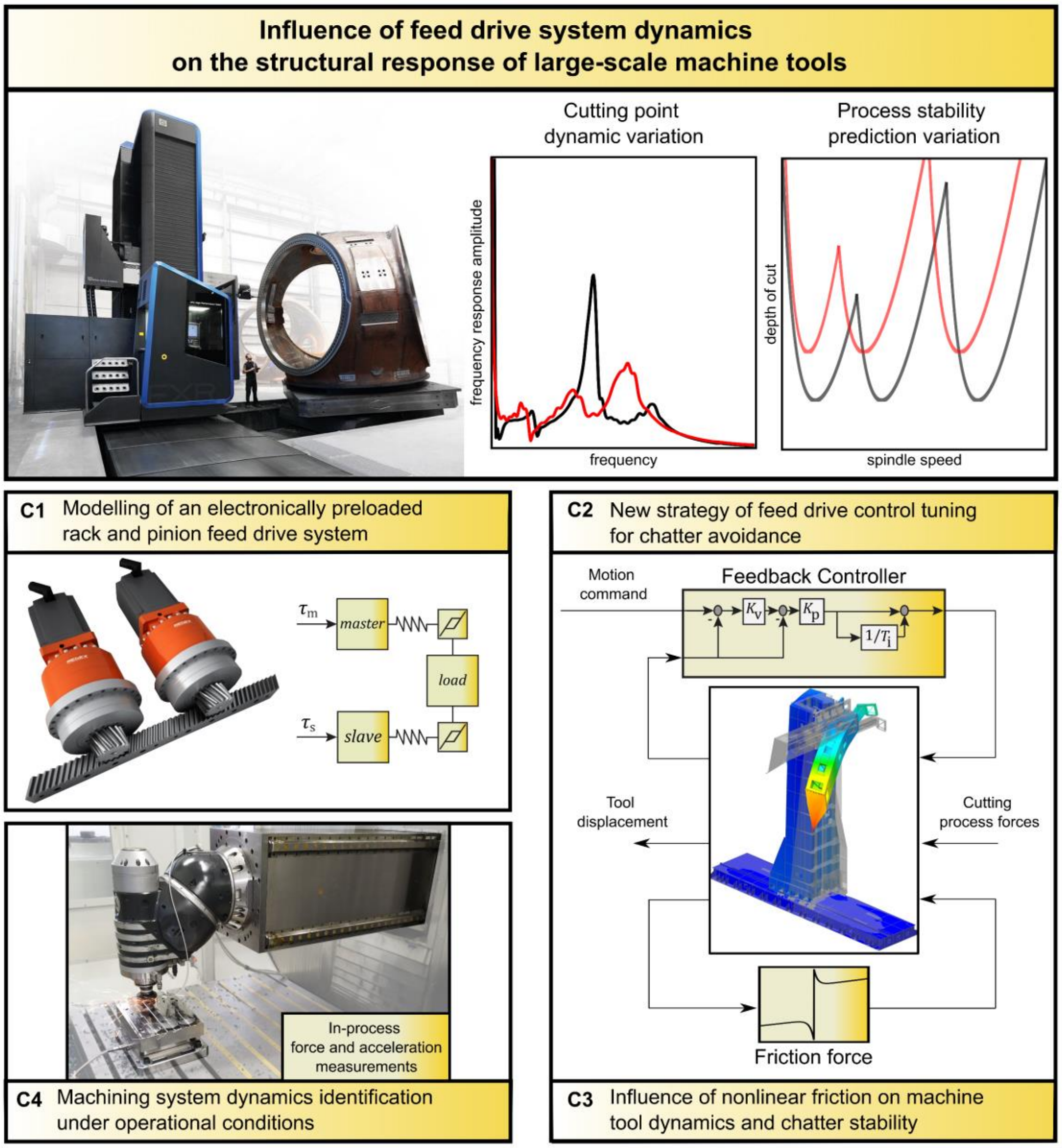

Figure 1.2 Research thesis contributions.

C1: Modelling of an electronically preloaded rack and pinion feed drive system. When machining large workpieces, long travelling distances are required. Double pinion and rack feed drive systems are usually employed by large machine tool builders as the stiffness of this mechanism is not influenced by the axis stroke. To suppress the existing backlash between the pinion and rack interface, a master-slave control configuration is implemented in the machine controller (CNC). This thesis presents time and frequency domain modelling approaches to analyze the master-slave control parameters influence on the machine tool operational

behavior. The models provide insights about this feed drive mechanism and accurately predict the observed experimental static and dynamic trends.

C2: Development of a new strategy for the feed drive control tuning considering machine dynamics and chatter stability. The standard feed drive motion controller tuning only pays attention to the motor side response captured by the machine controller. However, the commissioning procedure should be responsible to get the best behaviour at the cutting point and not only at the motor side. The proposed strategy has been successfully implemented on the industry standard P-PI cascade control structure achieving up to 44% damping increase on an industrial machine tool and 33% increase in machining productivity by avoiding chatter.

C3: Description of the influence of friction on the tool centre point dynamics. For the particular case of large-scale heavy-duty machining applications, where low frequency structural chatter vibrations limit the cutting capabilities, the influence of the damping generated in the machine joints can be a fundamental parameter for determining the machine tool damping and hence, the cutting capabilities. Experimental chatter tests demonstrate the strong influence of friction on the prediction of the stability lobes where deviations of 240% in the expected depth of cut have been obtained.

C4: Development of a machining system dynamic characterization technique under operational conditions. Already established milling process stability prediction models can accurately predict the appearance of chatter vibrations. However, for certain cases, significant experimental deviations are experienced. The source of inaccuracies is usually attributed to process nonlinearities or errors associated to the dynamic parameters identification. The prediction of the process stability limit has been improved by using the proposed technique with respect to traditional impact hammer testing.

The thesis is organized as follows:

Chapter 2 presents a literature review and background information related to chatter vibrations, challenges in machine tool dynamics identification and how friction can affect them. A description of the feed drive system and its control is provided next, with a

detailed section about rack and pinion feed drives that are commonly installed in large machine tools.

Chapter 3 describes the modelling of a double pinion and rack feed drive system (Contribution C1). Time and frequency domain models are introduced and the model parameters are extracted from experimental characterization tests. On one hand, the time domain model which considers the contact mechanics shows that the preload level can be tuned to handle high load forces generated during the cutting process to ensure a preloaded system. On the other hand, the frequency domain model based on Linear Fractional Transformation formalism concludes that the servo control parameters can affect the cutting point compliance, especially the proportional velocity loop gain.

Chapter 4 presents a new feed drive control tuning strategy to enhance the damping properties at the cutting point (Contribution C2). The interaction of the machine tool dynamics and the servo control is described. Then a semi-analytical MIMO model is developed to predict the tool tip receptance under different control settings. Experimental tests demonstrate that chatter vibration can be avoided by a judicious selection of the control parameters.

Chapter 5 introduces an analysis of the influence of friction on the nonlinear dynamics (Contribution C3). Experimental tests conducted in different industrial machines show the significant variation of the cutting point compliance in machine idle and in-motion conditions. A simulation model which considers machine tool dynamics, guideway friction, feed drive controller and motion commands is experimentally validated on a laboratory test bench. Experimental tests conducted on a large-scale machining centre demonstrate the motion effect and how this can lead to considerable chatter stability prediction errors.

Chapter 6 introduces an alternative machining system dynamic characterization technique under operational conditions (Contribution C4). The Sweep Milling Force Excitation technique is firstly described, and an optimization of the process parameters is carried out by means of time domain simulations. Proposed methodology is validated through simulations and experimental tests in a ram-type milling machine.

Finally, the conclusions and future works are presented in Chapter 7.

Chapter 2

Literature review

2.1 REGENERATIVE CHATTER IN MACHINE TOOLS

The presence of self-excited vibrations during the machining process is a classical problem that limits the productivity. The avoidance of this kind of vibration is important, since its occurrence prevents the achievement of the required surface quality. It also increases tool wear and can also damage the machine tool components. Moreover, this problem appears in a wide range of machining operations, as shown in Figure 2.1. Self-excited vibrations, also called chatter vibrations, constitute a complex phenomenon which involves different aspects, such as the cutting process parameters, selected tool geometry, workpiece material, and the dynamical properties of the machining system.

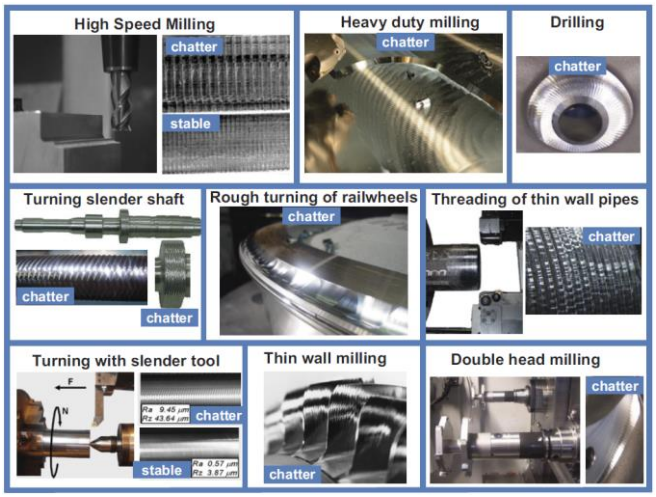

Figure 2.1 Chatter problem in numerous industrial machining applications [2].

New developments in the material employed by tool manufacturers allow for increasing the cutting conditions (feed and speed) and consequently the chip load. This, in combination with increased machine power, makes the chatter-free cutting conditions more demanding. In addition, the rising requirements in terms of geometrical precision and accuracy has led to the introduction of lower friction guideway systems, which result in machine tool structures with low damping ratios.

2.1.1 Chatter origin

After the first studies conducted by Taylor [3] in 1907, the regenerative effect was reported as the main cause of chatter vibrations by Tobias and Fishwick [4] and Tlusty and Polacek [5,6]. In 2001, Wiercigroch and Budak [7] described the existing different mechanisms that generate chatter. The regenerative chatter mechanism is based on the dynamic excitation of the system due to the cutting forces, and as a result a wavy surface is left on the workpiece. When the next tooth of the cutter cuts this wavy surface, it causes a new wavy pattern over the newly generated surface (Figure 2.2-left). Depending on the phase difference between the former and current pass, the resulting vibration may grow, based on the amount of damping in the system's structure. If the process is repeated with successive teeth, a regenerative effect will be produced. Figure 2.2-right shows a schematic view of the regenerative mechanism. If no phase shift is presented between the prior and current wavy surface, the chip thickness remains constant and thus, the process is stable (top case). In contrary, for middle and bottom cases, there is a delay which results in a variable chip thickness and a consequently growing vibration.

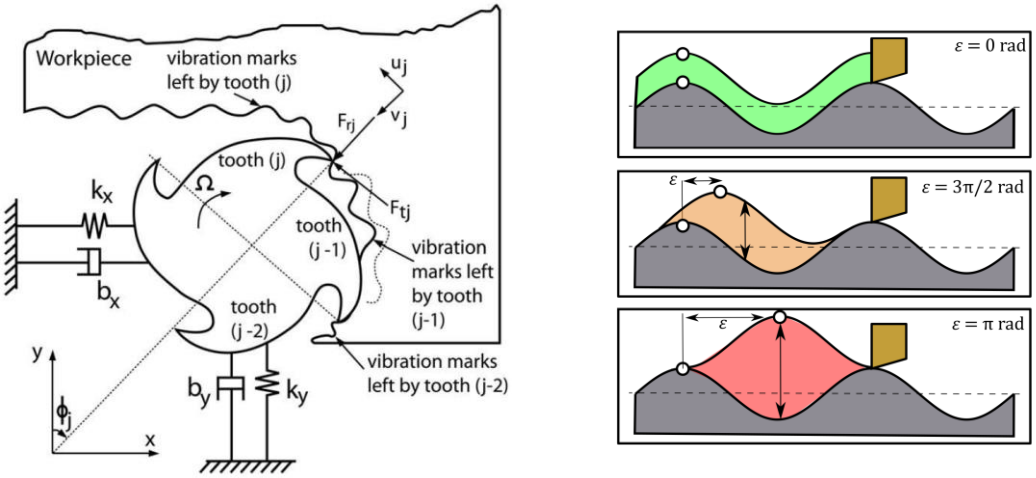

Figure 2.2 Regenerative chatter effect [8] (left); Phase delay of waviness in a milling model (right).

As reviewed by Munoa et al. [2] in 2016, the machining chatter appears when one or more vibration modes of the machining system are self-excited due to the cutting process. An exemplary representation of a machining system is shown in Figure 2.3, comprising the tool (1) which removes material from the workpiece (2). Sometimes the fixture (3), which holds the workpiece or even the machine itself (4), may not be stiff enough and can lead to regenerative chatter vibration. Depending on which component is the weak link, contributing most to chatter, different frequency ranges will be excited. For example, in the case of large masses like machine tool structure or large flexible fixture, the expected frequency range is from 20 to 200Hz, and from 500Hz to 10kHz for high frequency tooling-related chatter.

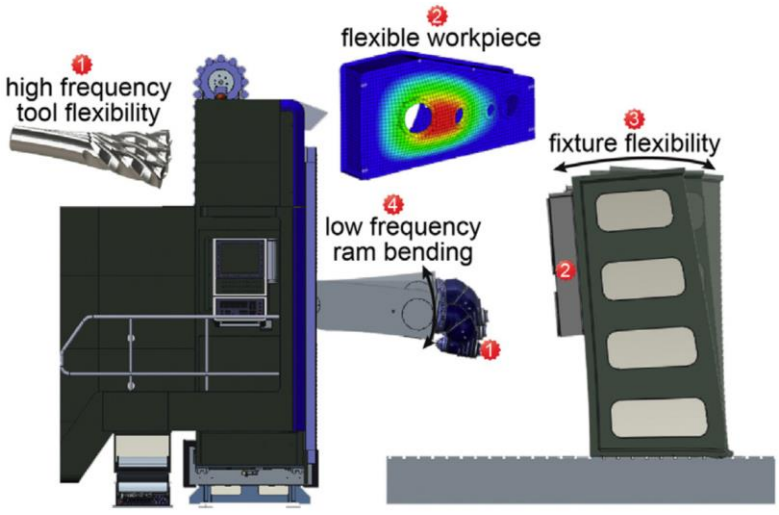

Figure 2.3 Machining system components with potential contribution to chatter [2].

2.1.2 Stability models

In 1958, Tobias and Fishwick [4] suggested the use of stability charts in order to distinguish the stable and unstable machining conditions depending on the spindle speed and depth of cut. Later, in 1965 Merrit [9] presented the regenerative chatter problem as a feedback loop, which helped to clarify and to understand the underlying physics. However, almost all theoretical and experimental developments were focused on continuous cutting processes such as turning. For interrupted milling processes, the stability analysis is more complicated because of the discontinuous nature of the process. By the end of 1970, the initial value time domain simulations became popular as process nonlinearities such as contact loss between the cutter and workpiece due to severe vibration amplitude could be introduced [10]. This stability prediction model was extensively used for the following 20 years, providing detailed information about the cutting process. In 1995, Altintas and Budak [11] presented a semi-analytical method for chatter analysis in frequency domain based on previous works [12–14]. This method called single frequency or Zeroth Order Approximation (ZOA) is very fast, but in case of low immersion milling, the existence of additional stability lobes called double period chatter or flip bifurcation was found [15,16]. Three years later, they improved the model by considering multiple terms of the Fourier development of the directional matrix [17]. The existence of additional stability lobes was a trigger for time domain based method application, where the stability lobe is obtained by scanning different depth of cut and spindle speeds. Methods like Gamma-distribution [18], semi-discretization [19], full discretization [20], collocation method [21] or time domain finite element [22] have been reported in the literature to solve the milling operation mathematical model.

In 2004, Altintas and Weck [23] reviewed the different stability models for several machining operations such as turning, milling, drilling and grinding operations. The stability lobe diagram is fed with four different inputs: the cutting coefficient describing the force, the dynamic parameters of the machining system, the process parameters and the tool geometry (Figure 2.4). Tool geometry and cutting conditions are inputs that are chosen by the process planners or machine operators. However, cutting coefficients and dynamic parameters of the machine structure depends on more variables, and they have to be obtained experimentally.

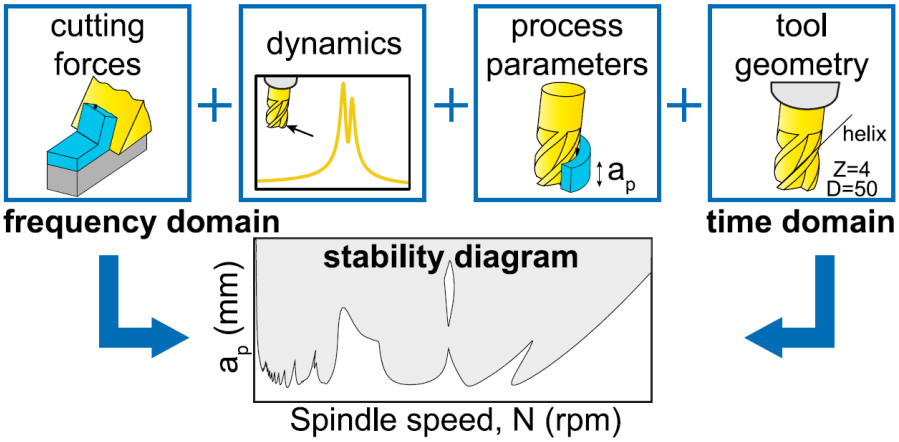

Figure 2.4 Procedure to obtain the stability lobe diagram [2].

Table 2.1 summarizes the advantages and disadvantages of each previously presented stability lobes computation. In the same manner, the prediction results for ZOA, Multi frequency and Semi-discretization methods are compared in Figure 2.5.

Table 2.1: Stability prediction method comparison.

Advantages	Disadvantages
Single frequency	
- Fast method	- Nonlinearities not supported
- Measured FRF direct input	- Inaccuracies in interrupted cutting
Multi frequency	
- Simulation speed and precision depends on number of harmonics selected	- Nonlinearities not supported
- Measured FRF direct input	- Slower than single frequency
Time domain	
- Very complex mill models can be handled	- Modal parameter extraction from the FRF is needed
- Robustness	- Slower than single frequency
Initial value time domain	
- Nonlinearities can be taken into account	- Modal parameter extraction from the FRF is needed
- Very accurate simulations	- Time consuming

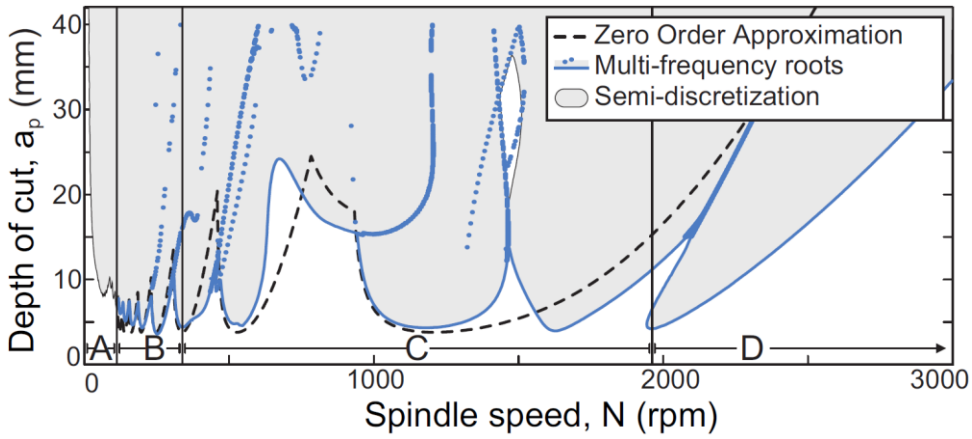

Figure 2.5 Comparison between stability models [2].

Considering the review of the state-of-the-art on the chatter stability limit prediction and the contributions presented in this thesis, the Zeroth Order Approximation method is used as it provides fast and accurate results for large radial immersion processes that are present in heavy-duty machining. For transient phenomena simulations, the initial value time domain method is used.

2.2 CHALLENGES IN MACHINE TOOL DYNAMICS IDENTIFICATION

An accurate machine dynamic characterization is essential to properly describe the dynamic response of the machine and predict its cutting stability (Figure 2.4). Brecher and Esser [24] concluded that the cutting coefficients describing the force and the dynamic parameters of the machining system were subjected to higher uncertainty. Later, Rasper et al [25] concluded that measured machine tool compliance was the principal source of inaccuracies in chatter stability predictions.

The hammer test (also called impact testing) is the usual method for the dynamic characterisation of machine tools. It consists of exciting the structure by means of a dynamometric hammer and measuring the response by means of an accelerometer, velocimeter or any other displacement sensor. Different aspects such as poor signal to noise ratio, overload problems or differences of each impact force constitutes the main limitations of this method. Kim and Schmitz [26] reported statistical variations, calibration coefficients and misalignment of the impact force as the major contributors of the existing uncertainty.

The existing nonlinearities in a machine tool, such as friction at the mechanical interfaces (Trendafilova et al. [27]), rolling elements of translation carriages (De Moerlooze et al. [28]) or backlash in the mechanical joints (Trendafilova et al [29]), make the hammer excitation not well suited (Halvorsen et al. [30]). For these cases, an electrodynamic shaker should be considered where the generated force is controlled; however, this implementation is usually more complicated and time-consuming.

The experimental dynamic characterization of the machine tool presents a certain degree of uncertainty (Munoa et al. [31]). Many effects rising under operational conditions have been reported as possible sources of error for dynamic identification (Rebelein et al. [32]). The machine tool is not a static passive structure, since it is controlled through electric drives. It can move, rotate or cut material and the possible side effects of these events are not considered when performing a classical hammer or shaker test. Table 2.2 summarizes the main effects that have been reported in the literature which rise under operational conditions and results in deviations in the machine tool dynamics measurements. The academic community has developed alternative theoretical and experimental methods, which consider additional effects that influence the dynamic behaviour of the machine tool and cannot be captured by standard methods.

Table 2.2: Machine tool factor affecting dynamic behaviour.

Factor	Effect on dynamics	Reference
Variable dynamics	Diverse variations	[33–44]
Gyroscopic effect	Increase of natural frequency	[45–52]
Bearing preload	Increase of natural frequency	[53–60]
Control parameters	Dynamic stiffness change	[61–65]
Friction in structural joints	Increase of damping and change of stiffness	[66–72]
Tool-workpiece contact	Increase of stiffness and damping	[73–77]

2.2.1 Inverse characterization methods

One procedure to reduce all sources of inaccuracies (Table 2.2) is to identify the machine tool dynamic parameters from actual cutting tests. The main idea is to perform a set of cutting tests to identify the stability limit for different spindle speeds. Then, an inverse mathematical procedure is used to extract the main dynamic parameters based on the

limit depth of cut and chatter frequency identified in the stability limit. Ismail et al. [78] sculptured the experimental stability lobes on a workpiece by varying the spindle speed. Quintana et al. [79] performed a similar experiment on a roof-shaped workpiece. Later in 2015, Grossi et al. [80] replicated the experiments presented in [78] but maintaining the feed per tooth constant. Using these procedures, the stability diagrams are obtained directly by means of cutting tests. Kruth et al [81] inversely extracted a tool tip FRF from chatter stability tests. In 2017, Grossi et al. [82] performed the inverse identification, where major influence of the spindle speed on the dynamics was reported (Figure 2.6) Postel et al. [83] performed a tool tip FRF prediction combining inverse stability and receptance coupling approaches, concluding that the spindle dynamics are also affected by the feed rate. Suzuki et al. [84] extended this approach by studying a spindle having symmetric modes in two orthogonal directions. In 2010, Kilic et al. [85] developed an analytical formulation for the case of two equal orthogonal modes. Özsahin et al. [86] developed a similar approach, concluding that tool tip FRF is affected by the spindle speed and cutting forces simultaneously. Recently, Eynian et al. [87] improved the inverse identification computation time by using two closed forms methods, which avoids the iterative resolution.

This inverse methodology can even solve current deviations related to dynamic behavior which are not yet considered by standard theoretical machining stability prediction methods, such as the damping increase due to the so-called process damping effect. Budak and Tunc [88] proposed an analytical inverse stability solution where their major assumption was that the dynamic contact between the cutting tool flank face and the workpiece only alters the damping value. From this perspective, they used the ratio between experimentally identified and the theoretically expected stability limits. Later, they extended their approach to milling processes [89]. In their proposed approach, they used the ratio between the experimentally identified stability limits and the theoretical stability limits.

Although the inverse methodology provides a very accurate dynamic characterization, the limitations of the method are significant. Extensive cutting tests must be conducted and the method is only valid for very simple dynamics, with one or two dominant modes.

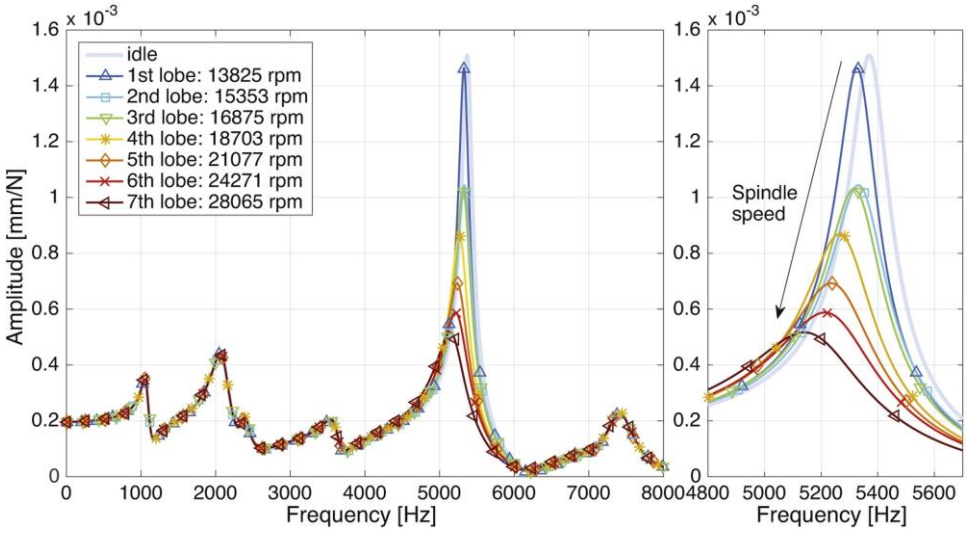

Figure 2.6 Speed-varying FRF calculated by Grossi et al. [82].

2.2.2 Real cutting force excitation characterization methods

The measurement of machine tool dynamics using real cutting forces as input excitation has also been reported in the literature. The response is obtained under operational conditions, thus nonlinear effects which are not considered under the standard idle hammer test are included in the measurement.

Opitz and Weck [90] for milling and Minis et al. [91] for turning used specifically designed workpieces to generate a random-type excitation through cutting forces. Employing load sensors and accelerometers, the authors extracted the machine tool FRF, which resulted in different responses than the ones obtained by impact hammer testing. Effects such as preload or feed variations were identified as the main deviation causes. Liu et al. [92] extended these works by performing an experimental modal analysis. The cutting forces excite the machining system at the tooth passing frequency and its higher harmonics. Therefore, it becomes impossible to obtain the FRF for the frequencies that are not excited. Özsahin et al. [93] obtained the dynamic characteristics by two different approaches. First, employing randomly distributed workpiece geometry as in previous studies. Second, exciting the system at discrete frequency points at specific cutting speeds using a conventional workpiece. Li et al. [94] and Cai et al. [95] developed similar techniques to obtain dynamic parameters from a random cutting force excitation. They pre-machined a thin wall on a workpiece and performed cutting tests in order to apply a random excitation. Li et al. reported a damping decrease with respect to hammer test results.

Instead of using a random excitation, Iglesias et al. [96] proposed an identification technique called Swept Milling Force Excitation (SMFE) where the cutting forces were replicating a chirp excitation signal. The authors applied the technique on a milling machine and observed a considerable variation with respect to the hammer test FRF. They combined the measurements of three different cutting test to define a linearly independent system and obtain the different FRFs. Takagusi et al. [97] employed a similar approach in a turning machine, applying a varying speed cut over a sinusoidal workpiece pattern. They obtained FRFs with lower natural frequencies and compliances than what was measured with a classical impact hammer test (Figure 2.7).

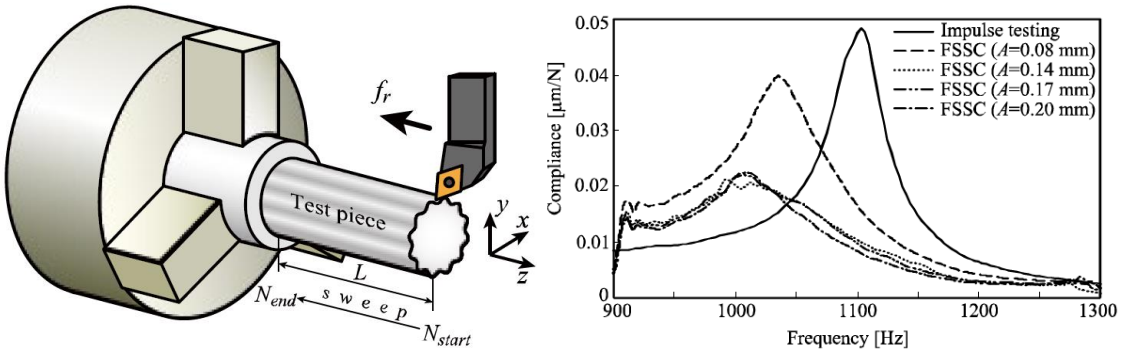

Figure 2.7 Operational scheme and resultant compliance [97].

For the particular case of heavy-duty rough milling operations, the chatter vibrations arise from the large flexible fixture holding the workpiece, from the flexible machine tool structure or, in certain cases, a combination of them. Chapter 6 presents an identification technique for the machining system dynamics (workpiece and tool side) under operational conditions that has not been reported in literature. As a result, the inaccuracies related to the dynamic parameters identification are minimized and hence, the computed process stability prediction is improved over the traditional impact hammer approach. In addition, an optimization of the identification process parameters is conducted and analytical expressions for optimal radial engagements are provided for the identification of a generalized 2D system.

2.3 INFLUENCE OF FRICTION IN MACHINE TOOL DYNAMICS

In machine tools, friction is considered one of the main sources of disturbance that causes positioning errors during motion, especially during velocity reversals where the direction of friction force changes.

The demand to build faster and more precise machines brought important advances to reduce the existing friction between parts with relative motions. Altintas et al. [98] summarized the different guiding systems typically used in machine tools (Figure 2.8). The first adopted solution is the so-called friction guides, which offer a combination of high load and impact capacity. At the same time, it provides a high structural damping as a result of the high friction. However, this feature directly restricts the precision of the driven machine due to the 'stick-slip' effect. To increase the speed and accuracy of the machine tool, rolling elements were developed. This solution maintains the load capacity of the previous solution but minimizes the friction effect. The easy modular integration in the machine together with its good operational characteristics, make this option the most used one in the machine tool sector. Hydrostatic, aerostatic or magnetic solutions are generally used in high precision applications that justify their additional costs.

In 1970, Koenigsberger et al. [99] stated that the damping of the machine tool is mainly generated in the existing joints. This is because the structural material absorbs only a small fraction of the total dissipated energy. In this way, the damping of the assembled structure is about 30 to 50 times higher than the individual components. Later, in 2003, Zhang et al. [66] concluded that approximately 60% of the total dynamic stiffness and approximately 90% of the machine damping is originated at the machine joints. Therefore, the damping generated at the machine guiding system can be a fundamental parameter for determining the machine tool damping.

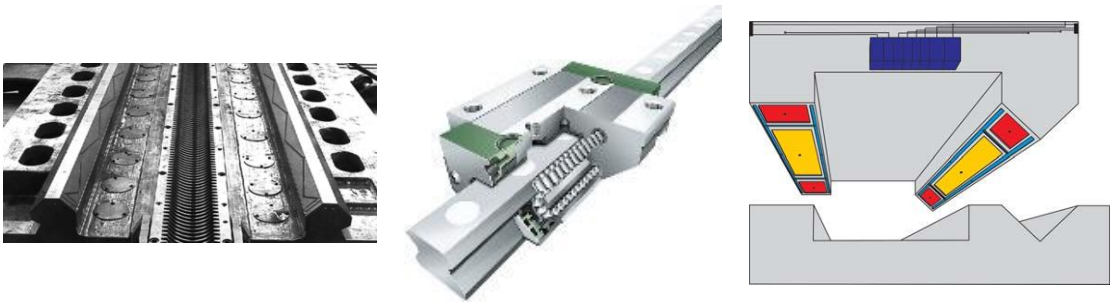

Figure 2.8 Different machine tool guiding systems [98].

2.3.1 Friction modelling

Friction is a result of a complex interaction between two contacting surfaces with relative motion. In 1994, Armstrong et al. [100] described the physics behind this phenomenon and summarized the different models and compensation techniques. The friction force can be described considering two main regimes: pre-sliding (also called sticking) and

sliding regimes (Figure 2.9). During the pre-sliding, the asperities of the surfaces in contact (at which micro-welds are hypothesized) act like springs which are being broken one by one and the friction force is displacement dependent until the sliding regime begins. As the sliding regime becomes dominant, solid to solid contact between the surfaces starts to disappear and the friction force depends on the sliding velocity.

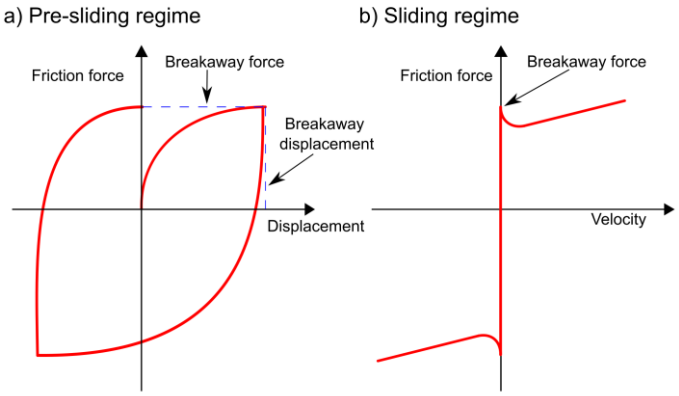

Figure 2.9 Representation of pre-sliding and sliding regimes.

According to the general friction literature, there are two main groups for its characterization: static and dynamic models. In static friction models, the friction force is a function of the applied force and axis velocity. Coulomb or Stribeck [101] based models face modelling problems at very low speed and motion reversals due to undetermined friction force at zero-sliding speed [102]. The transition from positive to negative motion is always associated with small relative displacements between the two bodies before full slip is reached. Several researchers found that static friction models were not able to capture effects associated with frictional interaction such as pre-sliding displacement or frictional lag [103,104]. Hence, more advanced friction models were required. These models are known as dynamic models since they evaluate the friction forces not only based on the actual state of the contact but also based on the contact history by using an extra state variable. This variable represents the average deflection of the bristle that emulates the behaviour of the surface asperities during the contact interaction. The bristles may behave as springs during the sticking phase. LuGre [105] or GMS [106] models capture this behaviour but are more complex to identify and not always easy to use in dynamic simulations (Hagman [107]).

When using friction models in time domain simulations, the discontinuity at very low speed of the static friction models often causes numerical stability problems. To avoid them, the shape of the friction force-velocity curve can be approximated by continuous

functions. Combined models using saturation or $tanh$ functions can be implemented to create a smooth transition around the velocity reversal [108–110]. The main assumption is to consider zero friction force at zero-velocity; thus, friction force only exists in presence of relative motion. The $tanh$ smoothly accommodates the transition to a full sliding regime for low-velocity increments. In 2007, Andersson et al. [108] compared their proposed continuous model against a dynamic model named Dankowicz [111], concluding that the model was well adapted for transient oscillating simulations. However, this model solely depends on the velocity, so the prediction of the final position is less accurate than with dynamic friction models (Figure 2.10).

Even though friction has been extensively studied for accurate motion positioning [112,113], some works have been done regarding the friction influence on the dynamics and chatter stability prediction.

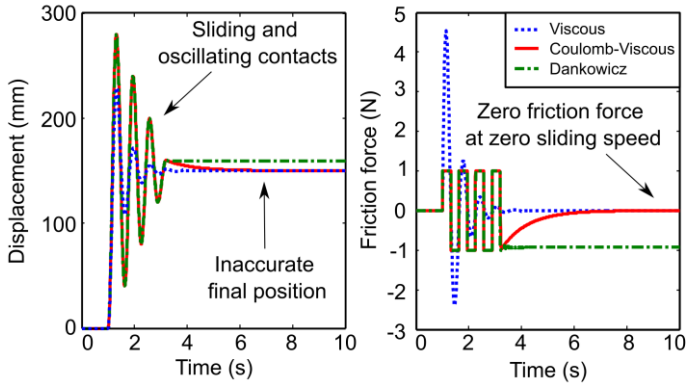

Figure 2.10 Step response of the system with different friction models (based on Anderson et al. [108]).

2.3.2 Friction influence on the cutting point compliance

In 2014, Bianchi et al. [114] analysed the friction influence on the dynamic compliance of the machine tool at the cutting point. This is the first study that combines tool centre point frequency response function and frictional effects. The authors characterized the friction curve by means of LuGre [105] model and added it to their Finite Element model. However, no experimental tool tip compliance evidence was reported. Later, in 2016, Rebelein et al. [115] developed a virtual machine tool model that considers multiple damping sources. The authors extracted, modelled and validated the virtual characterization by impact testing. Their conducted analysis focused on the first resonance of a ball screw drive, where the friction effect was modelled by a combination of Leuven and enhanced Stribeck model. Based on this research, [32,116] extended the

model by adding feed drive servo controls and machine movements. They concluded that linear dissipation sources and nonlinear friction forces had the highest influence on the machine tool vibration characteristics. Analogously, for a certain feedrate level, the damping of the resonance remains constant. Comparing standstill and moving responses, the damping can vary up to 35%. However, as in the previous study, the main flexibility comes from the first resonance of the feed drive, so no extrapolation to the cutting point was conducted.

Kossack et al. [117] simulated and measured the force related dynamics nonlinearity on a friction measuring machine. Similarly, Irino et al [118] modelled the nonlinear dynamic characteristics of the machine tool structure with respect to the excitation force level. The authors found the biggest dynamic variation in the ball screw–nut and guideway block-rail interfaces. Apart from the force level nonlinearity, the machine dynamics are also modified by the axes feedrate. In 2020, Sato et al. [119] pointed out that existing friction in guiding and process level can modify the amplitude of the cutting forces and the dynamics of a ball screw driven table. Similarly, Oshita et al. [120] showed that the damping and stiffness properties of the guideways are modified in the radial and vertical directions when the axis is moving at different feedrates.

Recently, Tunc and Gonul [68] showed the difference of the tool tip FRF of a robot with milling capabilities, under static and quasi-static conditions (Figure 2.11). The root cause of this variation has not been stated, but the authors attributed this effect to variations of gear dynamics at the joints such as frictional damping and stiffness.

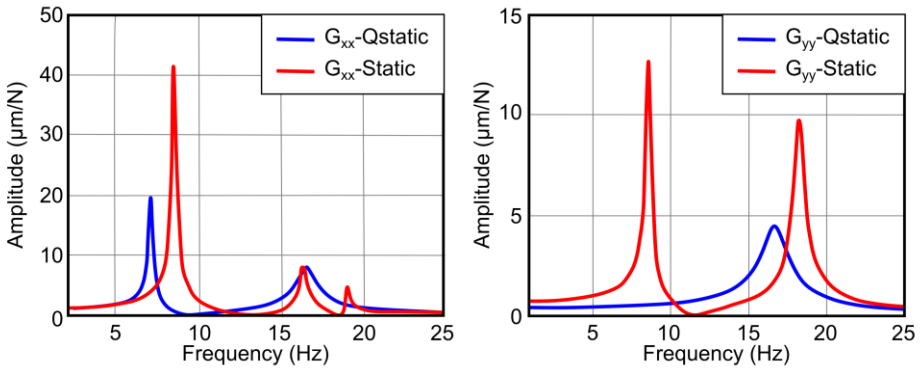

Figure 2.11 Static and quasi-static conditions (based on Tunc et al. [68]).

As concluded in the literature, friction in the guiding system can affect the machine tool dynamics. However, the interaction between the machine structural response and the different elements that are present at the feed drive system, such as friction, control loops

and machine movements are not clearly studied in literature. Therefore, Chapter 5 presents an analysis of the friction on the nonlinear dynamics of machine tools and its effect on chatter stability predictions. A theoretical model is experimentally validated on a laboratory single axis test bench. Experiments conducted in a machining centre show the strong influence of friction on the process stability predictions where deviation up to 240% in the expected depth of cuts are obtained.

2.4 CONTROL OF MACHINE TOOL FEED DRIVES

Industrial machine tools classically use a cascade control loop structure with current, velocity and position feedback loops as well as feedforward actions (Figure 2.12). As the control of machine tool feed drives has the particularity that the setpoints are known in advance and respect certain kinematical constraints in terms of velocity, acceleration and jerk, the velocity and acceleration calculated during the trajectory interpolation can be sent to the inner control loops to anticipate the movements with feedforward actions. The control structure is often referred as P-PI cascade control due to the fact that the position loop uses a proportional gain and the velocity loop is closed with a proportional gain and integral time. This control scheme offers good parameterisation and extensibility with good dynamic characteristics (Gross et al. [121] and Koren et al.[122]). In a standard numerically controlled machine, the axial position is measured by a linear scale and the velocity is obtained by numerically differentiating the measured position from the motor encoder or the linear scale.

The current loop is the innermost loop and is tightly linked to the model of the motor. As the tuning of the PI gains is not affected by the mechanical modes of the machine, the parameters given by the motor manufacturer are usually satisfactory. In addition to the current loop, filters such as notch or low pass can be used to avoid the excitation of higher frequency content, giving the opportunity to boost the controller bandwidth.

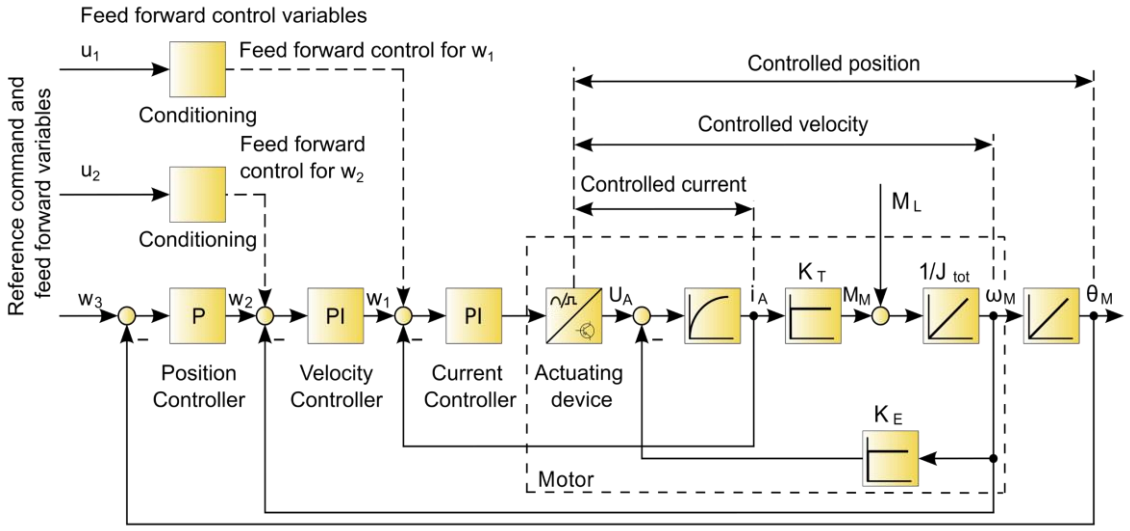

Figure 2.12 General machine tool feed drive control scheme (Gross et al. [121]).

Although the principal objective of the feed system is to drive the machine to the desired location, they can also be used for vibration control. This control is principally used for reducing vibrations caused by the inertial forces generated during the acceleration and deceleration of the machine. As the motion commands constitute a major source of excitation, several pre-filtering techniques and improvements in tool trajectory generation have been reported with the aim to avoid exciting the natural frequencies of the driven machine (Khoshdarregi et al. [123] and Erkorkmaz et al. [124]). Nonetheless, when external excitations are presented, such as cutting forces, only vibration modes that are controllable by the feed drives actuation direction and that are observable through the feedback sensors available in the machine can be damped.

2.4.1 Damping increase using classical P-PI control loops

The structural chatter vibration appearing in the low frequency range have modal shapes that can be observable by the feed drives feedback encoder system, therefore the motion controllers used in industrial application can significantly modify the cutting point dynamic behaviour. In 2008, Zirn [125] remarked the influence of the velocity proportional gain in the damping coefficient of the vibratory behaviour of the mechanical system. The author proposed a specific tuning method for this gain with the aim to maximize the damping coefficient that the feed drive controller can provided to the driven flexible system. In 2012, Albertelli et al. [126] proposed a process stability oriented tuning method to maximize the disturbance rejection transfer function around the chatter frequency region. In 2013, Uriarte et al. [1] reviewed the design and engineering principles for large

machine tools. They described how the low structural natural frequency of the machine is usually the limitation for the behaviour of the servo axes. In large machines, the drives tend to have higher natural frequencies and therefore it is the vibration of the structure that limits the control loop gains and the achievable acceleration and jerk values. They discussed the regular servo tuning methods, which only pays attention to the motor side and neglects the tool centre point dynamics. Although the control loop will follow the CNC commands in the best possible way, it should be responsible to get the best behaviour at the tool centre point and not only at the motor side. Following this statement, Beudaert et al. [63] simulated in 2016 that a correct tuning of the controller could significantly impact the machining capabilities, especially when the tool centre point FRF is taken into account in the commissioning procedure. In a similar way, Lehotzky et al. [127] studied the effect of a proportional-derivative controller on the stability of a turning process.

2.4.2 Damping increase by additional control loops

The feed drive systems are normally located far from the tool and have a narrow bandwidth, especially in large machine tools applications. In order to extend the observability and add the main point of interest into the control scheme, Futami et al [128] studied for the first time in 1983 the use of an external acceleration sensor for actively suppressing the resonances of an industrial robot arm. Alter and Tsao [129] investigated in 1994 the use of an actively controlled linear motor to increase the turning process stability. Later in 1995, Chen and Tlusty [130] simulated the use of an additional acceleration loop to improve the machine dynamics. In 2005, Forster et al. [131] patented a method for attenuating chatter vibrations using a controllable force in both feed and transverse directions in a linear motor driven machine tool. At the same time, machine tool CNC manufacturers also worked to implement this kind of solution in their commercially available products. In 2009, Siemens [132] patented a solution called Advanced Position Control which enables to damp the mechanical vibrations for machine tool applications. On the other hand, Heidenhain [133,134] presented their Active Chatter Control solution for their CNC systems, which uses the machine's own feed drives to remove the energy from the vibration. In 2014, Kakinuma et al. [135] proposed a band-limited force control to actively suppress chatter vibrations in a desktop-sized turning machine. In 2015, Munoa et al. [136] presented a new technique for improving the cutting capabilities of the machine by injecting active damping through the feed drives using an external accelerometer (Figure 2.13-left). They experimentally showed that the proposed strategy can increase the productivity between 85 and 600% by suppressing the low-

frequency structural chatter. In 2016, Beudaert et al. [137] analysed the limitations of adding the extra loop for chatter suppression, finding that non-collocated controller amplifies the counter phase mode, which prevents it from obtaining an optimum system. In 2017, Franco et al. [138] actively damped the structural resonance of a large vertical lathe machine adding damping signals in different control architecture set points (Figure 2.13-right). In 2021, Dumanli et al. [139] presented a controller to mitigate high frequency chatter vibrations by shaping the stability lobes of a turning process.

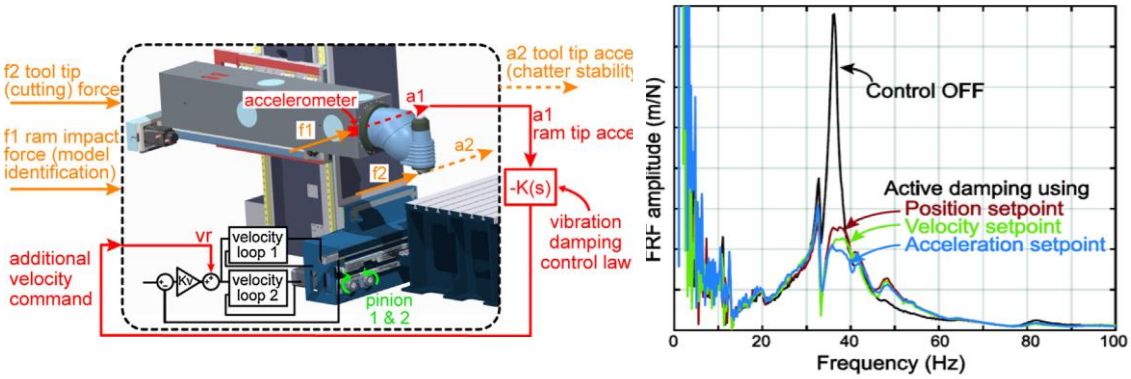

Figure 2.13 Active damping strategy implementation [136] (left); b) FRF compliance with active damping feedback introduced in different setpoints [138] (right).

2.4.3 Non-conventional control techniques

However, apart from standard control configurations or addition of extra loops, different control techniques are presented in the literature (Altintas et al. [98]). The use of pole placement control technique has also been reported in the literature. With this, the closed loop poles of the system are placed in pre-determined locations in the *s*-plane (Astrom et al. [140]). In 2013, Gordon and Erkorkmaz [141] concluded that this technique was simple and effective for positioning and actively damping vibrations of a ball screw drive (Figure 2.14-left). The Sliding Mode Controller has also been employed for feed drive control in different approaches to actively damp the natural vibrations of a ball screw [142–144] (Figure 2.14-right). Recently, Neubauer et al. [145] applied this control approach instead of the conventional P position controller. The authors obtained a considerable improvement of tracking and disturbance rejection performance on an industrial ball screw drive.

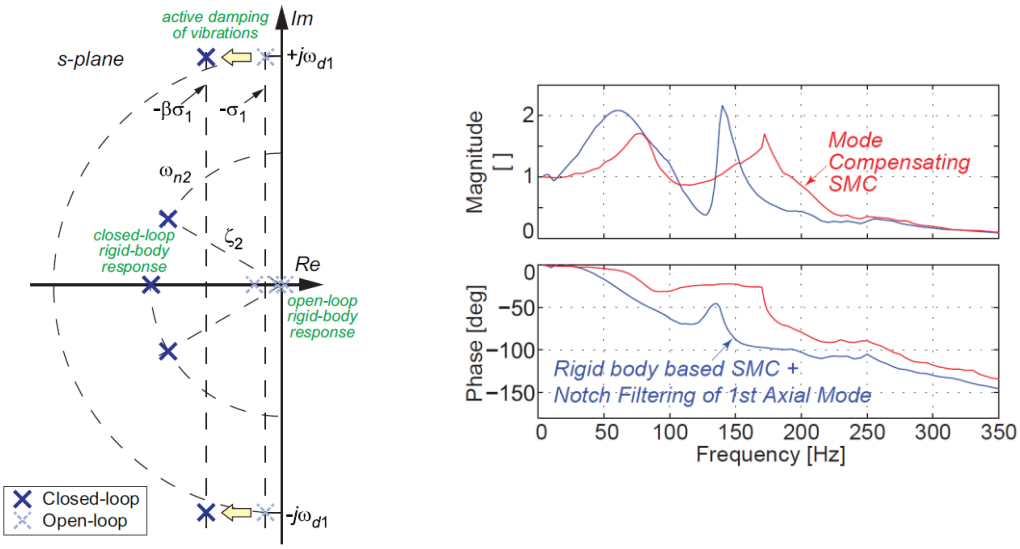

Figure 2.14 Pole location modification [141] (left); Sliding Mode Controller application [143] (right).

As a result of their strong performance in tracking and disturbance rejection applications, Linear-Quadratic Regulators are often used in literature for active vibration control of machine tools. Al-Zaharnah [146] applied this controller for a turning model to maintain a constant relative position between tool and workpiece. Analogously, Van Brussel et al. [147] proposed the implementation of H_∞ robust control to control feed drives, using the nominal position of the machine tool and adding the information of the dynamic variations in model uncertainties. The application of Generalized Predictive Control has been applied by Dumur et al. [148] in flexible feed drives to compensate for structural mode variations. However, the effects of external disturbances were not considered. Berners et al. [149] optimized a linear Model Predictive Controller as a closed loop position controller for feed drives based on a genetic algorithm. They obtained lower overshoot and contour deviations compared to a regular proportional controller.

Additionally, Sun et al. [150,151] boosted the bandwidth (> 80%) of a standard cascaded controller by introducing changes in the control structure, adding either a second P velocity control loop (table velocity added to regular motor speed) or a derivative action to the regular position proportional gain.

Although several publications have demonstrated that advanced control structures can outperform the classical P-PI configuration, the cascaded control loops give satisfactory results for the vast majority of machine tools applications. However, in literature, only simplified dynamics are considered during the existing commissioning approaches.

Therefore, Chapter 3 presents a frequency based MIMO model that couples the servo controller and machine dynamics to analyze the influence of each control parameter on the tool centre point compliance. Later, Chapter 4 presents a new strategy to achieve optimum vibration damping and improve the chatter stability via a servo controller tuning procedure which can be implemented in every regular industrial machine tool.

2.5 VIRTUAL MACHINE TOOLS

Finite Element modelling can provide valuable dynamic characteristics like natural frequencies and mode shapes during the machine design stage with reasonable accuracy. However, at this point, the damping properties are very difficult to estimate, due to the fact that machine joints are the main contributors (Munoa et al. [2]). Additionally, classical Finite Element modelling approaches exclusively considers mechanical components. For this reason, Altintas et al. [61] pointed out the importance of coupling the servo control loops to the structural dynamics. With this, the interactions between the mechanical structure and the controller during the design stage can be estimated. The authors summarized the most common approaches for coupled simulation, where two main groups are introduced (Figure 2.15).

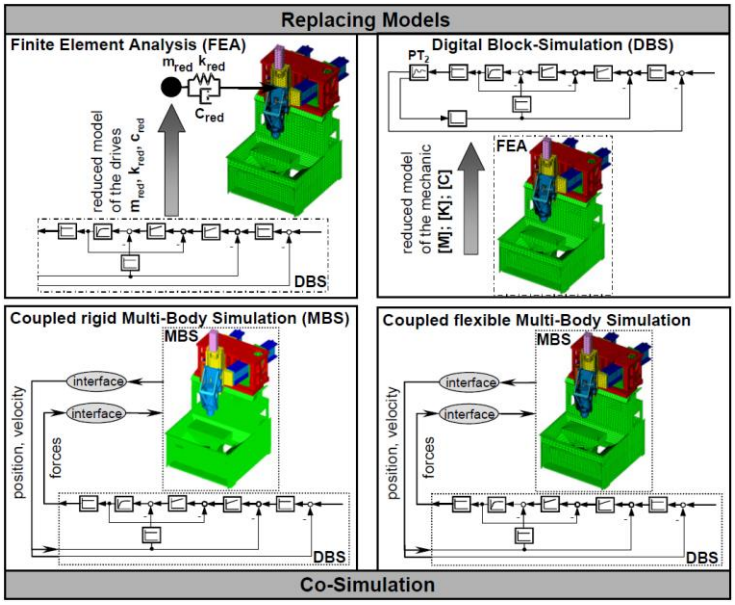

Figure 2.15 Different approaches for coupled simulation of structural dynamics and control loops [61].

For the so-called replacing models, an analogue model of the control scheme is added into the Finite Element model or the machine dynamics are added into the simulation of the control loop [152]. In the co-simulations, two independent simulation environments

(one for control loops and one for machine structure) are coupled via interfaces during the simulation [153]. Bartelt et al. [154] developed a new software architecture which synchronizes concurrent simulations performed in different environments to facilitate the employment of this technique. Matlab Simulink [155], Dymola [156] or Simcenter Amesim [157] software offers interfaces to generate the mechatronic model of the machine tools. Abdul-Kadir et al. [158] presented an extensive review on virtual manufacturing, concluding that even though there are already plenty of tools to analyse different aspects of machine tools and machining, they felt a lack of integration.

The research community has been working in the development of more integrated virtual models. In 2004, Zaeh et al. [159] developed a Finite Element model of the feed drive system and simulated the performance of the axis control law under the influence of structural vibrations. In 2009, Vesely et al. [160] outlined the procedures and trends for the machine tool mechatronic modelling. Later, Neugebaur et al. [161] described the steps and a new compact form of mechatronic simulation for the determination of static and dynamic stiffness, obtaining good experimental validations. Recently in 2019, Zaeh et al. [116] improved the simulation model by introducing linear damping, nonlinear friction and motion commands. Following a similar approach, Wiesbauer et al. [62] validated their coupled model by using a tubular linear motor to measure FRFs during uniaxial carriage movements. Analogously, position-dependent dynamics can be evaluated by reduced-order substructure Finite Element models [162–164]. Apart from Finite Element modeling, multibody dynamic modelling is also presented in the literature. Huynh et al. [165] presented a methodology for developing a multibody dynamic model of a 5 axis machining centre. Similarly, in-process data from actual machine tools can be used for generating a digital twin (Wang et al. [166]). In 2009, Brecher et al. [167] reviewed the different solutions to relate machine-process interactions for different manufacturing processes, stating that to fully understand the manufacturing system (with respect to vibrations, deflections or thermal deformations) these interactions must be studied (Figure 2.16). Full Finite Element based process and machine modelling was presented by Schermann et al. [168] for a turning process. However, extremely long calculation times were required. A comprehensive representation of the machining process forces, process stability and machining results were obtained by Witt et al. [169] coupling a flexible multibody simulation and an analytical process model.

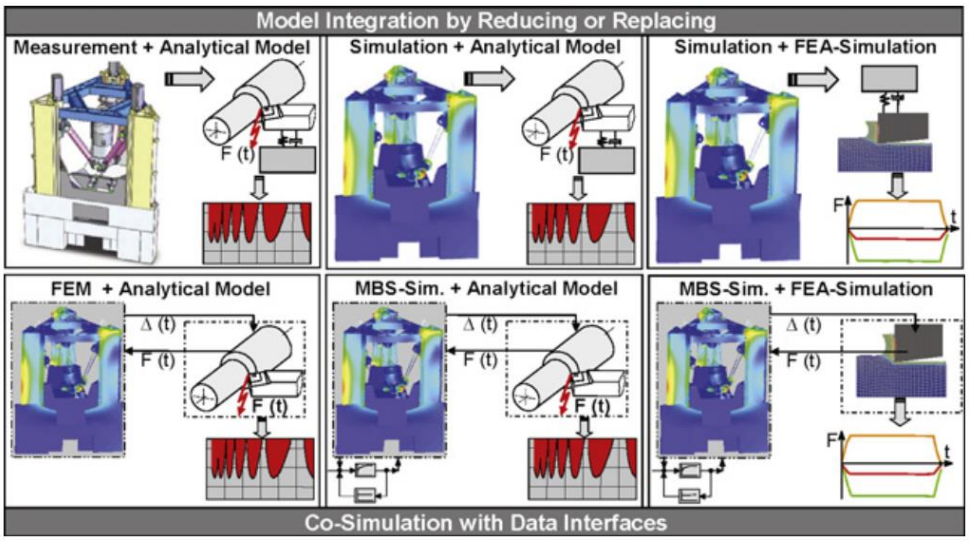

Figure 2.16 Overview of different approaches for machine-process coupled simulations [167].

These machine digital twins can be used for early stage machine redesigns (Neugebauer et al. [170]) or to virtually commission the control gains (Berkemer [171]). Following this goal, Kolar et al. [172] developed a virtual machine tool to increase the productivity by optimizing the control system interpolator settings. As described by Armendia et al. [173], virtual machine tool packages can interpret the G-code to check machine movements according to the programmed tool path and kinematics with the aim of training and process checking (i.e. collision avoidance [174]). Recently, Hänel et al. [175] presented a general model structure for digital twins applied to machining processes.

Table 2.3 summarizes the different virtual machine tools proposed in the literature. Significant research efforts have been oriented to the modelling of ball screw feed drives but very few publications are dealing with rack and pinion feed drives.

Table 2.3: Virtual machine tool models presented in literature.

Reference	Friction model	Purpose	Control loops	Machine dynamics	Feed drive type
Zaeh et al. [159]	No	Dynamics	Yes	FE	Ball screw
Zirn [125]	Coulomb	Dynamics Tracking	Yes	FE	Linear drives
Neugbauer et al. [161]	No	Dynamics	Yes	FE	Ball screw
Neugbauer et al. [170]	No	Dynamics	Yes	FE	Ball screw/Linear motor/Rack and pinion
Bianchi et al. [114]	LuGre	Dynamics	Yes	FE	Ball screw
Rebelein et al. [115]	Leuven + enhanced Stribeck	Dynamics	No	MB	Ball screw
Rebelein et al. [32]	Leuven + enhanced Stribeck	Dynamics	Yes	MB	Ball screw
Zaeh et al. [116]	Leuven + enhanced Stribeck	Dynamics	Yes	FE	Ball screw
Kolar et al. [172]	No	Tracking	Yes	FE	Not defined
Wang et al. [166]	Stribeck	Tracking	Yes	MB	Ball screw/ Linear motor
Sato et al. [119]	Own model [176]	Dynamics	Yes	MB	Ball screw
Huynh et al. [165]	No	Dynamics	No	MB	Ball screw
Wiesbauer et al. [62]	LuGre	Dynamics	Yes	FE	Ball screw

As indicated above, in order to generate the machine digital twin which considers the controller effect, friction characteristics and machine motion profiles, the modelling of the feed drive system is a mandatory step. Therefore, the next section describes the characteristics of each feed drive system. A deeper description of the rack and pinion feed drive mechanism employed in the large machine tool industry is provided later in Section 2.6.

2.5.1 Feed drive technologies

Current machine tools are sophisticated mechatronic systems as reviewed by Altintas et al. [98]. The machine tool feed drive system is used for positioning the machine components carrying the tool and workpiece to the desired location. Hence, the machine positioning accuracy and dynamics will determine the quality of the produced part and the manufacturing productivity. Machine tool manufacturers typically implement one of three main kinds of feed drive systems: ball screw, linear motor or double pinion and rack, according to each machine's operational requirements [98,177] (Figure 2.17). One of the main aspects to consider while choosing the feed drive system is the travelling distance of the axis, as it directly affects the cost and performance of the driven machine. The ball-screw drive is the most widespread system for travel distances not exceeding 4-5 m [178], as it achieves the required precise positioning at a high efficiency to cost ratio. The second most industrially implemented feed drive type is the direct drive or so-called linear motor solution. The main characteristic of this system is the lack of mechanical transmission elements; hence, backlash or wear problems are eliminated. However, the cost of this type of feed drive is high and therefore, linear motors are generally not used for heavy machines with long strokes. The third solution is the double pinion and rack system, typically installed in long travel applications exceeding 5 meters. By adding several racks together, very long strokes can be realized without modifying the stiffness of the system, which is independent of the travelled distance. Uriarte et al. [1] reviewed the engineering principles of large machine tools, concluding that this feed drive system should be installed in machines combining long travelling distances and high loads.

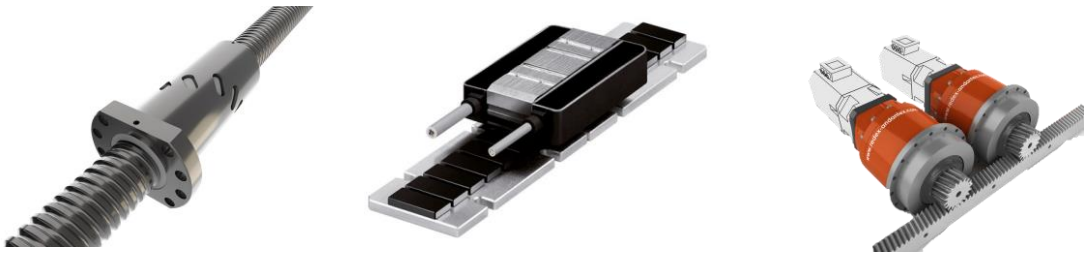

Figure 2.17 Ball screw [179], linear motor [180] and rack and pinion feed drives [181].

The accuracy requirements of machine tools demand the use of drives where the backlash has been reduced to the largest possible extent. Even though the machine powertrain system is designed to minimize the clearance, the achievable precision and rigidity can be increased by generating a preload. The value of the preload force is an important property that greatly influences the quality of the feed motion, dynamical

operational behavior as well as the expected service life and energy consumption. As concluded by Altintas et al. [98], direct drives powered by linear motors have zero backlash; therefore, no preload is required. However, ball-screw and rack and pinion feed drive systems require a tensioning force to suppress the existing clearance.

2.5.2 Ball screw drives

For ball screw applications, the nut is usually preloaded to remove any axial clearance generated between the recirculating balls and the guiding slots of the screw (Figure 2.18-left). As a result, the contact stiffness of the recirculating balls with the nut's thread is increased. The most popular solution among ball screw manufacturers for high demanding applications is to generate the preload by adjusting a spacer between two nuts, where the thickness of the spacer determines the generated preload force [182]. The existing clearance can be also minimized by using recirculating balls of slightly larger diameter than the available space. Despite its simplicity, this kind of preload is only valid when the required preload is small, as the recirculating balls undergo sliding at the contact points, which generates high wear and tear. Excessive preload increases the wear and heat generation. For that reason, the preload force is approximately limited to 12% of the dynamic load capacity, where the regular value is set around 6-8% [178]. Verl et al. [183] proposed a novel design principle for ball screws, allowing a considerable reduction of the preloading and improving the operating characteristics by introducing a passive overload mechanism.

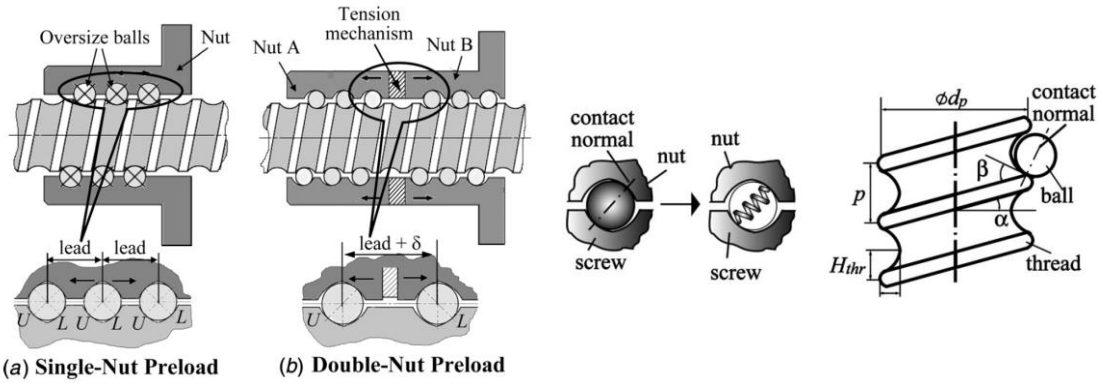

Figure 2.18 Single and double-nut preload screw-nut interface [184] (left); Spring model of balls in screw-nut interface [185] (right).

The direct identification of the ball screw preload is generally complex and expensive. However, the preload level of an assembled ball screw can be determined by measuring the drag torque at 100 rpm when no external loads are applied as described by the

standard DIN ISO 3408-3 [186]. Verl et al. [187] studied the correlation between the feed velocity and the effective preload through a preload sensing mechanism. They concluded that the pretension value changes depending on the velocity of the commanded feed motion. The variation at lower speeds can be neglected but it has to be taken into consideration for rapid motions. Following this idea, Zhou et al. [188] conducted an analysis of the difference between the estimated preload based on traditional formulas and experimentally measured values. The researchers designed and built a preload-adjustable ball screw mechanism to examine the relationship between preload force and drag torque. They proposed and compared a new modelling approach for three different preload levels, obtaining a considerable prediction improvement.

As a result of modifying the preload amount, the contact stiffness is also modified and hence, a variation of the system dynamics can be expected. Feng et al. [189] and Zhang et al. [190] show the influence of the preload on the natural frequencies of the feed drive system. In 2019, Ngueyn et al. [191] monitored the preload value by evaluating the natural frequency of the screw nut in the axial direction and Denkena et al. [192] by a sensor fusion approach.

For the interface modelling, Zaeh et al. [159] derived the stiffness elements for the preloaded nut interface and coupled it to a FE model. The model contained the cross-coupling effects of the axial and torsional directions. In 2009, Okwudire et al. [185] expanded Zaeh's formulation to also consider the effect of lateral stiffness. By doing so, the proposed model was able to capture additional cross-coupling terms between the deformations in the axial, lateral and torsional directions. Later in 2011, Okwudire [184] proposed an improved model for screw-nut interface (Figure 2.18-right), which considered the elastic deformations of the screw within the nut for accurate natural frequencies prediction. In 2018, Brecher et al. [193] introduced a calculation methodology to analyse the interaction of the load distribution and single rolling element contacts within a ball screw (Figure 2.19). The influence of the inner geometry on the system behaviour such as elastic deformation of the nut and spindle or load distribution can be determined by the proposed methodology. Also, the model allows a detailed analysis of the contact characteristics of the rolling elements.

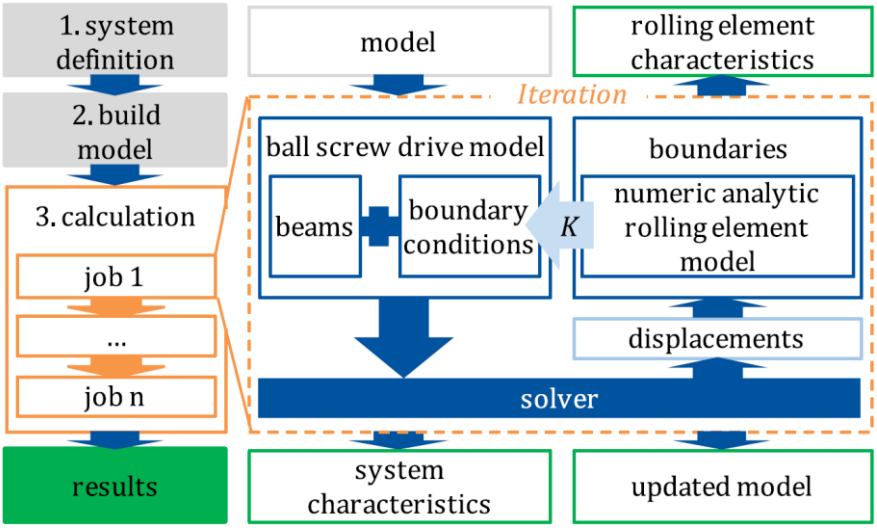

Figure 2.19 Calculation model to identify rolling element contact characteristics [193].

The ball screw feed drive modelling has been well addressed in the literature with several test benches, machine tool measurements and model correlation. However, little attention has been devoted to the rack and pinion by the academic community. This reduced attention might be associated to the fact that rack and pinion drives are generally used for large machines that are not present in the university facilities. However, there is an industrial need to accurately model the complex rack and pinion feed drives.

2.6 RACK AND PINION FEED DRIVES

As described in Section 2.5.1, rack and pinion feed drives are employed in applications with long travelling distances. Apart from the machine tool field, this technology is used in different sectors such as automotive for the steering wheel, oil and gas for self-elevation of the offshore platforms or for elevator design purposes (Figure 2.20). Additionally, the use of a single pinion and rack is also present in machine tools for secondary services like door opening-closing systems or for building lower cost machines in applications where the backlash effect can be neglected (e.g., laser cutting machines).

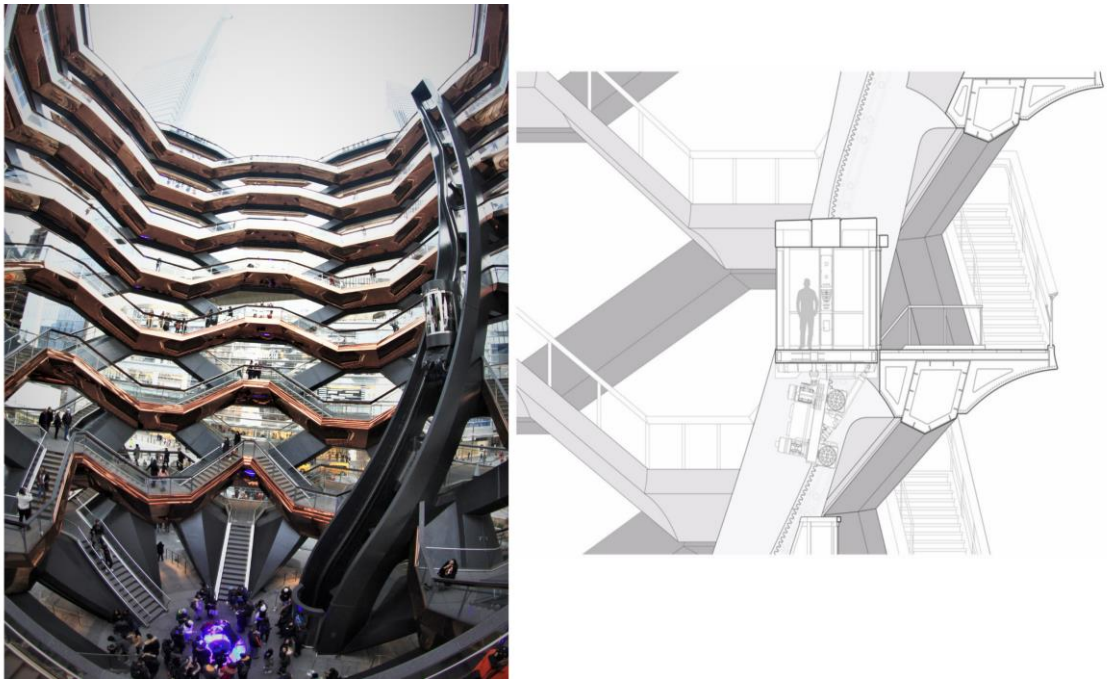

Figure 2.20 Use of rack and pinion feed drive in elevator industry (detail [194]).

There are very few publications dealing exclusively with rack and pinion feed drives for machine tool application. Table 2.4 provides an exhaustive review of all relevant research publications.

Table 2.4: Summary of rack and pinion research in the machine tool field.

Feed drive	Research topic	Reference
Double pinion and rack	Backlash	[125,195–199]
	Static/dynamic stiffness	[65,200]
	Disturbance compensation	[138]
Single pinion and rack	Design	[201]
	Disturbance compensation	[202,203]
Single/double pinion and rack	Monitoring	[204]

In 2006, Choi et al. [201] presented a design optimization of a single rack and pinion feed drive installed in a router machine. As a result, the feed drive vibration amplitude decreased by almost 50% with respect to the original design. Disturbance compensation minimization (such as process forces) has also been studied in literature. In 2021, Brenner et al. [202] developed an acceleration-based disturbance compensation method

for a single pinion and rack feed drive system by generating a torque computed from the difference between estimated and real table accelerations. By using the standard master-slave configuration, Franco et al. [138] actively damped the structural resonances of a vertical lathe. Similarly, friction-generated disturbance minimization has also been studied in literature (Karim et al. [203]). In 2016, Ehrmann et al. [204] showed the prospect of condition monitoring of rack and pinion drive systems to reduce unforeseen failures and machine stops. The authors concluded that there is a need for action for this specific feed drive mechanism.

Additionally, the preload effect on static and dynamic stiffness has been addressed. In 2015, Engelberth et al. [200] experimentally identified the variation of the feed drive system stiffness with respect to different preload values. The authors showed that in higher force range, the equivalent stiffness is approximately invariant to the commanded preload value (Figure 2.21-left). Inversely, Franco et al. [65] experimentally showed the machine tool dynamics variation for different preload values (Figure 2.21-right).

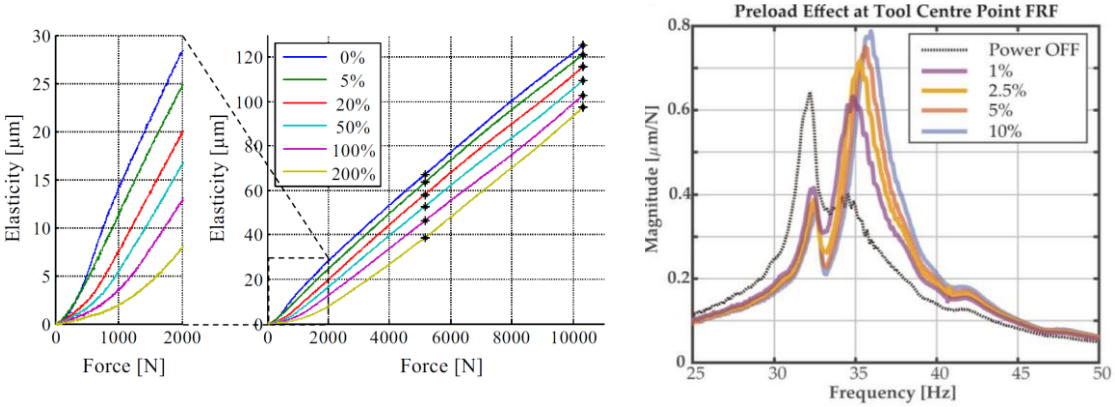

Figure 2.21 Stiffness of a rack and pinion drive with different preloads [200] (left); Tool centre point compliance with different preloads [65] (right).

However, the majority of the publications are focused on backlash compensation approaches or analysis (Table 2.4) as it is a major concern when using this feed drive system. The next section describes the different techniques presented in the literature to minimize this effect.

2.6.1 Backlash suppression techniques

For the particular case of the double pinion and rack feed drive model, the backlash is defined as the distance measured along the pitch line, that a gear needs to move until it engages with another gear that is fixed or immovable. As described by Smith et al. [205],

gear backlash is needed to provide running clearance, as well as to handle manufacturing tolerances or reduce factors such as heat generation, noise, unusual wear and possible overload that can end up generating a failure of the drive. In literature, two different approaches have been proposed to minimize the existing clearance by exerting a preload.

Mechanical means

On one hand, mechanical solutions have been proposed to tackle this existing clearance, such as the utilization of split pinions [206] (Figure 2.22-left) or mechanical assemblies [207]. Alternative approaches, such as hydraulic actuation, have been also proposed [208]. However, as concluded by Prodan et al. [199] this approach cannot completely eliminate the existing play between the two segments of the sliced gears. Similarly, industrial commercial solutions are also available using a single motor connected to a gearbox [181]. Variations of traditional rack and pinion mechanism are available in the market [209], called roller pinion solutions. Unlike traditional joints, the system is designed to run with interference which allows two rollers to remain preloaded at all times (Figure 2.22-right). Despite its cost-effectiveness, in these kinds of solutions, the existing preload value cannot be changed or adapted without a mechanical reconfiguration of the systems.

Figure 2.22 Split pinion [206] (left); Existing variations of rack and pinion [209] (right).

Control means

On the other hand, in large machine tool applications, where a driven axis or load can exceed the maximum capabilities of standard servo motors, a parallelization of the drives increases the input torque. In addition, the second drive can be used to generate the pretension torque suppressing nonlinear vibrations that can be originated by backlash in combination with the axis feedback control (Zirn [125]). Current industrial trend is to use a double motor actuation where the preload is managed electronically by the machine's CNC controller. This approach helps simplify the mechanical design of the drive at the

cost of increasing the controller complexity, but nowadays industrial CNC manufacturers provide this control solution.

In the absence of a separate linear encoder, the rotary encoder of one of the motors can be used to close the position loop for both drives. In this case, the corresponding motor becomes the master and the other one the slave motor. However, in high-end machine tools which offer additional linear scale feedback used to close the position loop, the overall control system assumes a symmetrical structure with only the motor designations to be called ‘master’ and ‘slave’ (Figure 2.23).

To perform the electronical preload, the velocity control loop differs from other feed drives mechanisms as it follows a master-slave coupling. The master drive is completely position and velocity controlled, whereas the slave drive follows the velocity setpoint computed by the master position control loop. Engelberth et al. [200] summarized the different existing control structures for inducing a preload in double pinion and rack feed drives. The control scheme integrated in regular commercial CNCs is an extra PI type controller that is implemented to adjust the desired preload torque (Figure 2.23). This controller, which is usually called the torque equalization controller, generates an additional speed setpoint for each motor by considering the desired torque preload. This configuration also allows to use different motor powers, as it offers individual weighting factors to adapt the torque distribution. In the case of using two identical motors, these factors have to be equal ($K_{\mathrm{Tm}} = K_{\mathrm{Ts}} = 0.5$). The desired preload can be defined in the CNC controller by modifying the parameter, called torque bias or tension torque (τ_{p}), which is defined as a percentage of the motor rated torque. In 2008, Zirn [125] stated that a moderate integral time value could be defined to ensure the static pretension torque independently of the defined weighting factors.

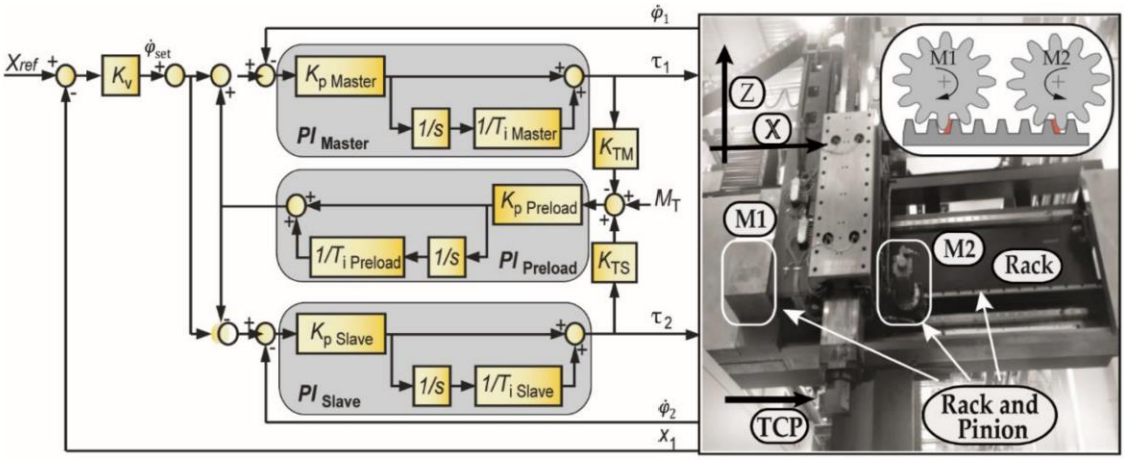

Figure 2.23 General master-slave configuration control structure [65].

Although a clearance-free system is desirable, the increment of the preload level leads to a reduction of the maximum achievable acceleration. In 2013, Heidenhain [210] provided a CNC option called Motion-dependent Adaptation of Control parameters (MAC) which varies the tensioning torque for increasing the achievable acceleration. This tool provides a way to change machine parameter values depending on certain inputs such velocity, following error or motor acceleration. Later, Verl et al. [197] introduced an adaptive preload approach to adjust the preload value during the machine operation and increase the drive system's energy efficiency. However, there is not a clear tuning rule stablished for preload commissioning. Zirn [125] defined a range between 10–30% of the motor rated torque whereas regular industrial values are established at 20-25% [210]. Verl et al. [197] concluded that only 4% level was enough to compensate the existing clearance.

Variations of the industrial standard control schemes are also reported in the literature. Uchida et al. [195,196] presented two control scheme feedback modifications for backlash compensation, obtaining an improvement in the position accuracy of the system. Similarly, Jiang et al. [198] proposed the utilization of PID controllers to eliminate the gear clearance of a rotary table in a heavy-duty vertical lathe, obtaining an improvement of 56% in the position accuracy.

2.6.2 Description of geared interface modelling

Figure 2.24 shows the overall joint model extensively employed in the gear modelling community. The gears are coupled by a parallel connection of spring and damper elements, in addition to the nonlinear function describing the backlash effect. This modelling approach has also been employed in machine tool geared interface simulations. Zirn [125] modelled the contact area between a worm and worm wheel, where the spring-damper unit represented the combined tooth stiffness of the worm and worm wheel as well as the worm-bearing stiffness. Similarly, the same author proposed a double pinion and rack physical model following the same joint modelling. Later, Engelberth et al. [211] also followed this same modelling approach.

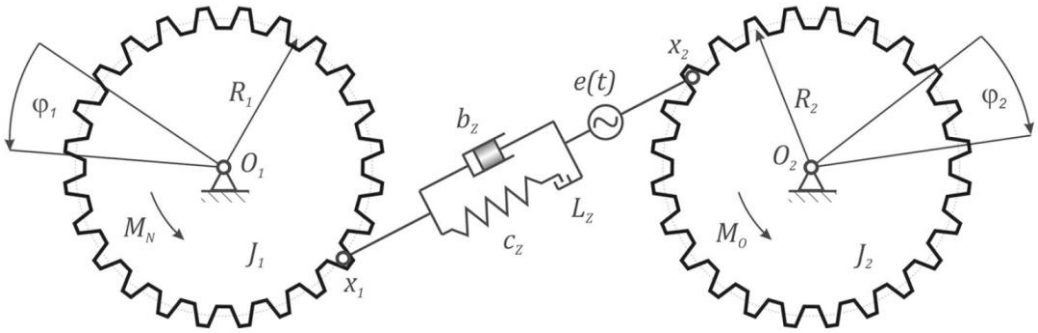

Figure 2.24 Single stage gear transmission model [212].

However, the literature offers very little resources about the double pinion and rack mechanism for the machine tool industry. Therefore, the rest of this literature review focuses on the general analysis of gear contact and gear box dynamics as it provides valuable information for the rack and pinion feed drive analysis.

Mesh stiffness

In 2014, Cooley and Parker [213] reviewed the dynamics and vibration research of planetary and epicyclic gears. The authors summarized the different tools that are available to analyse the transmission vibrations, such as Finite Element tools which can be used for high fidelity contact modelling and analysis [214]. However, accurate contact between the bodies requires long computational times. Lumped mass models can be employed which have shown good correlations with experimental tests and finite element simulations (Cooley and Parker [213]).

The ability to accurately calculate the dynamic response depends to a large extent on how well the gear mesh is modelled. During the operation, as a result of the gear rotation, the contact conditions at the tooth mesh interface vary periodically (Figure 2.25). This results in a periodic stiffness variation at each gear mesh. According to Cooley and Parker [213], four different mesh stiffness models approaches are used in the literature: constant or fluctuating mesh stiffness models, fluctuating mesh stiffness with tooth contact loss and computational models. The first model approximates the real varying mesh stiffness into a constant value. This approach captures the system's features correctly with a simple implementation and resolution comparing to the other models. The second model considers the actual varying mesh stiffness characteristics. This variable stiffness can be approximated using periodic functions (Jingyue et al. [215]), rectangular (Walha et al. [216]) or trapezoidal (Litak et al. [217]) profiles. As a result, a more precise model is obtained where internal dynamic excitations are captured. The

third model is based on the previous one with the addition of the tooth contact loss, as a result of vibrations near resonances. The loss of contact is a strong nonlinearity where the mesh stiffness vanishes suddenly. This nonlinearity leads to classical softening type behaviour of the resonances in the frequency domain. Finally, utilising computational tools, the instantaneous contact conditions and mesh forces are calculated at each time step as the gear rotates kinematically.

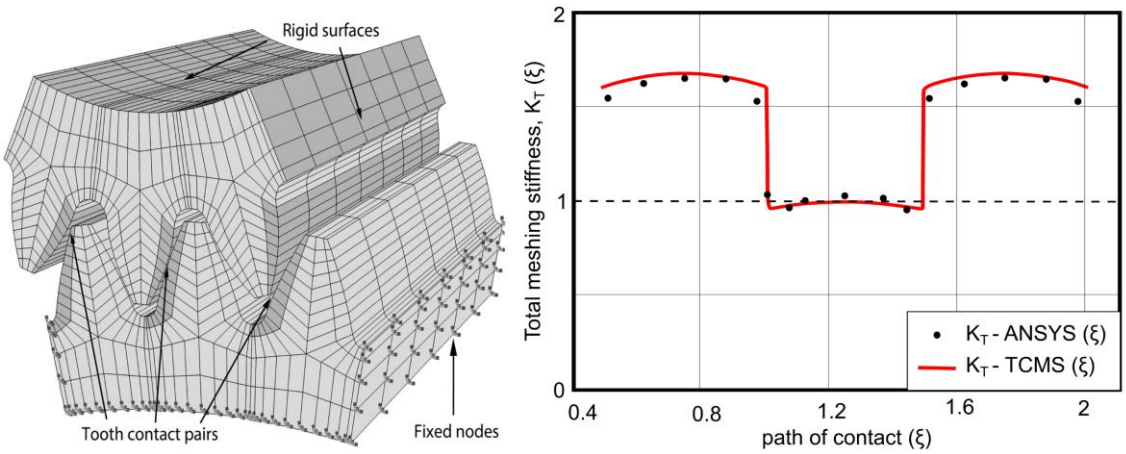

Figure 2.25 Finite Element model and total mesh stiffness evolution along the contact path (based on Sanchez et al. [218]).

As in ball screw drives, where the interface (lead screw, recirculating balls, and nut) equivalent stiffness can be estimated analytically, the ISO 6336 standard establishes a uniformly accepted method for geared transmission wear and bending capacities computation. In the Tooth Contact Analysis (TCA), as a result of the gear tooth elasticity, their contact area is spread over an elliptic surface, and the centre of the contact ellipse is the theoretical point of contact (Figure 2.26). The instantaneous line contact of gear tooth surfaces exists only theoretically (under no gear misalignments or manufacturing errors).

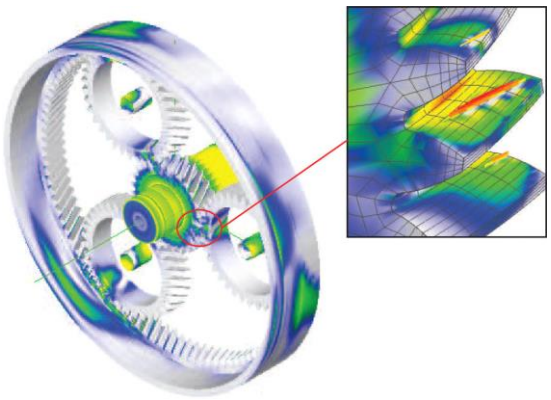

Figure 2.26 Contact stress and pressure using Finite Element simulations [219].

The tooth contact area computation is not standardised, and the different commercially available software packages are validated by experimental measurements, finite element calculations and field experience. In 2004, Wang et al. [220] concluded that not only the rotation of the tooth influences the expected mesh stiffness, but also the applied load amplitude. Kiekbusch et al. [221] shown that as applied load increases, the mesh stiffness varies as a result of the Hertzian contact stiffness (Figure 2.27). In 2016, Xue et al. [222] reported that a variation of 23.5% of torsional mesh stiffness under 5 Nm and 200 Nm of the applied load. Similarly, Mahr and Kissling [223] performed a comparison of the most used commercial software packages where they compared, among many other results, the tooth meshing stiffness. The authors concluded that a correlation factor should be applied to their Hertzian deformation contribution.

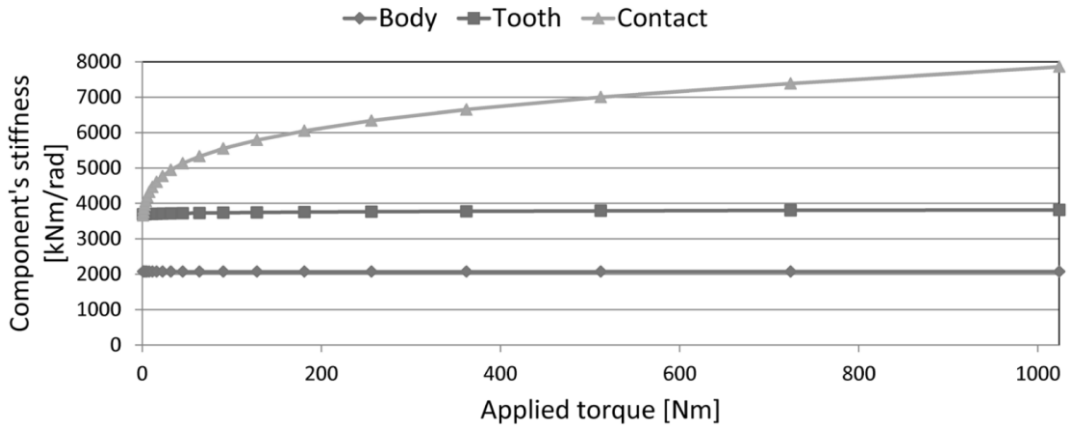

Figure 2.27 Influence of the applied torque on body, tooth and contact stiffness [221].

The ISO 6336-1:2006 standard [224] provides analytical equations to compute an equivalent gear mesh stiffness. The mesh stiffness ($c_{\gamma\alpha}$) is the mean value of the stiffness considering all the teeth in mesh, as shown in Eq. (2.1). The stiffness value depends on two different parameters: the contact ratio (ε_α) and the equivalent stiffness of a single tooth pair (c').

$$c_{\gamma\alpha} = c'(0.75\varepsilon_\alpha + 0.25) \tag{2.1}$$

The contact ratio represents the average number of teeth meshing at the same time. Having multiple teeth in contact means that the load is shared, which increases the average stiffness of the gear, obtaining lower deflection at the teeth. This parameter can be computed following well-known formulas [225]. The single stiffness parameter computation, however, requires a detailed step-by-step procedure. The main expression for its computation is shown in Eq. (2.2). The theoretical tooth pair single stiffness (c'_{th})

is adjusted by means of different weighting factors to adjust theoretical and experimental deviations.

$$c' = c'_{\mathrm{th}}\, C_{\mathrm{M}}\, C_{\mathrm{R}}\, C_{\mathrm{B}}\, C_{\mathrm{F}}\, \cos\beta \tag{2.2}$$

The computed mesh stiffness ($c_{\gamma\alpha}$) can be multiplied by the face width of the tooth (b) to obtain the prediction of the total mesh stiffness, Eq. (2.3).

$$K_{\mathrm{mesh}} = b c_{\gamma\alpha} \tag{2.3}$$

Gearbox dynamics

The gearbox provides a torque multiplication at a cost of a speed reduction. The servo application demands, not only high torque with low added inertia, but also high precision and stiffness. The planetary gearbox meets these specifications with an addition of low maintenance and long operating life. This kind of gearbox consists of multiple planetary gears that revolve around a central sun gear while engaging with an internal gear and rotating on their axes. The continuous engagement of the planetary gears means that the load is shared by multiple teeth, which increases the torsional stiffness. This fact makes them an ideal selection for processes that involve frequent start and stop motions or changes in the rotational direction, which are common characteristics of servo applications. According to Cooley and Parker review [213], the planetary gears can have as little as three planets (which is the lowest number of planets to take advantage of the multiple load paths) or more than ten planets, which can be used in high power applications like aerospace engines (Figure 2.28).

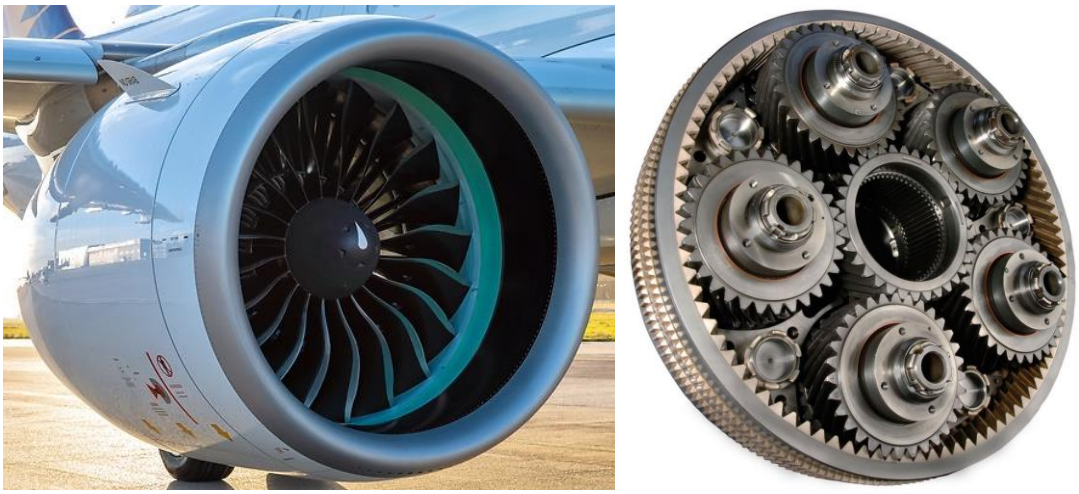

Figure 2.28 Airbus A320neo PW1100G-JM geared turbofan jet engine [226].

In 1973, Cunliffe et al. [227] proposed a two degrees of freedom (torsional and transversal) lumped mass model under lineal and nonlinear mesh stiffness. The linear model was used to determine the natural frequencies and mode shapes. This work classified the mode shapes into overall, sun, radial, tangential and torsional modes. Later, in 1999, Lin and Parker [228] proposed a model to examine the mode shapes properties of a planetary gear with equal spacing. They proved that planetary gears have three types of vibrations modes, independent of the number of planet gears and system parameters. The three modes types are planet, rotational and translational (Figure 2.29).

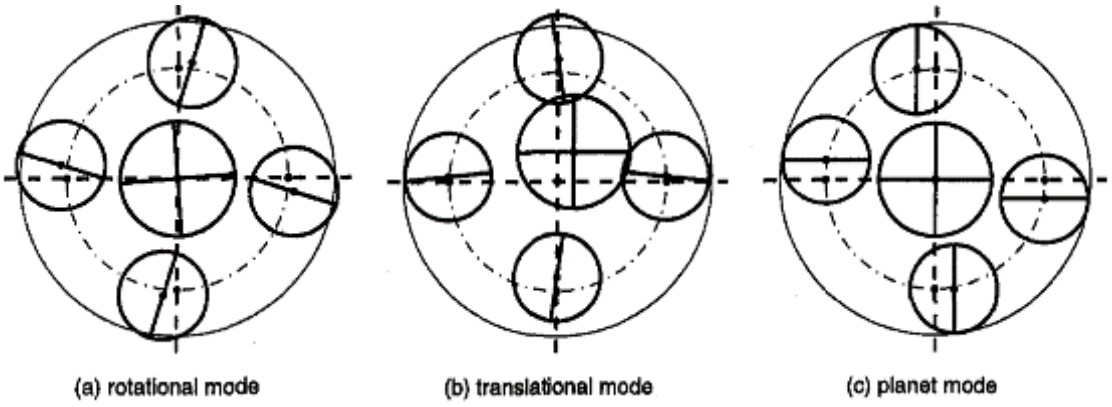

Figure 2.29 System modal shapes [228].

In 2013, Ericson and Parker [229] concluded that the modal shapes of the planetary gears could be divided into two different categories depending on the frequency range. At low frequencies, they are called fixture modes and at higher frequencies gear modes. Within the gear modes, the authors grouped the modes into three clusters consisting of translational, rotational and planet modes (with four or higher planets). The proposed clustering phenomena was experimentally validated. Later, the same authors conducted a research where these two frequency bands were detailed [230]. On one hand, the low-frequency fixture modes (below 1500 Hz) are characterised by the deflection of fixture components such: shaft, inertias and entire planetary gear as a uniform body. On the other hand, high-frequency gear modes are predominantly characterised by the motion of individual planetary gear components, particularly of the planet gears.

This section provided a deep analysis of the existing literature of the rack and pinion feed drive system in the machine tool field. The different backlash suppression techniques are summarized showing that control oriented techniques are more flexible in terms of commissioning than mechanical approaches. The literature in the machine tool field is

limited; therefore, the gear specialized academic community literature is also analyzed to provide a better understanding of the gear and rack interface.

Chapter 3 presents a study of the different control parameters present in the widely used master-slave control configuration. A time domain model which considers the backlash alongside the stiffness of the drive train is presented. The proposed model can predict the observed experimental nonlinear stiffness behaviour for different electronic preload levels. Additionally, a generalized framework is presented to couple linearized machine tool dynamics with the master-slave control parameters. As a result, the influence of each control parameter on the cutting point compliance is predicted by a frequency based MIMO model.

2.7 SUMMARY OF THE LITERATURE REVIEW

This chapter has introduced the chatter vibration problem present in the machine tool industry and how it can be characterized through the stability models. One of the required inputs is the system compliance and the challenges that are faced during the identification process have been also described. Among the different difficulties, the friction present on the machine's guiding system has been described. Existing alternative machine tool dynamics characterization techniques that minimize the stability limit deviations have been also discussed. Additionally, the different machine tool feed drive systems, its control and modelling approaches have been also summarized. This literature review has reflected some unsolved problems that are summarized below and tackled in the present thesis.

While the stiffness, mechanics and backlash properties of ball screw drives have been extensively studied in literature, little work has been done regarding the double pinion and rack feed drive mechanism. This thesis presents, on one hand, a time domain modelling approach that considers the contact conditions and on the other hand, a generalized framework to couple the linearized machine tool dynamics with the master-slave controller. With this, the influence of the control parameters effect on the tool centre point can be predicted.

The feed drive control tuning has been widely studied in literature. For improving the machine tool accuracy, different compensation techniques or feedforward terms tuning guidelines are proposed. The increase of machine's damping by means of non-conventional control techniques is also described in literature. However, this kind of

control solutions are difficult to introduce in industry. Therefore, the industry standard P-PI cascade controller is analyzed in this thesis. The commissioning of this control scheme has also been studied in literature; however, in earlier methods a single vibratory mode was considered and no experimental evidence of the influence of the control parameters on the cutting point compliance is reported in literature. This thesis presents a new feed drive control approach for avoiding chatter, which can be generalized for complex machine tool dynamics.

The existing guideway friction has been modelled and studied in literature, especially for motion and control performance. However, little work has been done regarding the effect of guideway friction on the cutting point compliance. This thesis describes the interaction of machine tool structural dynamics, guideway friction, feed drive controls and motion commands and how this interaction affects the tool centre point compliance. By understanding this effect, the chatter stability limit can be predicted more accurately.

The obtention of the machining system dynamics is a complex task, as different factors can alter the expected dynamics. Alternative system compliance identification techniques are present in literature, which by means of dedicated cutting tests try to identify the dynamics under real cutting conditions. This thesis introduces an alternative approach which significantly improves the signal to noise ratio of the obtained dynamics with respect to the state of the art approach. This is obtained by optimizing the tool radial engagement of the identification cutting tests which ensures a high quality excitation. Additionally, the quality of the spectra signals is improved by using the Welch's method. With this, not only the effect of guideway friction or feed drive controller can be consider, but also the nonlinearity related to the excitation force, obtaining as a result, a better chatter stability limit prediction.

Chapter 3

Analysis of an electronically preloaded rack and pinion drive

3.1 INTRODUCTION

In 2011, Altintas et al. [98] described the feed drive system types that are available for the different machine tool applications. For large heavy-duty machining operations, Uriarte et al. [1] concluded that the preloaded rack and pinion feed drive mechanism should be selected when large travelling distances and high loads are combined. As summarized in Sections 2.5 and 2.6, the accuracy requirements of modern machine tools demand the use of drives where the existing backlash is reduced to the largest possible extent. Therefore, an electronic preload is generated to suppress the existing clearance. The preload value greatly influences the quality of the feed motion, the dynamic operational behaviour as well as the expected service life and energy consumption. The current industrial trend is to use a double motor actuation following a master-slave control configuration, where the preload value is managed electronically by the machine CNC. In literature, there is no clear and systematic guideline for the preload commissioning. In

2008, Zirn [125] defined a range between 10-30% of the motor rated torque, whereas regular industrial values are established at 20-25% (Heidenhain [210]). In 2018, Verl et al. [197] concluded that only a 4% level was enough to compensate the existing clearance.

So far, the double motor pinion and rack feed drive system has not extensively been targeted by the academic community and only a few publications can be found that study this feed drive technology. Furthermore, the existing documentation focuses mainly on energy and positioning improvements, neglecting its dynamic behavior and interaction with the machine. Therefore, this chapter presents two different approaches to analyze the master-slave control parameters of a double pinion and rack feed drive system on the operational behavior of a large-scale machine tool (Figure 3.1). On one hand, in large heavy-duty machine tools, the acceleration capabilities might not be limited by the commanded preload level. Hence, this chapter studies the effect of the defined electronical preload on the static stiffness behavior of the double pinion and rack mechanism. On the other hand, the influence of the master-slave control parameters on the cutting point compliance is analyzed. A frequency domain based response prediction approach is proposed using the Linear Fractional Transformation (LFT) technique which allows the coupling of the analytical definition of the P-PI servo controller scheme and the structural machine tool dynamics.

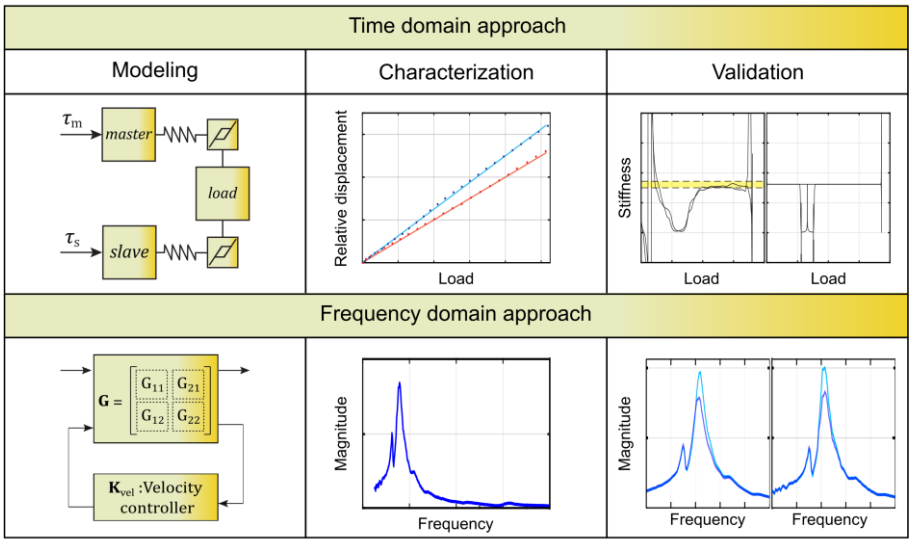

Figure 3.1 Steps of the proposed approach.

3.2 TIME DOMAIN FEED DRIVE MODEL DEFINITION

Figure 3.2 shows the double pinion and rack feed drive model presented in this chapter. The CNC generated trajectory (x_{ref}) is controlled by the proportional position control gain (K_{v}) which utilizes the driven load position, usually acquired by a linear encoder (x_{load}). The velocity reference ($\dot{x}_{\mathrm{ref}}$) is controlled by the master-slave control configuration where each motor has a proportional-integral (PI) controller (PI_{master} and PI_{slave}), which employs each motor's rotational velocity acquired by the rotary encoders already installed in the back of the motors ($\dot{\varphi}_{\mathrm{m}}$ and $\dot{\varphi}_{\mathrm{s}}$). The desired preload level can be modified varying the parameter called torque bias or tension torque (τ_{p}), which is defined by a percentage of the motor rated torque. The torque equalization controller (PI_{preload}) generates an additional speed setpoint for each motor by considering the desired torque preload. This control configuration allows the utilization of motors with different powers, as it provides individual weighting factors to adapt the torque distribution (K_{Tm} and K_{Ts}). If both motors are identical, the load must be shared proportionally by defining a value of K_{Tm} = K_{Ts} = 0.5. The generated torque commands for master and slave are denoted as τ_{m} and τ_{s}, respectively. Additionally, external disturbance forces (F_{load}) can be directly applied to the load. Next subsection describes the different components of this feed drive system.

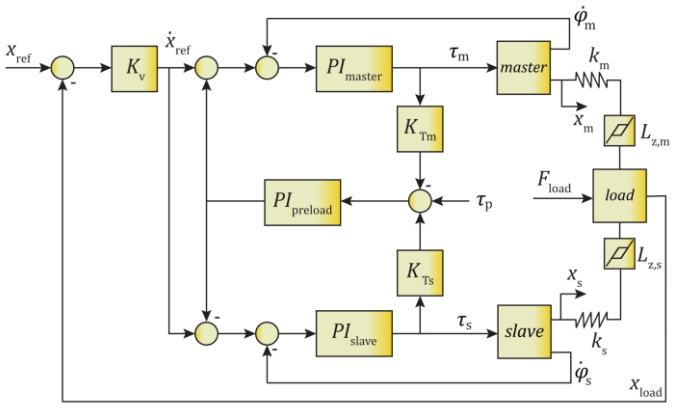

Figure 3.2 Double pinion and rack feed drive model.

3.2.1 Electronic preload

As a result of a commanded trajectory (x_{ref}), a reference torque (τ_{ref}) is generated to achieve the desired displacement. For the standstill case ($\tau_{\mathrm{ref}} = 0$ Nm), the net torque (τ_{net}), which is the summation of each motor torque, must be zero otherwise the machine will move (Eq. (3.1)). As a result of the electronic preload, each motor in the standstill

case generates the desired preload torque level τ_p. Both master and slave torques (τ_m and τ_s) have inverse polarity within the $-2\tau_p < \tau_{ref} < 2\tau_p$ interval, hence both pinions are in opposite flanks of the rack (Figure 3.3 zone ②). A reference torque outside this interval induces a flank change of one of the pinions, which depends on the moving direction. In this case, both motor torques have the same polarity. Eq. (3.2) indicates the maximum net torque ($\tau_{net,max}$) that can be obtained under preload conditions. This shows that increasing the preload torque leads to a reduction in the achievable acceleration.

$\tau_{net} = \tau_m + \tau_s$, where

$$\tau_m = \frac{\tau_{ref}}{2} + \tau_p \tag{3.1}$$

$$\tau_s = \frac{\tau_{ref}}{2} - \tau_p$$

$$\tau_{net,max} = 2(\tau_{m,max} - \tau_p) \tag{3.2}$$

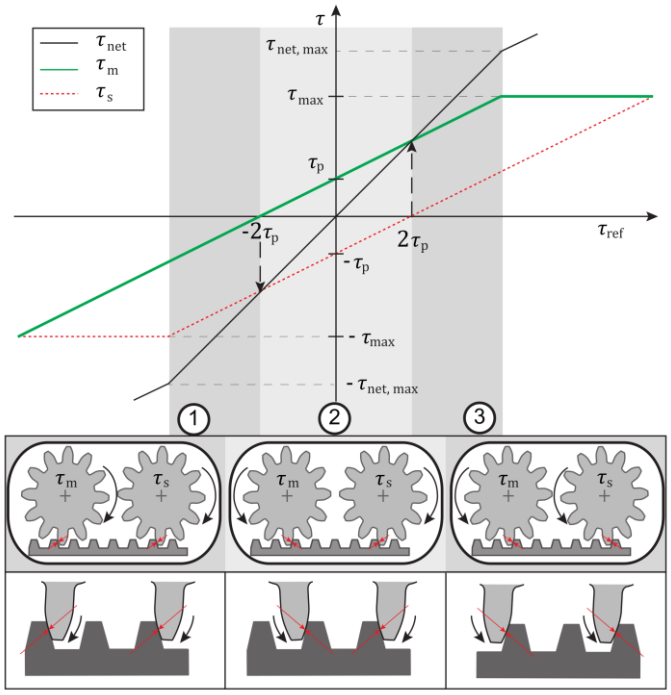

Figure 3.3 Electronic preload for backlash suppression [98].

3.2.2 Joint stiffness

The power transmission of this feed drive mechanism is characterized by low revolutions and high torque. For this reason, additional gear steps are required to fulfill the torque requirements. Planetary gearboxes are usually installed as the continuous engagement

of multiple teeth increases the torsional stiffness [213]. As a result, each motor equivalent inertia can be computed following Eq.(3.3), where motor, gearbox and pinion inertias are jointly considered. Note, that as a result of employing a gearbox, the reduction factor (i_{red}) must be considered while computing the equivalent inertia.

$$J_{\mathrm{eq}} = \left(J_{\mathrm{motor}} + J_{\mathrm{gearbox}}\right) + \frac{J_{\mathrm{pinion}}}{i_{\mathrm{red}}^2} \tag{3.3}$$

Similarly, as described by Altintas et al. [98], the stiffness of this feed drive mechanism is dominated by the torsional stiffness of the motor coupling (k_{coupling}), installed gearbox (k_{gearbox}) and shaft (k_{shaft}), as well as the contact stiffness of the pinion and rack combination ($k_{\mathrm{p-r}}$) (Eq.(3.4), Figure 3.4). In the proposed model, each motor is coupled to the load by a connection of a spring element (i.e., k_{m}), which is an equivalent linear stiffness of the previous components.

$$\frac{1}{k_{\mathrm{m}}} = \frac{1}{k_{\mathrm{coupling}}} + \frac{1}{k_{\mathrm{gearbox}}} + \frac{1}{k_{\mathrm{shaft}}} + \frac{1}{k_{\mathrm{p-r}}} \tag{3.4}$$

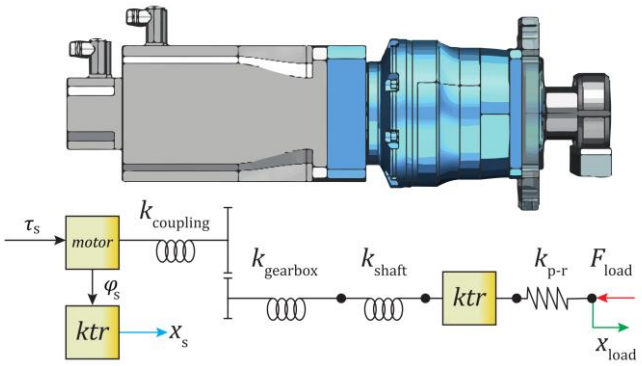

Figure 3.4 Equivalent stiffness model.

3.2.3 Joint backlash

The equivalent backlash in the power transmission path can come from different sources, such as the motor-gearbox and pinion-rack joint interfaces, as well as a summation of existing clearances within the gearbox. This mechanical nonlinear behavior has been modeled by a dead zone approach which simplifies the exact physical model (Moradi et al. [231]). $L_{\mathrm{z,m}}$ and $L_{\mathrm{z,s}}$ are the existing equivalent backlash values (master and slave respectively) between load and motor positions (i.e., x_{load} and x_{s}).

With this, the different elements needed to simulate the model of Figure 3.2 are defined. Section 3.4 presents the experimental identification and validation of the proposed model. Analogously, next section describes the derivation of the proposed modelling MIMO approach for coupling the master-slave controller with the machine structural dynamics.

3.3 FREQUENCY DOMAIN FEED DRIVE MODEL DEFINITION

A frequency domain modeling approach based on experimental data is present in this research to predict the influence of the servo control on the driven machine tool dynamics. With this, all the complexity of the machine dynamics is implicitly contained in the measured data. As multiple actuators and sensors are used to drive the machine, a multivariable prediction model is required. The LFT technique is chosen to build the prediction model (Skogestad et al. [232]). This technique is convenient and powerful for MIMO cases since it allows decomposing the control system into open and closed loop signals to work independently with each part. The formulation is based on a generalised control scheme (Figure 3.5-a), where the block $\mathbf{G}$ defines the open loop machine tool dynamics, and $\mathbf{K}_{\mathrm{fb}}$ the implemented feedback controller. The generalized controller obtains as inputs the measured variables ($\mathbf{q}$) to be able to generate the control signal ($\mathbf{p}$).

It is important to mention that since linear system analysis is applied throughout, it is assumed that the magnitude of all inputs (motor torque, disturbance force, preload torque, velocity command, etc.) are bounded in a way to avoid major nonlinearities such as actuator saturation or disengagement/damage to the equipment. Thus, the machine tool preserves linear dynamic behaviour and bounded-input bounded-output (BIBO) condition is satisfied.

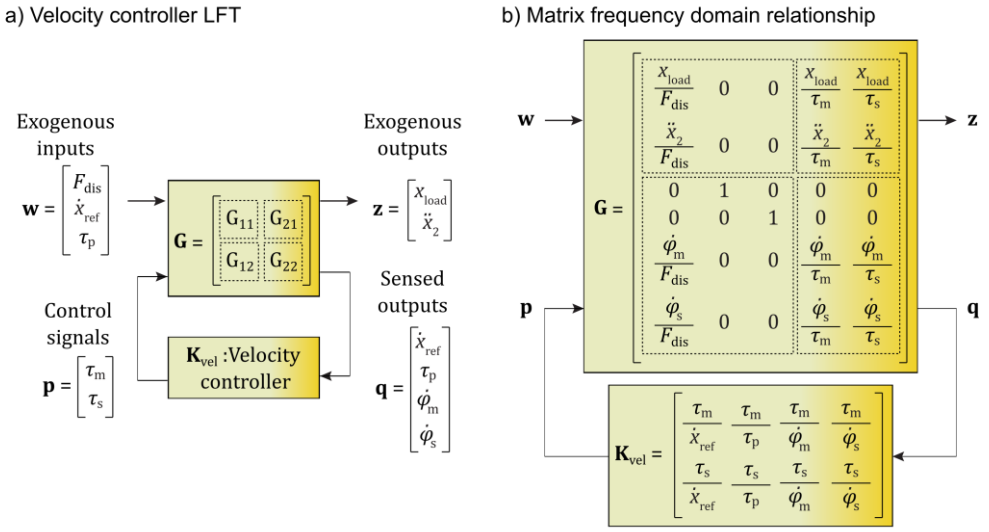

Figure 3.5 a) Velocity controller LFT definition; b) Matrix frequency domain relationship detail.

As shown in Eq. (3.5), the matrix $\mathbf{G}$ is usually partitioned, so that the system is mathematically compatible with the signals generated by the matrixes or vectors $\mathbf{w}$, $\mathbf{z}$, $\mathbf{p}$ and $\mathbf{q}$, Eq. (3.6).

$$\mathbf{G} = \begin{bmatrix} \mathbf{G}_{11} & \mathbf{G}_{12} \\ \mathbf{G}_{21} & \mathbf{G}_{22} \end{bmatrix} \tag{3.5}$$

$$\begin{bmatrix} \mathbf{z} \\ \mathbf{q} \end{bmatrix} = \mathbf{G} \begin{bmatrix} \mathbf{w} \\ \mathbf{p} \end{bmatrix}, \text{ where } \mathbf{p} = \mathbf{K_{fb}}\mathbf{q} \tag{3.6}$$

The closed loop frequency domain response from the defined inputs ($\mathbf{w}$) to outputs ($\mathbf{z}$) is denoted by the lower LFT as defined in Eq. (3.7) by Skogestad et al. [232].

$$\mathbf{F}_l\,(\mathbf{G}, \mathbf{K}_{\mathrm{fb}}) = \mathbf{G}_{11} + \mathbf{G}_{12}\,\mathbf{K}_{\mathrm{fb}}(\mathbf{I} - \mathbf{G}_{22}\,\mathbf{K}_{\mathrm{fb}}\,)^{-1}\mathbf{G}_{21} \tag{3.7}$$

One of the most important properties of the LFT technique is that the interconnection between LFTs generates a new LFT. In this case, since the controller used is a cascaded P-PI controller, the closed velocity loop will serve as input to the position loop LFT. The following subsections explain the velocity and position controller definitions.

3.3.1 Velocity control loop

Taking into account the general master-slave control structure and the described LFT generalized block diagram (Figure 3.5-a), the inputs and outputs vectors can be selected to build the dynamical model. Bearing in mind that the final objective is to be able to

couple the effect of the servo control parameters and the machine tool structural dynamics, the input and output vector variables have been selected as shown in Figure 3.5-a. The exogenous input vector **w** is composed of the disturbance force applied at the tool centre point of the machine, the velocity reference point and the pretension torque. The output vector **z** contains the measurements from the linear encoder and the accelerometer at the tool centre point. On the other hand, the sensed output vector contains all the required variables to close the velocity loop: the velocity reference point, the pretension torque and velocity measurement from the rotary encoder of each motor. Lastly, the control signal vector is filled by the two torque commands for master and slave motors. Figure 3.5-b defines the required FRFs needed to perform the prediction.

The three velocity PI controllers used in this control scheme are defined as follows.

$$PI_{\text{master}} = K_{\text{p,master}}\left(1 + \frac{1}{T_{\text{i,master}}\, s}\right) \tag{3.8}$$

$$PI_{\text{slave}} = K_{\text{p,slave}}\left(1 + \frac{1}{T_{\text{i,slave}}\, s}\right) \tag{3.9}$$

$$PI_{\text{preload}} = K_{\text{p,preload}}\left(1 + \frac{1}{T_{\text{i,preload}}\, s}\right) \tag{3.10}$$

Using the velocity controller defined in Figure 3.2, the eight transfer functions to define analytically the velocity control matrix are computed. Below, the derived expressions for the master motor (Eq. (3.11)-(3.14)) are shown.

$$\frac{\tau_{\text{m}}}{\dot{x}_{\text{ref}}} = \frac{PI_{\text{slave}}(s)\left(2K_{\text{Tm}}PI_{\text{master}}(s)PI_{\text{preload}}(s) + 1\right)}{K_{\text{Tm}}PI_{\text{master}}(s)PI_{\text{preload}}(s) + K_{\text{Ts}}PI_{\text{preload}}(s)PI_{\text{slave}}(s) + 1} \tag{3.11}$$

$$\frac{\tau_{\text{m}}}{\tau_{\text{p}}} = \frac{PI_{\text{slave}}(s)PI_{\text{preload}}(s)}{K_{\text{Tm}}PI_{\text{master}}(s)PI_{\text{preload}}(s) + K_{\text{Ts}}PI_{\text{preload}}(s)PI_{\text{slave}}(s) + 1} \tag{3.12}$$

$$\frac{\tau_{\text{m}}}{\dot{\varphi}_{\text{m}}} = -\frac{PI_{\text{slave}}(s)\left(K_{\text{Tm}}PI_{\text{master}}(s)PI_{\text{preload}}(s) + 1\right)}{K_{\text{Tm}}PI_{\text{master}}(s)PI_{\text{preload}}(s) + K_{\text{Ts}}PI_{\text{preload}}(s)PI_{\text{slave}}(s) + 1} \tag{3.13}$$

$$\frac{\tau_{\text{m}}}{\dot{\varphi}_{\text{s}}} = -\frac{K_{\text{Tm}}PI_{\text{master}}(s)PI_{\text{preload}}(s)PI_{\text{slave}}(s)}{K_{\text{Tm}}PI_{\text{master}}(s)PI_{\text{preload}}(s) + K_{\text{Ts}}PI_{\text{preload}}(s)PI_{\text{slave}}(s) + 1} \tag{3.14}$$

Similar expressions are obtained for the slave motor, Eq. (3.15)-(3.18).

$$\frac{\tau_{s}}{\dot{x}_{\text{ref}}} = \frac{PI_{\text{master}}(s)\left(2K_{\text{Ts}}PI_{\text{preload}}(s)PI_{\text{slave}}(s) + 1\right)}{K_{\text{Tm}}PI_{\text{master}}(s)PI_{\text{preload}}(s) + K_{\text{Ts}}PI_{\text{preload}}(s)PI_{\text{slave}}(s) + 1} \tag{3.15}$$

$$\frac{\tau_s}{\tau_p} = \frac{PI_{master}(s)PI_{preload}(s)}{K_{Tm}PI_{master}(s)PI_{preload}(s) + K_{Ts}PI_{preload}(s)PI_{slave}(s) + 1} \tag{3.16}$$

$$\frac{\tau_s}{\dot{\varphi}_m} = -\frac{K_{Ts}PI_{master}(s)PI_{preload}(s)PI_{slave}(s)}{K_{Ts}PI_{master}(s)PI_{preload}(s) + K_{Ts}PI_{preload}(s)PI_{slave}(s) + 1} \tag{3.17}$$

$$\frac{\tau_s}{\dot{\varphi}_s} = -\frac{PI_{master}(s)\left(K_{Ts}PI_{preload}(s)PI_{slave}(s) + 1\right)}{K_{Tm}PI_{master}(s)PI_{preload}(s) + K_{Ts}PI_{preload}(s)PI_{slave}(s) + 1} \tag{3.18}$$

The sampling frequency (8 kHz) of the velocity loop is taken into account during the controller discretization via Tustin's method. All the mathematical calculations are programmed in complex vector operations. The next Eq. (3.19) gives the frequency domain relationship between the defined exogenous inputs and outputs ($\mathbf{z}/\mathbf{w}$) taking into account the previously defined velocity controller parameters $\mathbf{K}_{vel}$ and the actual open loop machine tool structural dynamics $\mathbf{G}$.

$$(\mathbf{G}, \mathbf{K}_{vel}) = \mathbf{G}_{11} + \mathbf{G}_{12}\mathbf{K}_{vel}(\mathbf{I} - \mathbf{G}_{22}\mathbf{K}_{vel})^{-1}\mathbf{G}_{21} \tag{3.19}$$

3.3.2 Position control loop

Once the closed velocity loop is computed, the generated result matrix is directly used as an input for the closed position loop calculation (Figure 3.6). In this case, the controller matrix has been extensively simplified to just the position proportional gain. Like in the previous control loop, the existing sampling frequency (1 kHz) has been taken into account.

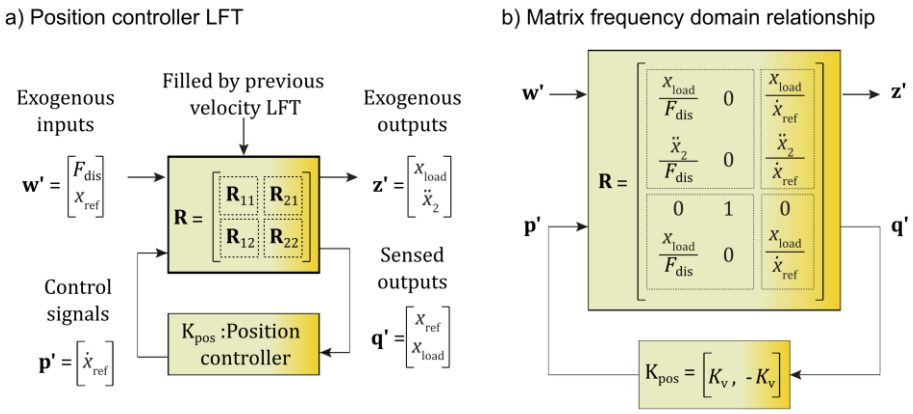

Figure 3.6 a) Position controller LFT definition; b) Matrix frequency domain relationship detail.

Then, by means of Eq. (3.20), the FRF between the desired exogenous inputs and outputs ($\mathbf{z}'/\mathbf{w}'$) can be computed taking into account the position controller effect. The FRF between the tool centre point acceleration and the applied disturbance force at the same location is of particular importance, as this response should be equivalent to the one that can be obtained by performing a regular modal test with an impact hammer.

$$\left(\mathbf{R}, \mathbf{K}_{\mathrm{pos}}\right) = \mathbf{R}_{11} + \mathbf{R}_{12}\mathbf{K}_{\mathrm{pos}}(\mathbf{I} - \mathbf{R}_{22}\mathbf{K}_{\mathrm{pos}})^{-1}\mathbf{R}_{21} \tag{3.20}$$

The frequency response of the feedback controllers can be analytically derived considering the gain values, which are known, and the control law structures. However, the main difficulty is in the acquisition of the actual machine tool's open loop FRF matrix represented by matrix $\mathbf{G}$.

3.3.3 Pseudo-open loop extraction

To be able to couple the analytically defined controller effect and machine tool structural dynamics, the response to excitation from both machine actuators is required. Usually, the machine feed drive actuators should be individually excited in order to characterize the response. However, as previously indicated, the master-slave controller couples both motors through the generated preload. This means that even if the excitation signal is carried out by a single motor, due to the torque equalization controller, the secondary motor also follows the excitation signal to get the desired torque bias. Hence, the response at a specific output point O is affected by both motors' excitation (τ_{m}, τ_{s}). In the following equations, the general output O can be replaced by any output of the matrix $\mathbf{G}$ (x_{load}, $\ddot{x}_2$, $\dot{\varphi}_{\mathrm{m}}$ and $\dot{\varphi}_{\mathrm{s}}$).

$$O = \left(\frac{O}{\tau_{\mathrm{m}}}\right)\tau_{\mathrm{m}} + \left(\frac{O}{\tau_{\mathrm{s}}}\right)\tau_{\mathrm{s}} \tag{3.21}$$

In order to be able to decouple the motor actuations and get the individual excitation response from each motor, the expressions in (3.22)-(3.23) can be used. The aim is to get at least two non-proportional measurements of the desired input (τ_{m}, τ_{s}) and output (O). These measurements can be obtained by modifying the velocity PI controller of each motor independently. This will generate a different torque command for each motor. As shown, the resolution of the system FRF composed of two or more experimental measurements with different controllers allows the open loop frequency response functions of the matrix $\mathbf{G}$ to be obtained.

$$\underbrace{\left[\underbrace{O}_{K_1} \quad \underbrace{O}_{K_2}\right]_{1x2}}_{\mathbf{X}} = \underbrace{\left[\underbrace{\left(\frac{O}{\tau_\mathrm{m}}\right) \quad \left(\frac{O}{\tau_\mathrm{s}}\right)}_{\forall K}\right]_{1x2}}_{\mathbf{G}} \underbrace{\left[\begin{matrix}\underbrace{\tau_\mathrm{m}}_{K_1} & \underbrace{\tau_\mathrm{m}}_{K_2} \\ \underbrace{\tau_\mathrm{s}}_{K_1} & \underbrace{\tau_\mathrm{s}}_{K_2}\end{matrix}\right]_{2x2}}_{\mathbf{U}} \tag{3.22}$$

$$\mathbf{X} = \mathbf{GU} \rightarrow \mathbf{G} = \mathbf{X}inv\,(\mathbf{U}) \tag{3.23}$$

Even though the procedure described above is valid for a general case, this method might fail due to the creation of an ill-conditioned system. Hence, this approach has not been implemented in this work. However, due to the machine topology, the following simplifications have been considered. Both motors are identical, they have the same weighting factors (K_Tm = K_Ts = 0.5) and PI gains ($PI_\mathrm{master} = PI_\mathrm{slave}$), so it is assumed that the same torque command is generated for both motors ($\tau_\mathrm{m} = \tau_\mathrm{s}$). In addition to this, if the excitation signal is given as a velocity command through a compiled cycle in the CNC, the generated reference torque (τ_ref) will be equally divided between both motors ($\tau_\mathrm{m} = \tau_\mathrm{s} = \tau_\mathrm{ref}/2$). This assumption is only valid when the static part of the torque command is removed, for example, for the selected excitation frequency band (25 to 100 Hz) (Eq. (3.24)).

$$O = \left(\frac{O}{\tau_\mathrm{m}}\right)\tau_\mathrm{m} + \left(\frac{O}{\tau_\mathrm{s}}\right)\tau_\mathrm{s} = \left(\frac{O}{\tau_\mathrm{m}}\right)\frac{\tau_\mathrm{ref}}{2} + \left(\frac{O}{\tau_\mathrm{s}}\right)\frac{\tau_\mathrm{ref}}{2} = \left(\left(\frac{O}{\tau_\mathrm{m}}\right) + \left(\frac{O}{\tau_\mathrm{s}}\right)\right)\frac{\tau_\mathrm{ref}}{2} \tag{3.24}$$

In addition, considering that the motors and sensors are symmetrically located with respect to the machine's main resonance mode shape, the frequency response can be equalized $(O/\tau_\mathrm{m}) = (O/\tau_\mathrm{s})$ (Eq. (3.25)). This assumption can be extrapolated to all measured outputs referred to in this research (x_load, $\ddot{x}_2$, $\dot{\varphi}_\mathrm{m}$ and $\dot{\varphi}_\mathrm{s}$).

$$O = \left(\left(\frac{O}{\tau_\mathrm{m}}\right) + \left(\frac{O}{\tau_\mathrm{s}}\right)\right)\frac{\tau_\mathrm{ref}}{2} = \cancel{2}\left(\frac{O}{\tau_\mathrm{m}}\right)\frac{\tau_\mathrm{ref}}{\cancel{2}} = \left(\frac{O}{\tau_\mathrm{m}}\right)\tau_\mathrm{ref} \tag{3.25}$$

With the previous hypotheses, it is assumed that pseudo-open loop frequency response functions can be obtained, even if both motors are simultaneously exciting the system. The experimental characterization and model validation is present in Section 3.5. The next section presents the experimental static characterization and validation of the described time domain model.

3.4 STATIC CHARACTERIZATION AND MODEL VALIDATION

The time domain model is implemented in a large-scale milling machine, where a double pinion and rack feed drive system is installed in the x axis. In order to characterize each

motor independently, the existing coupling between the master and slave should be removed. A modification in the machine tool configuration parameters has been implemented, which enables closing both velocity and position loops with the desired motor encoder while disabling the other motor. At the same time, the linear scale still monitors the load position, and hence, the load position can be used for further analysis.

3.4.1 Joint equivalent stiffness

In order to perform a static stiffness analysis, the machine tool has been placed at the initial traveling distance. The force F_{load} has been generated by imposing a stepped position trajectory through a CNC command while limiting the displacement against the mechanical rigid bumper (Figure 3.7). The load cell (Kistler 9212) has been placed between the carriage and the bumper.

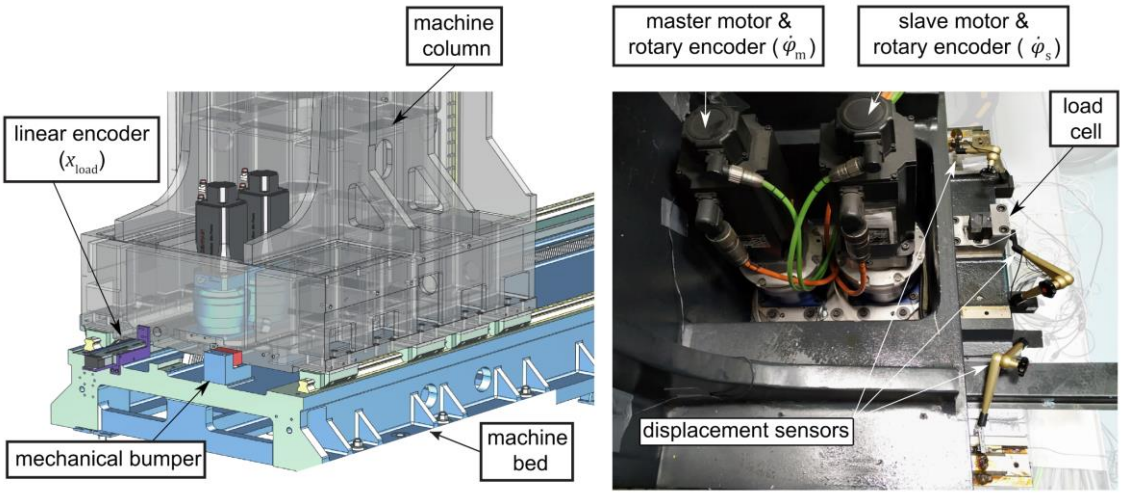

Figure 3.7 Machine tool component description in testing position.

The experimental commanded maximum displacement has been chosen to obtain a force level of around 10kN, which for this tested machine is approximately 300 µm (Figure 3.8-a). The displacements can be synchronously acquired by the internal sensors through a dedicated software provided by the CNC manufacturer (i.e., TNCscope from Heidenhain). As a result of the applied F_{load}, the generated deformation between the motor rotary encoder ($x_{\mathrm{m,s}}$) and load displacement acquired by the linear encoder (x_{load}) can be computed. With this, an equivalent linear stiffness can be obtained which considers all the transmission components within the force path (Eq. (3.4)). As described above, the identification must be done individually one motor at a time, breaking the master-slave coupling. Figure 3.8-b shows the fitted equivalent stiffness on top of the experimental results obtained from the test shown in Figure 3.8-a, obtaining different values for each motor k_{m} = 81 N/µm for the master and k_{s} = 100 N/µm for the slave. The

inertias of the model are obtained from the supplier's catalogues (J_{motor} =7500 e^{-6} kg/m^2, J_{gearbox} = 948 e^{-6} kg/m^2 on the motor side, i_{red} = 28) and the pinion inertia has been neglected. The axis driven load inertia is obtained from the machine CAD drawing (m_{load} = 8500 kg).

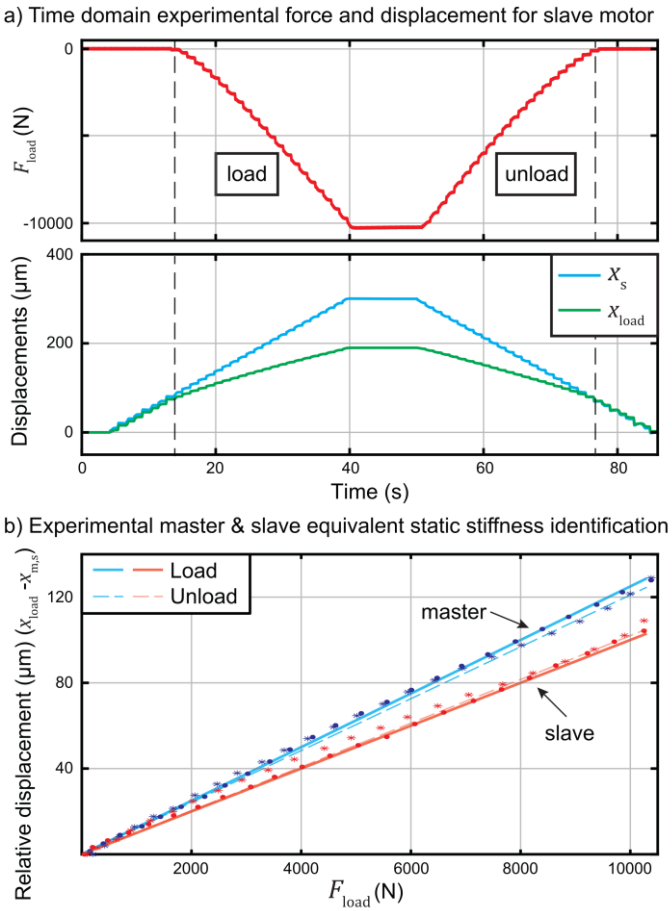

Figure 3.8 Experimental identification of individual master and slave static stiffnesses.

3.4.2 Joint equivalent backlash

In order to identify the existing equivalent backlash, as in the previous identification step, the master-slave coupling must be removed by operating each motor separately. In addition, for this case no force load is exerted to the machine and a back and forth movement of 1 mm is commanded. Figure 3.9 shows the identified position difference between each motor rotary encoder and load displacement ($x_{\mathrm{m,s}}$ and x_{load}). Here, as previously defined, the identified equivalent backlash is a summation of the existing one within the transmission. The contribution identification of each element is complex. As a rule of thumb, during gearbox design, the value of the backlash can be assumed to be 0.04 of the tooth module (Margielewicz et al. [212]). The identified equivalent backlash for the master and slave motors are 314 and 363 µm, respectively.

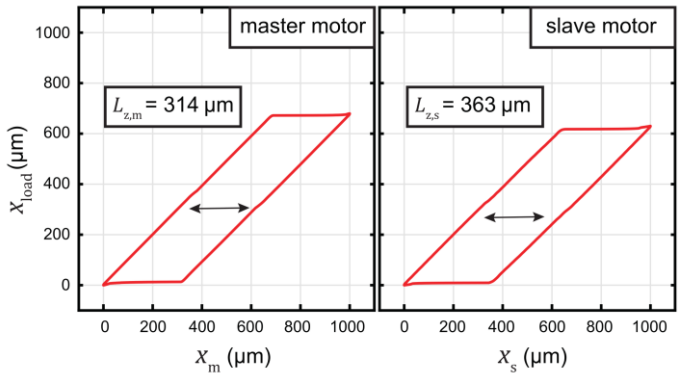

Figure 3.9 Experimental equivalent backlash identification.

Using the experimentally identified stiffness and backlash, the electronically preloaded rack and pinion feed drive model, previously shown in Figure 3.2, is validated in the next section.

3.4.3 Model validation

At the same location where the identification has been conducted, the machine control configuration is set to the original master-slave coupling as described in Figure 3.2. As in the previous case, while the machine load movement is constrained, a CNC position command of 300 µm is commanded achieving approximately 20 kN of F_{load}. Figure 3.10 summarizes the comparison between the experimental and simulated time domain results during static stiffness tests for different preload levels. Figure 3.10-a shows the obtained displacements (x_{load}, x_{s} and x_{m}) during the load and unload stages. Load displacement is very close to the commanded one since the position loop is closed with this signal. On the contrary, it is not the same for the displacements acquired from both motors. On one hand, analyzing the slave motor first, at maximum load it can be seen that the acquired displacement reaches an amplitude of approximately 400 µm, which matches the simulated result. On the other hand, the master motor displacement is significantly higher than the other two signals. In addition, there is an abrupt jump when the rack and pinion contacts are changing configuration from ② to ③ of Figure 3.3. The force level needed to change the configuration depends on the commanded preload level. This effect can be explained considering Figure 3.10-b, where the time domain torque value of each motor is shown throughout the test. At a certain point, the amplitude of F_{load} is high enough to compensate the commanded preload torque; therefore, the existing torque in one of the motors becomes zero. This means that the electronic preload is lost at that moment. As indicated in Figure 3.3, as the force level continues to

increase, the pinion rotates and meshes with another flank of the rack. Note that the transition between interval ② and ① or ③ depends on the load direction, hence the observed effect on the master motor will happen in the slave motor if the load is applied in the opposite direction. This pinion rotation coming from the flank change is captured by the master motor rotary encoder. Hence, it suffers much higher displacement than the slave encoder (Figure 3.10-a). This can also be seen in the polarity of the measured torques (Figure 3.10-b).

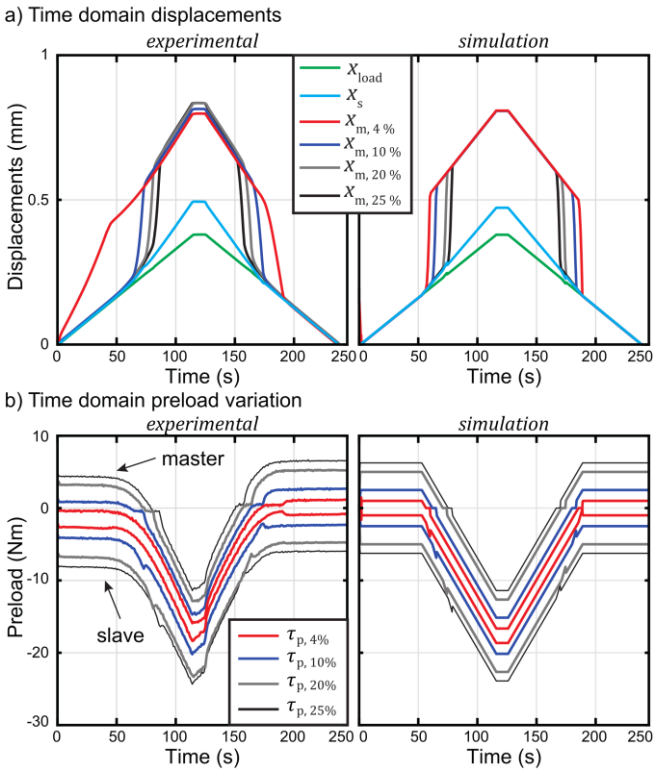

Figure 3.10 Model validation through time domain responses.

Four different preload levels have been proposed to analyze this effect (τ_p = 4, 10, 20 and 25%). As expected, both experimental and simulated results indicate that the preload losing point varies with respect to the commanded preload level. Figure 3.11-a shows the relative displacement of the master motor for the four analyzed preload levels based on the data shown in Figure 3.10-a. There is a significant variation in the force level which generates the pinion contact loss between 4% and the other three levels, going from 1100 N up to 5300 N or 6600 N. In the same way, as load increases and, hence, the pinion tooth contacts again, the linear behavior is recovered until the tested maximum force. A reciprocity can be seen between unload and load stages. Finally, it can be concluded that the relative displacement between the loss and contact recovery points is determined by the backlash value (Figure 3.11-a). As a coupled system, the

slave motor is susceptible to this effect since a change of 5 µm in the relative displacement is observed when losing the preload (Figure 3.11-b). This means that all of the F_{load}, which should be partially shared, is transmitted only through the slave motor, so the stiffness decreases, generating the excess displacement shown in Figure 3.11-b.

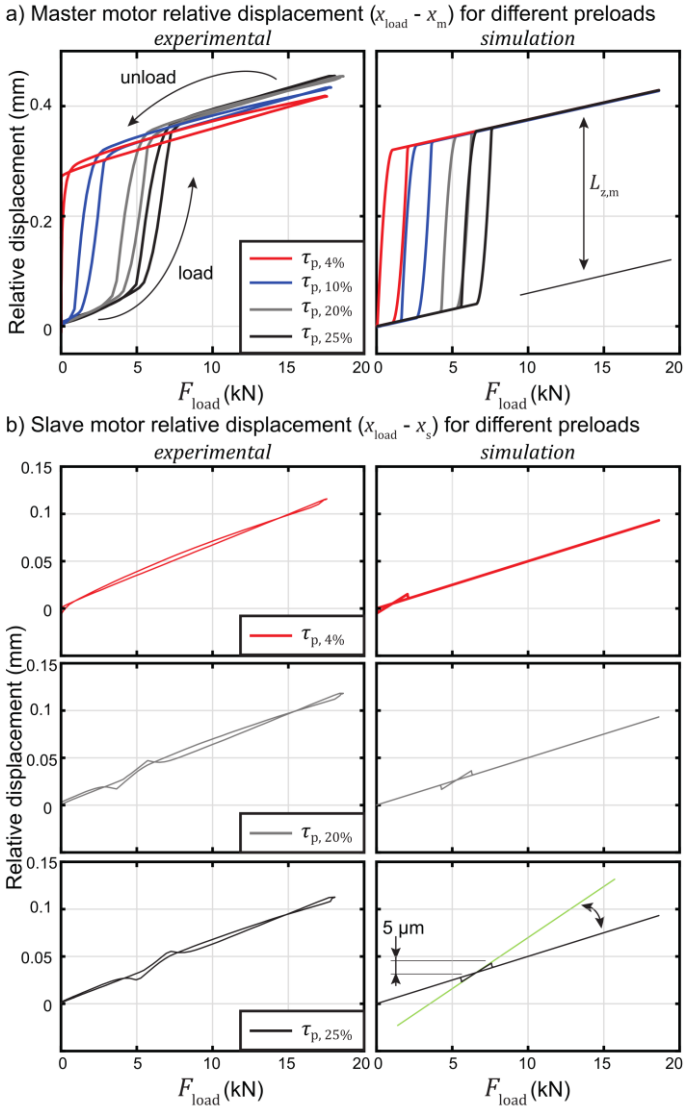

Figure 3.11 Master and slave motors stiffness model validation.

Equivalent stiffness variation analysis

From the relative displacements shown in Figure 3.11-a&b, the equivalent stiffness variation is computed following Eq. (3.26) (only k_{m} has been used in the equation but it is also valid for the slave motor).

$$k_{\mathrm{m}} = \frac{\Delta F_{\mathrm{Load}}}{\Delta \delta_{\mathrm{m}}} = \frac{0.5\left(F_{\mathrm{Load}}(t+1) - F_{\mathrm{Load}}(t)\right)}{\delta_{\mathrm{m}}(t+1) - \delta_{\mathrm{m}}(t)} \tag{3.26}$$

It is supposed that F_{load} is transmitted uniformly between the two motors in full contact conditions. However, the contact condition between the pinion and the rack ($k_{\mathrm{p-r}}$) when conducting the bottom-up characterization process can modify the extracted equivalent linear stiffness values (k_{m} and k_s). The DIN ISO 6336 standard [224] provides analytical equations to obtain the equivalent mesh stiffness ($c_{\gamma\alpha}$) while considering the influence of the teeth in mesh, which depends on the single tooth pair contact (c') and the contact ratio (ε_α) (Eq. (3.27)). Eq. (3.28) shows the expression to compute the single tooth pair stiffness according to the ISO standard, which for the studied feed drive mechanism is c' = 13.75 (N/mm)/µm. Similarly, the existing contact ratio is ε_α = 1.48, which means that 48% of the time two pairs of teeth are in contact, which increases the equivalent mesh stiffness ($c_{\gamma\alpha}$).

$$c_{\gamma\alpha} = c'(0.75\varepsilon_\alpha + 0.25) \tag{3.27}$$

$$c' = c'_{\mathrm{th}} \mathrm{C_M C_B C_R C_F} \cos\beta \tag{3.28}$$

In order to provide some variability analysis created by the contact ratio modification while the characterization test is performed, two bounds have been established. The lower bound considers that a single pair of teeth are in the mesh and the upper bound two pairs of teeth, ε_α = 1 and 2 respectively. By introducing these values into Eq. (3.27) and multiplying it by the width of the tooth gear (40 mm), the equivalent mesh stiffnesses are obtained and $k_{\mathrm{p-r}}$ varies from 550 to 962 N/µm. By adding these stiffness bounds into the total extracted equivalent stiffness (Eq. (3.4)) a variation of 7.4 and 9.5% for master and slave motors has been obtained, which is shaded in Figure 3.12-a&b. Figure 3.12-a shows the computed stiffness variation for the master motor under 25% preload levels (the other cases have been discarded for visualization purposes). It can be seen that by increasing the F_{load} amplitude, the obtained stiffness goes down to 0 N/µm. However, as the load increases it converges to the identified value of 81 N/µm. During the unload stage, the same trend as in loading conditions is followed. The simulation results illustrate a similar behavior to the experimental results. Analyzing the slave motor behavior under 25% of preload (Figure 3.12-b), at low disturbance forces the obtained stiffness is about 100 N/µm. Then, due to the contact loss of the master motor, the stiffness decreases by half as the entire force load is supported only by the slave motor. Next, when the contact is recovered, high stiffness transient zone is faced as a result of

the low relative displacement. However, the equivalent stiffness slowly converges to the expected initial value of around 100 N/µm.

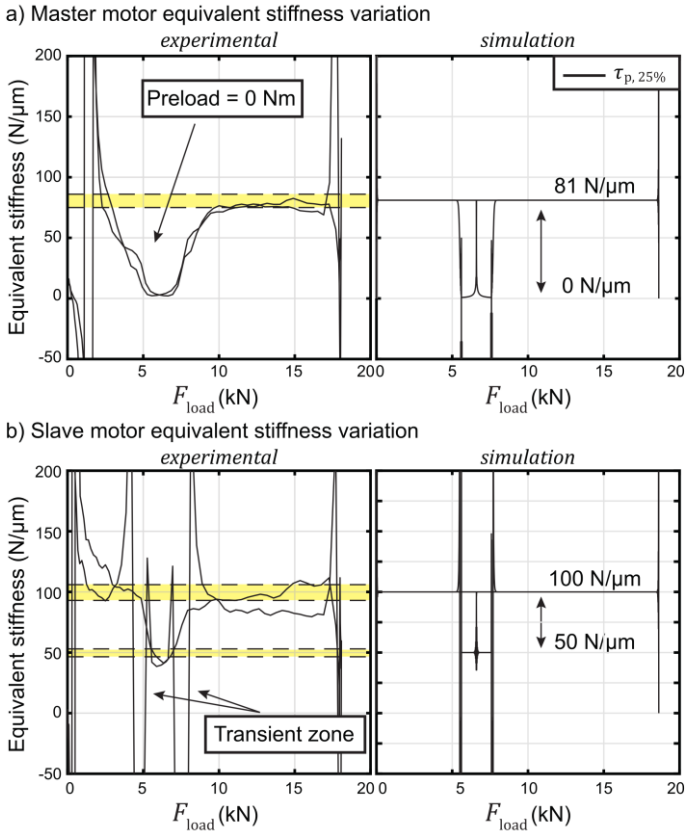

Figure 3.12 a) Master; b) Slave motor static stiffness variations.

Additionally, the experimental distribution of the torque is not proportionally shared, even though the same elements are employed in master and slave motors (Figure 3.10-b). This fact can cause prediction deviations of the preload loss force amplitude since it starts at the moment when one of the motor torques become zero. Similarly, the experimental equivalent backlash might not suit perfectly the employed dead zone model. However, the experimental results are very well captured by the proposed rack and pinion feed drive system model.

Static stiffness analysis at the machine ram

The identified effect not only appears by exerting the force at the column, but also if the load is applied close to the cutting point (i.e., the machine ram, Figure 3.13). Note that the maximum load force amplitude has been decreased to 10 kN to avoid any element breakage.

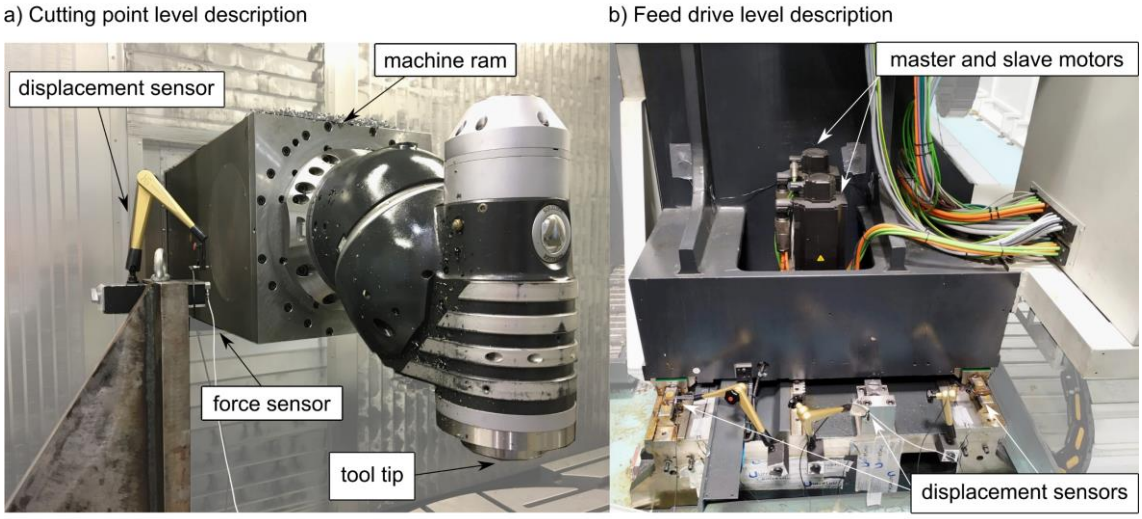

Figure 3.13 Machine setup description.

Figure 3.14 shows different experimental measurements of relative displacements. For the master and slave motors, the relative displacement is calculated between their respective motor encoder and linear encoder. For the ram measurement, the relative displacement is between the linear encoder and the ram displacement acquired with an inductive sensor. The ram tip stiffness is relatively linear with the force level and is not affected by the rack and pinion preload value. As a result of closing the position loop with the linear encoder, the backlash effect is limited and only appears at the feed drive level. However, the axis clearance modifies the linearity of the feed drive mechanism and might generate an increment of the tracking or following errors.

Additionally, considering the commissioned preload level in conjunction with the linear-rotary conversion factor (Ktr), the expected load force, in which the preload is lost, can be predicted. Within the identified bounds, the existence of preload (granted linearity) is ensured. A similar pattern is followed for the three analyzed cases, where the main differences appear at the preload losing point, which occurs at values ranging from ±1050 N to ±5300 N.

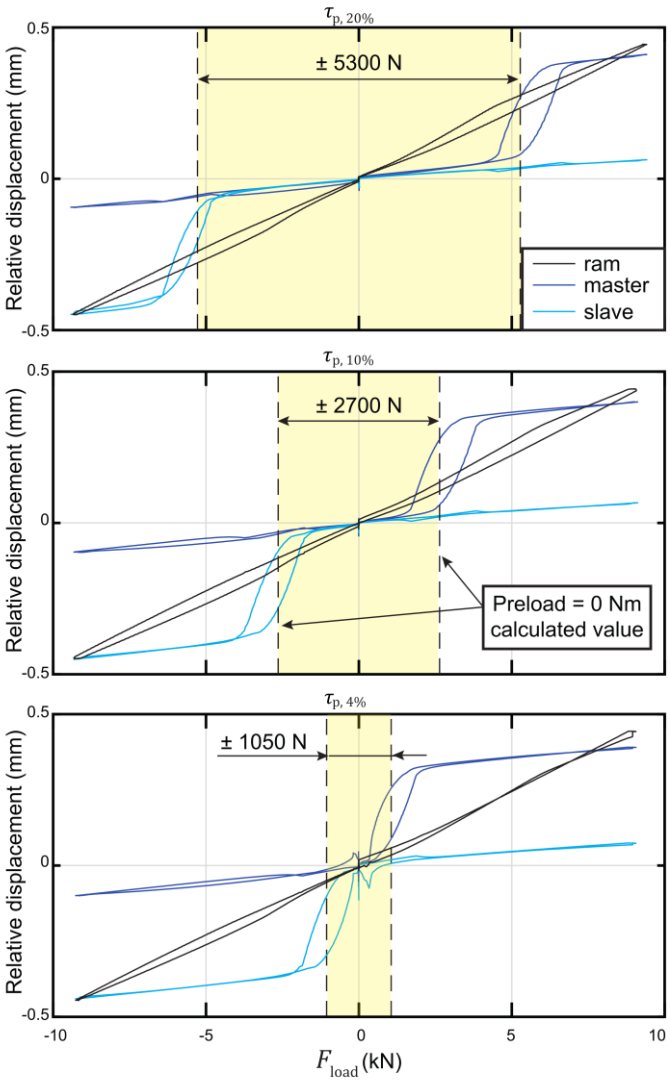

Figure 3.14 Experimental ram, master and slave motors static stiffness response.

The proposed time domain model can predict the displacements and torque commands accurately. Additionally, the nonlinear experimental feed drive system's static stiffness behaviour can be captured and explained. The commanded electronic preload plays a substantial role in defining the preload suppression in presence of static disturbances. The next section presents the dynamic characterization and the experimental validation of the proposed MIMO model to couple the master-slave control scheme and the machine tool dynamics.

3.5 DYNAMIC CHARACTERIZATION AND MODEL VALIDATION

For the dynamic analysis, a heavy-duty vertical turning centre that can perform turning and milling operations is selected (Figure 3.15). The machine has two axes: the

horizontal x axis is driven by the double pinion and rack, and the vertical z axis driven by a ball screw drive. Note that the master-slave control scheme used for the horizontal axis is the same as the previously described one in Section 3.2.

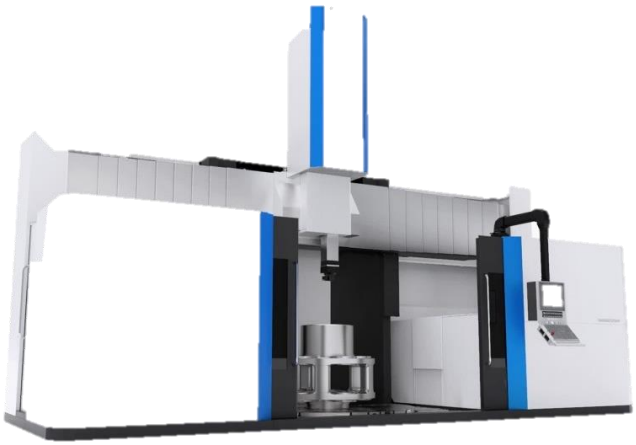

Figure 3.15 Analyzed heavy-duty vertical turning centre.

An experimental modal analysis is conducted to analyse the dynamic behaviour of the machine. An instrumented impact hammer (PCB 086D20) is used to excite the structure at the tool tip, and a triaxial accelerometer (PCB 356A16) is moved along several points of the machine structure to measure the acceleration response. Figure 3.16-a shows the main modal shape of the machine ram, with the ram placed at its maximum overhang (1500 mm). The identified main resonance is at 35 Hz with a damping ratio of 2.6%.

As the mode is coming from the whole carriage rocking movement and the ram bending, a disturbance applied at the tool centre point modifies the sensor readings. Figure 3.16-b shows the CNC internal variable readings when an impact at the tool centre point is applied. As external perturbations are observable through the feedback encoders, the control actuation force will be directly affected as shown in the commanded torque. This indicates that this particular mode shape is controllable and observable through the feed drive feedback system. Hence, the control parameters can affect the machine dynamic characteristics.

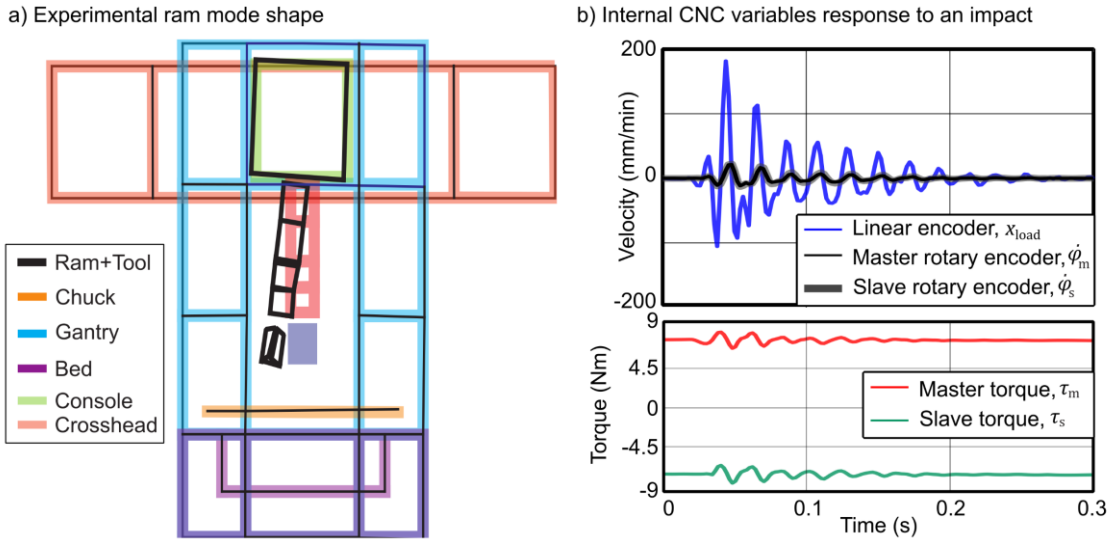

Figure 3.16 a) Experimental ram mode shape; b) Velocity and torque CNC internal variable response to a tool tip disturbance.

3.5.1 Machine pseudo-open loop extraction

In order to predict the effect of the control parameters on the dynamics of the machine, the first step is to characterize both the controller and the open loop response of the machine assembly. The controller can be characterized by the schemes that the CNC manufacturers provide in their documentation. The dynamic characterization of the machine, however, involves difficulties, such as nonlinearities due to friction or machine joints. In addition, the machine dynamics can significantly vary depending on the cutting position. Similarly, the dynamic behavior of the machine changes significantly with and without electrical power. Therefore, obtaining the response without the controller effect cannot be achieved by means of a nonpowered frequency response. In fact, this leads to a very significant nonlinear behavior in presence of the joint backlash, which is suppressed by the electronic preloads. For this reason, a fixed preload value of 10% has been applied during the proceeding tests. However, the invariance of this control parameter would lead to use of the assumptions that have been described previously in Section 3.3.3.

A dedicated compiled cycle has been developed to allow the addition of external commands to position, velocity and torque reference points. This offers the possibility to inject a specified signal into the machine and excite it through the existing feed drive actuators. The machine tool is equipped with a SIEMENS 840D Solution Line CNC which offers a data logger tool called ServoTrace. In addition, a fast analogue to digital switch

converter is installed to be able to measure both tool tip acceleration and applied disturbance force. This implies that internal and external variables are acquired synchronously at the same sampling frequency of 500 Hz. The disturbance is applied through a medium-size shaker which delivers up to 100N force (GW-V20/PA100E). The force used to dynamically excite the machine is measured by means of a load cell (PCB 208C02) placed at the shaker's stinger. At the same time, the tool tip acceleration is measured by an industrial accelerometer (PCB 603C01). As the mathematical model derived in Section 3.3 is based on complex vector operations, the quality of the FRFs used to build the model is of vital importance. For that reason, the use of the shaker rather than the dynamometric impact hammer is considered. With this, and the ServoTrace tool mentioned earlier, the matrix $\mathbf{G}$ that defines the open loop MIMO FRF for the machine, for a certain position, can be measured through excitation via the two kinds of input sources: the disturbance force at the cutting point F_{dis} and the motor torques (τ_{m}, τ_{s}).

Tool centre point force disturbance side characterization

As previously discussed, the machine dynamical behavior is different with and without electrical power, especially due to the variation of the preload. For that reason, in this research the machine has been powered up, but the control parameters have been set to low values (K_{v} = 1 (m/min)/mm, T_{i} = 50 ms and K_{p} = 0.05 Nms/rad) to minimize the influence of the control actuation force while maintaining the preload of 10%. On the other hand, in order to increase the signal quality and minimize the uncertainty, the experiment is conducted four times, obtaining as a result an average response with a successful signal coherence check. Figure 3.17-a shows the complete (four sections of 20 s) acquired time domain data for the disturbance force and tool tip acceleration. The exerted force amplitude of the electromagnetic actuator located at the tool tip decay almost linearly with the excitation frequency. At the beginning of the excitation (25 Hz), the force amplitude is close to 70 N, and as a result of the actuator's response characteristics, at 100 Hz the force has decreased to 60 N (Figure 3.17-b). However, under the assumption of a linear system, this does not generate major problems. The time domain acquired data shows the dynamic behavior of the tested machine, where two clear amplifications are present at 5.8 s and 6.3 s. The two rotary and linear encoders' data are synchronously registered in order to generate the FRFs that are shown in Figure 3.17-c. As expected from the experimental analysis and time domain data, the main two natural frequencies are located at 32 Hz and 35 Hz. Moreover, the

frequency domain magnitude difference of roughly ten between the cutting point (Figure 3.17-c top) and linear scale (Figure 3.17-c centre) sensors can be explained by the mode shape shown in Figure 3.16-a.

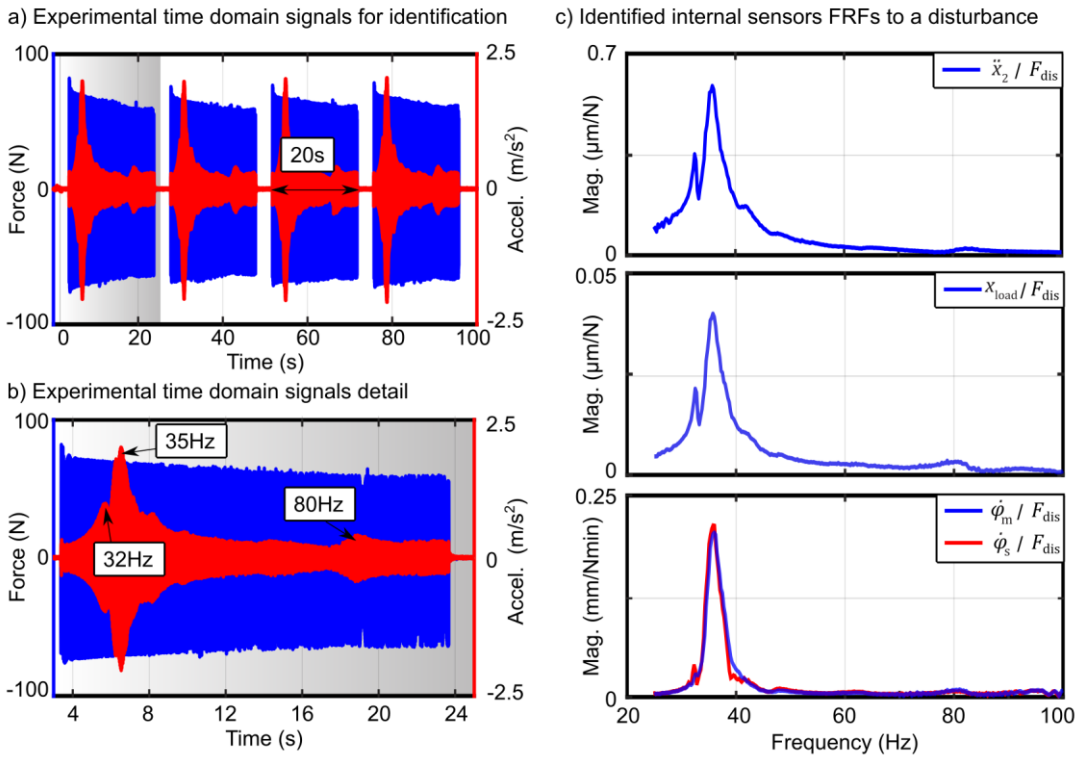

Figure 3.17 a, b) Time domain force and acceleration signals; c) Computed FRFs

The data represented in Figure 3.17-c is used to fill the first column of the $\mathbf{G}$ matrix (Figure 3.14-b).

Feed drive actuation response characterization

Similarly to the previous subsection, the acquired time domain signals are shown in Figure 3.18. As the excitation signal has been placed outside the velocity feedback loop, it can be seen in Figure 3.18-a that the torque commands are sensitive to the structural vibrations. In addition to this, as a result of the master-slave coupling configuration, both commanded torques are of inverse sign to successfully suppress the existing backlash. The static value is ±7 Nm as the preload value is set to 10% of the motor rated torque (70 Nm). The excitation chirp signal is added to this static value. Figure 3.18-b shows the acquired data for both rotary encoders and cutting point acceleration during the excitation process. The machine tool structural resonance at 35 Hz generates an anti-resonance at the same frequency in both rotary encoders as seen in Figure 3.18-c.

Moreover, this is how the machine tool natural frequency interacts with the specified servo controller. This resonance manifests itself as an anti-resonance in the encoder feedback. Furthermore, when commissioning the velocity loop, the implemented control parameters affect the characteristics of the resonance on the machine tool tip side, and its reflection back to the control loop as anti-resonance.

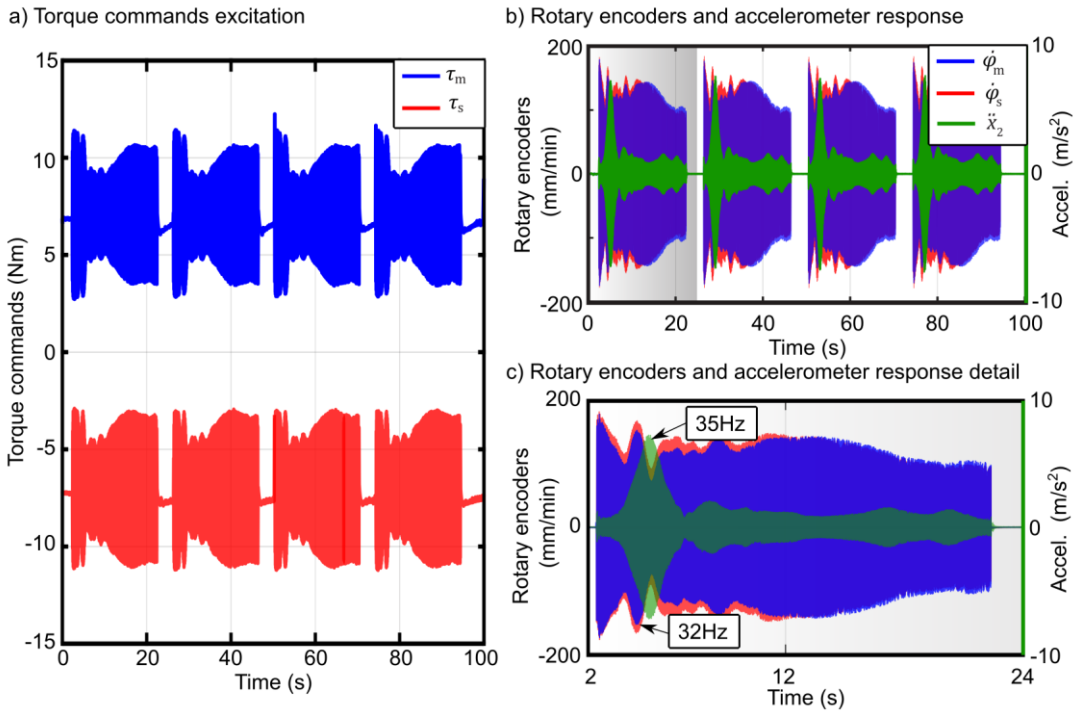

Figure 3.18 Time domain signals of: a) Torque commands; b-c) Rotary encoders and tool tip acceleration.

Figure 3.19 shows the computed frequency responses from both actuators to the linear scale, tool tip displacement and both rotary encoders (x_{load}, x_2, $\dot{\varphi}_{\mathrm{m}}$ and $\dot{\varphi}_{\mathrm{s}}$). Those frequency response functions are obtained directly from the experiment realized with both motors acting simultaneously on the system. These pseudo-open loop responses are used in the matrix $\mathbf{G}$ under the hypotheses that the motors and the velocity controllers are identical. The figure validates the hypotheses as the responses are practically similar up to 40 Hz. Furthermore, the complexity of the responses shows the advantage of deriving the model in the frequency domain rather than performing the curve fittings needed for time domain analyses. Analyzing the frequency response magnitudes in detail, the previously commented order of magnitude difference between the linear scale and tool tip accelerometer is present. Additionally, the commented resonance at 35 Hz

in the accelerometer generates an anti-resonance (or motor-locked frequency) in both rotary encoders.

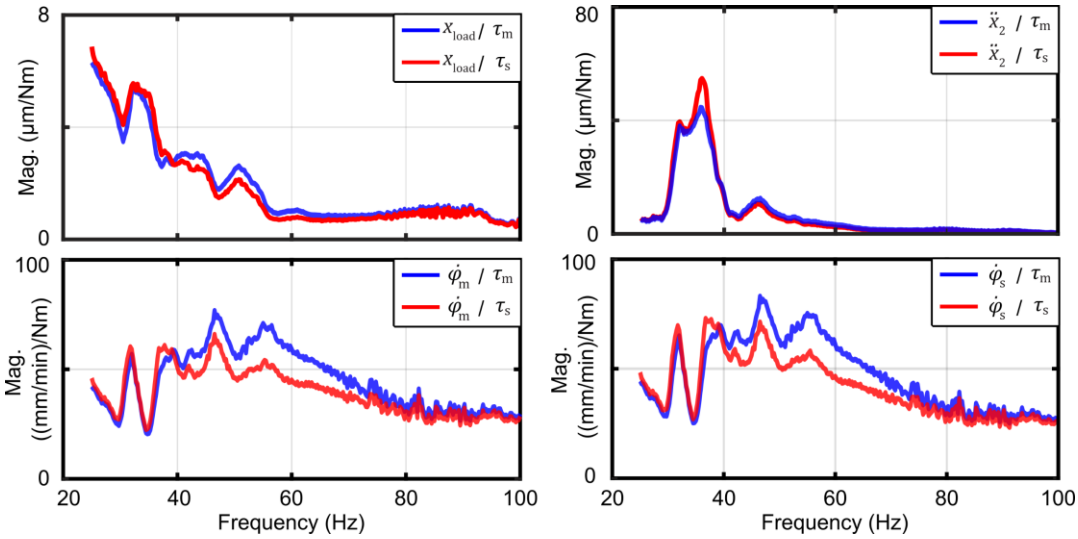

Figure 3.19 Computed FRFs from machine side actuation.

With the tested tension torque of 10%, the time domain amplitude difference between the torque commands (τ_m, τ_s) is ±0.5 Nm, or an 88% of equivalence. At the same time, the frequency response function between both torque commands have shown a +0% and -15% amplitude difference with respect to the ideal ratio of 1:1 within the frequency range of interest. These assumptions demonstrate the capabilities and limitations of the developed simulation model, as the velocity PI controller gains for each motor cannot be modified independently. Also, the followed measurement methodology cannot be generalized to all machine configurations, for example to machines having different motors and different weighting factors for the preload. Nonetheless, in the case of the studied machine tool, the practically obtained FRFs via dual motor excitation can still be used. Future research will address these points and investigate decoupling of individual single-input FRFs from experimental multi-input frequency response data.

The frequency domain signals that are shown in Figure 3.19 are used in the $\mathbf{G}$ matrix as pseudo-open loop responses. With the experimental characterization presented in this section, the analytical effect of the implemented controller can be coupled with the machine tool dynamics.

3.5.2 Model validation

This section shows the predicted and experimental tool centre point closed loop responses for velocity proportional (K_p), integral time (T_i) and position proportional (K_v) gain variations. In the subsequent comparisons, the value of the studied control parameter has been modified, defining as invariant the other two remaining parameters. Note, as previously commented, the commanded preload value is fixed at 10%. In addition, the same parameterization has been defined for both servomotor velocity controllers ($PI_\mathrm{master} = PI_\mathrm{slave}$).

Velocity proportional gain

The influence of the proportional velocity loop gain on the machine tool structural dynamics has been described previously in Section 2.4. This particular gain alters the mechanical pole location; thus, both the natural frequency and damping ratio vary. Figure 3.20 shows the comparison of the machine tool closed loop FRF at the tool centre point for different values of the tested control parameter value. In this example, the remaining feedback gains are tuned to conservative values that would typically be found in a production environment (K_v= 1 (m/min)/mm and T_i= 10 ms). The model can predict the tendency to increase the tool tip compliance when the proportional velocity gains are increased. In addition, the resonance of 32 Hz is not significantly modified with the variation of this gain.

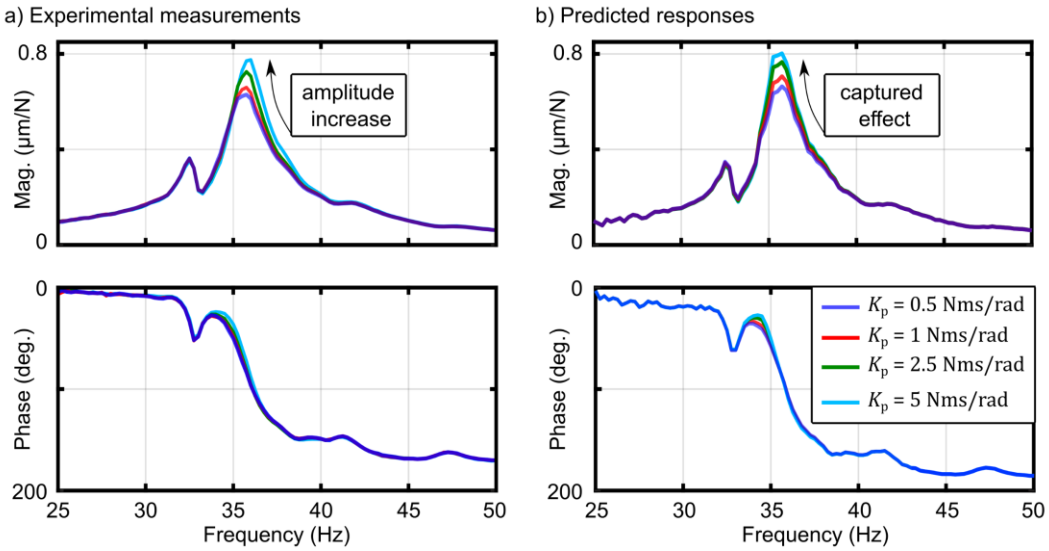

Figure 3.20 a) Experimental; b) Predicted closed loop tool centre point dynamics.

In order to see the effect of the velocity proportional gain on the machine tool compliance, the modal parameters for the 35 Hz mode are extracted. Table 3.1 shows how the natural frequency is slightly modified, but the damping ratio can be modified up to 20% for this machine.

Table 3.1: Modal parameters for different velocity proportional gain values.

K_p (Nms/rad)	Natural frequency (Hz)	Damping ratio (%)	Modal stiffness (N/µm)	Modal mass (kg)
0.5	35.7	3.2	24.3	483
1	35.7	3	24.7	492
2.5	35.6	2.7	24.4	486
5	35.9	2.6	24.4	479

Velocity integral time and position proportional gain

Figure 3.21-a shows the velocity integral time effect at the tool tip. As it can be seen in both experimental and predicted frequency responses, this gain does not modify the machine tool dynamic behaviour significantly. For this test, the proportional velocity and position gains were respectively fixed to 2.5 Nms/rad and 1 (m/min)/mm. Figure 3.21-b shows the position proportional gain effect. As in the previous case, the position loop gain does not change the tool tip dynamic response significantly, at least for the tested machine tool.

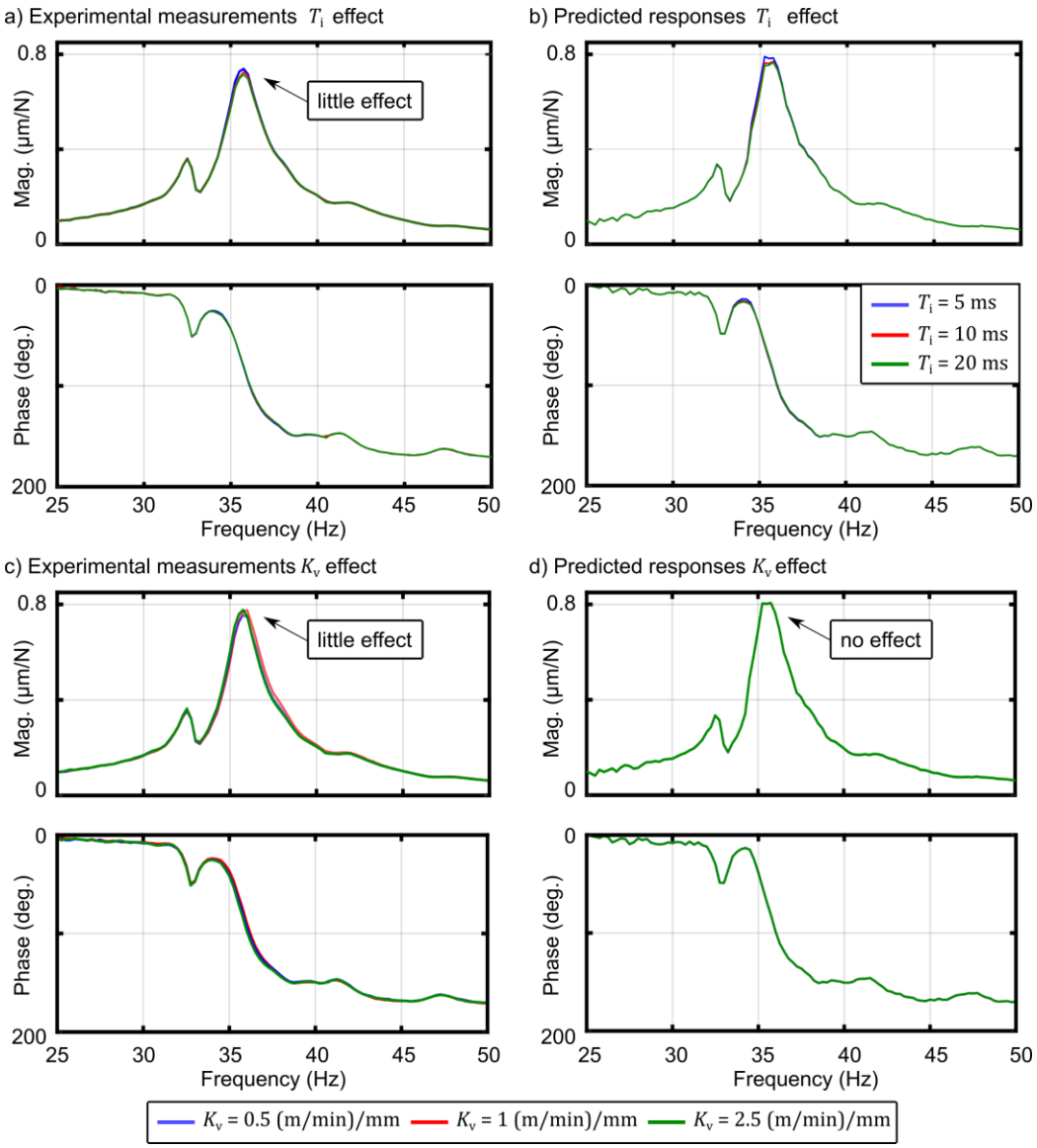

Figure 3.21 Experimental and predicted dynamics for velocity integral time and position proportional gain.

These conducted tests validate the frequency domain based MIMO model and the hypotheses carried out in Section 3.3.3, as it captures the experimentally observed tool centre point dynamic behaviour for different control parameter variations.

3.6 CONCLUSIONS

This chapter has analyzed the influence of the master-slave control parameters on the static and dynamic behavior of two different large machine tools. When applying a static disturbance force, it has been found that the pinion flank contact transition is not fast enough to be neglected. As a result, the commissioned preload level not only affects the acceleration capacity of the driven machine, but also the equivalent stiffness linear

behavior of the feed drive system. The proposed model provides significant insights about this feed drive mechanism as it is able to accurately predict the observed experimental trends. Conducted tests show that increasing the preload level through the electronic preload does not vary the master or slave equivalent stiffness values. For large heavy-duty machine tools, where the acceleration capabilities of the drive might not be the limitation, the preload level can be tuned to handle the high load forces generated during the cutting process ensuring a preload and, hence, linearity.

The dynamic analysis has shown the influence of the machine tool dynamics at the servo feedback sensor readings. The response amplitude is determined by the dynamic characteristics of the machine (experimentally obtained by modal analysis) and the location of the feedback sensors. A MIMO model for coupling the servo controller effect and machine tool structural dynamics has been developed. The machine tool dynamic behavior has been characterized from external disturbances by means of a shaker and the machine's own actuators, through a dedicated compiled cycle implemented in the industrial CNC. The frequency domain based model has been successfully validated by comparing the predicted machine closed loop frequency responses to the experimental ones. The proportional velocity loop gain is the most critical parameter that influences the tool centre point compliance. The integral time gain and the proportional position loop gain have minor influence.

Chapter 4

Feed drive control tuning for machining chatter avoidance

4.1 INTRODUCTION

The tuning of feed drive control parameters can significantly influence the performance of a machine tool in terms of motion accuracy and cutting stability (Altintas et al. [98]). For motion accuracy, high feedback control bandwidth and feedforward actions are required (Matsubara et al. [233]). However, as reviewed in Section 2.4, the vibratory modes that interact with the servo loop constitute a major limitation in the way of increasing the feedback control bandwidth.

CNC systems provide frequency response (Bode) plots of the feed drive response via the position feedback sensors. Relying solely on this information, however, leads to maximizing the measured positioning bandwidth and accuracy via high gain controller tuning, which can deteriorate the dynamic stiffness at the most important location, the cutting point (Uriarte et al. [1]). Assessing the influence of the cascade control system

parameters, shown in Figure 4.1, the velocity loop proportional gain K_p has the highest impact on the damping contributed by the feed drive (Zirn [125]). Simulation studies have been performed to identify the optimum settings for K_p, K_v (position loop gain) and T_i (velocity loop integration time constant), to improve the chatter stability limit (Beudaert et al. [63], Albertelli et al. [126]). However, these studies, and nearly all the others proposed in literature, have considered only a simplified lumped-mass feed drive model that captures just one vibration mode. The response of real machine tools is generally far more complex, rendering the effectiveness of these earlier guidelines or designs suboptimal in practice.

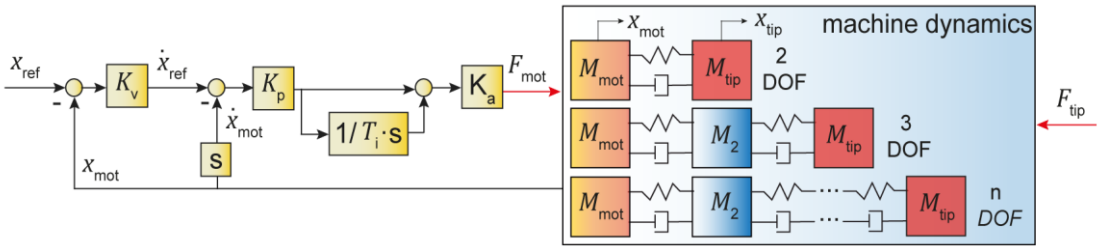

Figure 4.1 Feed drive system model.

This chapter introduces a new and comprehensive strategy to achieve optimum vibration damping and chatter stability augmentation via servo controller tuning, that is applicable to the generalized high order dynamics encountered in machine tool feed drives and their structural assemblies. The proposed strategy takes into account the servo feedback response and predicted tool tip compliance, and follows a hybrid approach synergistically combining model-based analysis, such as root locus, with data-driven design in the frequency domain. The resulting control parameters can be directly implemented on existing industrial CNC machine tools without requiring any extra sensors like accelerometers (Munoa et al. [136], Zatarain et al. [234], Sencer et al. [235]) or control law modification (Kakinuma et al. [135], Sun et al. [151], Erkorkmaz et al. [236]).

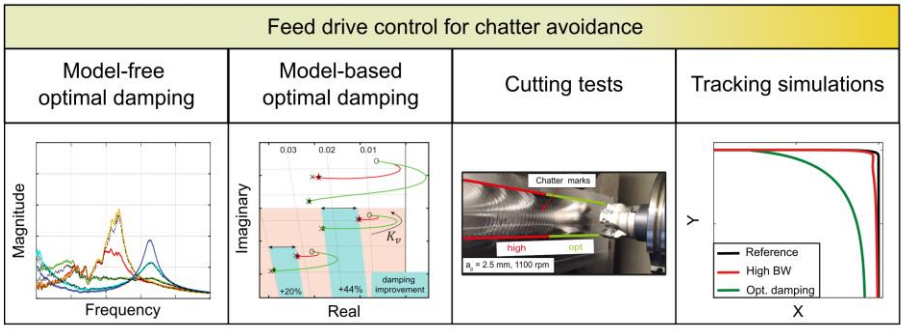

Figure 4.2 Steps for feed drive control tuning for chatter avoidance.

4.2 FEED DRIVE CONTROL TUNING WITH STRUCTURAL FLEXIBILITY

Machine tool feed drives are controlled using a cascade structure with current, velocity and position feedback loops, as well as feedforward actions. Feedforward control enhances the command following accuracy, but has no influence on the disturbance (i.e., cutting process forces) response. Thus, it is kept outside the scope of this thesis. The bandwidth of the current loop is in the order of hundreds of hertz. In the context of structural chatter vibrations, which in large machine tool applications classically occur at 20-100 Hz (Munoa et al. [2]), the current loop can thus be modelled as a constant gain preceding the motor torque/force constant K_{a}.

In large machine tools (such as gantry or travelling column type machine structure), the stiffness of the motion delivery chain from the feed drive actuator to the measurement point, which is typically a linear encoder, is much larger than the stiffness of the remaining mechanical assembly towards the cutting point. Thus, in modelling such a feed drive system via lumped mass elements, for simplicity, it can be assumed that the position and velocity control feedback are taken from the first mass M_{mot}.

The next subsection describes state-of-the-art servo controller tuning for its industrial deployment based on two degrees of freedom models.

4.2.1 State-of-the-art servo controller tuning

The cascaded control configuration used in almost every industrial machine presents the advantage of step-by-step loop commissioning from innermost to outermost control loop. As indicated in Section 2.4, the velocity loop PI type controller is first commissioned. The first parameter to tune is the velocity proportional gain (K_{p}), which strongly influences the velocity closed loop bandwidth (f_{bw}). For optimal gain computation, the integral time action (T_{i}) should be deactivated (Gross et al. [121]). As a result of removing the integral action, the order of the system decreases, obtaining a first order characteristic equation (Eq. (4.1)). The expression for computing the velocity proportional gain which depends on the axis total mass (represented by M_{total}) and velocity closed-loop bandwidth is shown in Eq. (4.2).

$$\frac{\dot{x}_{\mathrm{mot}}}{\dot{x}_{\mathrm{ref}}} = \frac{1}{\tau s + 1}\text{, where } \tau = M_{\mathrm{total}}/K_{\mathrm{p}} \tag{4.1}$$

$$K_p = 2\pi M_{\text{total}} f_{\text{bw}} \tag{4.2}$$

Once this value is computed, the integral action can then be calculated. However, the extra pole added by this parameter brings a second order transfer function, which induces a vibratory behaviour. Gross et al. [121] followed a method called double ratio for getting the maximum damping at the velocity closed loop. A generalized transfer function is described in Eq. (4.3). For a closed loop case, the numerator coefficients ($b_0 \cdots b_{\text{m}}$) determine the response characteristics and amplitude response of the zeros. On the other hand, the denominator coefficients ($a_0 \cdots a_{\text{n}}$) describe the damping and stability (poles) of the system.

$$tf\ (s) = \frac{b_0 + b_1 s\ +\ \ldots\ + b_{\text{m}} s^{\text{m}}}{a_0 + a_1 s\ +\ \ldots\ + a_{\text{n}} s^{\text{n}}} \tag{4.3}$$

As described by Gross et al. [121] an optimum damping response can be achieved by forming the coefficient ratios (($a_{\text{n}}/a_{\text{n}-1}$), ($a_{\text{n}-1}/a_{\text{n}-2}$),…, ($a_1/a_0$)) and defining the proportion of two adjacent ratios as 0.5 (Eq. (4.4)). This value provides a good command and disturbance response behaviour without performing extensive calculations.

$$\frac{\frac{a_{\text{n}}}{a_{\text{n}-1}}}{\frac{a_{\text{n}-1}}{a_{\text{n}-2}}} = \frac{a_{\text{n}}\, a_{\text{n}-2}}{(a_{\text{n}-1})^2} = 0.5 \tag{4.4}$$

Eq. (4.5) shows the closed velocity loop transfer function, which can be re-arranged in form of coefficient ratios as shown in Eq. (4.6). By applying the relation of 0.5 to the adjacent ratios Eq. (4.7) is obtained.

$$\frac{\dot{x}_{\text{mot}}}{\dot{x}_{\text{ref}}} = \frac{\frac{K_{\text{p}}}{T_{\text{i}}\, M_{\text{total}}}(T_{\text{i}} s + 1)}{s^2 + \frac{K_{\text{p}}}{M_{\text{total}}} s\ + \frac{K_{\text{p}}}{T_{\text{i}}\, M_{\text{total}}}} \tag{4.5}$$

$$\frac{a_2}{a_1} = \frac{1}{\frac{K_{\text{p}}}{M_{\text{total}}}} \text{ and } \frac{a_1}{a_0} = \frac{\frac{K_{\text{p}}}{M_{\text{total}}}}{\frac{K_{\text{p}}}{T_{\text{i}}\, M_{\text{total}}}} \tag{4.6}$$

$$\frac{\frac{a_2}{a_1}}{\frac{a_1}{a_0}} = \frac{a_2 a_0}{{a_1}^2} = \frac{\frac{K_{\text{p}}}{T_{\text{i}}\, M_{\text{total}}}}{\frac{{K_{\text{p}}}^2}{{M_{\text{total}}}^2}} = \frac{M_{\text{total}}}{T_{\text{i}}\, K_{\text{p}}} = \frac{1}{2} \tag{4.7}$$

Combining Eq. (4.2) and (4.7), the expression for the integral time calculation is obtained.

$$T_{\mathrm{i}} = \frac{1}{\pi f_{\mathrm{bw}}} \tag{4.8}$$

Following Eq. (4.2) and (4.8) the velocity loop proportional and integral time gains can be computed according to the desired bandwidth f_{bw}. As a result of the relationship between the two gains, the pole related to the integral time is located at 70% of damping.

During the machining process, the disturbances should be tackled as fast as possible, therefore an overshoot of up to 3dB is generally accepted in the velocity loop. In contrast, in the outer position loop an overshoot cannot exist, as it will be reflected in the geometry of the machined workpiece. Eq. (4.9) shows the closed position loop approximation to a second order transfer function (which considers $T_{\mathrm{i}} = \infty$). By using a damping value of 1, the relationships of Eq. (4.10) can be obtained by the equivalence of the classical second order response. By combining them the Eq. (4.11) is obtained.

$$\frac{x_{\mathrm{mot}}}{x_{\mathrm{ref}}} = \frac{\frac{K_{\mathrm{v}}K_{\mathrm{p}}}{M_{\mathrm{total}}}}{s^2 + \frac{K_{\mathrm{p}}}{M_{\mathrm{total}}}s + \frac{K_{\mathrm{v}}K_{\mathrm{p}}}{M_{\mathrm{total}}}} \tag{4.9}$$

$$\omega_0^2 = \frac{K_{\mathrm{v}}K_{\mathrm{p}}}{M_{\mathrm{total}}} \qquad \omega_0^2 = \left(\frac{K_{\mathrm{p}}}{2M_{\mathrm{total}}}\right)^2 \tag{4.10}$$

$$K_{\mathrm{v}} = \frac{K_{\mathrm{p}}}{4M_{\mathrm{total}}} \tag{4.11}$$

By re-arranging Eq. (4.2) and (4.11), the proportional position loop gain value is calculated by means of Eq. (4.12).

$$K_{\mathrm{v}} = \frac{\pi f_{\mathrm{bw}}}{2} \tag{4.12}$$

As a result, by applying Eq. (4.2), (4.8) and (4.12), the three main cascaded control structure parameters (K_{p}, T_{i} and K_{v}) can be computed by selecting the desired closed velocity bandwidth frequency (f_{bw}). The obtained parameter values will have a maximum 3dB and 0dB magnitude in closed velocity and position loops. However, the selection of the closed velocity bandwidth is not trivial and not only affects the motion performance, but can also extensively modify the cutting point dynamics. To analyse this interaction, the next subsection describes a two degree of freedom system where different bandwidths are applied.

4.2.2 Industrial tuning guidelines

It should be mentioned that there is not an exact tuning guideline for servo control loop commissioning, since there are different tuning criteria and the most suitable one should be selected depending on the initial situation and the objective of the controlled system. In 2001, Schafers et al. [237] (Siemens) proposed a limitation of the position proportional gain to approximately one tenth of the lowest natural frequency of the axis for cases where the resonance lies below 100 Hz with a position controller sampling time of 1 ms. Later in 2003, Schafers et al. [238] limited the maximum velocity gain to ensure a maximum amplitude on the closed velocity bode plot to 5dB. Lee et al. [239] (Heidenhain and Mazak) presented a practical servo tuning method for improving the contouring accuracy, by limiting the position loop gain such that the gain of the open-loop transfer function of the position feedback becomes -6dB at the mechanical resonance.

Automatic tuning routines are also proposed in the literature. In 2005, Rodríguez de Yurre et al. [240] (Tekniker and Fagor) presented an autotuning procedure to identify the optimal control parameters, which achieves the maximum possible damping of the mechanical pole. A function called Advanced Gain Search was presented by Wakana [241] (Mitsubishi Electric), in which by performing coarse and fine simulations, the tuning routine offers different parameter combinations considering the settling time and overshoot amount. Additionally, the original response used for controller commissioning can be extensively altered by the workpiece mass. Some machine tool builders provides CNC routines to optimize the servo control and maintain the surface quality finish eliminating the possible noise and vibrations (Servonavi [242] from Okuma).

4.2.3 Two degrees of freedom system

The analysis of a two Degrees Of Freedom (DOF) lumped mass feed drive system reveals the underlying motivation behind the tuning guidelines in Uriarte et al. [1] and Beudaert et al. [63]. For a flexible feed drive model with a single mode, two characteristic frequencies are presented. First, the so-called motor locked or quenching frequency (f_{t}), where load side vibratory dynamics cancel out motor side displacement (x_{mot}). Eq. (4.13) shows how machine tool resonances interact with the servo dynamics. Second, the resonance frequency (f_{r}) that is generated by the combination of the coupling stiffness (k) and the two mass values (M_{mot} , M_{tip}) (Eq. (4.14)).

$$f_{\mathrm{t}} = \frac{1}{2\pi}\sqrt{\frac{k}{M_{\mathrm{tip}}}} \tag{4.13}$$

$$f_{\mathrm{r}} = \frac{1}{2\pi}\sqrt{k\left(\frac{1}{M_{\mathrm{mot}}} + \frac{1}{M_{\mathrm{tip}}}\right)} \tag{4.14}$$

The model parameters can be identified by performing a curve fitting from the measured open loop response between the motor force (F_{mot}) and motor displacement (x_{mot}). The analytical open loop frequency response expression is described by Eq. (4.15), where viscous friction, coupling stiffness and damping are represented by σ, k and c, respectively. Electromagnetic servo actuators present a characteristic phase lag (Gross et al. [121]) that can be approximated by a time delay τ_{ol}.

$$\frac{X_{\mathrm{mot}}}{F_{\mathrm{mot}}} = \frac{\left(M_{\mathrm{tip}}s^2 + cs + k\right)e^{-\tau_{\mathrm{ol}}s}}{\left(M_{\mathrm{mot}}M_{\mathrm{tip}}s^4 + \left(c\left(M_{\mathrm{mot}} + M_{\mathrm{tip}}\right) + \sigma M_{\mathrm{tip}}\right)s^3 + \left(k\left(M_{\mathrm{mot}} + M_{\mathrm{tip}}\right) + \sigma c\right)s^2 + \sigma k s\right)} \tag{4.15}$$

Figure 4.3-a presents the experimental setup used for the development and validation of the proposed approach. It consists of a single axis driven by an ETEL ILM06-06-3RB-A20C linear motor with an added flexure carrying the workpiece on top of the slider. With the aim of having complete observability and controllability from the feed drive control system, the flexure acts as a single degree of freedom in the displacement direction. The current loop is closed by the ETEL controller, meanwhile the position, velocity, and the command reference are managed by a dSPACE DS1005PPC controller.

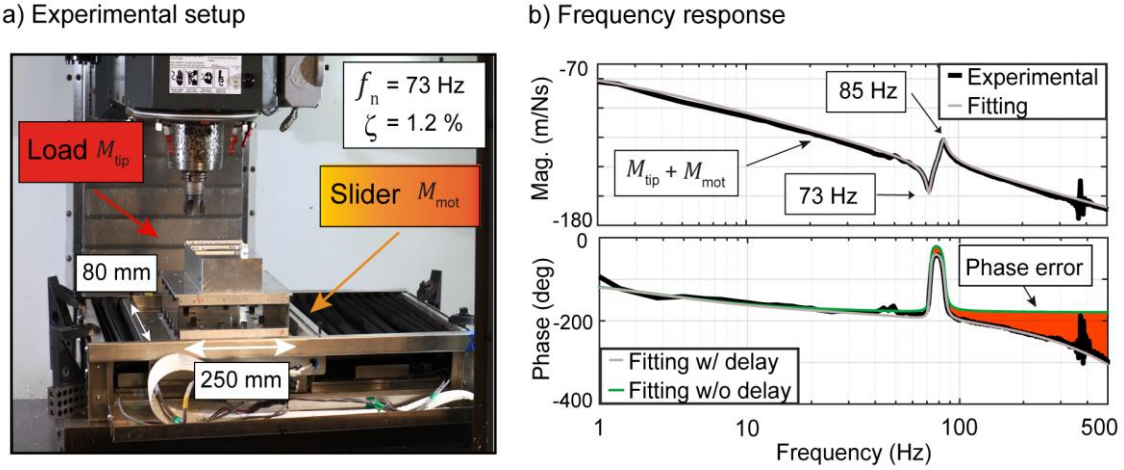

Figure 4.3 a) Experimental setup description; b) Experimental and fitted FRF.

The two DOF lumped mass model parameters can be obtained by fitting (via Eq. (4.15)) the experimental open loop compliance measurement shown in Figure 4.3-b. The

identified parameters are as follows: M_{mot} = 24.9 kg, M_{tip} = 9.5 kg, k = 1.98 N/µm, c = 104 Ns/m, σ = 792 kg/s and τ_{ol} = 0.75 ms.

Using the previously described state-of-the-art controller tuning (Section 4.2.1) and the identified parameters above, three different controller tunings are considered based on the closed velocity loop bandwidth: low (f_{bw}= 15 Hz), high (f_{bw}= 87 Hz) and optimum (f_{bw}= 58 Hz = 80% f_{t}). The latter achieves optimum damping by adjusting the terms K_{p}, T_{i}, and K_{v} according to Uriarte et al. [1] and Beudaert et al. [63]. Figure 4.4-a shows the closed loop velocity response ($\dot{x}_{\mathrm{mot}}/\dot{x}_{\mathrm{ref}}$), which can be measured through the machine's CNC, and the response at the second mass $\left(\dot{x}_{\mathrm{tip}}/\dot{x}_{\mathrm{ref}}\right)$, which is not explicitly considered when applying mainstream industrial tuning methods. The lack of information related to the cutting point can lead to high gain tuning, thereby disallowing the servo system to improve the overall structural damping. For example, in Figure 4.4-a, the motor encoder magnitude drops at f_{t} corresponds to a tip amplification.

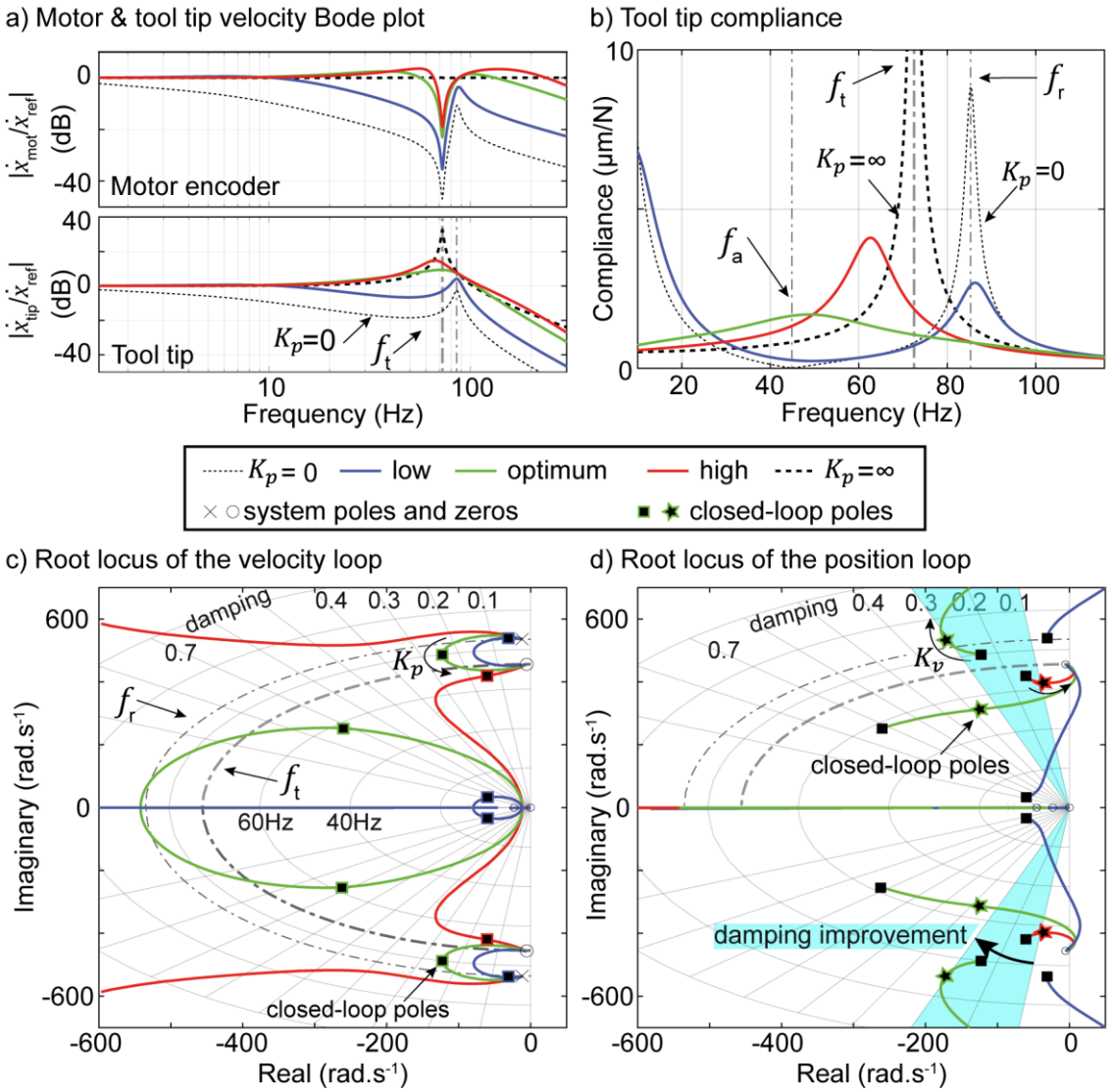

Figure 4.4 Analysis of a two degree of freedom flexible feed drive model.

For chatter characterization, it is important to analyse the compliance relating the tool tip displacement (x_{tip}) to the applied external force (F_{tip}). Figure 4.4-b shows that the high bandwidth configuration amplifies the structural resonance, which affects the cutting point dynamics in a detrimental manner. The optimally tuned velocity controller achieves the largest reduction in the tool tip compliance.

The interaction of the servo controller and machine tool structural dynamics can be analysed through the root locus technique (Figure 4.4-c&d), which displays the closed loop system pole locations as the controller gain is varied. The extracted delay term has infinite number of roots, which in continuous time LTI models can be approximated as a rational function by Padé approximation, Eq. (4.16). Where s is the Laplace operator,

$a_0, a_1 \cdots a_{\mathrm{L}}$ are the constants and L is the approximation order. It is very important to compare the experimental and approximate responses to choose the correct approximation order.

$$e^{-\tau s} \approx P_{\mathrm{d}}(s) = \frac{a_0 - a_1 s + \cdots (-1)^{\mathrm{L}} a_{\mathrm{L}} s^{\mathrm{L}}}{a_0 + a_1 s + \cdots a_{\mathrm{L}} s^{\mathrm{L}}} \tag{4.16}$$

The velocity loop locus starts at the poles of the open loop system $(K_{\mathrm{p}} = 0)$ and ends at the zeros as $K_{\mathrm{p}} \to \infty$. As shown in Figure 4.4-b, when $K_{\mathrm{p}} = 0$, the system has no static stiffness, and an anti-resonance appears at $f_{\mathrm{a}} = \sqrt{k/M_{\mathrm{mot}}}$. When $K_{\mathrm{p}} \to \infty$, M_{mot} is completely fixed due to the high stiffness of the controller, and the system behaves like a single suspended mass with a resonance frequency f_{t}. Between those extreme cases, the velocity controller can modify the apparent structural frequency and increase the damping of the machine. The position loop gain K_{v}, on the other hand, has only a secondary impact on the structural dynamics. The locus of the position loop starts at the pole locations left by the velocity controller. In general, the achievable K_{v} values that maintain system stability do not allow for a significant modification of the system dynamic response.

The current state-of-the-art controller tuning method based on the two DOF can, however, generate sub-optimal results when applied to feed drive and structural assemblies with higher order dynamics.

4.2.4 Three degrees of freedom system

A three DOF model is derived according to Figure 4.1. As deriving an analytical equation for ($X_{\mathrm{mot}}/F_{\mathrm{mot}}$) in a single transfer function expression is time consuming, this task is shortened using the State-Space approach (Eq.(4.17)-(4.19)).

$$\underbrace{\begin{bmatrix} \dot{x}_{\mathrm{mot}} \\ \dot{x}_2 \\ \dot{x}_{\mathrm{tip}} \\ \ddot{x}_{\mathrm{mot}} \\ \ddot{x}_2 \\ \dot{x}_{\mathrm{tip}} \end{bmatrix}}_{\dot{x}} = \underbrace{\begin{bmatrix} 0 & 0 & 0 & 1 & 0 & 0 \\ 0 & 0 & 0 & 0 & 1 & 0 \\ 0 & 0 & 0 & 0 & 0 & 1 \\ \frac{-k_1}{M_{\mathrm{mot}}} & \frac{k_1}{M_{\mathrm{mot}}} & 0 & \frac{-c_1}{M_{\mathrm{mot}}} & \frac{c_1}{M_{\mathrm{mot}}} & 0 \\ \frac{k_1}{M_2} & \frac{-k_1-k_2}{M_2} & \frac{k_2}{M_2} & \frac{c_1}{M_2} & \frac{-c_1-c_2}{M_2} & \frac{c_2}{M_2} \\ 0 & \frac{k_2}{M_{\mathrm{tip}}} & \frac{-k_2}{M_{\mathrm{tip}}} & 0 & \frac{c_2}{M_{\mathrm{tip}}} & \frac{-c_2}{M_{\mathrm{tip}}} \end{bmatrix}}_{A} \underbrace{\begin{bmatrix} x_{\mathrm{mot}} \\ x_2 \\ x_{\mathrm{tip}} \\ \dot{x}_{\mathrm{mot}} \\ \dot{x}_2 \\ \dot{x}_{\mathrm{tip}} \end{bmatrix}}_{x} + \underbrace{\begin{bmatrix} 0 \\ 0 \\ 0 \\ \frac{1}{M_{\mathrm{mot}}} \\ 0 \\ 0 \end{bmatrix}}_{B} \underbrace{F_{\mathrm{mot}}}_{u} \tag{4.17}$$

$$\underbrace{x_{\mathrm{mot}}}_{y} = \underbrace{[1 \quad 0 \quad 0 \quad 0 \quad 0 \quad 0]}_{C}\, x \tag{4.18}$$

$$\frac{X_{\mathrm{mot}}}{F_{\mathrm{mot}}} = C\,(sI - A)^{-1}B \tag{4.19}$$

In the case that the structural model becomes three degrees of freedom. Considering a 3 degree of freedom system representation of a different machine tool feed drive assembly, with parameters as summarized in Table 4.1, the root locus changes considerably, as shown in Figure 4.5-a. For example, two controller parameter sets can be considered. Controller setting C_1 applies the guidelines of Uriarte et al. [1] and Beudaert et al. [63], and yields the tool tip compliance shown in green in Figure 4.5-b. Controller setting C_2, however, achieves further improvement by additional adjustment of the P-PI gains via root locus analysis, as shown in Figure 4.5-a. The damping increment leads to a lower amplitude in the receptance response. It is important to mention that high order open loop dynamics lead to significantly more complex interactions between the control parameters and the resulting closed loop pole locations.

Table 4.1: System parameters for a three degrees of freedom feed drive system.

Name	f_{bw} (Hz)	K_{p} (N/(m/s))	T_{i} (ms)	K_{v} ((m/min)/mm)
C_1	56	62000	7.1	4.2
C_2	112	124000	7.1	0.9
Model parameters: M_{mot} = 80 kg, M_2= 130 kg, M_{tip}=10.8 kg, k_1=22 N/µm, k_2=1.75 N/µm, c_1= 1069 N/(m/s), c_2= 86.7 N/(m/s)				

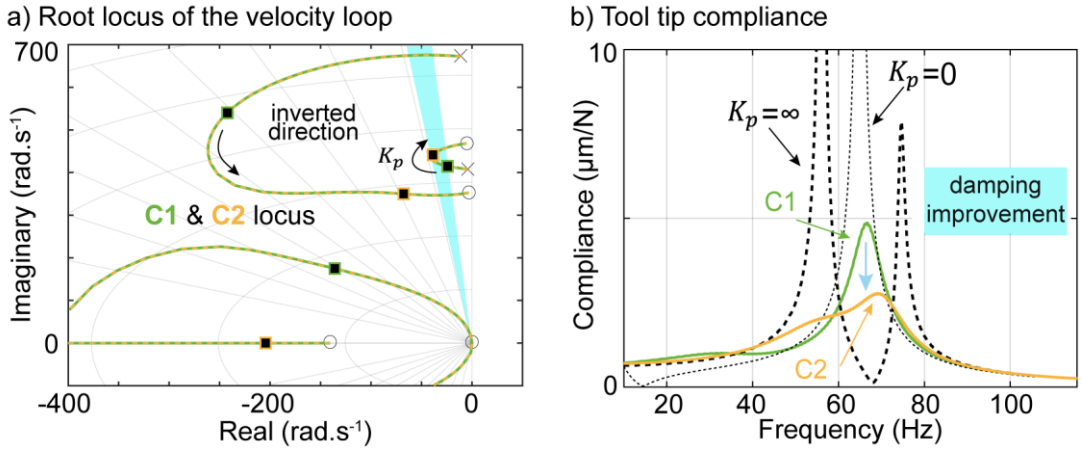

Figure 4.5 Analysis of a three degrees of freedom flexible feed drive model.

This academic analysis of three degrees of freedom system shows that the controller tuning guidelines presented in the literature might not be valid as they are based on the two degrees of freedom approximation. Hence, a more general controller tuning approach that considers complex machine tool dynamics is required.

4.3 MODELLING AND CONTROL FOR GENERAL MACHINE TOOL DYNAMICS

This section presents two complementary approaches to analyse and adjust the interactions between the controller and machine tool dynamics (Figure 4.6). Frequency domain operations via direct measurements allow the prediction of the motor side response (Steps 1-3) and the tool tip receptance (Steps 4-5). Then, fitting a model to the open loop mobility enables the root locus technique to be used in maximizing the damping of closed loop poles (Step 6). The proceeding analyses are based on the control structure in Figure 4.1. Also as mentioned in Section 3.3 the inputs are assumed to be bounded to justify linear analysis.

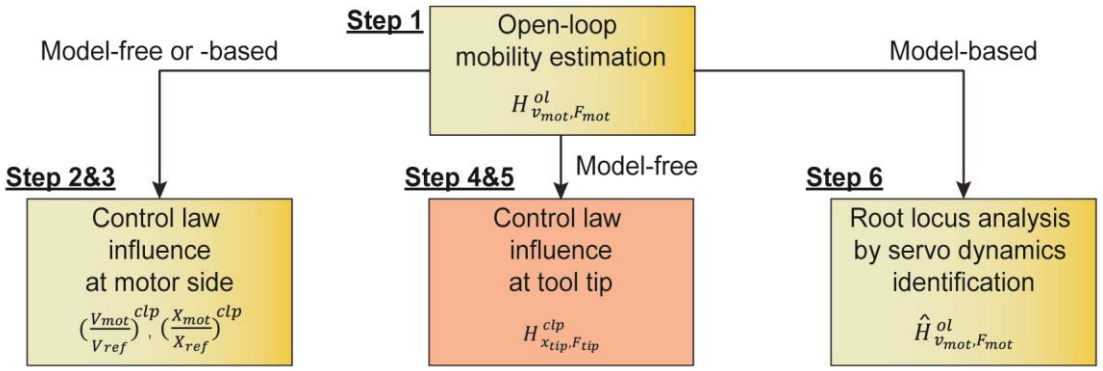

Figure 4.6 Overview of proposed strategy.

4.3.1 Frequency response prediction at the motor side

Open loop mobility estimation: A closed velocity loop (denoted: $'\mathrm{clp}'$) FRF is acquired via machine CNC ($\dot{x}_{\mathrm{mot}}/\dot{x}_{\mathrm{ref}}$), and the servo mobility open loop response (denoted: $'\mathrm{ol}'$) is computed with Eq. (4.20) at each frequency ω. Extra dynamics, due to unknown filters or the current loop, are also implicitly included in the extracted open loop response.

$$H^{\mathrm{ol}}_{\dot{x}_{\mathrm{mot}},F_{\mathrm{mot}}} = \frac{(\dot{x}_{\mathrm{mot}}/\dot{x}_{\mathrm{ref}})^{\mathrm{clp}}}{K_{\mathrm{p}}\left(1 + \frac{1}{T_{\mathrm{i}}\, j\omega}\right)(1 - (\dot{x}_{\mathrm{mot}}/\dot{x}_{\mathrm{ref}})^{\mathrm{clp}})} \tag{4.20}$$

Control law influence at motor side: Rearranging Eq. (4.20), the closed loop velocity response can be predicted for any value of K_p and T_i using frequency domain operations, and under the assumption of linearity (Eq. (4.21)).

$$\left(\frac{\dot{x}_\mathrm{mot}}{\dot{x}_\mathrm{ref}}\right)^\mathrm{clp} = \frac{H^\mathrm{ol}_{\dot{x}_\mathrm{mot},F_\mathrm{mot}}\, K_\mathrm{p}\left(1 + \frac{1}{T_\mathrm{i}\, j\omega}\right)}{1 + H^{ol}_{\dot{x}_\mathrm{mot},F_\mathrm{mot}}\, K_p\left(1 + \frac{1}{T_\mathrm{i}\, j\omega}\right)} \tag{4.21}$$

The closed position loop Bode ($x_\mathrm{mot}/x_\mathrm{ref}$) is predicted by Eq. (4.22). The effect of the sampling rate should be considered to successfully predict the phase response. The value of the pure delay τ_cl corresponds to twice the position loop sampling period.

$$\left(\frac{x_\mathrm{mot}}{x_\mathrm{ref}}\right)^\mathrm{clp} = \frac{K_\mathrm{v}\,(\dot{x}_\mathrm{mot}/\dot{x}_\mathrm{ref})^\mathrm{clp}}{j\omega + K_\mathrm{v}\,(\dot{x}_\mathrm{mot}/\dot{x}_\mathrm{ref})^\mathrm{clp}}\, e^{-\tau_\mathrm{cl}\, j\omega} \tag{4.22}$$

4.3.2 MIMO model for machine tool cutting point FRF prediction

The machine tool structure coupled with the servo controller can be represented as a multi-input multi-output (MIMO) system, as shown in Figure 4.7. The considered inputs are F_tip and F_mot, which are the process related force at the tool tip, and motor actuation force, respectively. The outputs are: x_tip, the displacement at the tool tip (i.e., performance point of interest); and x_mot, the displacement measured by the servo feedback (e.g., the linear encoder). Using the Linear Fractional Transformation technique, Eq. (4.23) predicts the closed loop compliance at the tool tip $H^\mathrm{clp}_{x_\mathrm{tip},F_\mathrm{tip}}$ under the influence of the controller. The closed loop dynamics depend on the open loop responses, the P-PI controller K in Eq. (4.24), which is known, and the open loop response $H^\mathrm{ol}_{x_\mathrm{mot},F_\mathrm{mot}}$ obtained by integrating Eq. (4.20) with respect to time.

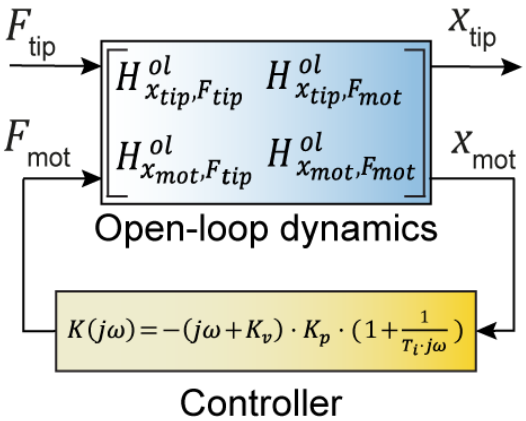

Figure 4.7 Linear Fractional Transformation scheme for tool tip compliance prediction.

$$H^{\mathrm{clp}}_{x_{\mathrm{tip}},F_{\mathrm{tip}}} = H^{\mathrm{ol}}_{x_{\mathrm{tip}},F_{\mathrm{tip}}} + H^{\mathrm{ol}}_{x_{\mathrm{tip}},F_{\mathrm{mot}}} K\left(1 - H^{\mathrm{ol}}_{x_{\mathrm{mot}},F_{\mathrm{mot}}} K\right)^{-1} H^{\mathrm{ol}}_{x_{\mathrm{mot}},F_{\mathrm{tip}}} \tag{4.23}$$

$$K(j\omega) = -(j\omega + K_{\mathrm{v}}) K_{\mathrm{p}} \left(1 + \frac{1}{T_{\mathrm{i}}\, j\omega}\right) \tag{4.24}$$

The challenge in industrial machine tools is to obtain the open loop measurements at the cutting point. It is critical to use only closed loop data, because the dynamic response can vary significantly due to factors like counterweight compensation or mechanical brakes when the servo controller is not activated. This problem is solved by two different approaches based on Eq. (4.23). On one hand, the first approach predicts new controller effect based on an approximated $H^{\mathrm{ol}}_{x_{\mathrm{tip}},F_{\mathrm{tip}}}$ and transmission dynamics identification. The second approach, however, estimates the direct term $H^{\mathrm{ol}}_{x_{\mathrm{tip}},F_{\mathrm{tip}}}$ and the cross terms product $H^{\mathrm{ol}}_{x_{\mathrm{tip}},F_{\mathrm{mot}}} \cdot H^{\mathrm{ol}}_{x_{\mathrm{mot}},F_{\mathrm{tip}}}$ from closed loop measurements.

Approach #1

Control law influence at tool tip: While the servo feedback loops (position, velocity and current) are active, the tool tip receptance FRF $H^{\mathrm{clp},\mathrm{K}_0}_{x_{\mathrm{tip}},F_{\mathrm{tip}}}$ is measured by impact hammer testing, under very low controller settings to approximate the acquired response to an open loop (K_0). At the same time, by sensing the displacement at the feedback location, the cross dynamic compliance $\left(H^{\mathrm{ol},\mathrm{K}_0}_{x_{\mathrm{mot}},F_{\mathrm{tip}}}\right)$ can be acquired. As both locations of interest are recorded, the displacement ratio between x_{mot} and x_{tip} can be characterized by the transmission dynamics $\left(T = x_{\mathrm{tip}}/x_{\mathrm{mot}}\right)$. Note, that the transmissibility parameter is not constant if it is acquired from load side excitation, as the response changes for different controllers. However, while the system is excited through the machine's feed drive system, this function remains independent from the defined controller.

Using the experimental frequency domain data gathered in the previous step, new controller gains can be proposed and their effect on the tool tip compliance can be predicted via Eq. (4.25).

$$H^{\mathrm{clp,Prd}}_{x_{\mathrm{tip}},F_{\mathrm{tip}}} \approx H^{\mathrm{clp},K_0}_{x_{\mathrm{tip}},F_{\mathrm{tip}}} + \underbrace{\left(H^{\mathrm{ol}}_{x_{\mathrm{mot}},F_{\mathrm{mot}}} T\right)}_{H^{\mathrm{ol}}_{x_{\mathrm{tip}},F_{\mathrm{mot}}}} K\left(1 - H^{\mathrm{ol}}_{x_{\mathrm{mot}},F_{\mathrm{mot}}} K\right)^{-1} H^{\mathrm{ol},K_0}_{x_{\mathrm{mot}},F_{\mathrm{tip}}} \tag{4.25}$$

Approach #2

Control law influence at tool tip: While servo feedback loops (position, velocity and current) are active, the tool tip receptance FRF $H^{\mathrm{clp},K_\mathrm{i}}_{x_\mathrm{tip},F_\mathrm{tip}}$ is measured by impact hammer testing, under at least two different controller settings (K_1 and K_2) that produce different responses. Using the data sets $H^{\mathrm{clp},K_\mathrm{i}}_{x_\mathrm{tip},F_\mathrm{tip}}$ for different controllers K_i, the unknown terms can be solved, frequency-by-frequency, by constructing and solving a set of linear equations (Eq. (4.26)). Here, the normalization by $H^{\mathrm{clp},K_i}_{x_\mathrm{tip},F_\mathrm{tip}}$ improves numerical conditioning.

$$\begin{bmatrix} \frac{1}{H^{\mathrm{clp},K_1}_{x_\mathrm{tip},F_\mathrm{tip}}} & \frac{K_1}{H^{\mathrm{clp},K_1}_{x_\mathrm{tip},F_\mathrm{tip}}\left(1-H^{\mathrm{ol}}_{x_\mathrm{mot}F_\mathrm{mot}}K_1\right)} \\ \frac{1}{H^{\mathrm{clp},K_2}_{x_\mathrm{tip},F_\mathrm{tip}}} & \frac{K_2}{H^{\mathrm{clp},K_2}_{x_\mathrm{tip},F_\mathrm{tip}}\left(1-H^{\mathrm{ol}}_{x_\mathrm{mot}F_\mathrm{mot}}K_2\right)} \\ \vdots & \vdots \\ \frac{1}{H^{\mathrm{clp},K_n}_{x_\mathrm{tip},F_\mathrm{tip}}} & \frac{K_n}{H^{\mathrm{clp},K_n}_{x_\mathrm{tip},F_\mathrm{tip}}\left(1-H^{\mathrm{ol}}_{x_\mathrm{mot}F_\mathrm{mot}}K_n\right)} \end{bmatrix} \cdot \underbrace{\begin{bmatrix} H^{\mathrm{ol}}_{x_\mathrm{tip},F_\mathrm{tip}} \\ H^{\mathrm{ol}}_{x_\mathrm{tip},F_\mathrm{mot}} \cdot H^{ol}_{x_\mathrm{mot},F_\mathrm{tip}} \end{bmatrix}}_{Unknowns\ to\ be\ estimated} = \begin{bmatrix} 1 \\ 1 \\ \vdots \\ 1 \end{bmatrix} \tag{4.26}$$

While a minimum of two measurements are required, further data can be added to enhance the estimation accuracy of $H^{\mathrm{ol}}_{x_\mathrm{tip},F_\mathrm{tip}}$ and $H^{\mathrm{ol}}_{x_\mathrm{tip},F_\mathrm{mot}} \cdot H^{\mathrm{ol}}_{x_\mathrm{mot},F_\mathrm{tip}}$. Then, new controller gains can be proposed and their effect on the tool tip compliance can be accurately predicted via Eq. (4.23). This methodology was successfully validated, as shown in Figure 4.8, in predicting the tool tip compliance in the laboratory setup moving at 500 mm/min. The implemented controllers (K_1 and K_2) for Eq. (4.26) resolution constitute two boundaries for prediction accuracy. The prediction accuracy of different proposed control bandwidths between these two boundaries is very high (cyan and green colours). However, when predicting responses outside this boundary, the prediction accuracy decreases although the trend is correctly captured (yellow).

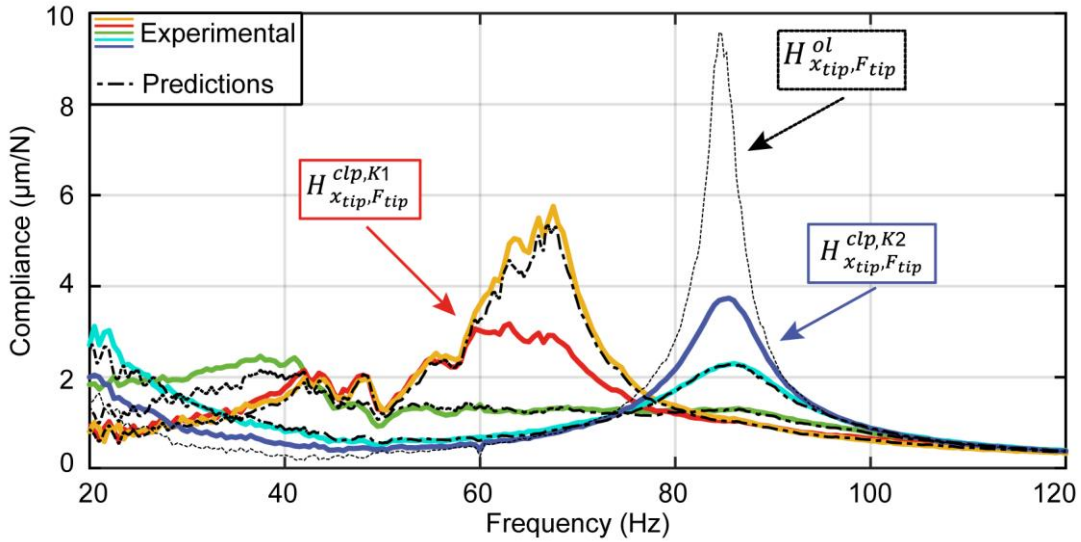

Figure 4.8 Experimental tool tip compliance prediction.

Similarly, it should be noted that since the blue and red functions (K_1 and K_2) have been used for solving the system, the prediction error is zero for both responses. Additionally, the experimental unknown function $H^{\mathrm{ol}}_{x_{\mathrm{tip}},F_{\mathrm{tip}}}$ is very similar to the one previously shown in Figure 4.4-b (K_{p} = 0). With this, the proposed MIMO model for model-free tool tip compliance prediction is validated.

4.3.3 Model based servo dynamics analysis

The root locus method provides valuable insight into the influence of controller gains on the damping of the structural modes. This model-based approach, however, requires an accurate analytical representation of $H^{\mathrm{ol}}_{\dot{x}_{\mathrm{mot}},F_{\mathrm{mot}}}$ to be identified a priori.

Root locus analysis by servo dynamics identification: The multiplicative pole-zero model presented by Suzuki et al. [243] has been extended for machine tool feed drive systems, by adding rigid body and delay dynamics, as shown in Eq. (4.27). Compared to the classical modal parameter model, this formulation simplifies the fitting of the complex dynamics encountered in feed drive systems and their structural assemblies. Both the resonances and anti-resonances can be estimated independently. Correct fitting of the anti-resonances in $\widehat{H}^{\mathrm{ol}}_{\dot{x}_{\mathrm{mot}},F_{\mathrm{mot}}}$ is especially important, as they generally correspond to tool tip compliance resonances. In Eq. (4.27), first the rigid body dynamics are adjusted to capture the low frequency response. Then, resonances and anti-resonances are fitted one by one. Finally, the delay term (τ_{ol}) enables further matching of the phase.

$$\widehat{H}^{\,\mathrm{ol}}_{\dot{x}_{\mathrm{mot}},F_{\mathrm{mot}}} = \underbrace{\frac{\overbrace{e^{-\tau_{\mathrm{ol}}s}}^{Delay\ Effect}}{m_{\mathrm{total}}s + \sigma}}_{\substack{Rigid\ Body \\ Dynamics}} \underbrace{\prod_{i=1}^{i=n}\left(\frac{\omega_{\mathrm{p},i}^2}{\omega_{\mathrm{z},i}^2}\cdot\frac{s^2 + 2\zeta_{\mathrm{z},i}\omega_{\mathrm{z},i}s + \omega_{\mathrm{z},i}^2}{s^2 + 2\zeta_{\mathrm{p},i}\omega_{\mathrm{p},i}s + \omega_{\mathrm{p},i}^2}\right)}_{Vibratory\ Dynamics} \tag{4.27}$$

Once an accurate model is obtained, the velocity and position control loop root loci enable the selection of the optimum parameters (K_{v}^*, K_{p}^*, T_{i}^*) that maximize the damping of the closed loop poles.

Overall, the new methodology proposed in this work generalizes successfully to high order feed drive dynamics, thus achieving a major improvement over earlier methods (Uriarte et al. [1] and Beudaert et al. [63]). It can also be applied with control structures other than P-PI, such as loop shaping (Munoa et al. [136]), pole placement (Erkorkmaz et al. [236]), or optimal control (Sencer et al. [235]).

4.4 EXPERIMENTAL DYNAMIC VALIDATION ON A RAM TYPE MILLING MACHINE

The modelling and tuning strategy presented in Section 4.3 has been validated on a ram type milling machine controlled by a Siemens 840D Powerline CNC, shown in Figure 4.9-a. The ram bending at 60 Hz is the principal mode that limits the cutting stability. The mode shape obtained by an experimental modal analysis indicates that the tool tip vibrates mainly in the x-direction, and that the base of the column, where the linear motor is actuating, also has a relative displacement for this mode (Figure 4.9-b).

Two controller settings are selected to demonstrate the accuracy of the proposed modelling approach. The controller named *high* is designed to achieve the highest bandwidth on the motor side. The controller named *optimum damping* is adjusted following the methodology of Section 4.3 to maximize the structural mode damping. To build the model, the closed velocity loop Bode plot was obtained via the standard functions in the Siemens CNC. As shown in Figure 4.9-c, the experimental servo mobility response is accurately estimated up to 100 Hz using Eq. (4.27). The orange shaded area in the phase response emphasizes that the delay term has a strong influence above 40 Hz.

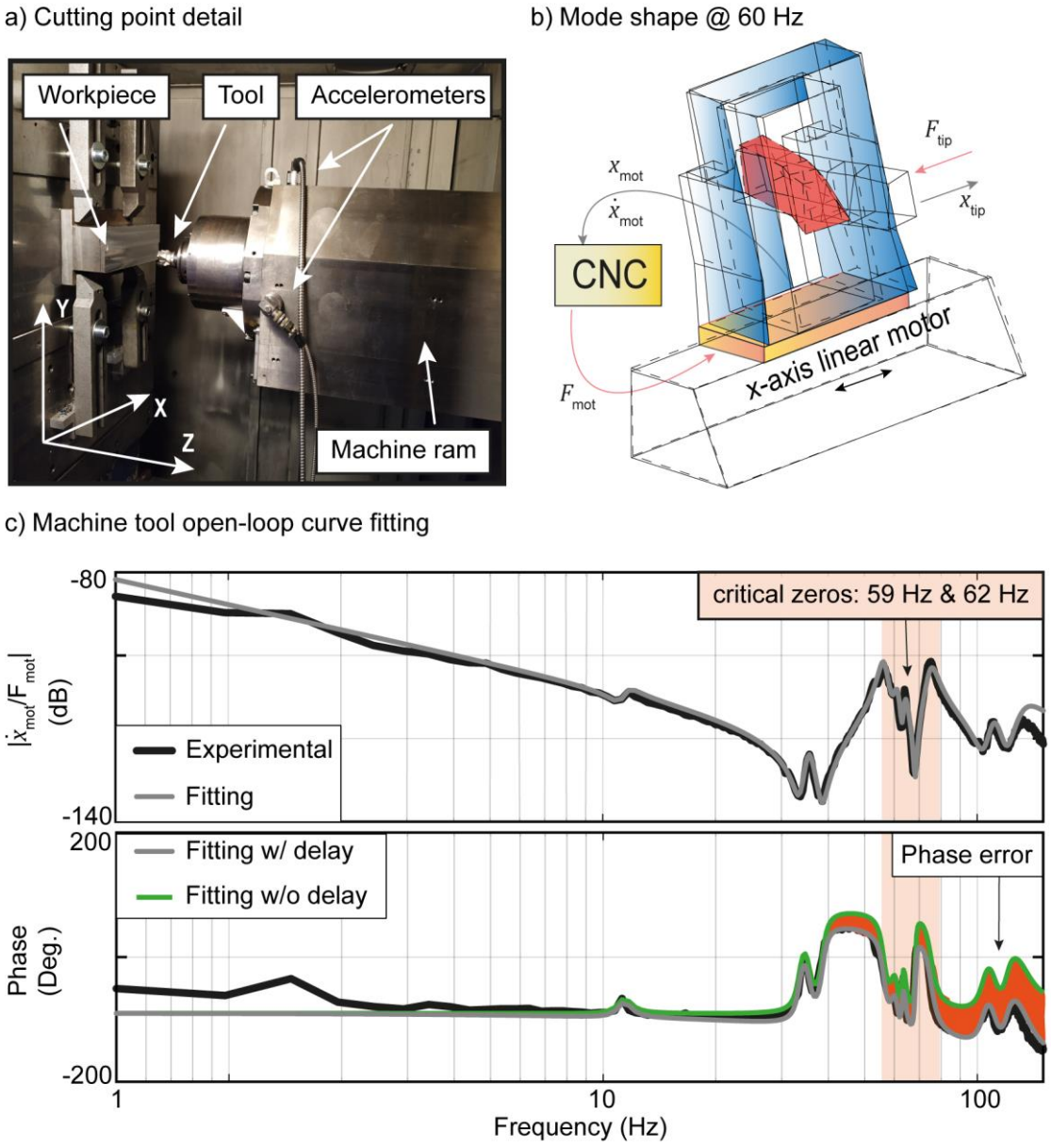

Figure 4.9 Machine tool a) Cutting point detail; b) Main modal shape; c) open loop curve fitting.

The prediction of the tool tip compliance is performed by the two different approaches of Section 4.3.2. For the first one, the transmission dynamics between x_{tip} and x_{mot} are experimentally identified. As previously indicated, the transmissibility function remains invariant when the machine tool is excited through the feed drive actuator, F_{mot}. Figure 4.10-a shows the time and frequency domain accelerometer response placed at the machine column next to the linear encoder ($\ddot{x}_{\mathrm{mot}}$) and tool tip ($\ddot{x}_{\mathrm{tip}}$).

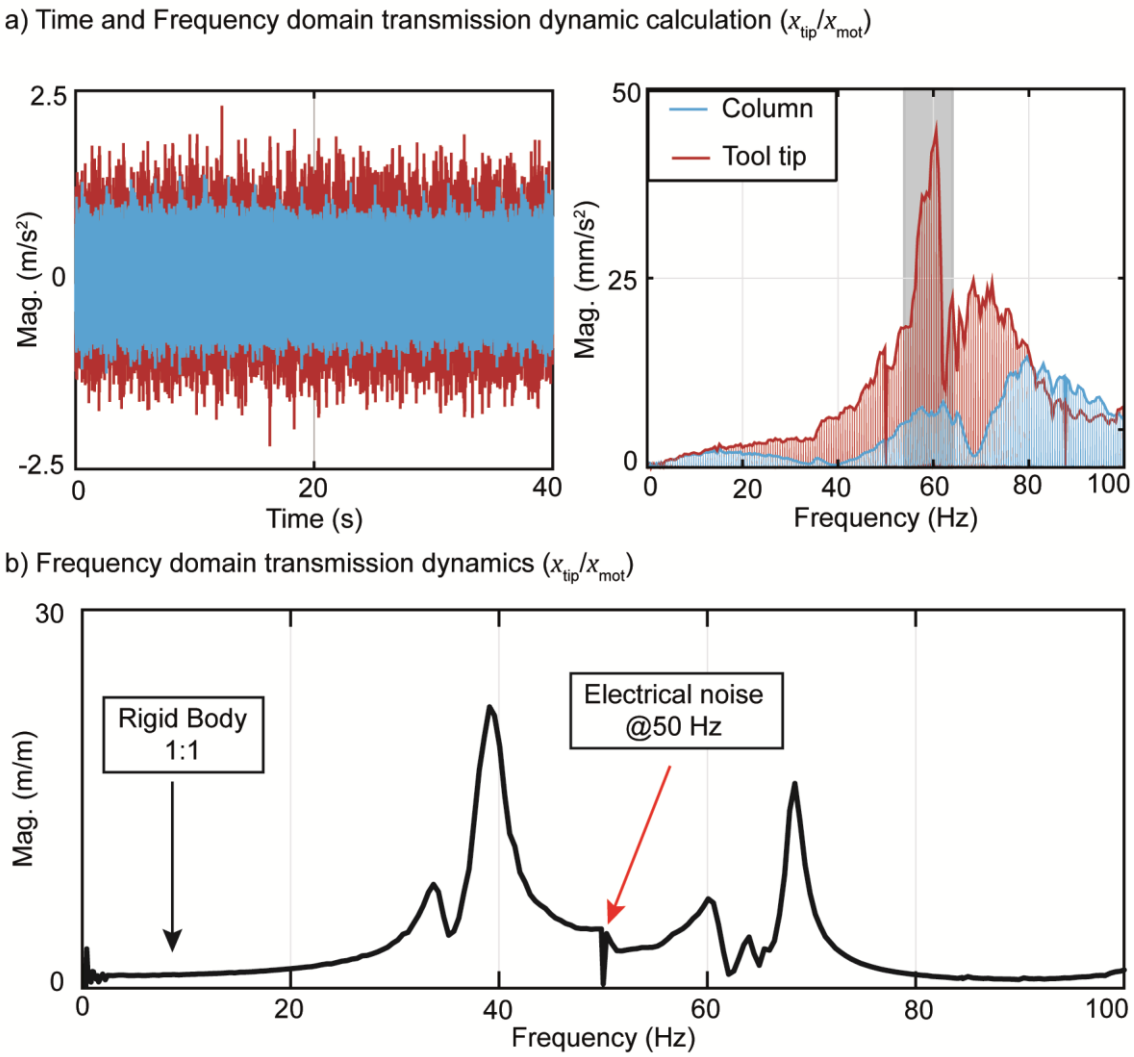

Figure 4.10 Transmission dynamics from motor excitation.

As the machine is excited by the standard routines for velocity and position bode plots computation, the acquired signal shows a discrete frequency excitation (Figure 4.10-a). Therefore, in order to dismiss the frequencies without excitation and remove associated noise, an intermediate signal processing step is required for peak location. Then, as shown in Figure 4.10-b the motion relationship between x_{tip} and x_{mot} can be computed. No matter the selected controller bandwidth, the obtained function shape will remain constant. Figure 4.11-a shows the tool tip compliance prediction by using the first approach. Note, that for this machine axis, the feed influence has little effect, hence, the tool tip dynamics are obtained in idle conditions.

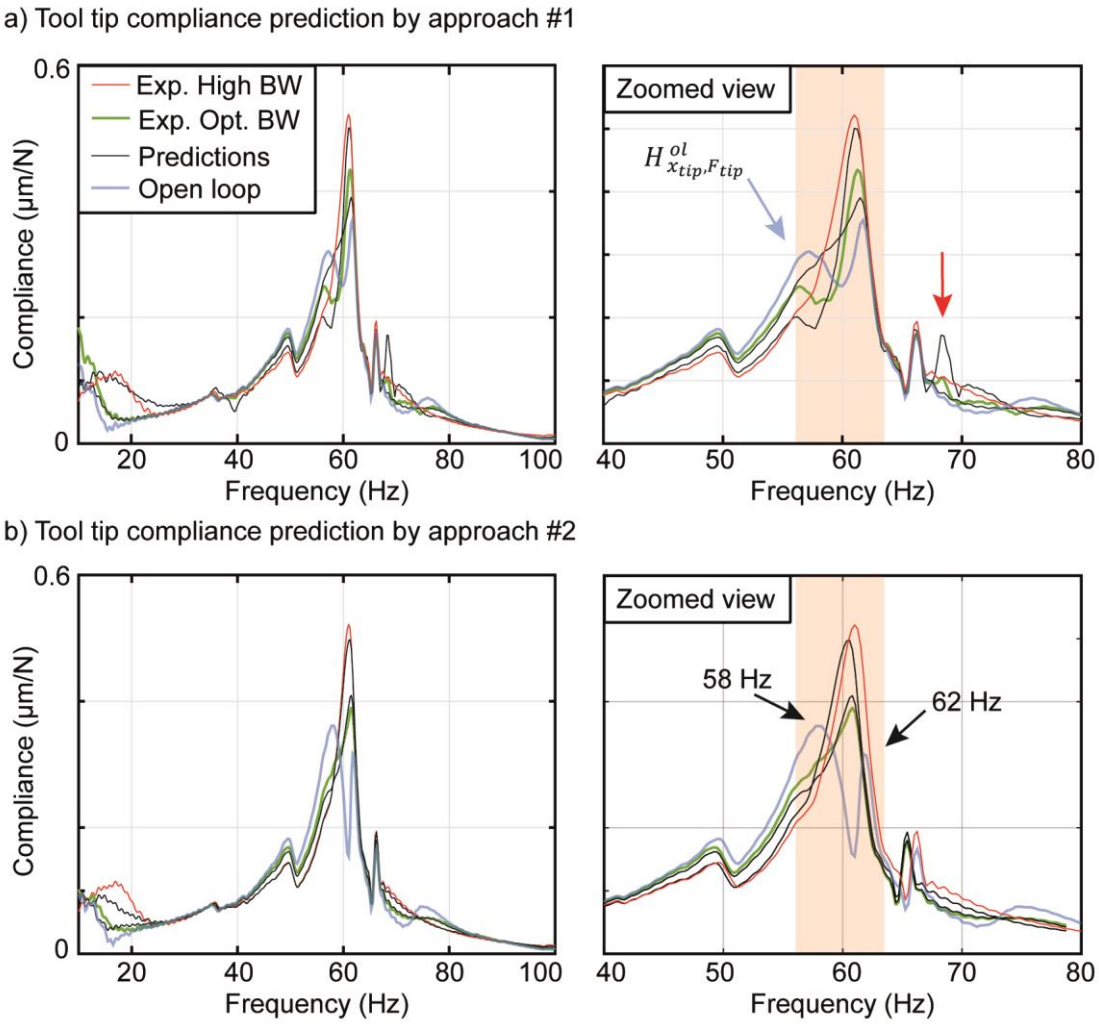

Figure 4.11 Tool tip dynamics prediction with the two different proposed approaches.

Figure 4.11-b shows the prediction following the second approach, where two tool tip compliances were measured by impact hammer tests, using relatively high and low control gains to obtain different responses. The zoomed view verifies that the frequency domain operations using the direct measurements indeed enable higher accuracy prediction of the effect of control parameters on the tool tip compliance.

Finally, the fitted model of the open loop mobility (Figure 4.9-c) is used to estimate the closed velocity and position loop Bode plots in Figure 4.12. The very accurate predictions demonstrate that the model parameters are well adjusted and that the root locus analyses (Figure 4.13) are reliable.

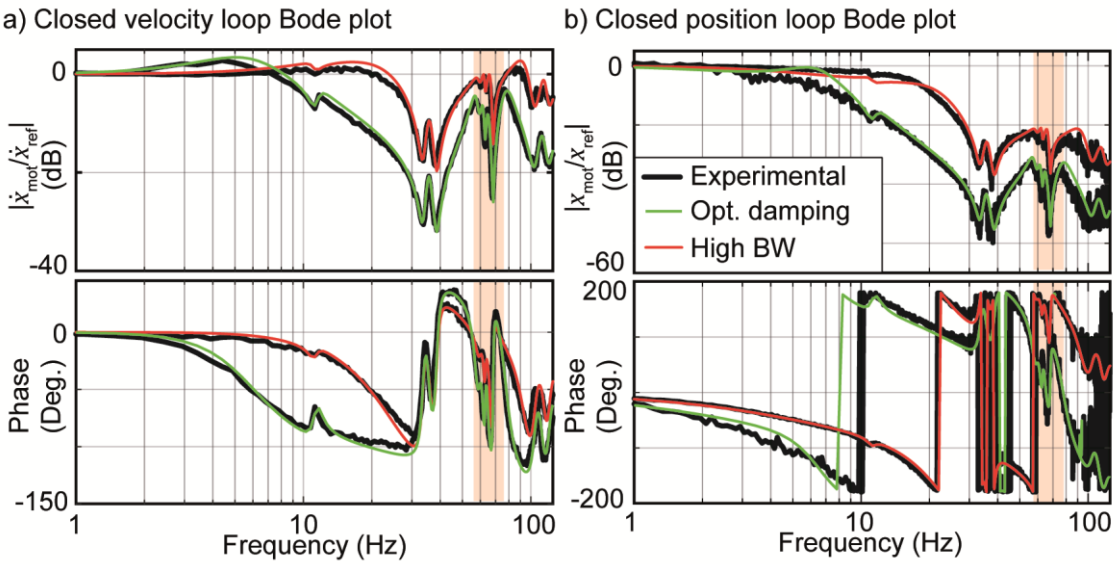

Figure 4.12 General view of velocity and position loop the root locus plot.

Figure 4.13-a shows the general root locus plot of the velocity loop, where different pole sources can be observed. For example, controller poles are present at very low frequencies. Those are particularly important for rapid motion trajectory commands when the pole is located at low damping values. Then, machine tool mechanical poles which can induce chatter vibrations are present in the critical frequency range. And finally, the delay poles of the Padé approximation appear at higher frequencies. Three nearby modes are close to the chatter frequency (Figure 4.13-b). In that zone, the shape of the root locus is also affected by the other modes which influence the pole-zero connection paths and directions. Compared to the *high* bandwidth controller, the *optimum damping* controller increases the damping ratio of the most critical mode by 44% as highlighted in blue in Figure 4.13-d. However, the bandwidth reduction deteriorates the motion performance and can increase by up to ten times the contouring error as analyzed in Section 4.6. In the studied critical frequency range, the machine tool poles show a high sensitivity with respect to the proportional velocity loop gain, as a little variation can quickly alter the achievable damping (Figure 4.13-b). On the other hand, in the position loop any proposed value of K_{v} will always degrade the achievable damping. In addition, by increasing the K_{p} gain, the machine can reach the stability limit as the real part of the pole around 72Hz can become positive. However, in contrast to the proportional velocity loop, the sensitivity is small and relatively high K_{v} values (such as 8 s^{-1}) are very far from reaching the imaginary axis. This explains why the proportional position loops do not modify the tool tip compliance.

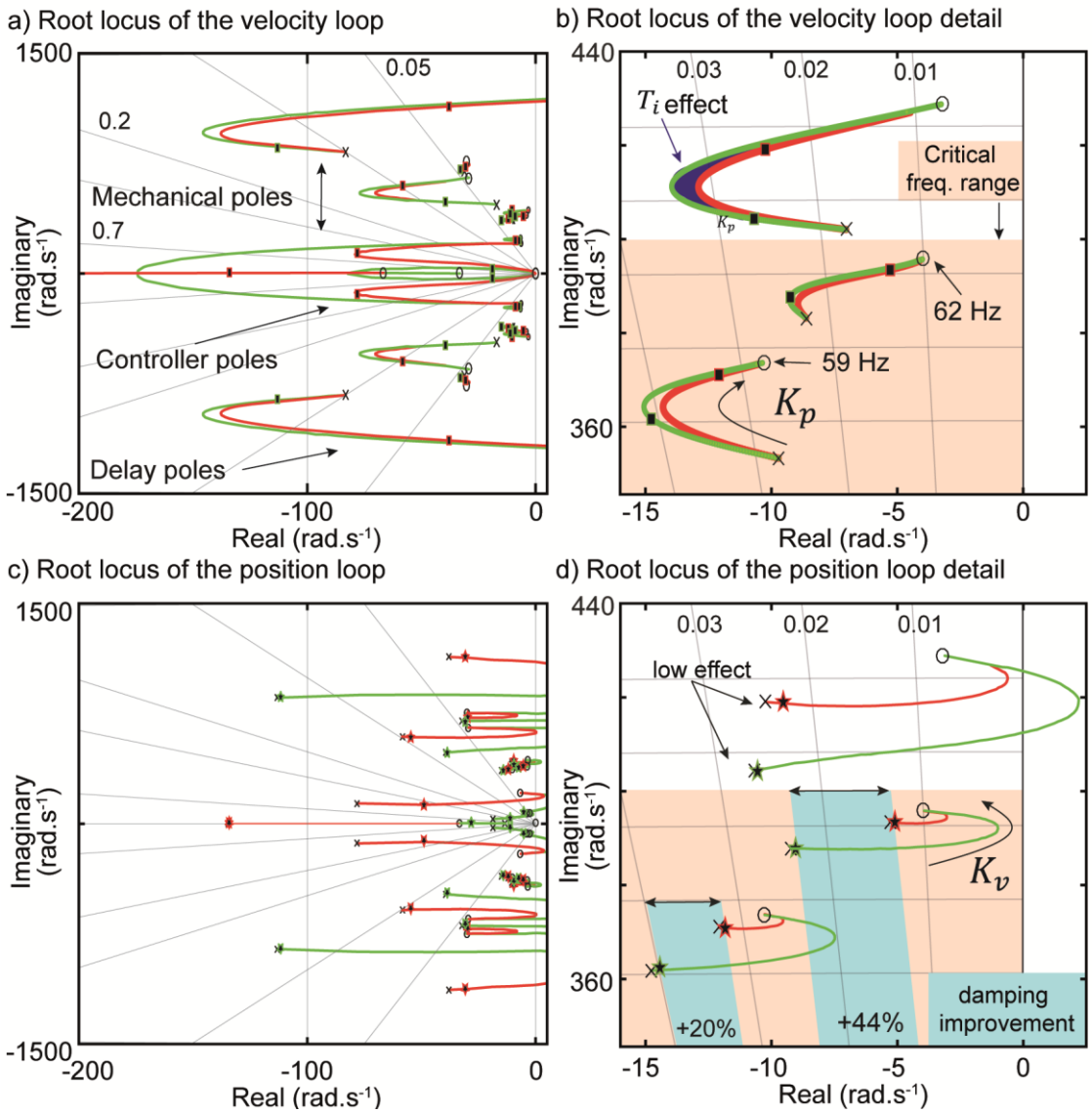

Figure 4.13 Velocity and position loops analysis.

4.5 CHATTER STABILITY PREDICTION AND EXPERIMENTAL VALIDATION

Direct and cross tool tip compliances have been measured by impact hammer testing to compare the theoretical chatter stability achieved with both controllers following the approach proposed by Altintas et al. [11]. The cutting process parameters are defined in Table 4.2.

Table 4.2: Cutting process parameters for chatter stability tests.

Cutting tool	
Reference	WALTER F4042 B16.040.Z04.15
Diameter, D	40 mm
Number of teeth, Z	4
Inserts reference	WKP35S ADMT160608R-F56
Lead angle, κ	90º
Cutting conditions	
Feed per tooth	0.2 mm/ Z
Radial engagement	32 mm (down-milling)
Workpiece material	F1140 Steel (C45)
Cutting coefficients	
Specific tangential, K_{tc}	1885 $\mathrm{N/mm^2}$
Specific radial, K_{rc}	749 $\mathrm{N/mm^2}$

The stability lobe predictions are experimentally validated, verifying up to 33% productivity improvement. From the eleven tested spindle speeds, only one case showed an unpredicted reduction of stability, which is worth further study. Nevertheless, as seen in Figure 4.14-a, a general improvement is achieved in the chatter stability through the application of the proposed new strategy in tuning the P-PI cascade control loops. In addition to this, the overall vibration severity decreased considerably in all the conducted tests. Figure 4.14-b shows the vibration spectra comparison for the two different cutting conditions with the selected controllers, where the optimally tuned one successfully avoids the chatter appearance. As a result, Figure 4.14-c shows the workpiece surface finish for the $Test\ B$ at 1100rpm and a depth of cut of 2mm.

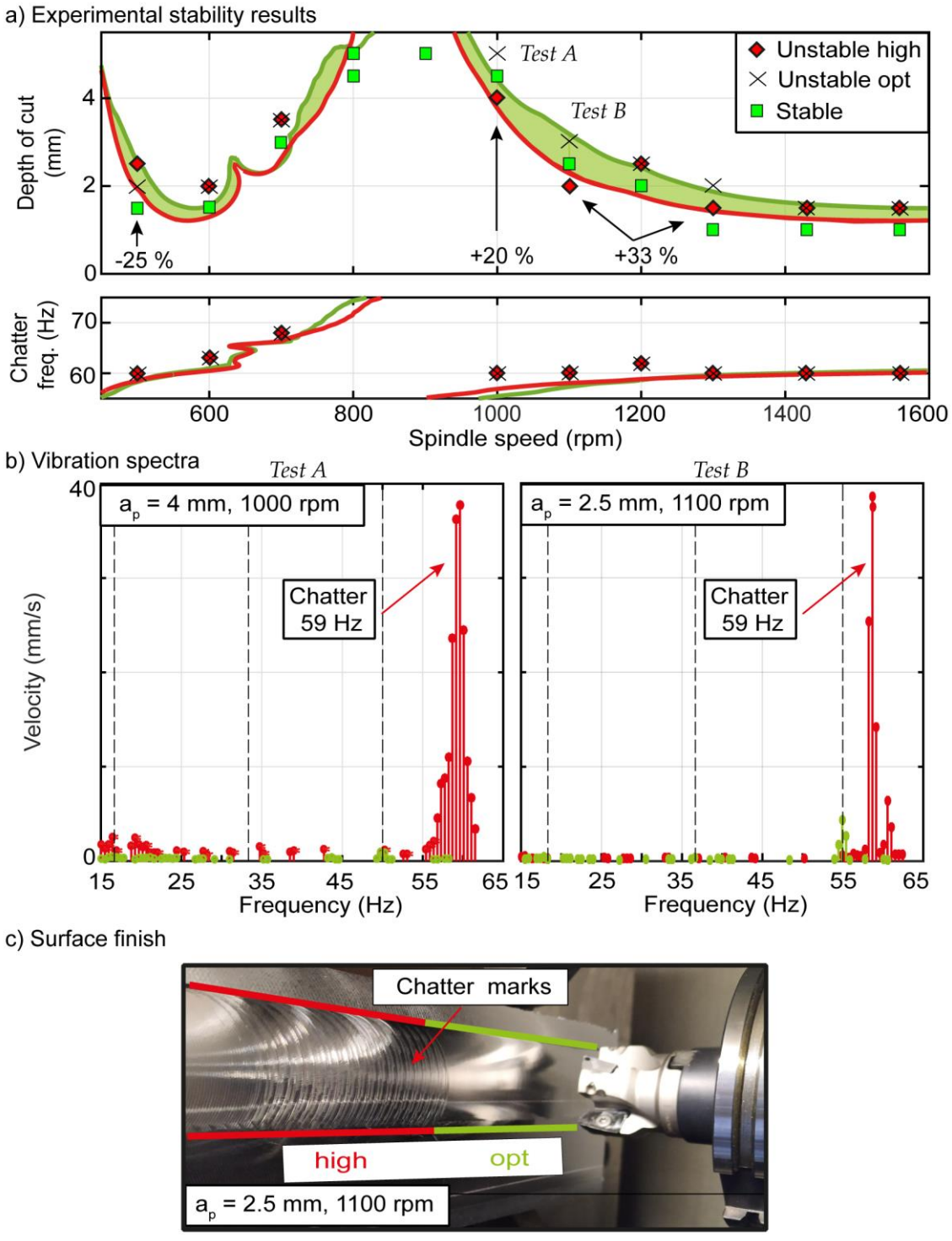

Figure 4.14 Experimental chatter stability tests.

4.6 TRACKING PERFORMANCE ANALYSIS

As a result of the previous analysis, lower control bandwidths are desirable to obtain the maximum allowable structural damping, prioritizing the process stability rather than

machined part accuracy. On the other hand, the higher bandwidth tuning approach, which follows the usual industrial tuning guidelines, improves the motion performance. From the previous industrial implementation, the velocity and position bandwidths have been reduced from 25 to 9Hz and 20 to 6Hz respectively. Even though *optimum damping* controller is designed for heavy duty roughing operations, where the dimensional accuracy of the part is not a big concern yet, the decrease of the control dynamics weakens the precision of the manufactured part.

Figure 4.15 shows the feed drive system model that has been used to simulate the contour errors. The position reference is modified by balancing filters (also called symmetry filters) available to improve the performance of the velocity feedforward action (K_{ffv} = 1). The Siemens 840D CNC offers the possibility to use a first order transfer function as a balancing filter (where the optimum time constant, corresponding to the considered machine dynamics, is selected as τ_{BF} = 1ms). To avoid introducing synchronization errors, the y-axis (vertical axis) is considered to have matching dynamics with the x-axis in the simulations. The closed velocity loop dynamics are the ones illustrated in Figure 4.12-a.

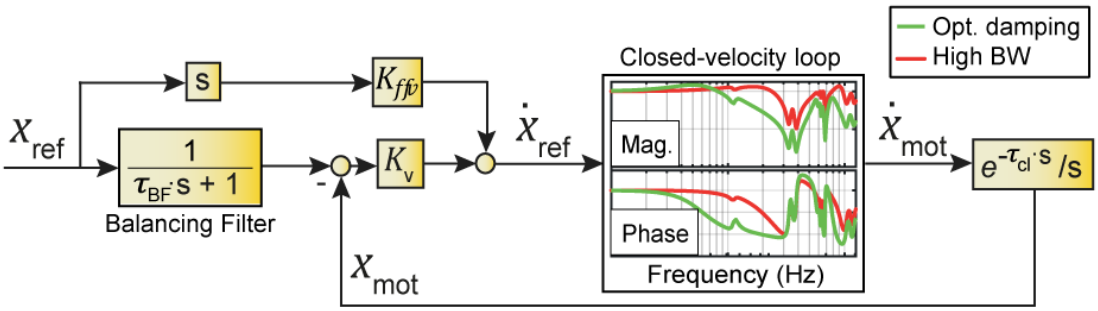

Figure 4.15 Feed drive system model for motion performance analysis.

Table 4.3 summarizes the contour and tracking error results (see also Figure 4.16). On average, the contour errors have been increased by a factor of 10, and the tracking errors by a factor of 6. Hence, the obtained machined part accuracy is reduced. However, as structural chatter vibrations are usually faced during roughing operations and accuracy is especially important for the finishing passes, two different controller sets can be implemented by the machine tool builder in their CNC applications. The first one, providing the optimal damping for initial heavy duty roughing operations, and then the higher bandwidth setting, which provides a better contouring accuracy for the finishing

operations. With this, the machine user can benefit from the advantages of both tuning approaches.

Table 4.3: Tool path motion error summary.

	Contour Error		**Tracking Error**	
	Max.	Rms	Max.	Rms
Opt. damping (µm)	110.5	23.8	212.9	75.5
High BW (µm)	9.4	2.42	31.7	12.1
Difference (ratio)	11.7	9.8	6.7	6.2

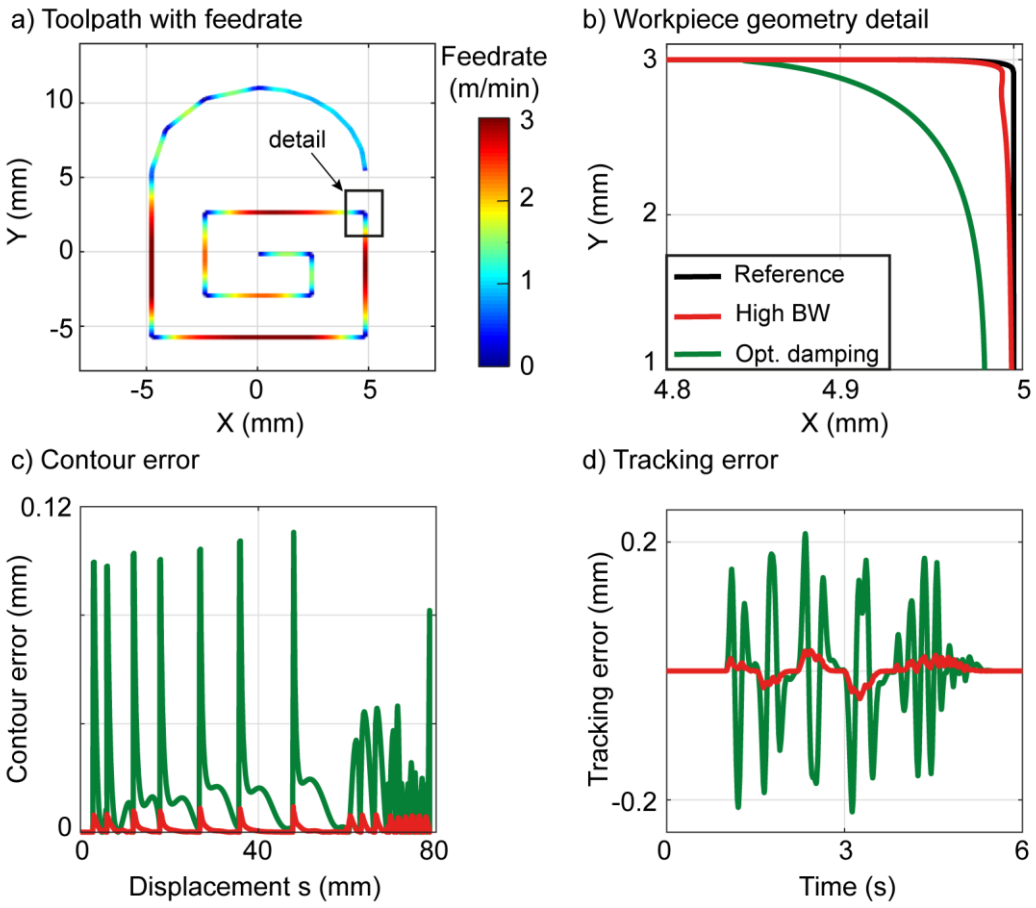

Figure 4.16 Simulated tool path results.

4.7 CONCLUSIONS

This chapter has presented a new strategy for feed drive controller tuning, to enhance the damping properties at the cutting point. The interaction of the servo controller with the machine tool's generalized high-order dynamics has been studied through the root locus technique. A semi-analytical MIMO model has been developed to accurately

predict the tool tip receptance under different control settings. Experimental validations show that optimum tuning can increase the machine's chatter stability. To avoid reducing the final machining accuracy, different control tunings can be used for roughing and finishing operations.

Chapter 5

Influence of friction on the nonlinear dynamics of machine tools

5.1 INTRODUCTION

In large machine tools, where structural dynamics significantly influences the cutting capabilities, inaccurate machine dynamic characterization leads to poor stability predictions. In such machines, the critical resonances are usually related to the major structural assemblies (typically in the low frequency range between 15 to 200 Hz) which can generate relative motion at the machine joints. Most research considers the dynamic response of machine tools in idle conditions. However, there is evidence showing that the dynamics can vary during the cutting process (see Sections 2.2 and 2.3).

This chapter aims at demonstrating for the first time that friction has an important influence on the structural dynamics of large-scale machine tools at near the machining point. Experimental evidence obtained from several machines indicate that the dynamics variations between the in-motion and idle conditions are quite common. However, up to

now, the underlying cause of this was not studied. In this chapter, a fundamental study that considers the influence of nonlinear friction, structural dynamics, feed drive control loops and the machine movements is experimentally validated on a laboratory test bench. A mechanical equivalence of the feed drive controller is provided, as well as an analysis of three different static friction models for predicting the transient behaviour. Finally, a machining centre is analyzed in detail to show the effect of the axis velocity on the cutting point compliance and its influence on the chatter stability prediction.

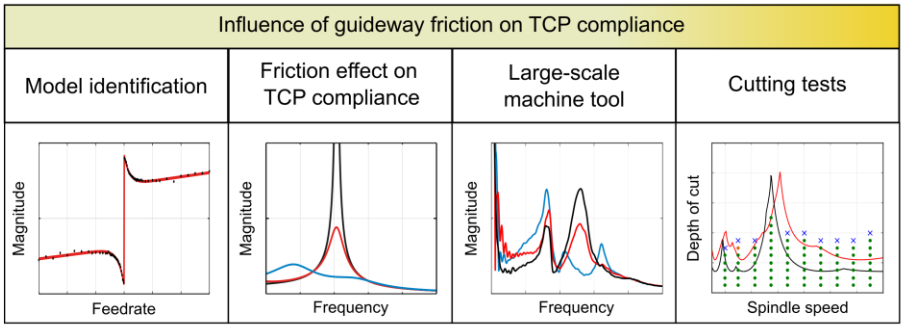

Figure 5.1 Steps for the analysis of the guideway friction on TCP compliance.

5.2 IDLE AND IN-MOTION FRFS EXPERIMENTAL DIFFERENCES

The influence of the axis velocity on the cutting point compliance has been measured on seven different machine tools, including two large portal milling machines, three ram type milling machines, one turning machine, and also a robot equipped with a milling spindle (Figure 5.2). For all the measurements, each cartesian axes xyz are commanded with a back-and-forth movement with the same axis velocity; hence the tool centre point performs a 3-axis linear interpolation trajectory. The axis displacements are lower than 40 mm, so the dynamic compliance modification is not strongly related to the posture variation. All the measurements presented in this section have been obtained from impact hammer tests performed after the axis inversion to avoid axis reversal and transient effects. Additionally, the measurements do not show a significant influence of the axis travelling direction on the tool tip dynamics, hence this effect is discarded here. For confidentiality reasons, the magnitude value is not displayed.

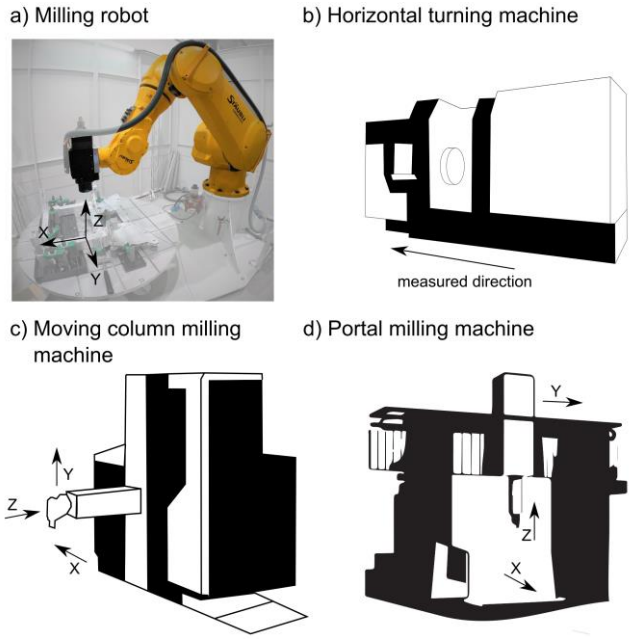

Figure 5.2 Graphical summary of the tested machine configurations

Milling robot: The first analyzed machine is a Stäubli robot with a milling spindle head. Figure 5.3-a summarizes the nine direct and cross compliances for the three cartesian directions. Initially, each joint of the robot is braked generating a highly undamped response. However, just by energizing the joints and hence, giving authority to each joint controller, the initial damping values for the resonance increase. When the joints are moving, the response is damped even further. Figure 5.3-b shows the Φ_{zz} direct compliance for different feedrates, where the initial 12 Hz resonance is significantly modified by the control interaction (with vs. without brake) and due to the feed command.

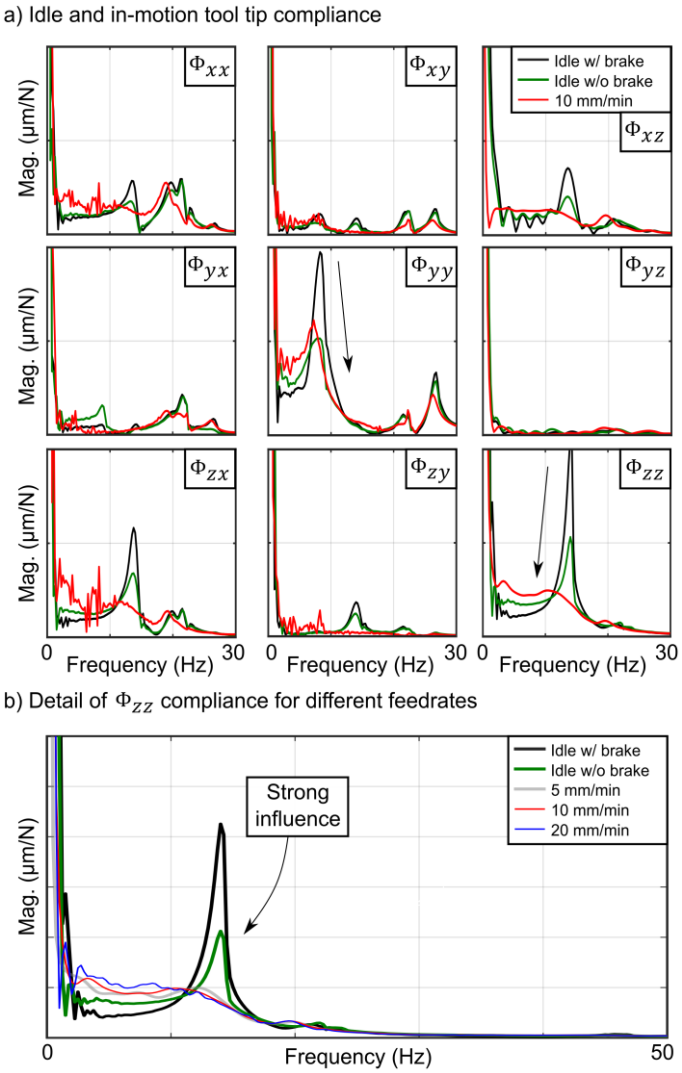

Figure 5.3 Idle and in-motion FRF for a robotic milling machine.

Turret of a horizontal turning machine: Figure 5.4 shows the direct compliance of the longitudinal axes of a horizontal lathe driven by a ball screw drive and that uses friction guides with Turcite®. The FRF is significantly affected by the movement both in the main resonance at 95Hz and in the low frequency range (<50Hz).

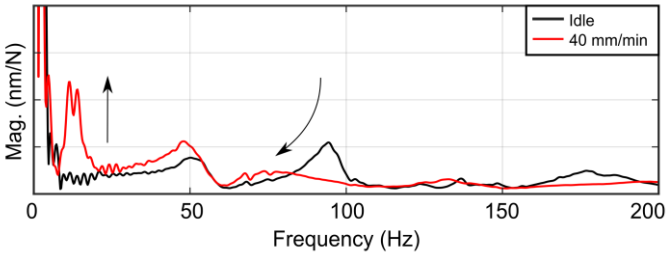

Figure 5.4 Idle and moving FRF for a horizontal lathe.

Moving column milling machine: Three different moving column machine tools have been dynamically characterized. The horizontal x axis is driven by a double pinion and rack feed drive system. The vertical and ram axes (y and z respectively) are driven by ball screw feed drives. The vertical axis has a hydro-pneumatic accumulator for the weight compensation. As a result of the large ram overhang, the most flexible directions are in x and y, where usually ram bending resonances govern the dynamic response. Figure 5.5-a shows the nine direct and cross FRFs in idle and moving conditions. The vertical direct compliance (Φ_{yy}) is significantly modified. This frequency modification also affects Φ_{xy} and Φ_{yx} cross compliances as the main resonance encounters a damping increase. Figure 5.5-b shows a second moving column type machine tool, which follows a similar trend as the previous machine. The most significant compliance variation is faced in the direct vertical FRF (Φ_{yy}). Additionally, as a result of the feed influence, a major increment in damping is generated in the Φ_{xy}, Φ_{yx}, Φ_{yz} and Φ_{zy} cross FRFs.

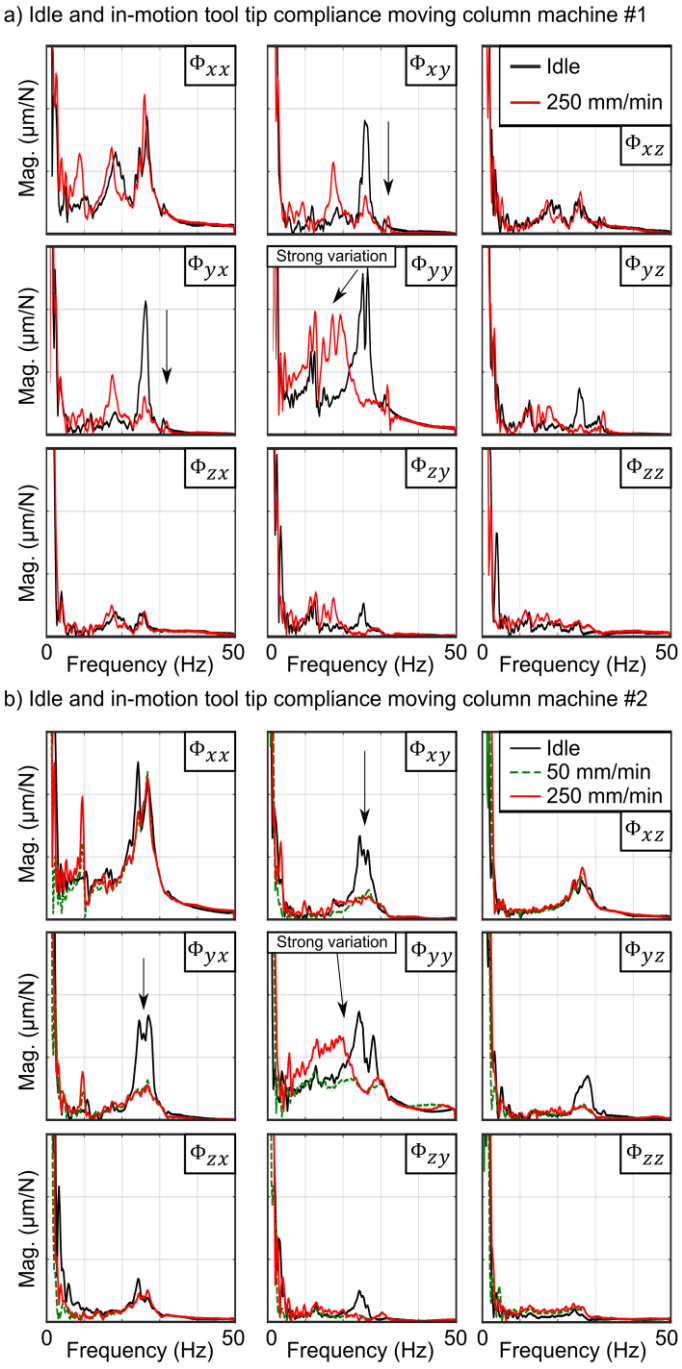

Figure 5.5 a) First; b) second analyzed moving column milling machine.

Figure 5.6-a shows the dynamic characteristics of the third moving column milling machine. As in previous machines, the direct vertical compliance (Φ_{yy}) suffers the biggest variation. Cross FRFs (Φ_{xy}, Φ_{yx} and Φ_{yz}) decrease their main resonance amplitude as a result of the Φ_{yy} compliance modification. Figure 5.6-b shows a more detailed analysis conducted at different axis velocities. By providing a small velocity command such as 25 mm/min, the initial idle compliance is modified both in amplitude

and frequency. Then, by increasing the feed command the compliance varies up to a certain limit where the variation is small (250 to 500 mm/min) or remains similar (500 to 1000 mm/min).

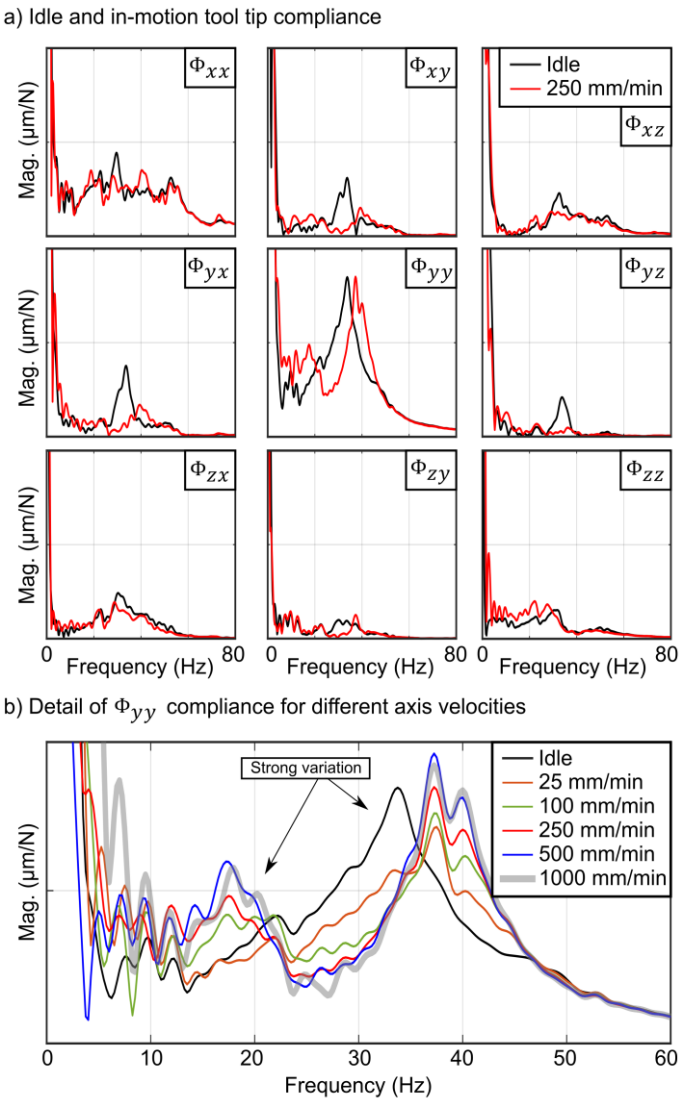

Figure 5.6 Third analyzed moving column milling machine.

Portal milling machine: Two different gantry type portal milling machines have been analyzed. For portal milling machines, the x axis is driven by a gantry master slave configuration, where each machine leg has a double pinion and rack feed drive system. Meanwhile, the y axis is powered by a double pinion and rack and vertical z axis by a ball screw drive.

The first studied machine tool dynamics are summarized in Figure 5.7. As a result of the motion, the main resonance amplitude in Φ_{xx} decreases drastically. In addition, the

secondary resonance gains importance as its magnitude and frequency characteristics are altered. Similar effects can be observed in the Φ_{yy} compliance. In fact, the main resonance of the machine in idle and in-motion conditions is totally different, both in frequency and damping.

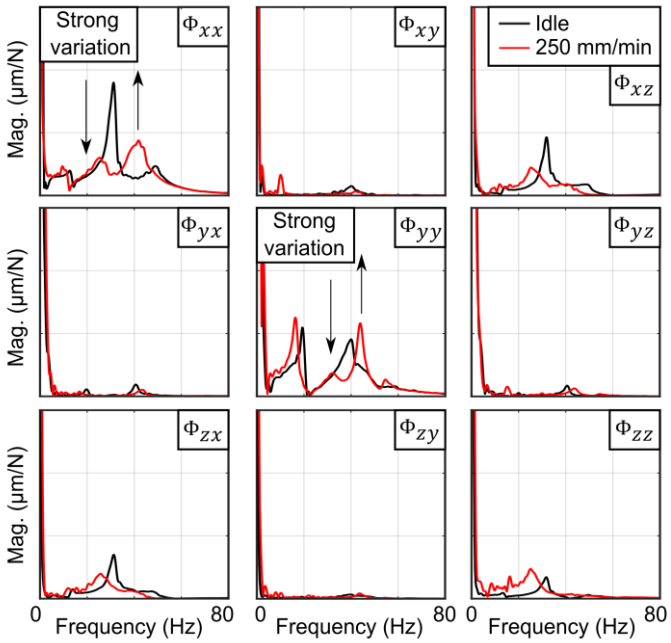

Figure 5.7 First analyzed portal milling machine.

In the second portal milling machine, the x axis is independent from the other two axes, as a moving table with turning capabilities has been installed. Therefore, the motion of the ram is only in vertical and transverse directions (y and z). Figure 5.8-a shows the nine FRFs of the ram tip, where the frequency of the main resonance decreases while achieving a considerable amplitude reduction (60%) in Φ_{xx} compliance. It is important to note that Φ_{xx} is significantly affected even if there is no feed in x direction. Figure 5.8-b illustrates the evolution of the dynamic compliance for different feeds, where initial idle characteristics converge to a different in-motion invariant frequency response.

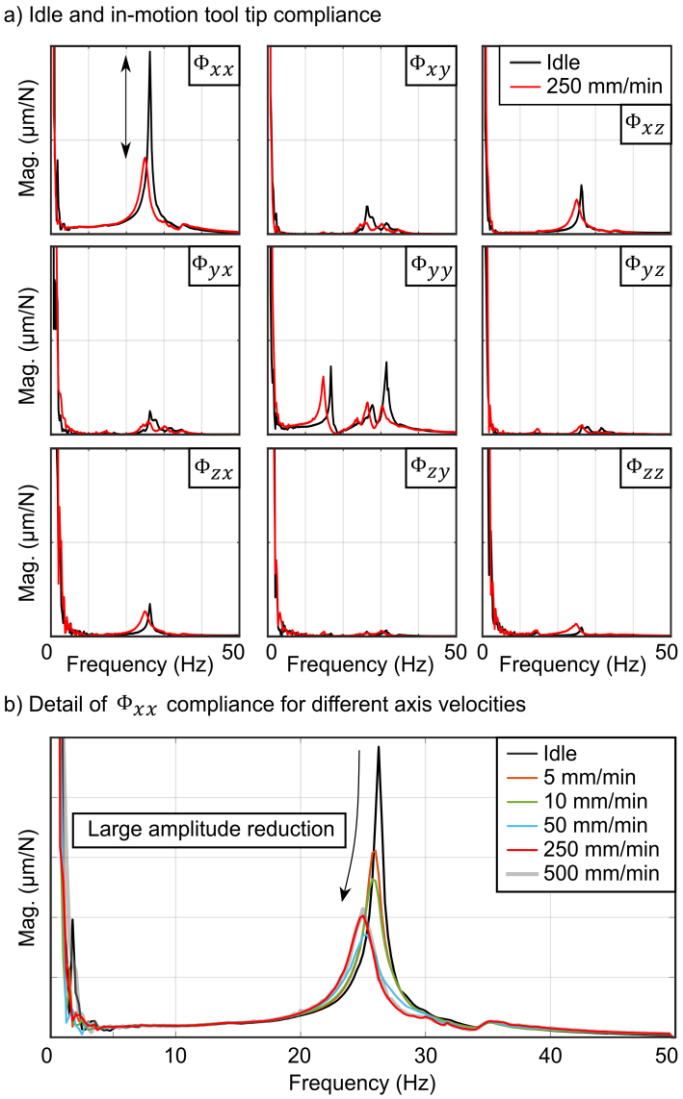

Figure 5.8 Second analyzed portal milling machine.

The experimental evidence presented in this section show that the axis motion can have a very significant influence on the cutting point dynamics, changing both the natural frequency and damping of the main machine tool modes. The identification of this phenomena can be crucial for different aspects such as model-based active damping techniques, process planning using stability lobes and Finite Element models correlation. This effect has been reported in very few publications (Zaeh et al. [116], Sato et al. [119] and Tunc et al. [68]) and has not been explained in detail, especially considering the nonzero axis velocity case, up to now.

5.3 FUNDAMENTAL STUDY

The fundamental explanation of the dynamics modification observed in the previous section is developed using a simple two mass model that considers the feedback control loops and the axis friction.

5.3.1 Model description

A single degree of freedom flexible structure mounted on a linear motor is used to model and validate the effect of friction on the dynamic response. Figure 5.9 presents the schematic model that considers friction forces F_{friction} and the classical control loops to generate the drive force F_{control} from the linear encoder position and velocity feedback measurement (x_{mot} and $\dot{x}_{\text{mot}}$). Additionally, a disturbance force F_{tip} can be applied on the flexible structure as well as a motion command to the feed drive system through x_{ref}. Multiple feed commands are analyzed, resulting in different forces generated by the controller and friction, and their implications on the tool tip dynamic compliance is simulated ($x_{\text{tip}}/F_{\text{tip}}$).

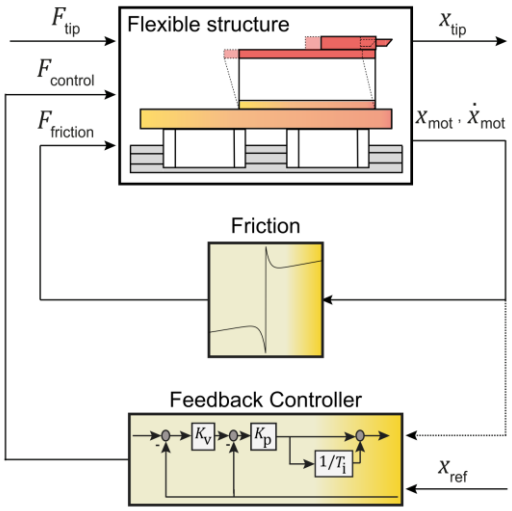

Figure 5.9 Proposed mechatronic simulation model to analyze the influence of guideway friction on the tool tip dynamics.

Structural dynamics

This simplified flexible test bench can be dynamically characterized as a two degree-of-freedom system. The driven load or vibrating structure is represented by M_{tip} and the carriage by M_{mot}. Eq. (5.1) shows the analytical expression of the open loop system response ($X_{\text{mot}}/{F_{\text{control}}}^{\text{ol}}$) with stiffness and damping of the mechanical flexure characterized by k_2 and c_2 respectively. τ_{ol} is a delay corresponding to a phase drop

due to the sampling rate and the linear motor response. The expression also considers the viscous friction term σ which modifies the response in the low frequency range. However, for this research, the effect of viscous friction is not used in this expression, as it is modelled in the friction characteristics described in the next section Eq. (5.2).

$$\frac{X_{\text{mot}}}{F_{\text{control}}}^{\text{ol}} = \frac{\left(M_{\text{tip}}s^2 + c_2 s + k_2\right)e^{-\tau_{\text{ol}}s}}{M_{\text{mot}}M_{\text{tip}}s^4 + \left(c_2\left(M_{\text{mot}} + M_{\text{tip}}\right) + \sigma M_{\text{tip}}\right)s^3 + \left(k_2\left(M_{\text{mot}} + M_{\text{tip}}\right) + \sigma c_2\right)s^2 + \sigma k_2 s} \tag{5.1}$$

Friction characteristics

As indicated in Section 2.3, friction is a result of a complex interaction between two contacting surfaces with a relative motion. Complex dynamic models (such as LuGre or GMS) capture the friction characteristics at small relative displacements before full slip regime is reached. However, these models are difficult to identify and not always easy to use in dynamic simulations (Andersson et al. [108] and Hagman [107]). The discontinuity at very low speeds associated with static friction models can be overcome by implementing continuous velocity-based functions. The Andersson $tanh$ type model of Eq. (5.2) is used here as it smoothly accommodates the transition to a full sliding regime for low-velocity increments; and it is well adapted for transient oscillating simulations (Andersson et al. [108]). F_{c} and F_{s} correspond respectively to the Coulomb and static frictions while σ is the viscous friction coefficient. The coefficient $k_{\tanh}$ determines how fast the friction force changes near pre- and sliding portions. v_{s} is the sliding speed coefficient and δ is the velocity shape factor, which is equal to 1.

$$F_{\text{friction}} = \left[F_{\text{c}} + (F_{\text{s}} - F_{\text{c}})exp^{-\left(\frac{|\dot{x}_{\text{mot}}|}{v_{\text{s}}}\right)^{\delta}}\right] tanh\left(k_{\tanh}\,\dot{x}_{\text{mot}}\right) + \sigma\,\dot{x}_{\text{mot}} \tag{5.2}$$

Pennestri et al. [244] compared eight different friction models in terms of computational efficiency concluding that continuous velocity-based friction models demonstrated to be sensitive to the selected Ordinary Differential Equation (ODE) solver. Furthermore, they recommended the use of a stiff solver, such as ode15s, as it considerably improves the computational efficiency and accuracy. For that reason, in preparing the simulation MATLAB's variable step ode15s solver is selected to get a fast and accurate simulation.

Quasi-FRF

The concept of FRF is only mathematically valid for linear systems and the term quasi-FRF is preferred for nonlinear systems (Farago et al. [245]). In this work, the quasi-FRF

is obtained using the traditional impact hammer testing approach, where an accelerometer measures the flexure vibration ($\ddot{x}_{\mathrm{tip}}$) and an impact hammer generates the force (F_{tip}). Both excitation and response time domain signals are synchronously acquired, and each frequency domain response spectrum is computed by FFT analysis. Eq. (5.3) shows the quasi-FRF computation by the division of the cross-spectrum over input's auto-spectrum (Ewins [246]).

$$\Phi_{\mathrm{quasi}}(\omega) = \frac{S_{\mathrm{x_{tip},F_{tip}}}(\omega)}{S_{\mathrm{F_{tip},F_{tip}}}(\omega)} \tag{5.3}$$

For simulations, the impact hammer force has been characterized as a Dirac delta function. With this, the machining system nonlinear sensitivity to different force excitation levels (F_{tip}) or different feedrate commands ($\dot{x}_{\mathrm{ref}}$) can be studied.

5.3.2 Test bench validation

Figure 5.10-a presents the single-axis linear motor (ETEL ILM06-060) with an added flexure oriented in the feed direction that is used to validate the proposed models.

Identification of mechanical parameters

The model parameters have been extracted from an experimental open loop response measurement ($x_{\mathrm{mot}}/{F_{\mathrm{mot}}}^{\mathrm{ol}}$) (Figure 5.10-b). A pseudo-random binary sequence input has been applied to the experimental setup while the axis was moving at 500 mm/min. As a result, the setup stays on the sliding friction regime; hence, only viscous friction component affects this measurement. In addition, the excitation force has been selected not to generate motion reversals. The natural frequency of the flexure f_{t} = 61.3 Hz corresponds to the so-called motor-locked frequency. This load side resonance corresponds to an anti-resonance of the motor open loop response as load side vibrations cancel out the displacement of the motor mass. Due to the combination of inertias and stiffness, a resonance is generated at f_{r} = 75 Hz. The extracted model parameters are summarized as follows; M_{mot} = 23.1 kg, M_{tip} = 11.3 kg, k = 1.68 N/µm, c = 104 Ns/m, σ = 1250 kg/s and τ_{ol} = 0.75 ms. However, as previously said, the viscous friction term effect (σ) will be considered within the externally coupled friction model.

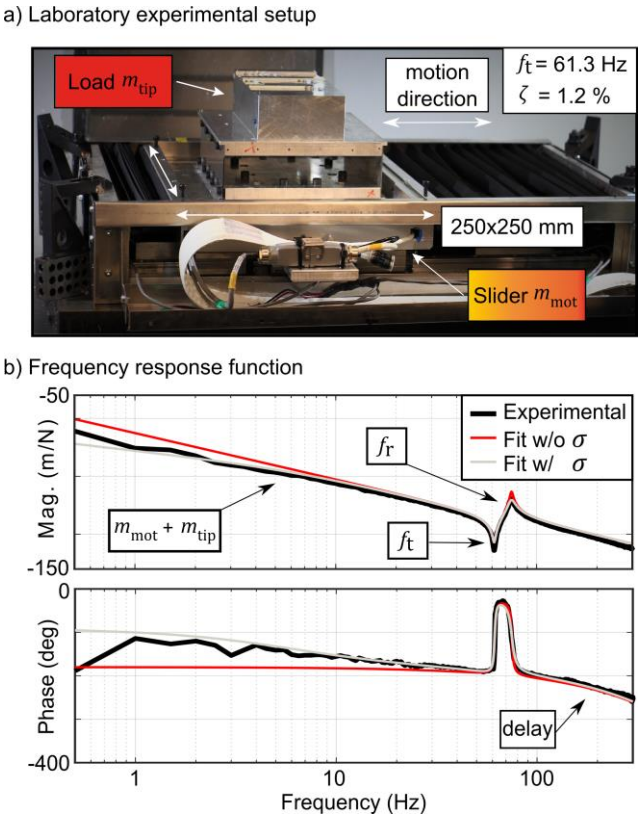

Figure 5.10 a) Experimental setup; b) Experimental and fitted open loop response.

Identification of friction parameters

The friction force characteristics are identified by running the test bench at different steady-state sliding feeds and computing the average of the motor force. Figure 5.11-a shows the experimental and computed mean values of motor force for continuous displacements performed at 25 and 1500 mm/min. Figure 5.11-b shows the fitted friction model on top of the experimental characterized points. The extracted model parameters, which have been obtained by the minimization of the RMS error, are as follows: Coulomb sliding friction (F_c) = (44.2$^+$, 38.7$^-$) N, maximal static friction (F_s) = (84$^+$, 88$^-$) N, sliding speed coefficient (v_s) = (387.4$^+$, 421$^-$) mm/min, viscous friction coefficient (σ) = (0.0028$^+$, 0.0025$^-$) Nmin/mm, model constant ($k_{\tanh}$) = (0.25$^+$, 0.25$^-$) min/mm and the velocity shape factor (δ) = (1$^+$, 1$^-$). Note that the identified parameters vary depending on the motion direction (as in Erkorkmaz et al. [247]).

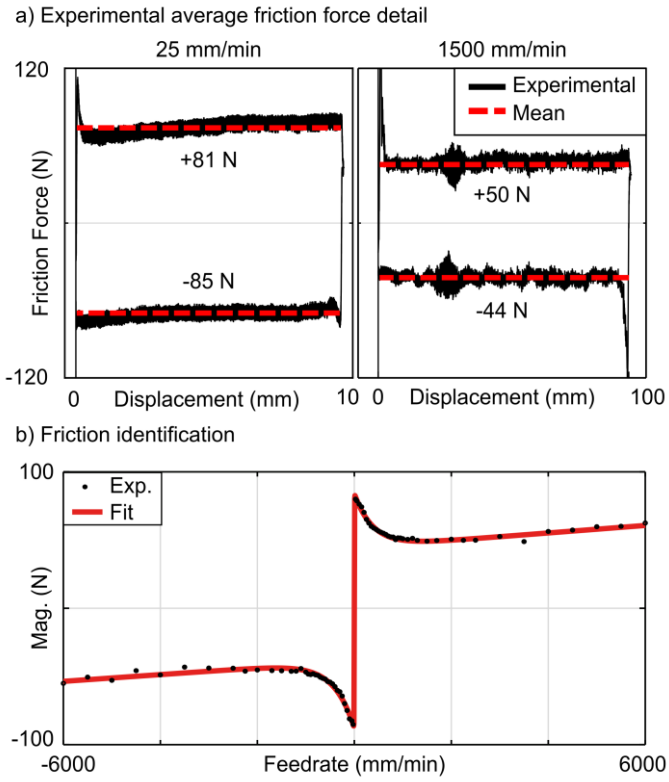

Figure 5.11 Friction a) Experimental identification; b) Model fitting.

Simulation and validation of tool centre point compliance variation

The experimental and simulated quasi-FRF are obtained considering impact hammer testing. The simulated excitation amplitude has been selected according to experimental impact tests performed on the test bench flexure with a PCB 086C03 hammer and a soft rubber tip. The nonlinearity related to the impact force is negligible compared to the influence of the feed drive dynamics.

Figure 5.12-a shows the cutting point quasi-FRFs simulation and experimental compliances for different axis feeds and 25 N excitation force. For the idle machine case ($\dot{x}_{\mathrm{ref}}$ = 0 mm/min), the dynamic compliance shows a poorly damped resonance coming from the flexure at 61.3 Hz. As the commanded feed increases, the in-motion FRF varies significantly, both in amplitude and frequency, up to a certain feedrate level ($\dot{x}_{\mathrm{ref}} \approx$ 500 mm/min), where the dynamic response remains 'invariant'. This modification is a result of the interaction of the servo controller and friction forces for different feedrate commands. This can be further explained following Figure 5.12-b:

- For idle case ($\dot{x}_{\mathrm{ref}}$ = 0 mm/min), as the reference feedrate is zero, the servo controller force is negligible compared to the friction force ($F_{\mathrm{friction}} >> F_{\mathrm{control}}$).

- As the reference feed increases, so does the servo controller force, generating interactions between the control and friction forces ($F_{\text{friction}} \approx F_{\text{control}}$).

- Above a certain feed ($\dot{x}_{\text{ref}} \approx$ 500 mm/min), the servo controller force becomes dominant; therefore, the system response become more linear (i.e., less amplitude dependent) and the dynamic compliance remains 'invariant' ($F_{\text{friction}} << F_{\text{control}}$). Therefore, the effect of the selected servo bandwidth (f_{bw}) on the obtained dynamic response can be observed.

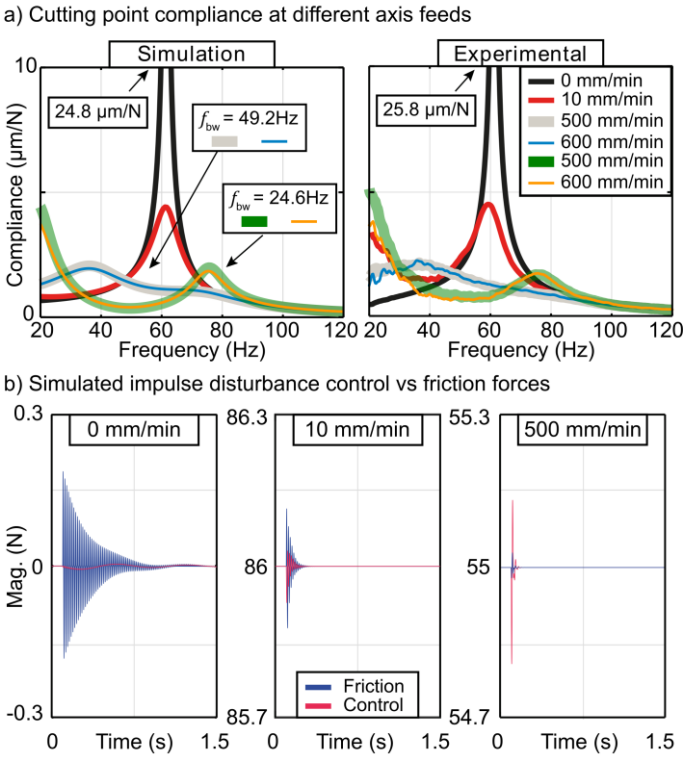

Figure 5.12 a) Simulated and experimental idle and in-motion FRFs; b) Simulation variation of different force sources for different axis feeds.

This single axis laboratory setup has provided clear experimental evidence of the friction influence on the cutting point dynamics and validates the proposed modelling approaches with experimental results that match the simulations. The next section goes further in the analysis of the interaction of control and friction dynamics.

5.4 CONTROL AND FRICTION INTERACTIONS

Based on the conclusions previously obtained, the effect of the control parameters on the tool tip dynamics can be clearly identified when the axis is moving. In this section, the influence of the control parameters on the tool tip compliance is presented with an

equivalent mechanical model. In addition, different friction models have been compared to analyse the idle and in-motion FRF prediction capabilities.

5.4.1 Effect of the control parameters on cutting point dynamics

Figure 5.13 shows the equivalence between the control feedback model and a purely mechanical model of two degrees of freedom. The controller is the classical P-PI controller implemented in machine tool CNCs, which utilizes proportional and integral actions (K_p and T_i) in the velocity loop whereas a single proportional gain in the position loop (K_v) is used. The controller force (F_control) depends on the feedback sensor reading x_mot as shown in Eq. (5.4).

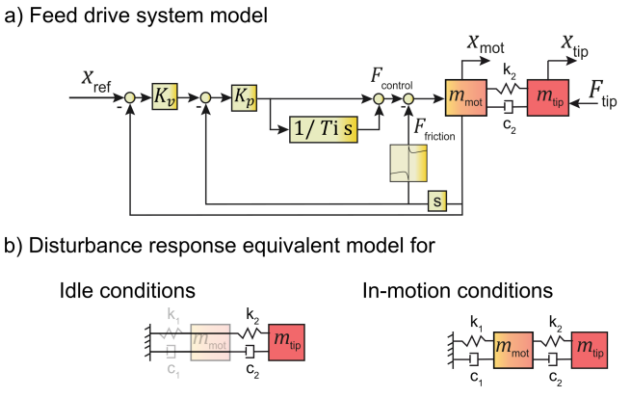

Figure 5.13 Equivalent mechatronic feed drive model.

$$F_\mathrm{control} = (s + K_\mathrm{v})K_\mathrm{p}\left(1 + \frac{1}{T_\mathrm{i}s}\right)(x_\mathrm{ref} - x_\mathrm{mot}) \tag{5.4}$$

As indicated in Chapter 4, the selected controller bandwidth can extensively modify the tool tip compliance. Eq. (5.5) shows the tool centre point compliance under the effect of selected control parameters. Additionally, the viscous friction term (σ) has been added to the equation.

$$\frac{\boldsymbol{x_\mathrm{tip}}}{\boldsymbol{F_\mathrm{tip}}} = \frac{(\boldsymbol{s} + \boldsymbol{K_\mathrm{v}})\boldsymbol{K_\mathrm{p}}\left(\boldsymbol{1} + \frac{\boldsymbol{1}}{\boldsymbol{T_\mathrm{i}s}}\right) + \boldsymbol{m_1 s^2} + \boldsymbol{c_2 s} + \boldsymbol{k_2}}{(\boldsymbol{m_2 s^2} + \boldsymbol{c_2 s} + \boldsymbol{k_2})(\boldsymbol{s} + \boldsymbol{K_\mathrm{v}})\boldsymbol{K_\mathrm{p}}\left(\boldsymbol{1} + \frac{\boldsymbol{1}}{\boldsymbol{T_\mathrm{i}s}}\right) + \boldsymbol{m_1 m_2 s^4} + \left(\boldsymbol{m_1 c_2} + \boldsymbol{m_2}(\boldsymbol{\sigma} + \boldsymbol{c_2})\right)\boldsymbol{s^3} + \left((\boldsymbol{m_1}+\boldsymbol{m_2})\boldsymbol{k_2} + \boldsymbol{\sigma c_2}\right)\boldsymbol{s^2} + \boldsymbol{\sigma k_2 s}} \tag{5.5}$$

The tool tip compliance response for the two degrees of freedom mechanical model of Figure 5.13-b is described in Eq. (5.6), where controller provided force has been replaced by equivalent stiffness and damping elements.

$$\frac{x_{\mathrm{tip}}}{F_{\mathrm{tip}}} = \frac{1}{(m_2 s^2 + c_2 s + k_2) - \dfrac{(c_2 s + k_2)^2}{(m_1 s^2 + (c_1 + c_2)s + k_1 + k_2)}} \tag{5.6}$$

The integral action feedback term does not have a mechanical equivalent. It gives an infinite static stiffness to the drive at low frequency and creates a control pole at low frequency, whose damping depends on the integral time (T_{i}) and commissioned proportional velocity loop gain (K_{p}). If the integral action is neglected ($T_{\mathrm{i}} \approx \infty$), the control loops can be substituted with an equivalent stiffness and damping, as shown in Figure 5.13-b and Eq. (5.8). The damping is provided by the proportional velocity gain whereas the stiffness corresponds to the product of the position and velocity loop gains.

$$F_{\mathrm{control}} = -\left(K_{\mathrm{p}} s + K_{\mathrm{p}} K_{\mathrm{v}}\right) x_{\mathrm{mot}} \text{ with } T_{\mathrm{i}} \approx \infty \tag{5.7}$$

$$\begin{aligned} c_1 &= K_{\mathrm{p}} \\ k_1 &= K_{\mathrm{p}} K_{\mathrm{v}} \end{aligned} \tag{5.8}$$

Figure 5.14 shows that the control loops modify the dynamic compliance between two asymptotic cases. The first one with zero stiffness ($k_1 = K_{\mathrm{p}} = 0$), which is an equivalent of an open loop response. As a result, no static stiffness is present in the system; hence, an antiresonance is present at $f_{\mathrm{a}} = \sqrt{k_2/m_1}$. Additionally, a resonance is located at $f_{\mathrm{r}} = \sqrt{k_2(1/m_1 + 1/m_2)}$. The second asymptotic case corresponds to $K_{\mathrm{p}} \to \infty$, m_1 is completely fixed due to the high controller stiffness and the two degrees of freedom model behaves like a single suspended mass with a resonance frequency at $f_{\mathrm{t}} = \sqrt{k_2/m_2}$. Between these extreme cases, the controller can be tuned to improve the dynamic response as shown in Chapter 4. Note that the equivalent mechanical model offers a satisfactory approximation as long as the integral time gain is set to a large value or the main frequencies of the system are far from the integral action range.

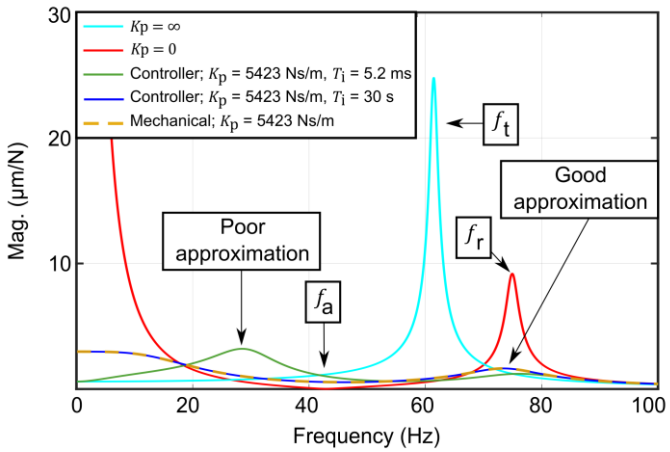

Figure 5.14 Cutting point compliance prediction with the two different models.

5.4.2 Influence of friction model on the quasi-FRF

To analyse the effect of the friction model on the dynamics, three different friction model configurations are shown in Figure 5.15-a. In the first configuration, only viscous friction component is considered (σ). Then, the second configuration neglects the Stribeck effect by considering Coulomb and viscous friction effects. This model can be obtained through Eq. (5.2) by equalizing the maximal static (F_s) and Coulomb sliding (F_c) friction values. The last proposed friction model configuration is the previously employed Andersson type friction model.

Figure 5.15-b-d summarizes the cutting point dynamics with the different proposed friction models. Figure 5.15-b shows the compliance results using the viscous friction component, which cannot capture the effect of machine idle conditions. This is because the controller generated force, even though being in idle conditions, is much more dominant than the friction generated force. Similar results are obtained when friction characteristics are not added into the simulation. Then, by using the combined viscous and Coulomb model, machine idle, in-motion and 'invariant' dynamics can be predicted. However, certain amplitude deviations exist compared to the ones obtained with the Andersson friction model, which has been experimentally validated earlier (Figure 5.12-a).

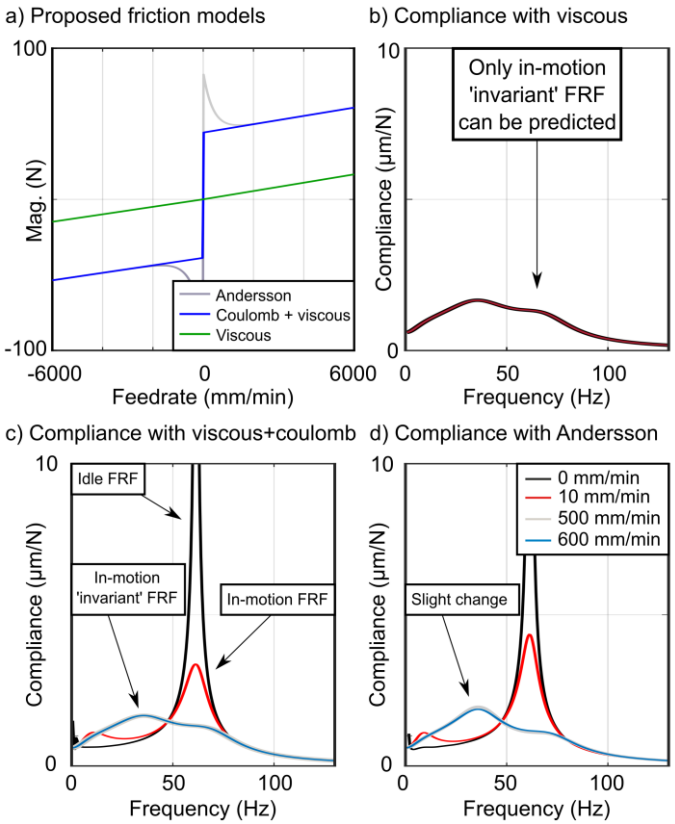

Figure 5.15 Friction models and quasi-FRF simulations.

Using the Andersson type friction model, the transition between idle and in-motion 'invariant' quasi-FRF can be simulated accordingly to the experimental results. However, the Coulomb with viscous friction model can give a reasonable approximation with minor modelling effort as well, albeit with less accurate prediction of the compliance peak.

5.5 EXPERIMENTAL VALIDATION

Figure 5.16-a shows the DS630 machining centre where the effect of friction on the tool centre point dynamics is studied. The horizontal x axis is powered up by a linear motor and y and z axes with ball screw drives. The difference between idle and in-motion dynamics in the x axis is not very relevant. However, the vertical axis demonstrates the effect of nonlinear friction on tool tip compliance. In this machine, the dynamics vary with the selected ram height. Consequently, the travelling distance for the dynamics characterisation is limited to 40 mm to minimize the posture dependent influence on both FRF measurements, and the cutting process stability results. Figure 5.16-b shows the direct and cross tool tip FRFs demonstrating that the in-motion dynamics variations cannot be attributed to the posture variation.

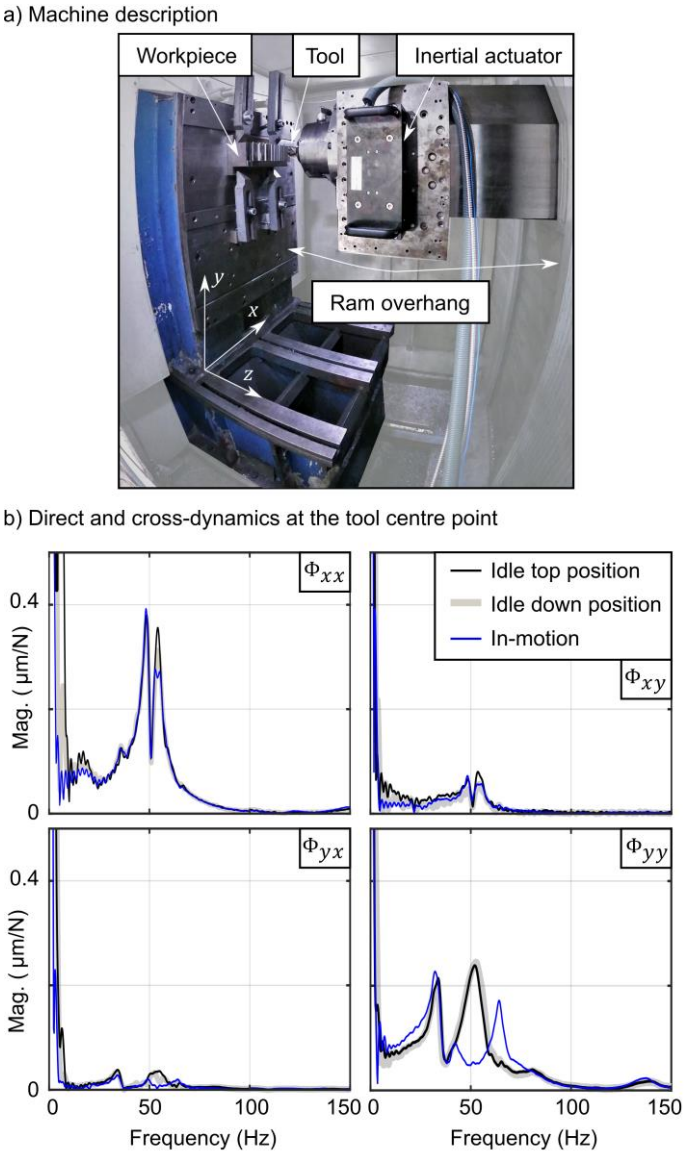

Figure 5.16 a) DS630 machine tool; b) Direct and cross-dynamics at the tool centre point.

An experimental modal analysis has been conducted in idle conditions. Four main vibratory modes have been identified. The first one at 34 Hz corresponds to machine column rocking with respect to the x axis (Figure 5.17-a). The modal displacement has projections in y and z directions and is barely observable in the x axis. In contrast, the second mode at 50 Hz is a pure ram bending mode in the x-z plane (Figure 5.17-b). The third mode at 52 Hz is a summation of a translational mode of the vertical feed drive system and ram bending in the y-z plane (Figure 5.17-c). Finally, the fourth mode at 57 Hz has a similar modal shape to the second one at 50 Hz.

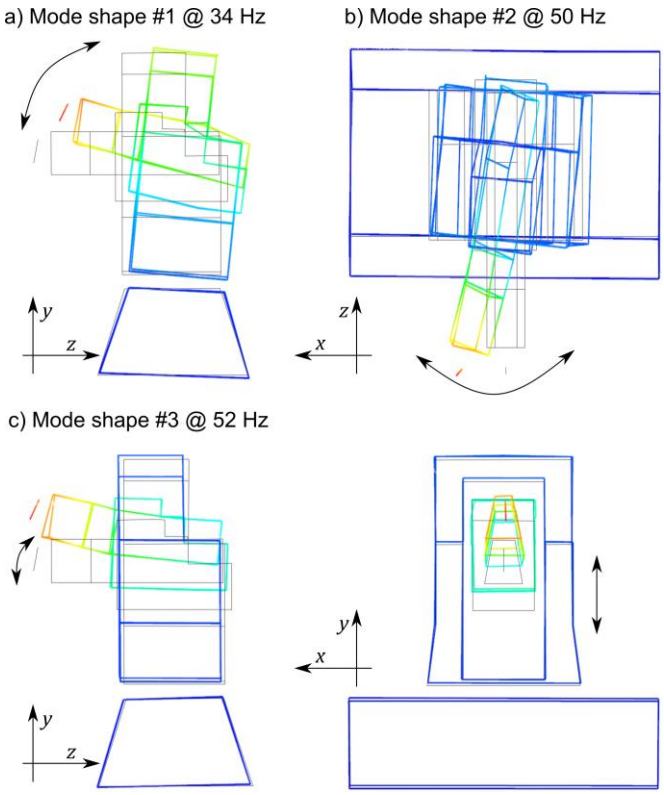

Figure 5.17 Experimental modal analysis.

5.5.1 Quasi-FRF

Figure 5.18 shows the vertical y axis direct ram compliance measurements in idle and in-motion conditions for different axis velocities acquired by impact hammer tests. All impact tests presented in this section have been realized with a PCB 086D20 impact hammer and a PCB 356A17 triaxial accelerometer. The impact hammer allows performing a rapid measurement of the machine dynamics with only four impact tests of few seconds each. The good coherence indicator value confirms the quality of the measurements.

The initial idle dynamic response varies significantly under the effect of the axis feedrate. The amplitude of the first natural frequency located at 34 Hz increases, while the amplitude of the next natural frequency at 52 Hz is significantly modified passing from a resonance-like response to one line an anti-resonance. As a result of the amplitude change, a new natural frequency which is not seen in the idle FRF appears at 42Hz. A very similar effect is observed at 66 Hz, where the amplitude strongly increases once a feed of 80 mm/min is reached.

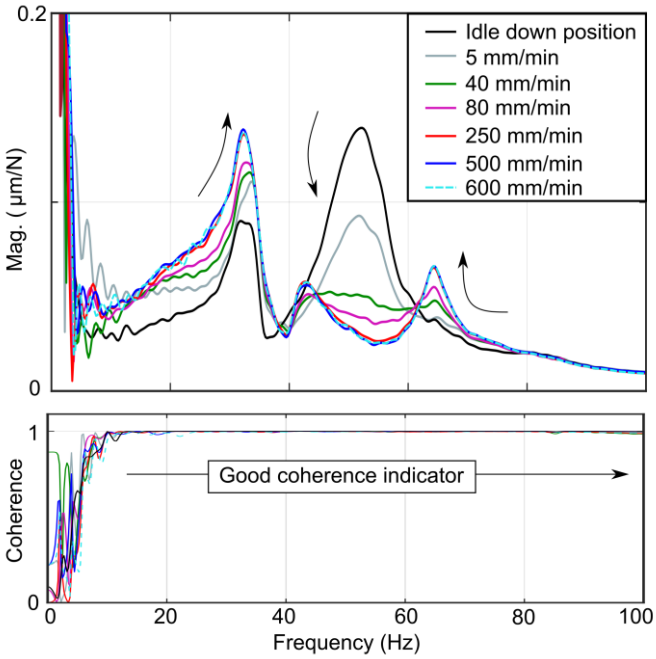

Figure 5.18 Experimental y axis compliance measured with impact hammer.

The in-motion 'invariant' FRF is reached at approximately 250 mm/min. However, the effect of the commanded axis velocity on the compliance is noticeable at very low speeds (20 mm/min). It can be observed that a smooth transition from idle to in-motion 'invariant' FRF exists. These measurements give a very clear demonstration of the influence of the axis feed on the structural dynamics, where initial dynamic behavior (idle conditions) and in-process dynamics (>250 mm/min) are totally different.

5.5.2 Friction characteristics identification

The characterization of the y axis friction is performed by running the axis at different sliding speeds and monitoring the motor current. Figure 5.19 shows the experimental and the fitted friction curves using the previously described Andersson type model of Eq. (5.2). A good approximation of the feed in which the in-motion 'invariant' FRF is reached can be obtained from the friction curve. Indeed, it corresponds to the point where the viscous linear friction is dominant (≈ 250 mm/min). The noticeable discrepancy between the perceived 'friction characteristics' for positive and negative velocity cases can be caused by the effect of gravity and the counterweight installed in this vertical axis. The feed direction was been modified to analyze if this asymmetric characteristic creates a motion direction dependent tool tip compliance, concluding that little effect is generated on this machine.

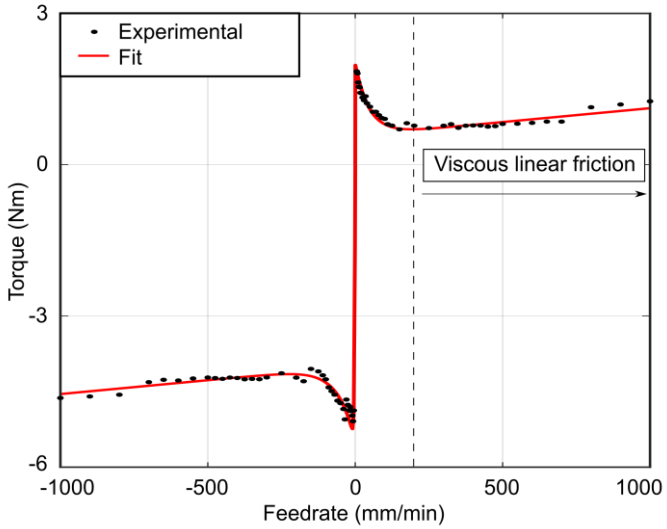

Figure 5.19 DS630 vertical axis friction characteristics.

5.5.3 Influence of the excitation force level

When dealing with nonlinear dynamics, it is well known that the excitation type can have a significant influence on the measured FRFs (Ewins [246]). Apart from the excitation type, the excitation level should also be controlled to obtain robust results. In general, electromagnetic shakers are the preferred option to measure nonlinear structure responses. However, the analyses conducted in this research involve machine movements at different feeds which cannot be handled with traditional hanging shakers. For that reason, an inertial actuator based on a linear motor and attached to the moving structure is used (Figure 5.20). A Bosch ML3P03-B_BW linear motor generates a controlled force by accelerating an inertial mass.

The so-called sine stream excitation signal is selected to perform a frequency sweep from 20 to 80 Hz with steps of 0.25 Hz. Each frequency is maintained for 5 oscillation cycles and two sinewaves are fitted to the input force and output acceleration to obtain the FRF at each known frequency. The magnitude and phase are computed using the ratio between the sinewave amplitudes and their phase shift. Figure 5.21 presents the inertial force obtained from an accelerometer mounted on the inertial mass and the output response. As a coherence indicator, the R-squared goodness-of-fit is provided.

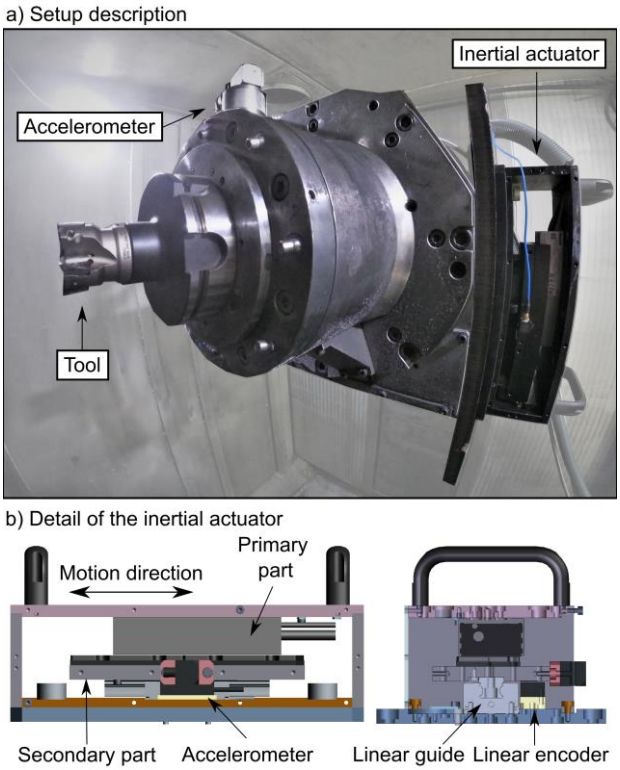

Figure 5.20 Inertial actuator mounted on the moving ram.

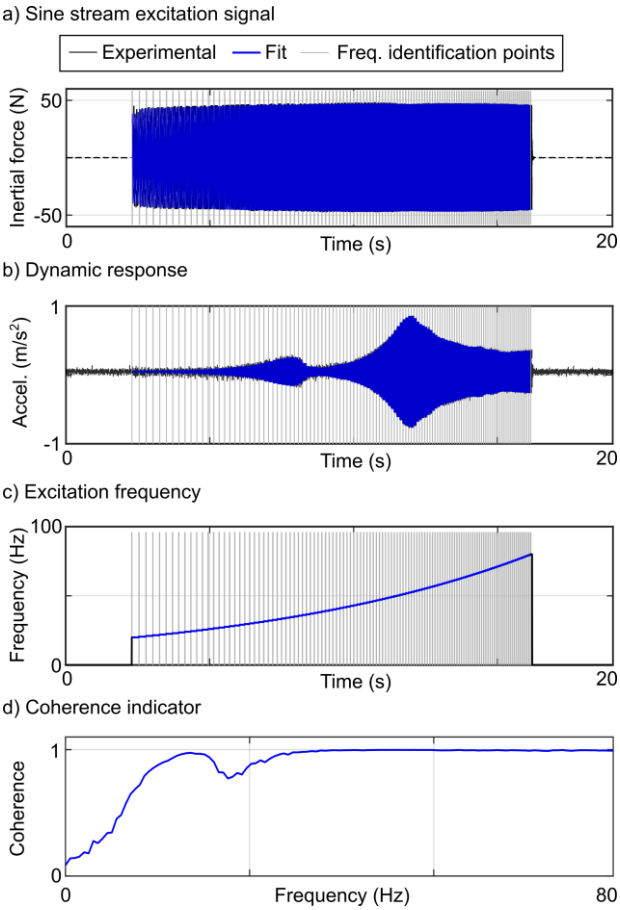

Figure 5.21 Excitation force and measured acceleration signals for FRF computation.

Three different force amplitudes have been applied with the linear motor to analyse the response linearity related to the force level at different axis velocities. Figure 5.22 shows a large influence of the excitation amplitude on the measured responses in machine idle conditions. However, the response is progressive, as higher excitation force levels lead to the observation of lower amplitudes at the main resonance. The same trend with higher influence is observed for the 5 mm/min in-motion FRF. As the feed increases, a linearization can be observed, as the dynamic responses obtained with different excitation force levels are very similar (40 and 100 mm/min). For those and higher axis velocities, the servo control force is relatively larger than the friction force, so a linearized behaviour is reached and the in-motion FRF is independent from the perturbation level.

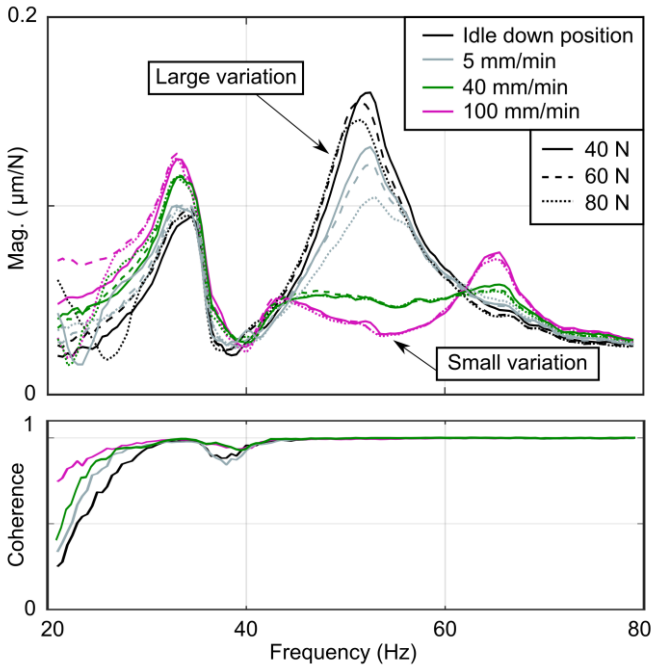

Figure 5.22 Force and axis velocity linearity analysis.

Experimental characterisations made on two different machines show that the impact hammer is a good tool to analyse the effect of friction of the dynamics. Indeed, when the machine is moving the force level nonlinearity is not dominant.

5.5.4 Idle vs in-motion time domain response

To give further evidence of the strong modification of the machine dynamics due to the axis feed, the machine ram is perturbed with a constant force sinewave of 80 N at the main natural frequencies using the inertial actuator. Figure 5.23 shows the acceleration response of the machine ram for the three conducted tests, starting from

idle condition, performing a y-axis movement at a constant feed of 500 mm/min and finishing at idle condition again. As expected from the evolution of the quasi-FRF, the response at 33 Hz has a small amplitude variation. However, at 52 Hz, the vibration amplitude decreases by 75 % as a result of the quasi-FRF magnitude drop. In contrast, at 66 Hz, the initial vibration amplitude increases as a result of the resonance created at that particular frequency.

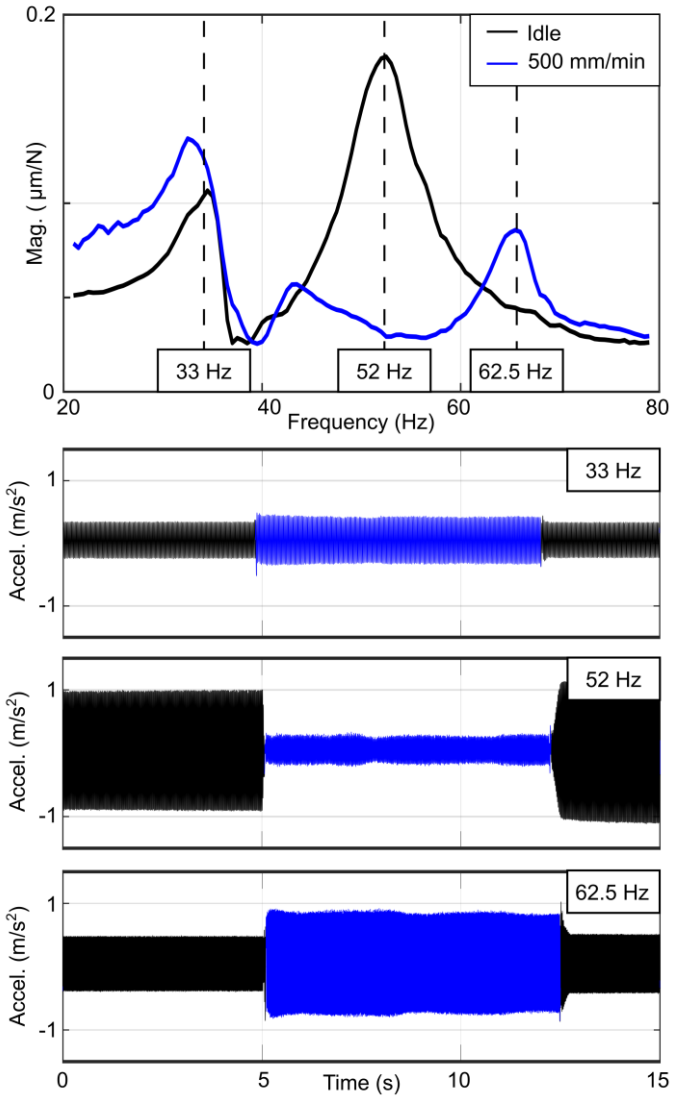

Figure 5.23 Sinewave response at characteristic frequencies in idle and in-motion conditions.

5.5.5 Influence of the control parameters

Another important novelty of this work is the demonstration that the real contribution of the control feedback on tool centre point dynamics can mostly be seen once the

linearized axis feed regime is achieved. Figure 5.24 shows the effect of the variation of the proportional velocity gain on tool tip compliance characterized with the inertial actuator. Although the proportional velocity gain is modified, the effect at idle conditions is minor comparing to the one measured at 300 mm/min.

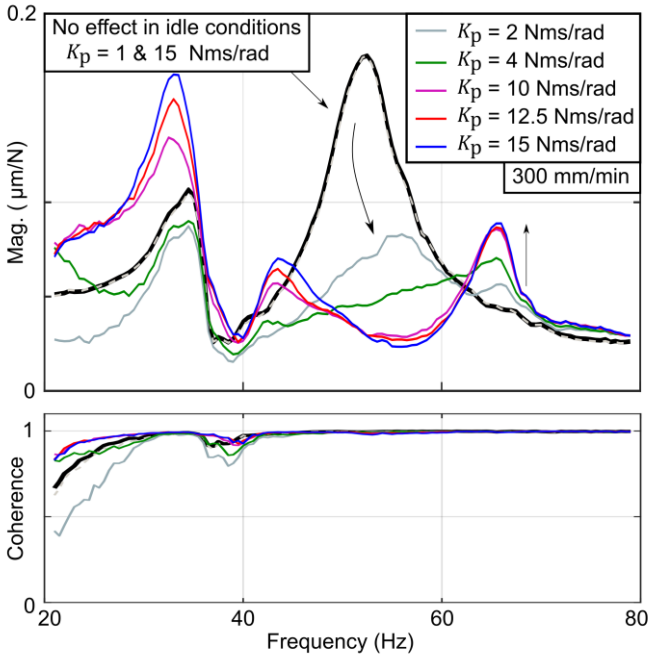

Figure 5.24 Servo control bandwidth effect.

These experimental results demonstrate that the commanded axis velocity plays a significant role in the cutting point dynamics. The next section shows how the machining stability predictions can be improved by comparing the chatter stability predictions obtained from the idle and in-motion 'invariant' FRF.

5.5.6 Chatter stability analysis

By using the frequency responses indicated in Figure 5.16-b the chatter stability predictions are computed following the approach presented by Altintas et al. [11]. The measurements are obtained with traditional impact hammer approach. A minor cross-coupling effect is present in x direction as a result of the axis motion in y axis. Additionally, the cross dynamics Φ_{xy} and Φ_{yx} have relatively small amplitudes compared to the direct terms.

The cutting process parameters for chatter stability tests are summarized in Table 5.1. z direction is very stiff and a tool with a lead angle of 90 degree is used so a 2D stability

model is applied. The feed per tooth of 0.2 mm/Z ensures that even for the lowest spindle speed of 400 rpm, the axis velocity is higher than the in-motion 'invariant' feed of 250 mm/min.

Table 5.1: Cutting process parameters for chatter stability tests

Cutting tool	
Reference	WALTER F4042 B16.040.Z04.15
Diameter, D	40 mm
Number of teeth, Z	4
Inserts reference	WKP35S ADMT160608R-F56
Lead angle, κ	90º
Cutting conditions	
Feed per tooth, f_Z	0.2 mm/Z
Radial engagement, a_{e}	32 mm (down-milling)
Workpiece material	F1140 Steel (C45)
Cutting coefficients	
Specific tangential, K_{tc}	1885 $\mathrm{N/mm^2}$
Specific radial, K_{rc}	749 $\mathrm{N/mm^2}$

Figure 5.25-a shows the experimental stability lobes on top of the theoretical predictions. It can be concluded that the dynamic variation related to the axis position has very small impact on the process stability. Using the in-motion FRF at 500 mm/min, the critical depth of cut increases by 53 % (from 1.5 to 2.3 mm). The cutting tests confirm that the experimental stability is closer to the prediction that uses the in-motion dynamics. This can also be seen in the chatter frequency predictions, where up to 6 Hz difference can be measured. Figure 5.25-b indicates the experimental vibration spectra for 1000 rpm cutting conditions in which the depth of cut and chatter frequency have a significant deviation from the expected ones by using idle dynamics (240 % and 8 % respectively).

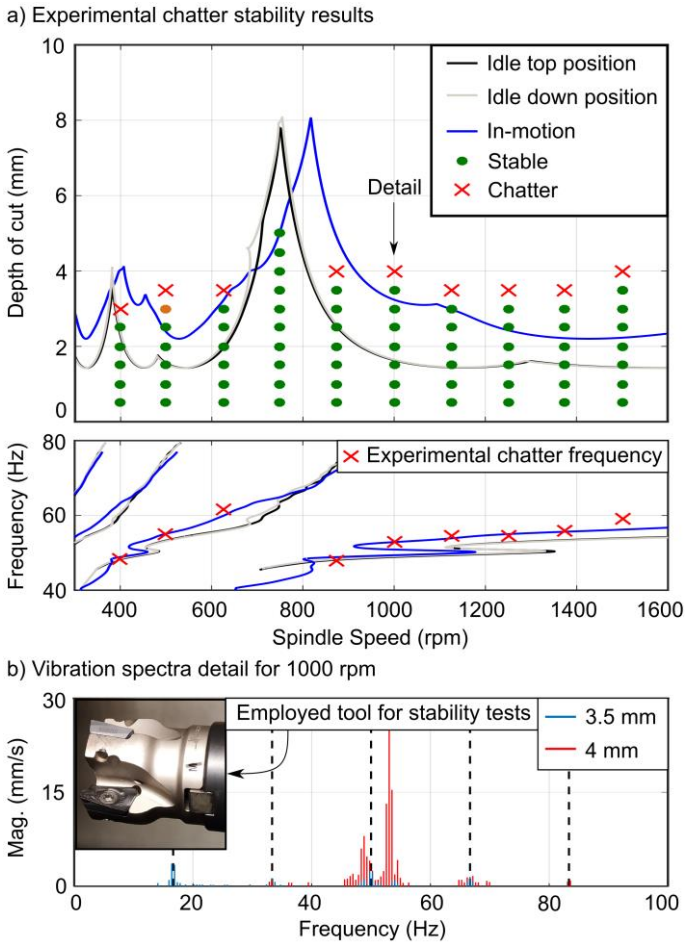

Figure 5.25 Cutting process stability results.

This experimental validation shows that better process stability predictions are obtained using in-motion FRFs instead of idle FRFs. Although the stability prediction is clearly improved, modelling improvements are needed to further improve the accuracy of the predicted stability limit between 1250 and 1500rpm.

5.6 CONCLUSIONS

This chapter shows that the feed drive axis movements highly influence the structural dynamic compliance of large machine tools near the cutting point. The measurements conducted on seven machine tools demonstrate that this is a widespread phenomenon, and it has not received sufficient attention in earlier research. This work clearly explains the influence of friction and control loops on the dynamics. A two-mass model, coupled with the Anderson friction model and servo controller dynamics accurately predicts the dynamics variations measured on a laboratory setup, comprising a flexure mounted on a linear drive. Another important contribution of this chapter is that the effect of the control loops on the dynamics is seen mostly when the axis is moving. Hence, this finding will

help when adjusting the control loops to improve the dynamics of the structural modes affected by the feed drives, especially in the contexts of machining disturbance force response. After the theorical understanding of the influence of friction on the structural dynamics, a detailed analysis of a three-axis milling centre is used to demonstrate the main results on an industrial machine. The nonlinearities related to the excitation force and axis feed were analysed, and it was concluded that the axis feed has a much greater impact on the dynamics. Finally, it was shown that chatter stability prediction is improved when in-motion FRFs are considered, as demonstrated by the cutting tests.

Chapter 6

Operational machining system dynamics identification by Sweep Milling Force Excitation

6.1 INTRODUCTION

As introduced in Section 2.1, the presence of regenerative chatter vibrations is a classical problem that limits the machine tool productivity. Chatter occurs when one or more vibratory modes of the machining system are self-excited during the cutting process (Munoa et al. [2]). Stability lobe diagrams can be used for the prediction and prevention of this unwanted phenomenon. To obtain these diagrams, four different inputs are required: tool geometry, process-related data, material cutting coefficients and dynamic characteristics of the machining system. However, as a result of the challenges in the machine tool dynamics identification (described in Section 2.2) this chapter proposes a combined identification of the machining system dynamics under operational conditions which can capture any nonlinearities that are not identified in traditional characterization

methods (Figure 6.1). Temporal simulations of the milling force excitation allow for optimization of the process parameters used for the characterization of the dynamics. To switch from time to frequency domain, a new signal processing methodology is applied using Welch's method. Hence, high-quality FRFs are obtained. The mathematical derivations to compute the coherence of each identified FRF is also provided. In addition, the effect of a poor-conditioned set of identification cutting tests is experimentally identified. For the particular case of heavy-duty rough milling operations, the common chatter vibrations arise from the large flexible fixture holding the workpiece or from the machine tool structure. They are both experimentally measured with the proposed method in a 3-axis machining centre. The obtained machining system dynamics are compared to impact hammer results and validated through experimental chatter stability tests.

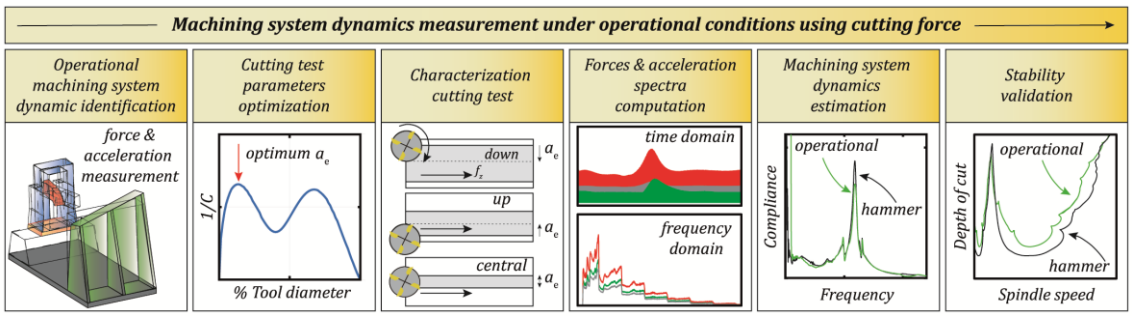

Figure 6.1 Proposed methodology.

6.2 SWEEP MILLING FORCE EXCITATION (SMFE) FOR MACHINING SYSTEM RECEPTANCE IDENTIFICATION

The main objective of this work is to identify the receptance of the machining system for chatter stability prediction by means of cutting force sweep. In this section, the required mathematical and dynamic concepts are described.

6.2.1 Milling cutting process

In the milling cutting process, a rotating tool with one or multiple teeth Z removes material in the commanded feed direction. Figure 6.2-a shows a schematic face milling cutting operation where the spindle speed is denoted N, the feed per tooth f_Z, the axial depth of cut a_p, the tool radial engagement a_e, and ϕ_j is the immersion angle of the tooth j. As shown in Figure 6.2-b, the generated cutting forces of each tooth j are decomposed into

tangential ($F_{t,j}$), radial ($F_{r,j}$) and axial ($F_{a,j}$) directions, and their orientations depend on the lead angle of the tool κ.

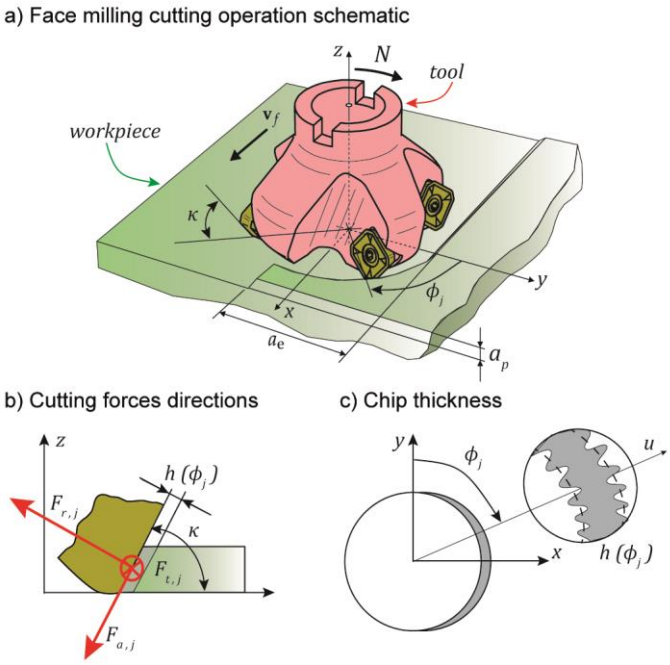

Figure 6.2 a) Face milling cutting operation schematic; b) Cutting forces directions; c) Chip thickness.

For the particular case of regular equally spaced inserted face milling operation, the engagement can be defined by the chip thickness $h(\phi)$ which can be decomposed into dynamic and stationary components (Eq. (6.1)). The difference between the wavy surfaces left by the previous and successive tooth produces a dynamic variation of the chip thickness $h_{\mathrm{d}}(\phi)$. Therefore, this dynamic component is the result of the relative motion between tool ($\mathbf{r}_{\mathrm{t}}$) and workpiece ($\mathbf{r}_{\mathrm{w}}$) in current $\mathbf{r}(t) = [x(t) \quad y(t) \quad z(t)]^{\mathrm{T}}$ and previous time instant $\mathbf{r}(t-\tau)$. Where τ is the period between two successive teeth, which is the tooth passing period in this regular case, that is $\tau = 60/N \cdot Z$. The vibrations are defined in the machine (xyz) coordinate system, while chip thickness for a given tooth j is oriented along the vector $\mathbf{u}(\phi_j)$ at the angular position ϕ_j (Eq. (6.1)) (Figure 6.2-c).

$$
\begin{aligned}
&h(\phi_j) = h_{\mathrm{s}}(\phi_j) + h_{\mathrm{d}}(\phi_j) \\
&\text{where , } h_{\mathrm{s}}(\phi) = f_Z \sin\phi \sin\kappa \\
&\qquad h_{\mathrm{d}}(t) = \mathbf{u}^{\mathrm{T}}(\phi_j(t))\, \Delta\mathbf{r}(t), \text{ and} \\
&\qquad \mathbf{u}(\phi) = [\sin\phi \sin\kappa \quad \cos\phi \sin\kappa \quad -\cos\kappa]^{\mathrm{T}}
\end{aligned}
\tag{6.1}
$$

The static chip thickness h_s is a function of the feed per tooth f_Z as well as the lead angle κ and the position angle ϕ of each j tooth as $\phi_j(t) = \Omega\, t + \frac{j-1}{Z} 2\,\pi$, where $\Omega = \frac{2\pi N}{60}$. The relative regenerative term and the local normal vector have the form

$$\Delta\mathbf{r}(t) = \mathbf{r}_{\mathrm{t}}(t) - \mathbf{r}_{\mathrm{t}}(t-\tau) - (\mathbf{r}_{\mathrm{w}}(t) - \mathbf{r}_{\mathrm{w}}(t-\tau)) \tag{6.2}$$

In machining processes, it is usual to model the cutting forces as a function of the chip thickness and to consider proportional cutting coefficients. Eq. (6.3) defines the employed cutting force expression, which represents a linear force model while considering the edge rubbing influence (Amarego et al. [248]). The cutting force is decomposed as a sum of shear forces (subscript c) as a result of the material's shear process, and edge forces (subscript e) to represent the friction between the tool edge and the workpiece surface (S_{e}).

$$\mathbf{F}_{tra,j}(t) \coloneqq \begin{bmatrix} F_{t,j}(t) \\ F_{r,j}(t) \\ F_{a,j}(t) \end{bmatrix} = \left(\begin{bmatrix} K_{tc} \\ K_{rc} \\ K_{ac} \end{bmatrix} h\left(\phi_j(t)\right) + \begin{bmatrix} K_{te} \\ K_{re} \\ K_{ae} \end{bmatrix} S_{\mathrm{e}} \right) g\left(\phi_j(t)\right), \tag{6.3}$$

where $g(\phi)$ is the screen function determining whether the tooth is engaged or not by considering the entry (ϕ_{en}) and exit angles (ϕ_{ex}).

$$g(\phi) \;= \begin{cases} 1 & \phi_{\mathrm{en}} < \phi \bmod 2\pi < \phi_{\mathrm{ex}} \\ 0 & \text{otherwise} \end{cases} \tag{6.4}$$

The cutting forces on the tooth $\mathbf{F}_{tra,j}$ can be projected onto (xyz) cartesian axes following Eq. (6.5). With this, by adding the contribution of all teeth Z, the total forces can be obtained.

$$\mathbf{F}(t) = \sum_{j=1}^{Z} \begin{bmatrix} -\cos\phi_j(t) & -\sin\phi_j(t)\sin\kappa & -\sin\phi_j(t)\cos\kappa \\ \sin\phi_j(t) & -\cos\phi_j(t)\sin\kappa & -\cos\phi_j(t)\cos\kappa \\ 0 & \cos\kappa & -\sin\kappa \end{bmatrix} \mathbf{F}_{tra,j}(t). \tag{6.5}$$

6.2.2 Machining system receptance FRF

The response $\mathbf{r}(\omega)$ and the force excitation $\mathbf{F}(\omega)$ relationship can be defined by means of the Frequency Response Function (FRF) $\mathbf{\Phi}(\omega)$ assuming linear or sufficiently perturbed nonlinear dynamics. Considering a universal milling machine and workpiece defined in Cartesian directions, a generalized FRF matrix can have up to nine unknowns at tool/workpiece single spatial point of excitation (Eq. (6.6)). For the case of the tool,

this frequency domain dynamics relation is represented by $\mathbf{\Phi}_{\mathrm{tt}}(\omega)$; while for the workpiece it is denoted $\mathbf{\Phi}_{\mathrm{ww}}(\omega)$ (Eq. (6.7)-(6.8)).

$$\begin{aligned} x^{\mathrm{t}} &= \Phi_{xx}^{\mathrm{tt}}(\omega)F_x^{\mathrm{t}} + \Phi_{xy}^{\mathrm{tt}}(\omega)F_y^{\mathrm{t}} + \Phi_{xz}^{\mathrm{tt}}(\omega)F_z^{\mathrm{t}} \\ y^{\mathrm{t}} &= \Phi_{yx}^{\mathrm{tt}}(\omega)F_x^{\mathrm{t}} + \Phi_{yy}^{\mathrm{tt}}(\omega)F_y^{\mathrm{t}} + \Phi_{yz}^{\mathrm{tt}}(\omega)F_z^{\mathrm{t}} \\ z^{\mathrm{t}} &= \Phi_{zx}^{\mathrm{tt}}(\omega)F_x^{\mathrm{t}} + \Phi_{zy}^{\mathrm{tt}}(\omega)F_y^{\mathrm{t}} + \Phi_{zz}^{\mathrm{tt}}(\omega)F_z^{\mathrm{t}} \end{aligned} \tag{6.6}$$

$$\mathbf{r}_{\mathrm{t}} := \begin{bmatrix} x^{\mathrm{t}} \\ y^{\mathrm{t}} \\ z^{\mathrm{t}} \end{bmatrix},\ \mathbf{F}_{\mathrm{t}} := \begin{bmatrix} F_x^{\mathrm{t}} \\ F_y^{\mathrm{t}} \\ F_z^{\mathrm{t}} \end{bmatrix} \text{ with } \mathbf{\Phi}_{\mathrm{tt}}(\omega) := \begin{bmatrix} \Phi_{xx}^{\mathrm{tt}}(\omega) & \Phi_{xy}^{\mathrm{tt}}(\omega) & \Phi_{xz}^{\mathrm{tt}}(\omega) \\ \Phi_{yx}^{\mathrm{tt}}(\omega) & \Phi_{yy}^{\mathrm{tt}}(\omega) & \Phi_{yz}^{\mathrm{tt}}(\omega) \\ \Phi_{zx}^{\mathrm{tt}}(\omega) & \Phi_{zy}^{\mathrm{tt}}(\omega) & \Phi_{zz}^{\mathrm{tt}}(\omega) \end{bmatrix} \tag{6.7}$$

$$\mathbf{r}_{\mathrm{w}} := \begin{bmatrix} x^{\mathrm{w}} \\ y^{\mathrm{w}} \\ z^{\mathrm{w}} \end{bmatrix},\ \mathbf{F}_{\mathrm{w}} := \begin{bmatrix} F_x^{\mathrm{w}} \\ F_y^{\mathrm{w}} \\ F_z^{\mathrm{w}} \end{bmatrix} \text{ with } \mathbf{\Phi}_{\mathrm{ww}}(\omega) := \begin{bmatrix} \Phi_{xx}^{\mathrm{ww}}(\omega) & \Phi_{xy}^{\mathrm{ww}}(\omega) & \Phi_{xz}^{\mathrm{ww}}(\omega) \\ \Phi_{yx}^{\mathrm{ww}}(\omega) & \Phi_{yy}^{\mathrm{ww}}(\omega) & \Phi_{yz}^{\mathrm{ww}}(\omega) \\ \Phi_{zx}^{\mathrm{ww}}(\omega) & \Phi_{zy}^{\mathrm{ww}}(\omega) & \Phi_{zz}^{\mathrm{ww}}(\omega) \end{bmatrix} \tag{6.8}$$

Note that from the Newton's reaction principle, the excitation forces $\mathbf{F}_{\mathrm{t}}$ and $\mathbf{F}_{\mathrm{w}}$ will be equal in magnitude and in opposite direction during the cutting process ($\mathbf{F}_{\mathrm{t}} = -\mathbf{F}_{\mathrm{w}}$). As described by Iglesias et al. [96], in certain machine architectures the tool and workpiece side dynamics can be coupled. In these cases, the cross dynamics $\mathbf{\Phi}_{\mathrm{tw}}$ and $\mathbf{\Phi}_{\mathrm{wt}}$ should be considered as presented in Eq. (6.9).

$$\mathbf{r}_{\mathrm{t}}(\omega) = \mathbf{\Phi}_{\mathrm{tt}}(\omega)\,\mathbf{F}_{\mathrm{t}}(\omega) + \mathbf{\Phi}_{\mathrm{tw}}(\omega)\,\mathbf{F}_{\mathrm{w}}(\omega) \text{ and } \mathbf{r}_{\mathrm{w}}(\omega) = \mathbf{\Phi}_{\mathrm{ww}}(\omega)\,\mathbf{F}_{\mathrm{w}}(\omega) + \mathbf{\Phi}_{\mathrm{wt}}(\omega)\,\mathbf{F}_{\mathrm{t}}(\omega) \tag{6.9}$$

It is assumed that the cross FRFs are equal due to the reciprocity principle ($\mathbf{\Phi}_{\mathrm{tw}} = \mathbf{\Phi}_{\mathrm{wt}}$). Hence, the relative displacement between the tool and the workpiece $\mathbf{r}(\omega)$ is given by Eq. (6.10).

$$\begin{aligned} &\mathbf{r}(\omega) = \mathbf{r}_{\mathrm{t}}(\omega) - \mathbf{r}_{\mathrm{w}}(\omega) \text{ with } \mathbf{F}_{\mathrm{t}}(\omega) = -\mathbf{F}_{\mathrm{w}}(\omega) \\ &\mathbf{r}(\omega) = \big(\mathbf{\Phi}_{\mathrm{tt}}(\omega) - \mathbf{\Phi}_{\mathrm{tw}}(\omega)\big)\mathbf{F}_{\mathrm{t}}(\omega) + \big(\mathbf{\Phi}_{\mathrm{ww}}(\omega) - \mathbf{\Phi}_{\mathrm{wt}}(\omega)\big)\mathbf{F}_{\mathrm{t}}(\omega) \end{aligned} \tag{6.10}$$

Finally, as proposed by Iglesias et al. [249], the chatter stability can be analysed considering the machining system resultant FRF $\mathbf{\Phi}\,(\omega)$ of Eq. (6.11).

$$\mathbf{\Phi}\,(\omega) = \mathbf{\Phi}_{\mathrm{tt}}(\omega) + \mathbf{\Phi}_{\mathrm{ww}}(\omega) - 2\mathbf{\Phi}_{\mathrm{tw}}(\omega) \tag{6.11}$$

By performing the machining system dynamics identification through the Sweep Milling Force Excitation proposed in this article, the coupling effect between tool and workpiece sides are jointly considered because the excitation is applied to both sides simultaneously. Hence, $\mathbf{\Phi}_{\mathrm{tt}}^{\mathrm{SMFE}}(\omega) = \big(\mathbf{\Phi}_{\mathrm{tt}}(\omega) - \mathbf{\Phi}_{\mathrm{tw}}(\omega)\big)$ and $\mathbf{\Phi}_{\mathrm{ww}}^{\mathrm{SMFE}}(\omega) = \big(\mathbf{\Phi}_{\mathrm{ww}}(\omega) - \mathbf{\Phi}_{\mathrm{wt}}(\omega)\big)$. However, while characterizing the system with traditional methods such as

impact hammer testing, the coupling effect should be considered as shown in Eq. (6.11). In the rest of the paper, the superscript “SMFE” is omitted to simplify the notations.

6.2.3 Sweep Milling Force Excitation

As described above (Eq. (6.6)-(6.8)), up to nine unknowns are presented for both the tool and workpiece dynamics ($\Phi_{xx}^{\mathrm{tt}} \dots \Phi_{zz}^{\mathrm{tt}}(\omega)$ and $\Phi_{xx}^{\mathrm{ww}} \dots \Phi_{zz}^{\mathrm{ww}}(\omega)$), meaning that the mathematical description of the characterisation methodology must provide at least nine independent algebraic equations in the frequency domain for solvability. Iglesias et al. [96] proposed the utilization of three different cutting operations such as up-, down- and central-milling to generate independent equations from the measurement of the triaxial excitation and triaxial vibration responses. For simplicity, further explanations will be centred for tool side identification taking the FRF $\mathbf{\Phi}_{\mathrm{tt}}(\omega)$ as the base for the mathematical derivations.

In a regular cutting process, the spindle rotates at the commanded speed N. For the particular case of the Sweep Milling Force Excitation, the milling tool rotating speed is continuously varied in such a way that the tooth passing frequency sweeps over the frequency range of interest (Figure 6.3-a). In addition to this, to maintain the force level constant, the feedrate is also continuously modified to obtain a constant feed per tooth f_Z. In this regard, it is important to emphasize that in this measurement only the static component of the chip thickness is utilized, any transient vibration dies out and during the sweep measurement stable stationary cutting should be granted with a chatter free cutting process. Figure 6.3-b shows the evolution of the chip thickness of a single tooth which generates a kind of chirp excitation. Similarly, Figure 6.3-c shows the frequency domain response of the chip thickness for the specific time range of Detail A and B. In addition, the averaged frequency response of the whole chip thickness modification is overlayed showing that the excitation signal covers a large frequency band.

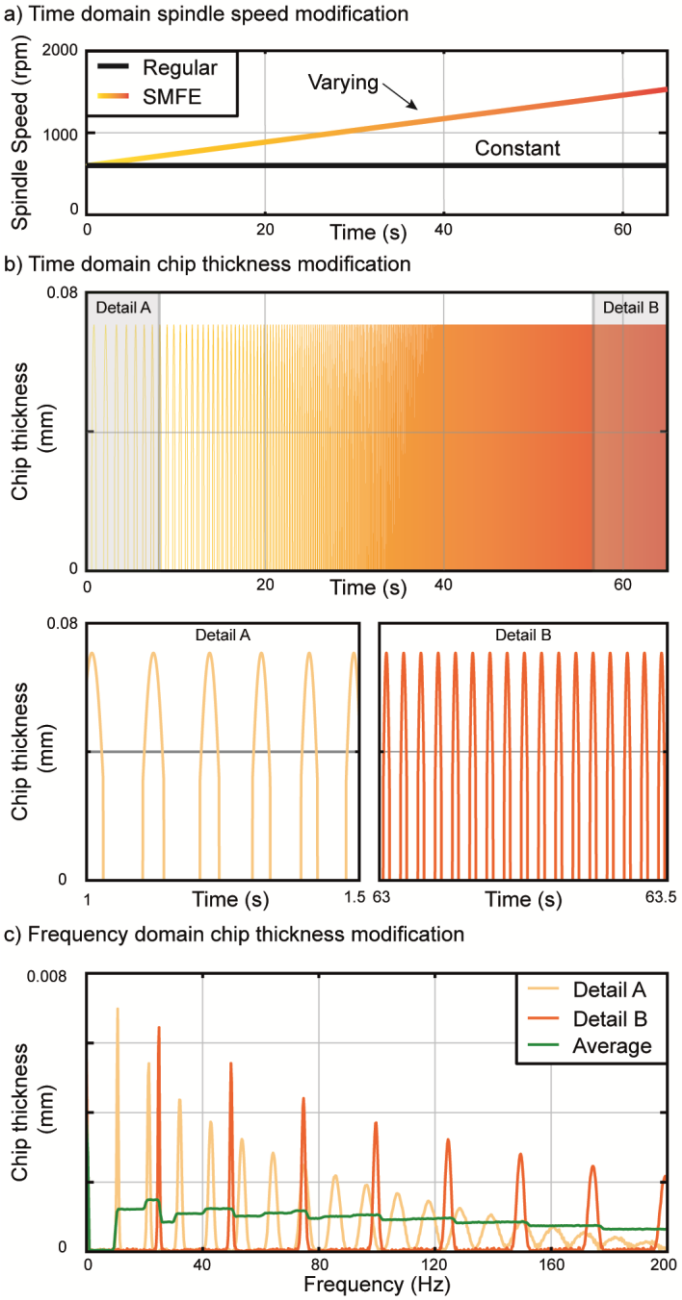

Figure 6.3 a) Spindle speed modification; b) Chip thickness of a single tooth through a simulated SMFE process; c) Chip thickness frequency domain response.

Apart from the spindle speed frequency sweep, the following guidelines should be considered to realize a proper dynamics identification using this operational technique:

Cutting zone selection: the machine dynamics variation between starting and ending positions should be considered. This is particularly important for ram type machines or robots that can have significant dynamics variations in the workspace. Moreover, the

chosen axis movements for the SMFE tests are important to analyse non-linearities related to backlash or friction effects that can be motion dependent.

Workpiece selection: a material with good machinability is necessary to correctly perform the identification cutting tests as the cutting conditions should vary significantly to cover a large frequency range. Additionally, the size of the workpiece will be limited by the size of the employed dynamometric plate.

Cutting tool selection: it is recommended the utilization of a low number of inserts for the identification process (Z = 1 or 2) to generate powerful harmonics and increase the signal to noise ratio. Finally, the tool diameter should be selected accordingly with the size of the workpiece and cutting conditions considering the frequency sweep rate.

6.2.4 Machining system FRF identification by SMFE

The acquired multi-directional responses generated by the multi-directional cutting forces result in a multi-input and multi-output (MIMO) system. Minis et al. [91] proposed a strategy to relate the various spatial force inputs to a single one (e.g. F_x^{t}) creating a set of equations only containing a single autospectrum $S_{Fx,Fx}^{\mathrm{t}}$ and the cross-spectra of the different inputs to the selected single force. The autospectrum is $S_{Fx,Fx}^{\mathrm{t}}(\omega) := \overline{F_x^{\mathrm{t}}(\omega)}\, F_x^{\mathrm{t}}(\omega)$ with $\overline{F_x^{\mathrm{t}}(\omega)}$ the complex conjugate of $F_x^{\mathrm{t}}(\omega)$. The cross-spectra of the different inputs to the selected single force is $S_{K,Fx}(\omega) := \overline{K(\omega)}\, F_x^{\mathrm{t}}(\omega)$ (where $K(\omega)$ is the force or relative displacement in x, y, z directions). The latter definition can describe cross-spectra of responses to the selected single input force as $S_{r,Fx}^{\mathrm{t}}$ ($r = x, y, z$) or the cross-spectra between other force inputs and the selected one $S_{F,Fx}^{\mathrm{t}}$ ($F = F_y, F_z$). These spectrum definitions satisfy the dynamics response related to the tool (t) (Eq. (6.12)). Considering the excitation type, this paper proposes the application of Welch's method [250] for the spectra calculations.

$\mathbf{S}_{r,Fx}^{\mathrm{t}}(\omega) = \mathbf{\Phi}_{\mathrm{tt}}(\omega)\, \boldsymbol{S}_{F,Fx}^{\mathrm{t}}(\omega)$ where

$$\mathbf{S}_{r,Fx}^{\mathrm{t}}(\omega) := \begin{bmatrix} S_{x,Fx}^{\mathrm{t}}(\omega) \\ S_{y,Fx}^{\mathrm{t}}(\omega) \\ S_{z,Fx}^{\mathrm{t}}(\omega) \end{bmatrix} \text{ and } \boldsymbol{S}_{F,Fx}^{\mathrm{t}}(\omega) := \begin{bmatrix} S_{Fx,Fx}^{\mathrm{t}}(\omega) \\ S_{Fy,Fx}^{\mathrm{t}}(\omega) \\ S_{Fz,Fx}^{\mathrm{t}}(\omega) \end{bmatrix}. \tag{6.12}$$

In order to establish a well-posed mathematical system, the following equation (Eq. (6.13)) is obtained by augmenting the expression of Eq. (6.12) by adding the three different cutting strategies (down-milling (DM), up-milling (UM), and central-milling (CM)).

Then, the machining system direct and cross dynamics responses of $\mathbf{\Phi}_{\mathrm{tt}}$ are computed frequency-by-frequency in the following manner:

$$\begin{aligned}&\mathbf{S}^{\mathrm{t}}_{r,Fx}(\omega) = \mathbf{\Phi}_{\mathrm{tt}}(\omega)\, \boldsymbol{S}^{\mathrm{t}}_{F,Fx}(\omega) \text{ where}\\ &\mathbf{S}^{\mathrm{t}}_{r,Fx} \coloneqq [\boldsymbol{S}^{\mathrm{t,DM}}_{r,Fx} \quad \boldsymbol{S}^{\mathrm{t,UM}}_{r,Fx} \quad \boldsymbol{S}^{\mathrm{t,CM}}_{r,Fx}] \text{ and } \mathbf{S}^{\mathrm{t}}_{F,Fx} \coloneqq [\boldsymbol{S}^{\mathrm{t,DM}}_{F,Fx} \quad \boldsymbol{S}^{\mathrm{t,UM}}_{F,Fx} \quad \boldsymbol{S}^{\mathrm{t,CM}}_{F,Fx}] \text{ with}\\ &\mathbf{\Phi}_{\mathrm{tt}}(\omega) = \mathbf{S}^{\mathrm{t}}_{r,Fx}(\omega) \left(\mathbf{S}^{\mathrm{t}}_{F,Fx}(\omega)\right)^{-1}\end{aligned} \tag{6.13}$$

Figure 6.4 summarizes the new alternative approach for the identification of the machine tool dynamics. With respect to the current state of the art approach, the proposed one achieves two major improvements. On one hand, the signal to noise ratio is significantly improved by using the Welch's method for the spectra computations. This is particularly important for the cross terms (such as $\Phi^{\mathrm{tt}}_{xy}(\omega)$), as the amplitude of these responses are usually lower than the direct terms. Additionally, in cases where multiple machine resonances are closed in frequency or even coupled, the minimization of the signal noise is necessary for the identification of the dynamics. On the other hand, as the quality of the identified dynamics are high, just a single set of characterization tests is mandatory. Whereas the state of the art approach, several identification cutting tests are required to improve the signal to noise ratio.

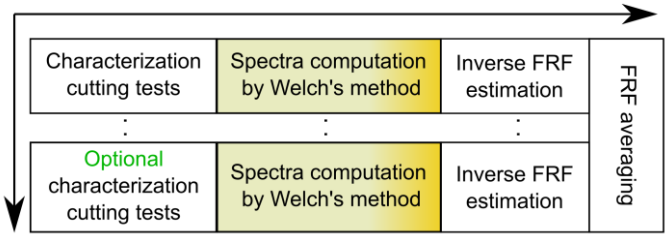

Figure 6.4 Proposed methodology for machining system dynamics identification.

6.2.5 Coherence and quality check

As it can be seen in Eq. (6.13), the determination of the tool dynamics $\mathbf{\Phi}_{\mathrm{tt}}$ is computed using measured cross-spectra related to the response $\mathbf{S}^{\mathrm{t}}_{r,Fx}$ and the input force $\boldsymbol{S}^{\mathrm{t}}_{F,Fx}$. The input force cross-spectra can be predicted preliminarily by suitable process model without performing the actual test. In this sense, it has a great importance to ensure that the inverse of $\boldsymbol{S}^{\mathrm{t}}_{F,Fx}$ exists, frequency-by-frequency, as its determinant should be kept away from zero. If the inverse is considered in Singular Value Decomposition (SVD) manner as a function of the excitation frequency ω, the excitation auto/cross-spectra matrix can be decomposed as:

$$\mathbf{S}^{\mathrm{t}}_{F,Fx}(\omega) := \sum_{k=1}^{3} \nu_k(\omega)\mathbf{u}_k\,(\omega)\mathbf{v}_k^{\mathrm{H}}(\omega) \text{ consequently}$$
$$\left(\mathbf{S}^{\mathrm{t}}_{F,Fx}(\omega)\right)^{-1} = \sum_{k=1}^{3} \frac{1}{\nu_k(\omega)}\mathbf{v}_k\,(\omega)\mathbf{u}_k^{\mathrm{H}}(\omega), \text{ with } \nu_k(\omega) > 0 \tag{6.14}$$

When performing an inverse operation, the condition number of the excitation matrix can be introduced as $C := \nu_{\max}/\nu_{\min}$ ($\nu_{\max}$ and $\nu_{\min}$ being respectively the largest and smallest singular values of $\boldsymbol{S}^{\mathrm{t}}_{F,Fx}$). This condition number is high if the force spectra matrix is numerically hard to invert. Consequently, the selected cutting operations are not suitable for the required dynamic characterization and the overall measurement process is ill-posed. The experimentally obtained condition number (C_{exp}), which depends on the selected cutting tests and on the machine dynamics, gives an indication on the quality of the identification procedure.

The problem conditioning greatly depends on the cutting operations that are selected. Hence, an initial theoretical condition number (C_{th}) is used in Section 6.3 to ensure that the cutting tests are well selected and generate independent excitations. This theoretical condition number is computed from cutting force simulations that do not consider the machine dynamics. This preliminary analysis gives valuable information because a poor value of C_{th} would result in a poor experimental condition number (C_{exp}).

As for conventional FRF diagnostics, an in-process coherence function is introduced in Eq. (6.15) as proposed in [251].

$$\gamma^2_{i,F_i}(\omega) = \frac{\sum_{l=1}^{M}\left(\overline{S^{\mathrm{t}}_{i,F_i}(\omega)}\right)_l\left(S^{\mathrm{t}}_{i,F_i}(\omega)\right)_l}{\sum_{l=1}^{M}\left(S^{\mathrm{t}}_{F_iF_i}(\omega)\right)_l\left(S^{\mathrm{t}}_{i,i}(\omega)\right)_l}, \text{ where } i \in \{x,y,z\} \tag{6.15}$$

The coherence γ^2_{i,F_i} shows the correlation between the excitation and system response for multiple measurement passes or performing calculations on multiple periodograms ($l = 1, 2, \ldots, M$). The coherence amplitude decreases significantly when force (input) and response (output) data are uncorrelated, for example due to high sensor noise or an insufficient forced excitation.

Even though the presented approach is relatively simple and fast to execute, a certain degree of knowledge before performing the identification cutting tests is required to obtain a successful outcome. Next section analyses the effect of the radial engagement value for each cutting operation to ensure a well-posed mathematical problem using the described milling model.

6.3 PARAMETERS OPTIMIZATION FOR THE MACHINE TOOL DYNAMICS IDENTIFICATION PROCESS

In this section, the process parameters are optimized to minimize the theoretical condition number (C_{th}). Then, the full simulation of the Sweep Milling Force Excitation methodology demonstrates the validity of the proposed approach.

6.3.1 Numerical stability analysis

At least two (2D case) or three (3D case) different cutting tests must be performed to solve the linear system (Eq. (6.7)&(6.8)). A low radial engagement a_{e} is desired to have an interrupted cutting process with high energy harmonics to provide a strong excitation. The study presented in this section describes the a_{e} cutting parameter's effect on the numerical conditioning by an iterative time domain simulation (Figure 6.5). For each simulated a_{e} (which varies from 0 to 100% of the tool diameter), the singular values of the force spectrum matrix and its condition number are computed (similar to Eq. (6.14)). Since the harmonics of the stationary cutting force only depends on the spindle speed, it is enough to determine the condition number for a single spindle speed. Moreover, it is important to remark that the machine dynamics are not considered at this point as the optimization focuses on the proper selection of the excitation signals, hence the theoretical condition number C_{th} is calculated. Table 6.1 summarizes the simulation model parameters employed in this section.

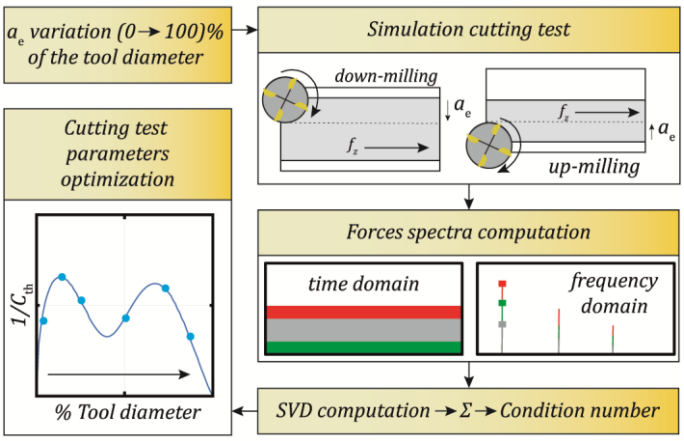

Figure 6.5 Iterative time domain simulation scheme.

Table 6.1: Simulation model parameters.

Cutting tool	
Diameter, D	80 mm
Number of teeth, Z	1
Spindle speed, N	200 rpm
Lead angle, κ	90º
Cutting coefficients	
Specific tangential, K_{tc}	1889 $\mathrm{N/mm^2}$
Specific radial, K_{rc}	806 $\mathrm{N/mm^2}$
Specific axial, K_{ac}	291 $\mathrm{N/mm^2}$
Edge tangential, K_{te}	63 $\mathrm{N/mm}$
Edge radial, K_{re}	114 $\mathrm{N/mm}$
Edge axial, K_{ae}	-3 $\mathrm{N/mm}$

Figure 6.6 summarizes the obtained numerical conditioning results for different combinations of cutting operations. The results indicated in Figure 6.6-a-c are for the particular case of using the same type of cutting operation twice for the identification of a two-dimensional system. In the diagonal the same forces are generated; hence, the illustrated inverse of the condition number is minimal (which gives poorer matrix conditioning) as the set of equations is not independent. Similarly, this study shows that the experimental identification is numerically viable and could be conducted by repeating the same cutting operation with different radial engagements.

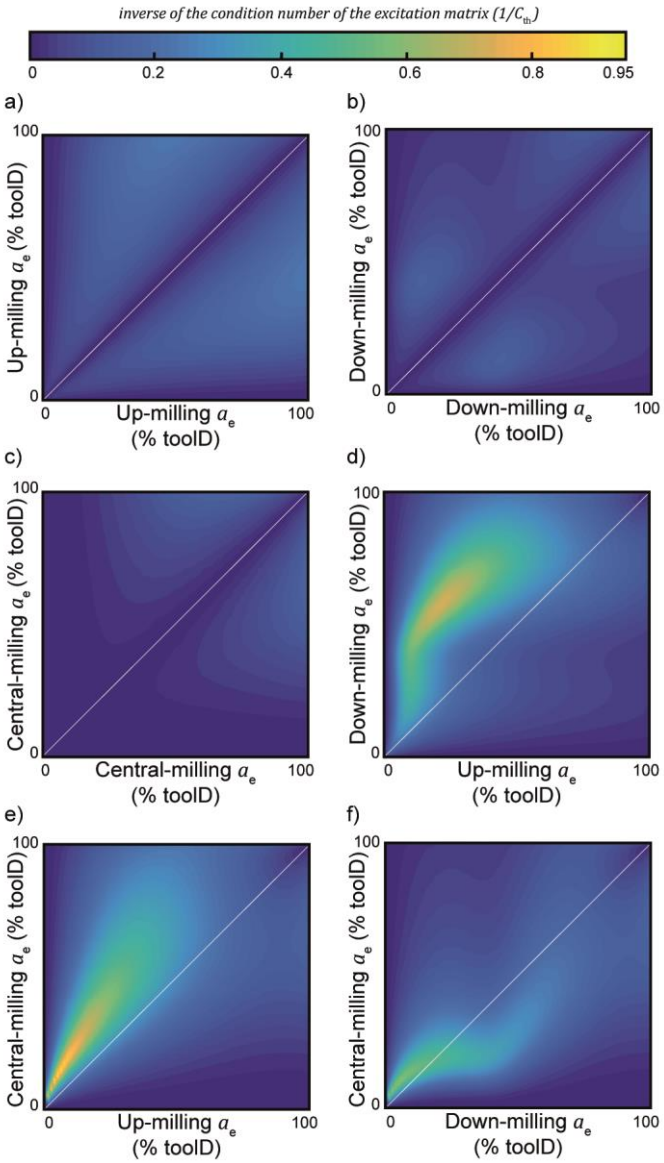

Figure 6.6 Identification cutting tests condition number by a-c) repeating; d-f) combining the cutting operations.

To improve the numerical conditioning, a combination of different cutting operations is preferred (Figure 6.6-d-f). Even though the global optimum for the characterization is not located on the diagonal, it is preferable to keep the same radial engagement for both cutting tests to generate equivalent identification force amplitudes. Indeed, the possible non-linearities inherent to the machining system can perturb the measurements if the excitation force varies significantly. Thus, similar excitation amplitudes are recommended to analyse the behaviour of the identified system with respect to the excitation level. Therefore, in the rest of the paper, the dynamic system identification will be conducted with equal radial engagements in all cutting tests.

Considering the need to have equal engagement values an analysis is carried out to localize the optimal radial engagement value. Following the iterative process presented in Figure 6.5, Figure 6.7-a shows the condition number analysis considering up- and down-milling cutting operations for a 2D case with a tool lead angle of 90º. Similarly, Figure 6.7-b shows the result for a full 3D case where three cutting operations are needed with a tool lead angle of 45º to excite x, y and z directions. For both cases, a similar pattern can be seen for a single or two teeth cutter. At extremely low a_e values (less than 5% of the tool diameter), the inverse of the condition number is low. However, the trend improves for the range between 5 to 30% of the tool diameter. Therefore, the experimental dynamic identification should be conducted within these bounds. In addition, a local optimum condition is presented at 12 and 16% of tool diameter respectively. This analysis concludes that not only low radial engagement values are necessary for creating powerful harmonic content but also to ensure a well-conditioned system that leads to appropriate results. In addition, Figure 6.7-b indicates three different cutting conditions (variation of Z and a_e) that have been used to show the effect of the condition number in the identified system dynamics.

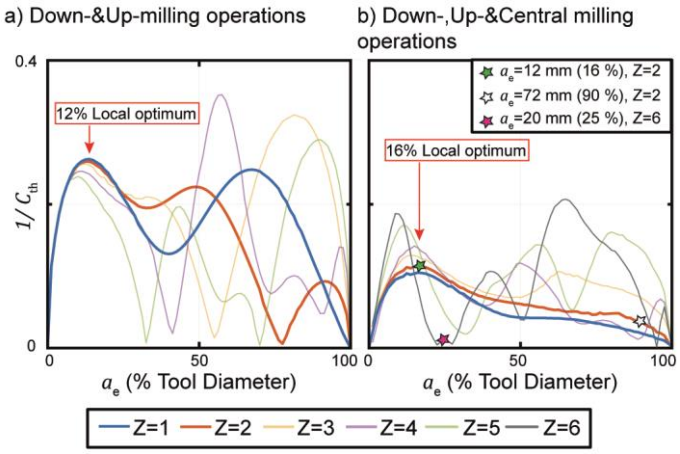

Figure 6.7 Numerical stability analysis for a) 2D; b) 3D cases.

To generalize this identification methodology and simplify its future deployment, some analytical expressions have been obtained. Note, that for these equations, a simplification has been made by not considering the edge force cutting coefficients that has a secondary impact. Hence, just by knowing the cutting force ratio ($K_r = K_{rc}/K_{tc}$) and the number of teeth of the selected tool, the optimal radial engagement value can be computed. The performed numerical simulations have been approximated by rational polynomials. Note that, as in the previous cases, only the 1st harmonic has been considered to compute the condition number associated with the excitation.

Figure 6.8-a shows the evolution of the optimal radial engagement with respect to the selected number of teeth and cutting force ratios for the case where both down- and up-milling operations have equal radial engagements. For the recommended number of inserts, the maximum radial engagement is between 12% and 35% of the selected tool diameter depending on the cutting force ratio. Additionally, the approximated analytical expression for the case of two inserts in provided in Eq.(6.16).

As previously shown in Figure 6.6, there is a global optimum location, which might not be located at the diagonal, where the numerical conditioning achieves its maximum value. Figure 6.8-b shows the evolution of this global optimum position determined by the different radial engagement values for up- and down-milling operations for Z = 1 and 2. For this case, as the cutting force ratio increases, both radial engagements values diverge. As in previous case, Eq. (6.17) provides an approximated analytical expression for the two insert case.

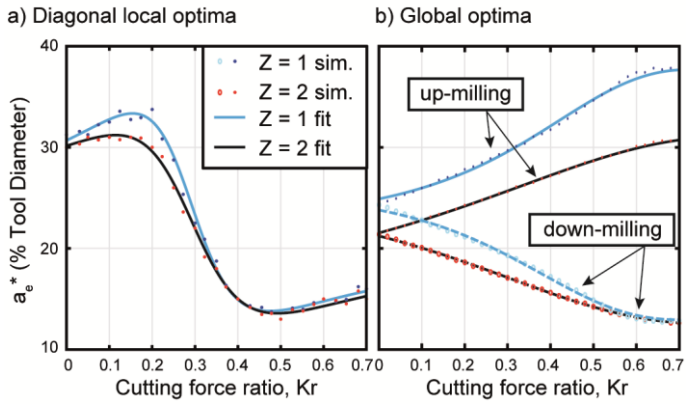

Figure 6.8 Optimal a_e considering cutting force ratio and number of teeth a) diagonal local optima; b) global optimum case.

$$\left(a_e^{*\mathrm{UM\&DM}}\right)_{Z=2} = \frac{21.65{K_\mathrm{r}}^2 - 15.75K_\mathrm{r} + 3.557}{{K_\mathrm{r}}^2 - 0.5749 + 0.118} \tag{6.16}$$

$$\left(a_e^{*\mathrm{UM}}, a_e^{*\mathrm{DM}}\right)_{Z=2} = \left(\frac{14.24{K_\mathrm{r}}^2 - 17.26K_\mathrm{r} + 25.25}{{K_\mathrm{r}}^2 - 1.439K_\mathrm{r} + 1.173}, \frac{23.81{K_\mathrm{r}}^2 - 30.67K_\mathrm{r} + 16.58}{{K_\mathrm{r}}^2 - 1.049K_\mathrm{r} + 0.7809}\right) \tag{6.17}$$

Finally, the optimum cutting tests are selected and the steps described in Section 6.2.4 -0 can be followed to obtain the system receptance and its associated measurement quality.

6.3.2 Simulation of the Sweep Milling Force Excitation

Once the optimal radial engagement has been identified, this section combines both Sweep Milling Frequency Excitation and a milling simulation model to virtually define the set of cutting conditions used for later experimental dynamic identification. In addition, to close the gap between simulation and real workshop environments, a statistical modelling of the accelerometer sensor noise has been included. Note that this sensor noise is acquired in machine idle conditions with no spindle rotation.

Figure 6.9-a shows an experimental time domain data set recorded for each cartesian axis at the machine ram. All the random information of a variable is contained in its Probability Density Function (PDF), as shown in Figure 6.9-b. For this case, the PDF follows a Gaussian normal distribution ($p = \mathcal{N}(m_x, v_x^2)$) that can be defined by the mean (m_x) and variance (v_x^2) parameters (Eq. (6.18)) for the particular case of x direction). Synthetic accelerometer noise can be added on top of the ideal noise-free data from the simulation environment.

$$p(x) = \frac{1}{\sqrt{2\pi}v_x} exp\left(-\frac{(x-m_x)^2}{2v_x^2}\right) \tag{6.18}$$

Similarly, machine tool dynamics need to be included in the simulation model to perform the identification and validation of the mathematical development described in Section 6.2. Table 6.2 shows the defined machine dynamic parameters, in which a variety of natural frequencies have been selected. In addition, a very small cross projection has been added to challenge the identification process, as the cross terms can extensively modify the process stability predictions. Usually, the cross terms of the dynamics response have a much lower amplitude than the direct terms, meaning that the signal to noise ratio is lower and hence the quality of the prediction can be poorer.

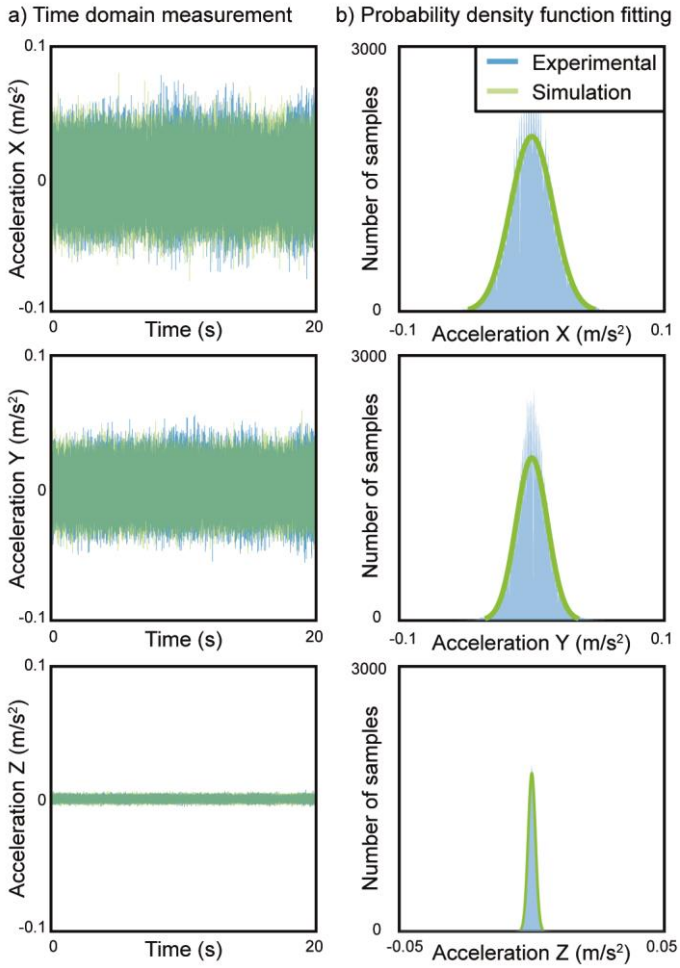

Figure 6.9 Probability Density Function fitting of experimental accelerometer data.

Table 6.2: Tool and machine dynamic parameters definition for the simulation model

Cutting tool			
Diameter, D	80 mm		
Number of teeth, Z	2		
Spindle speed, N	600-1500 rpm		
Lead angle, κ	45º		
Dynamic Parameters			
i	1	2	3
$f_{n,i}$ (Hz)	33.4	57.4	58.6
ζ_i (%)	6.1	8.2	2.9
k_i $(N/\mu m)$	45.5	32.1	36.7
Orientation	(-0.05, 0.62, 0.77)	(0.02, 0.99, -0.02)	(0.99, 0, 0.01)

Figure 6.10 shows the simulated results of tool vibration for the three cutting operations on the left side. By applying the spindle speed variation shown in Figure 6.3-a, amplitude variations can be observed due to the existence of resonance excitations. Similarly, the forces obtained throughout the characterization process are shown on the right side of Figure 6.10. It can be seen how the force amplitude varies, as a result of the existing vibration which modifies the chip thickness.

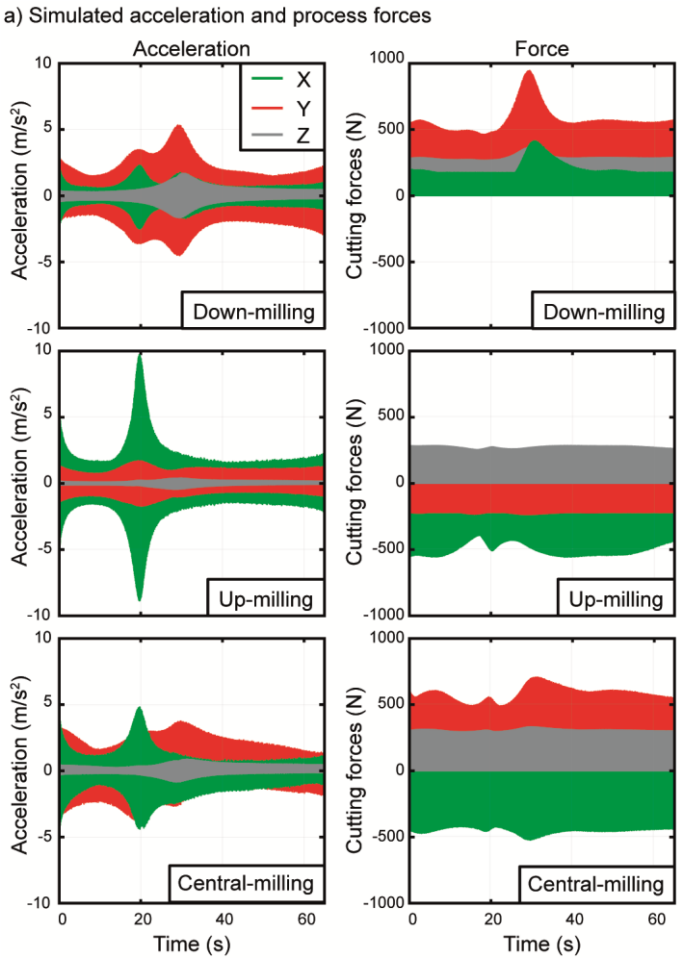

Figure 6.10 Simulated time domain acceleration and cutting forces for a_e = 12 mm.

Once the time domain data is obtained, the steps described in Section 6.2 can be followed for the system dynamics identification. Figure 6.11 shows two different cases (non-optimal and optimal a_e) on top of the analytical response. It can be observed that for direct compliances, which have higher amplitudes, both proposed values can correctly identify the system dynamics. However, for the cross responses (i.e., Φ_{xz}^{tt}), where the amplitude is considerably smaller, the quality of the estimated response has decreased as a result of the poor conditioning (Figure 6.11-b). In fact, significant prediction error can be seen at one of the main modes at 58 Hz. For machines that have

more complex dynamics, the mere fact of having external disturbances can change the response significantly.

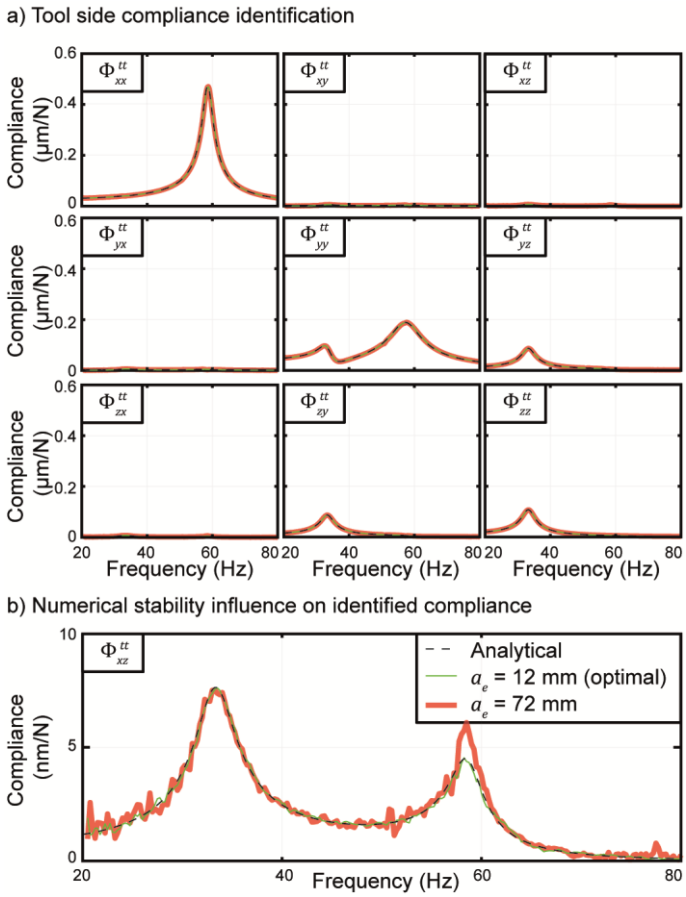

Figure 6.11 Tool side identification validation.

After the theoretical demonstration and validation of the proposed guidelines, the sweep milling dynamics identification method is applied to measure the dynamics of an industrial machine tool.

6.4 EXPERIMENTAL IMPLEMENTATION ON A RAM-TYPE MILLING MACHINE

This section shows the experimental implementation of the proposed methodology and analyses the differences between the classical impact hammer measurements and the Sweep Milling Force Excitation results.

6.4.1 Experimental setup description and characterization

The proposed characterization technique has been tested on a ram-type milling machine controlled by a Siemens 840D Powerline CNC shown in Figure 6.12-a. The workpiece

made of F-1140 C45E steel is attached to a Kistler dynamometric plate (9255B) which records the forces $\mathbf{F}(t) = \mathbf{F}_{\mathrm{t}}(t) = -\mathbf{F}_{\mathrm{w}}(t)$ during the identification process. Six single axis industrial accelerometers (IMI 602D01) acquire the time domain vibration response from the workpiece $\ddot{\mathbf{r}}_{\mathrm{w}}(t)$ and the tool $\ddot{\mathbf{r}}_{\mathrm{t}}(t)$. Since the limiting factor for roughing operations is related to low-frequency structural modes and that the sensor cannot be located on the rotating tool, the accelerometers are placed as close as possible to the cutting point on the spindle. With this, the obtained dynamic responses can be used for further analysis such as chatter stability lobes computation.

The selected tool for the full dynamics identification process is an 80 mm diameter tool from Sandvik (R245-080Q27-12M) with 2 inserts (R245-12 T3 M-PM 4230) and a lead angle of κ = 45º. Three independent cutting operations are required to solve the nine FRFs as explained previously (Figure 6.12-b). To perform the experimental sweep milling test, the spindle speed varies from 300 to 1500 rpm in 65 s and the feedrate override is continuously modified during the cutting test (300 to 60 mm/min) to keep a constant feed per tooth (0.1 mm/Z). With a Siemens 840D CNC, this modification is implemented using the $AA_OVR synchronous action [252]. The sweep milling test has also been performed on a Heidenhain TNC640 CNC but a modification of the PLC by the machine tool builder is required. Figure 6.12-c shows x direction force spectrogram during the central-milling characterization cutting test. The feed is oriented in x direction for the identification tests as the machine dynamics is not affected by the x axis position. Moreover, the chatter stability verifications are also performed in that direction to use the machine in the same operating conditions.

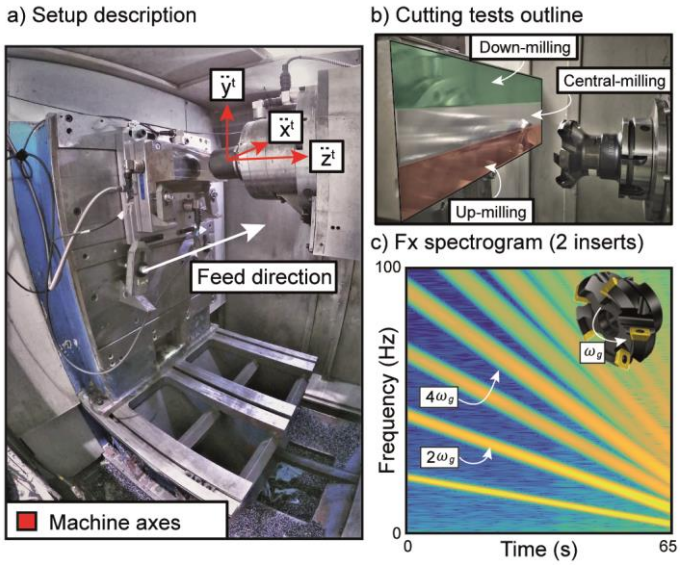

Figure 6.12 a) Experimental setup description; b) Cutting test outline; c) F_x spectrogram.

6.4.2 Characterized machining system dynamics analysis

Figure 6.13 shows the obtained experimental dynamics of the machining system. To be used as a reference, the response measured with an impact hammer is added to the figure. In addition, to analyse the influence of the excitation force on the identified dynamics, three different depth of cuts are proposed (a_{p} = 1, 2 and 3 mm).

Generally speaking, the overall quality of the responses are good and closely resembles the response obtained with the hammer, in spite of the dynamic complexity of the tested machine. Focusing on the tool side response (Figure 6.13-a), it can be seen that just by applying 1 mm of depth of cut, the principal mode around 60 Hz in Φ_{xx}^{tt} increases its damping by 26% (going from 2.3% to 2.9% of damping ratio) with respect to the hammer response, as indicated in Table 6.3. By increasing the characterization force by a factor of two and three (a_{p} = 2 and 3 mm) it can be observed that the identified damping ratios converge to 3.2%. This effect could be explained by the machine tool joints contact interaction, as once a certain force level is reached the response remains relatively constant.

Analysing the workpiece side (Figure 6.13-b), and comparing it to the tool side, it has higher dynamic stiffness overall. Hence, the process stability limitation source comes from the tool side. However, checking the most flexible response (Φ_{xx}^{ww}), a 50% damping decrement in the main mode around 60 Hz (decreasing the damping ratio from 5.3% to 2.7%) can be observed with respect to the hammer response. In addition, increasing the excitation force does not generate a change in the identified damping ratios.

Table 6.3: Identified damping ratios of the mode at 60Hz for x-direction using different approaches.

Identification approach	Tool side (%)	Workpiece side (%)
Impact hammer	2.3	5.3
SMFE 1mm	2.9	2.7
SMFE 2mm	3.2	2.7
SMFE 3mm	3.2	2.7

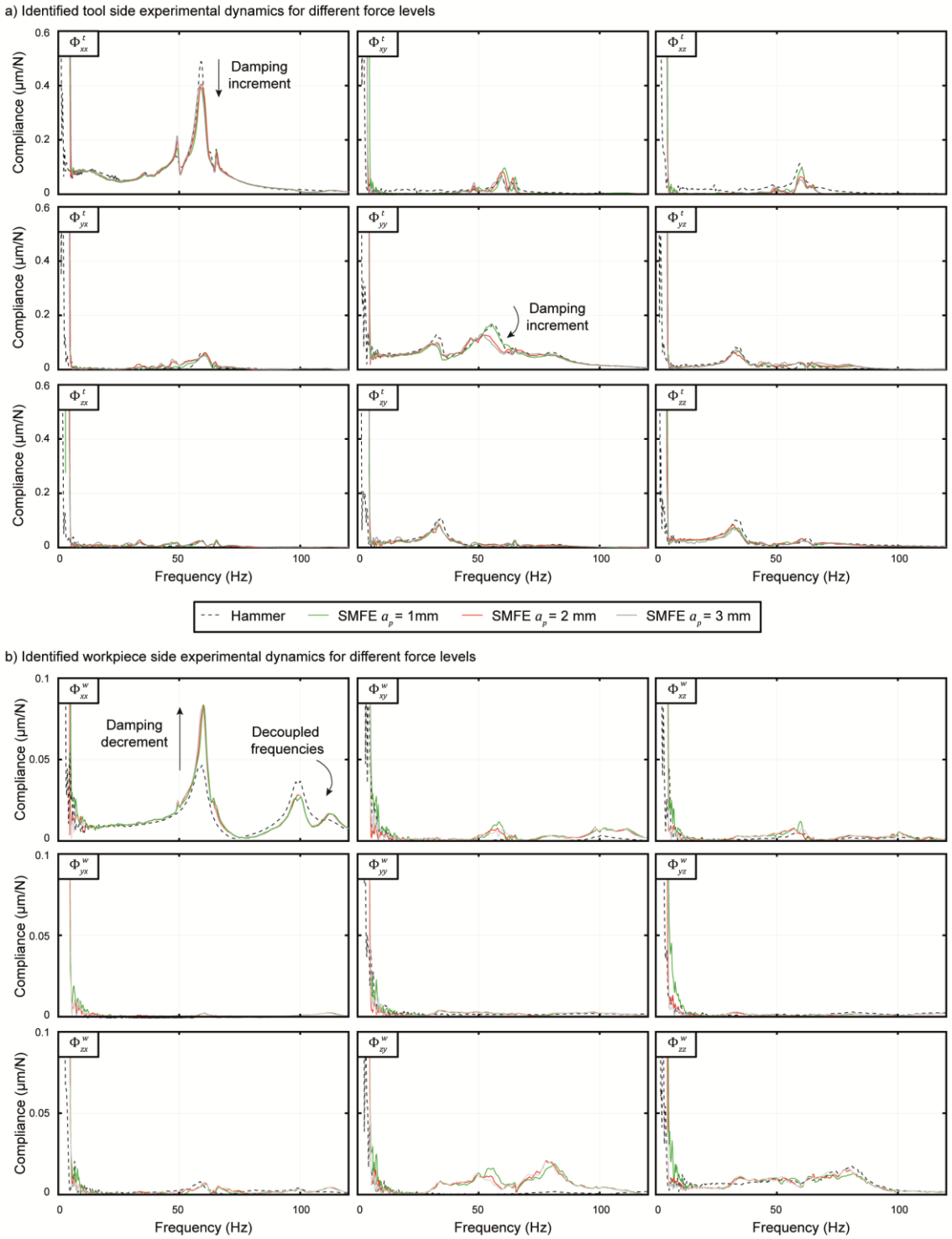

Figure 6.13 Tool side and workpiece side experimental dynamic characterization result.

Figure 6.14 shows the coherence indicator obtained for Φ_{xx}^{tt} and Φ_{yy}^{tt}. As in the previous case, the coherence obtained through impact hammer tests is shown to be used as a reference. The existence of three different coherences, one for each milling operation, during the SMFE process shows the difficulties faced for each operation during the

identification process. For example, the up-milling operation achieves a good coherence in Φ_{xx}^{tt}, but not as good in Φ_{yy}^{tt} especially at 63 Hz. For both FRFs, when there is an antiresonance or a zero, the coherence indicator decreases. At low frequencies, the measurement is valid starting from the frequency at which the excitation starts (5 Hz).

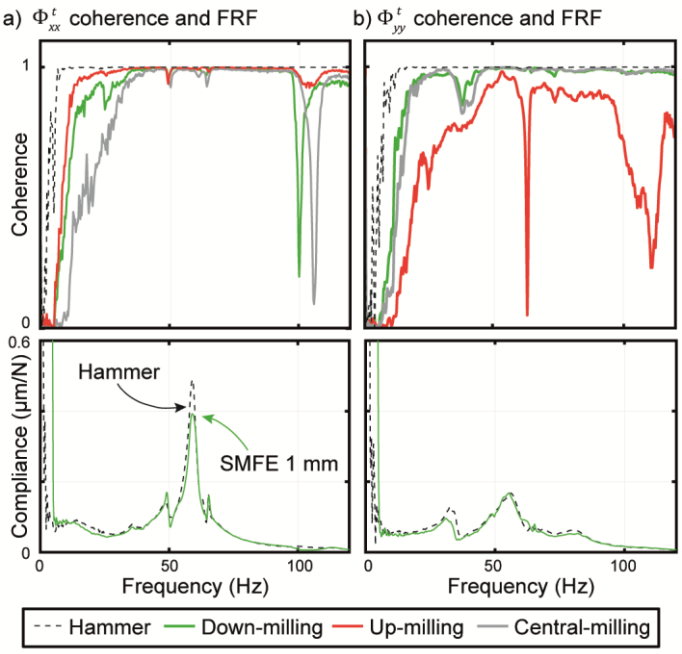

Figure 6.14 Coherence sample.

Figure 6.15-a shows the experimental influence of the condition number in the tool side characterization, where two identification conditions have been compared. On one hand, two teeth and a radial engagement of 12 mm (a_{e} local optima) is used. On the other hand, six teeth and an engagement of 20 mm (25% a_{e}), where the excitation condition number is high (see Figure 6.7). As a result of the badly conditioned system, the identified responses are noisy and of poor quality. The computed coherence response for Φ_{yy}^{tt} is shown in Figure 6.15-b, where a lower coherence value is achieved especially in the low-frequency range (20 to 50 Hz). However, focusing on the frequency of the main resonance, the coherence indicator shows a value close to one, but the obtained dynamics significantly differ from the expected ones. This experimentally shows the effect of a well-conditioned set of cutting tests, for that reason, the condition number (C_{exp}) of the inversely identified dynamics should be also checked (Figure 6.15-c).

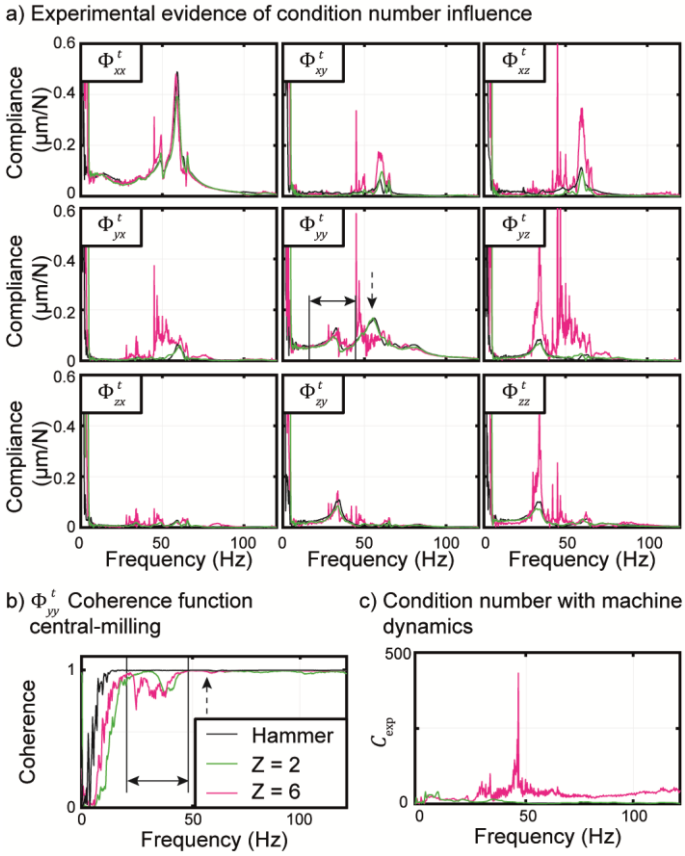

Figure 6.15 Condition number influence in experimental tool side dynamics characterization.

Finally, Figure 6.16 shows a comparison of the measurement quality between the current state of the art and the proposed approach. As commented earlier, the obtained improvement in the signal to noise ratio is essential to clearly identify the dynamics of the cross terms i.e. Φ_{xy}^{tt}.

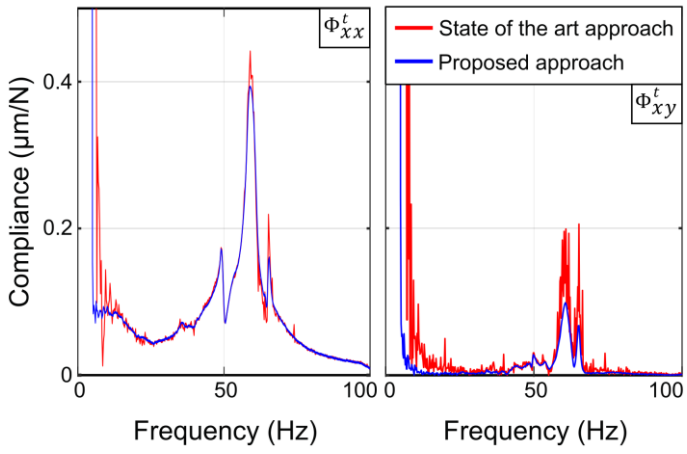

Figure 6.16 Machine tool dynamic identification with state of the art and proposed approaches comparison.

6.4.3 Machining system dynamics validation through experimental chatter stability tests

By using the direct and cross-measured FRFs, the machining system resultant compliance **Φ** is computed and employed to obtain the theoretical chatter stability lobes following the approach proposed by Altintas et al. [11] (Eq. (6.11)). Here, the classical Zeroth Order Approximation stability model is used considering that the measured frequency responses are a secant type of linearisation around the operating condition. The cutting process parameters for chatter stability tests are summarized in Table 6.4.

Table 6.4: Cutting process parameters for chatter stability tests.

Cutting tool	
Reference	WALTER F4042 B16.040.Z04.15
Diameter, D	40 mm
Number of teeth, Z	4
Inserts reference	WKP35S ADMT160608R-F56
Lead angle, κ	90º
Cutting conditions	
Feed per tooth, f_Z	0.4 mm/Z
Radial engagement, a_e	32 mm (down-milling)
Cutting coefficients	
Specific tangential, K_tc	1885 $\mathrm{N/mm^2}$
Specific radial, K_rc	749 $\mathrm{N/mm^2}$
Specific axial, K_ac	-370 $\mathrm{N/mm^2}$

Figure 6.17-a shows the theoretical and experimental comparison of the stability lobes. Important differences can be observed between the predictions obtained from the impact hammer and the method proposed in this paper (especially the responses characterized with a depth of cut a_p= 2 and 3 mm). The minimum stability limit increases from 1.6 to 2.4 mm. The experimental cutting tests at 1500 rpm demonstrate that the real stability limit is 50% higher than what is predicted from the hammer tests (see Detail A in Figure 6.17-b). Similarly, it is relevant to highlight the difference at higher speeds (> 1500 rpm), where the predictions made using the FRFs obtained with the impact hammer always underestimate the experimental stability limit. Detail B in Figure 6.17-b shows that the experimental stability is 66% higher than expected from the impact hammer test. In the absence of a significant change in the identified FRF frequencies, the chatter frequencies

can be accurately predicted with both characterization methods. However, with the proposed technique a slight improvement can be obtained. With these tests, the proposed machining system identification process is validated.

Analysing the stability predictions obtained by the proposed operational methodology, it is important to notice that slight changes in the measured FRF can generate significant differences in the stability limit predictions. This is especially remarkable comparing the stability limit predicted using a depth of cut of 1 mm with 2 and 3 mm during the SMFE characterization. Those differences highlight the importance of taking into account the nonlinearities in the frequency response measurements and subsequent stability limit predictions.

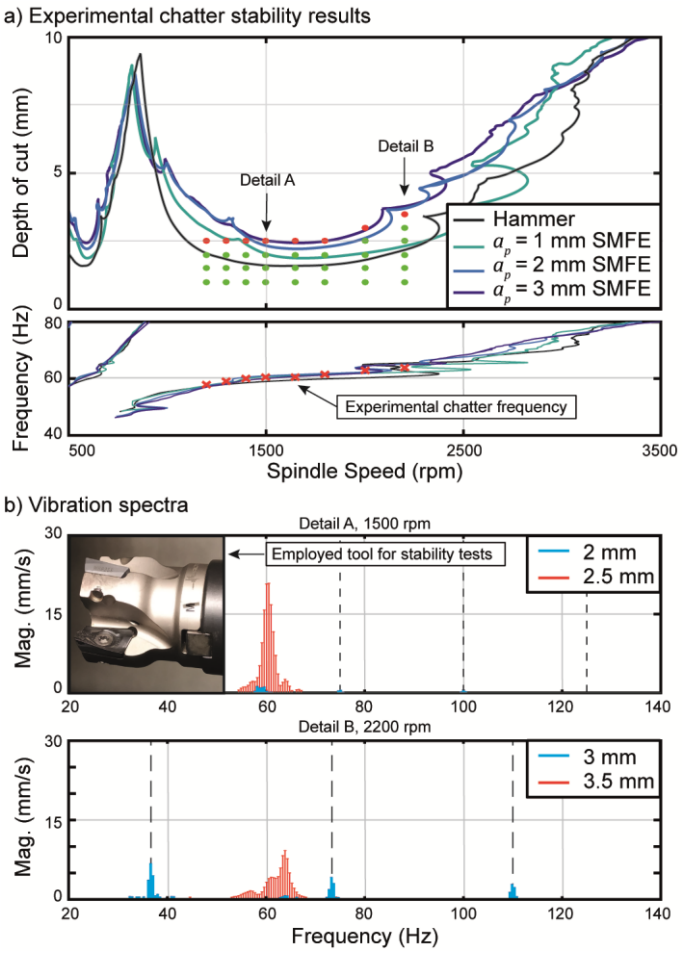

Figure 6.17 a) Experimental chatter stability results; b) Vibration spectra.

6.5 CONCLUSIONS

This chapter has presented a new technique for machining system dynamics identification under operational conditions. The three-axis process forces are acquired

by a dynamometric plate and the tool and workpiece responses are measured with accelerometers. Time domain simulations allow for optimization of the cutting parameters to ensure a well-conditioned set of experiments. Approximated analytical expressions to compute the optimal radial engagement values for a two dimensional problem have been provided. The proposed methodology has been validated through simulations and experimental tests in a ram-type milling machine. Different force excitation levels have been applied to analyse existing nonlinearities in both tool and workpiece sides. Variations in damping have been observed (+26% and -43% with respect to the hammer identified dynamics), while small changes have been measured in the natural frequency values. The condition number influence in experimental tests has been demonstrated. Dynamic compliances have been experimentally validated through chatter stability tests, where discrepancies between the experimental and predicted stability can be explained.

Chapter 7

Conclusions and further work

7.1 CONCLUSIONS

The productivity of the milling manufacturing process is limited by the apparition of self-excited vibrations, also known as chatter. Despite the academic effort conducted in recent years in understanding and modeling this effect, there are still many unknown factors and conditions that play a role in its onset. In applications involving large machine tools, the critical resonance is usually associated to the complete machine structure which can generate a relative motion at the machine joints. This thesis has presented a comprehensive study of the interaction between the feed drive elements and the structural behaviour of the driven machine. The four main scientific contributions are as follows:

Contribution 1: the effect of the master-slave control parameters on the machine tool's static and dynamic behavior is presented in Chapter 3. When applying static disturbances at the cutting point, the pinion flank contact transition is not fast enough to be neglected. Therefore, the preload level can be tuned to handle the load forces

generated during the cutting process ensuring a preloaded system. Additionally, the dynamic analysis concluded that the derived frequency based MIMO model can predict the experimental behaviors. By performing the model identification from the cutting point and the feed drive side, the interaction between the servo feedback system and the machine tool dynamics is described.

Contribution 2: a new strategy for the feed drive controller tuning considering machine dynamics and chatter stability has been introduced in Chapter 4. The tool tip compliance is minimized and the vibration mode giving rise to machine structural chatter vibrations is damped. This results in a higher chatter stability, and therefore an increased productivity as demonstrated experimentally. The proposed strategy can successfully handle complex machine tool dynamics. A new MIMO frequency domain estimation and analysis method is introduced for accurately predicting the influence of the servo dynamics on the tool tip compliance. In addition, an efficient and accurate model identification method is introduced. The proposed strategy is the first of its kind which makes comprehensive use of the root locus method to analyse the influence of multiple vibration modes in machine tool feed drive controller design. The proposed approach has been successfully implemented on the industry standard P-PI position-velocity cascade control structure. In experiments, the new strategy has achieved up to 44% damping increase on an industrial machine tool, and 33% increase in machining productivity by avoiding chatter.

Contribution 3: the influence of friction on the nonlinear tool centre point dynamics is described in Chapter 5. Measurements conducted in several industrial machines demonstrate that it is a common effect present in different machine tool configurations and feed drive systems. By using a two-mass model, the interaction of the structural dynamics, feed drive controller, friction characteristics and motion commands is clearly explained. Another important conclusion is that the effect of the feed drive controller can be mostly seen while the axis moves. A detailed analysis in a ram-type machining centre demonstrates the main results. The excitation force and axis feed related nonlinearities have been studied concluding that the latter one had greater impact on the dynamics. When in-motion FRFs are considered, the chatter stability predictions can be considerably improved compared to idle responses which faced prediction errors up to 240% in depth of cut and 8% in frequency.

Contribution 4: a new technique for identifying the machining system dynamics under operational conditions has been proposed in Chapter 6. The cutting process forces and the structural response of both tool and workpiece sides are synchronously acquired. With this, the gap between in-process and characterization conditions is closed, capturing nonlinear effects that can barely be extracted with traditional methods. Additionally, the influence of the tool radial engagement on the conditioning of the excitation matrix has been studied. Simulated and experimentally observed results prove the importance of selecting adequate cutting parameters during the identification. In order to generalize the proposed approach and aid its future deployment, analytical expressions for a 2D system have been provided. The end result is an improvement of the predicted chatter stability lobes with respect to traditional impact hammer approach. Experimental deviations of 50% in the absolute stability limit and up to 66% in higher spindle speeds have been faced.

As summarized above, this thesis has studied the influence of rack and pinion motion transmission, feed drive controller tuning, and guideway friction on the tool centre point structural compliance in large-scale machine tools. It is important to recognize that in addition to accounting for these factors, the source of parametric and dynamic uncertainty needs to be considered in a broader generalization of this work. The operational identification and measurement method proposed as Contribution 4 would be a good candidate to support future studies which aim to gauge the influence of such uncertainties.

7.2 FURTHER WORK

Based on the results and experience gained through this thesis, the following new research tasks are proposed below.

Future work related to double pinion and rack feed drive system:

- A virtual mechatronic model that combines the presented rack and pinion model of this thesis and the complex machine tool structure coming from Finite Element modeling could be created. This model could be used to optimize the drive selection and the machine tool design. The identification of the characteristic frequencies of the double pinion and rack feed drive system is an interesting outcome that can be used during the machine tool design stage.

- Implications of commanding a low electronical preload on tracking or following errors and its effect on the machined workpiece can be studied. More generally, the preload level selection and the preload controller tuning are still open research topics.

- The lumped mass and stiffness approach developed in this thesis has been successfully applied to a double pinion and rack feed drive system, as an alternate method two pinions can be preloaded against one another with a spring and connected to a single motor, referred to as an 'anti-backlash gear'. The methodology of Chapter 3 can be extended to this case as well.

Future work related to machine tool feed drive servo commissioning:

- The control tuning methodology introduced in Chapter 4 has been tested on a linear drive, where a single encoder is used by the feedback system. However, for ball screw and double pinion and rack feed drive systems, it is common to use two different encoders for closing the different loops. Hence, the equations developed in the thesis should be extended to include the intermediate dynamics between the two encoders.

- With the identified transmission dynamics between the feedback encoder system and cutting point, in combination with the accurately identified velocity and position bode plots, tracking and contour error simulations can be conducted. Hence, the control tuning could consider both the chatter stability and accuracy requirements with a holistic machine model.

- As machining chatter appearance can be avoided by selecting an adequate servo controller, it is appealing to develop an easy-to-use control tuning procedure that can be used by large machine tool manufacturers during the heavy-duty roughing operation. This procedure should combine bode plot analyses with tool tip dynamic compliance measurements.

Future work related to the influence of friction on the machine tool dynamics:

- The addition of friction characteristics to complex machine dynamics through a development of a virtual machine tool is proposed. With this, the fundamental study conducted in this thesis can be generalized to more complex machine tool structures.

- Friction and servo control loop effects could be considered with adequate hypotheses and simplifications to improve machine tool modelling within commercial Finite Element simulation software. This could be used for predicting the idle and invariant in-motion tool tip compliance during the design stage.

- The utilization of the root locus technique could provide additional knowledge of the effect of feed motion on the structural dynamics. This technique can clarify both damping and frequency variations of the critical resonances.

- It would be interesting to analyse if active damping controllers tunned in idle conditions would perform well for in-motion machine conditions. New tuning routines that consider the dynamics variations should be developed - this is especially important when model based controllers are employed.

- Knowing the influence of the friction and control parameters on the tool tip dynamics, the machine tool design could be optimized to maximize the damping provided by the feed drives for the most problematic structural mode shapes. Moreover, the guiding system technological choices could be revised having in mind the detrimental influence of the friction on the idle machine dynamics.

- Chatter stability simulations considering the nonlinear influence of friction could be realized. Including control and friction effects in the simulation, the stability limit prediction accuracy should improve. Moreover, the cutting feed direction could be optimized to benefit from the improved in-motion dynamics of the machine.

Future work related to in-process machining system dynamic characterization:

- The milling cutting forces can be accurately predicted by time domain simulations. It is proposed to replace the expensive dynamometric plate for measuring the experimental milling forces with synthetic simulated data. Following an iterative resolution, it might be possible to identify the unknown system dynamics.

7.3 PUBLIC DISSEMINATION OF RESEARCH RESULTS

Science Citation Index (SCI) Journals:

I. Mancisidor, A. Pena-Sevillano, R. Barcena, O. Franco, J. Munoa, L.N. Lopez De Lacalle. (2019). Comparison of model free control strategies for chatter suppression by an inertial actuator. International Journal of Mechatronics and Manufacturing Systems, 12(3-4), 164-179.

O. Franco, X. Beudaert, K. Erkorkmaz. (2020). Effect of rack and pinion feed drive control parameters on machine tool dynamics. Journal of Manufacturing and Materials Processing, 4(2), 33.

X. Beudaert, O. Franco, K. Erkorkmaz, M. Zatarain. (2020). Feed drive control tuning considering machine dynamics and chatter stability. CIRP Annals, 69(1), 345-348.

A. Iglesias, L.T. Tunc, O. Özsahin, O. Franco, J. Munoa, E. Budak. (2021). Alternative methods for machine tool dynamics identification: a review. Mechanical Systems and Signal Processing. *Under review.*

O. Franco, X. Beudaert, K. Erkorkmaz, J. Munoa. (2021). Influence of friction on the nonlinear dynamics of machine tools. Mechanical Systems and Signal Processing. *Under review.*

O. Franco, X. Beudaert, A. Iglesias, Z. Dombovari, K. Erkorkmaz, J. Munoa. (2021). Operational machining system dynamics identification by Sweep Milling Force Excitation. International Journal of Machine Tools and Manufacture. *Under review.*

International Conferences:

O. Franco, X. Beudaert, K. Erkorkmaz, A. Barrios, J. Munoa. (2019). Machining chatter stability limit improvement by means of feed drive control parameters. 8th International Conference on Virtual Machining Process Technology (VMPT), Vancouver, Canada, April 23-25.

O. Franco, X. Beudaert, K. Erkorkmaz, J. Munoa. (2021). Static stiffness analysis of an electronically preloaded rack and pinion feed drive system. 16th International Conference on High Speed Machining, Darmstadt, Germany, October 26-27.

Chapter 8

References

[1] L. Uriarte, M. Zatarain, D. Axinte, J. Yagüe-Fabra, S. Ihlenfeldt, J. Eguia, A. Olarra, Machine tools for large parts, CIRP Ann. - Manuf. Technol. 62 (2013) 731–750. https://doi.org/10.1016/j.cirp.2013.05.009.

[2] J. Munoa, X. Beudaert, Z. Dombovari, Y. Altintas, E. Budak, C. Brecher, G. Stepan, Chatter suppression techniques in metal cutting, CIRP Ann. - Manuf. Technol. 65 (2016) 785–808.

[3] F.W. Taylor, The Art of Cutting Metals, Sci. Am. 63 (1907) 25942–25944. https://doi.org/10.1038/scientificamerican01121907-25942supp.

[4] S.A. Tobias, W. Fishwick, Theory of regenerative machine tool chatter, Eng. 205 (1958) 199–203.

[5] J. Tlusty, M. Polacek, Beispiele der behandlung der selbsterregten Schwingung der Werkzeugmaschinen FoKoMa, (1957).

[6] J. Tlusty, The stability of the machine tool against self-excited vibration in machining, Proc. Int. Res. Prod. Eng. Pittsburgh, ASME. 465 (1963).

[7] M. WIERCIGROCH, E. BUDAK, Sources of nonlinearities, chatter generation and

suppression in metal cutting, Philos. Trans. R. Soc. London. Ser. A Math. Phys. Eng. Sci. 359 (2001) 663–396.

[8] G. Quintana, J. Ciurana, Chatter in machining processes: A review, Int. J. Mach. Tools Manuf. 51 (2011) 363–376.

[9] H.E. Merrit, Theory of self excited-tool chatter: Research 1, ASME J. Eng. Ind. 87 (1965) 447–454.

[10] J. Tlusty, F. Ismail, Special Aspects of Chatter in Milling., Am. Soc. Mech. Eng. (1981).

[11] Y. Altintaş, E. Budak, Analytical prediction of stability lobes in milling, CIRP Ann. 44 (1995) 357–362.

[12] R. Sridhar, R.E. Hohn, G.W. Long, A stability algorithm for the general milling process: contribution to machine tool chatter research 7, J. Manuf. Sci. Eng. Trans. ASME. 90 (1968) 317–324. https://doi.org/10.1115/1.3604635.

[13] I. Minis, R. Yanushevsky, A new theoretical approach for the prediction of machine tool chatter in Milling, J. Manuf. Sci. Eng. Trans. ASME. 115 (1993) 1–8. https://doi.org/10.1115/1.2901633.

[14] E. Budak, Mechanics and Dynamics of Milling Thin Walled Structures, Diss. Univ. Br. Columbia. (1994) 284.

[15] M.A. Davies, J.R. Pratt, B.S. Dutterer, T.J. Burns, Stability of low radial immersion milling, CIRP Ann. - Manuf. Technol. 49 (2000) 37–40. https://doi.org/10.1016/S0007-8506(07)62891-1.

[16] T. Insperger, G. Stépán, P. V. Bayly, B.P. Mann, Multiple chatter frequencies in milling processes, J. Sound Vib. 262 (2003) 333–345. https://doi.org/10.1016/S0022-460X(02)01131-8.

[17] E. Budak, Y. Altintaş, Analytical prediction of chatter stability in milling—part I: General formulation, J. Dyn. Syst. Meas. Control. Trans. ASME. 120 (1998) 22–30. https://doi.org/10.1115/1.2801317.

[18] T. Insperger, G. Stépán, Stability of the milling process, Period. Polytech. Mech. Eng. 44 (2000) 47–57.

[19] T. Insperger, G. Stépán, Semi-discretization method for delayed systems, Int. J. Numer. Methods Eng. 55 (2002) 503–518. https://doi.org/10.1002/nme.505.

[20] T. Insperger, Full-discretization and semi-discretization for milling stability prediction: Some comments, Int. J. Mach. Tools Manuf. 50 (2010) 658–662. https://doi.org/10.1016/j.ijmachtools.2010.03.010.

[21] G. Urbikain, L.N. López De Lacalle, F.J. Campa, A. Fernández, A. Elías, Stability

prediction in straight turning of a flexible workpiece by collocation method, Int. J. Mach. Tools Manuf. 54–55 (2012) 73–81. https://doi.org/10.1016/j.ijmachtools.2011.11.008.

[22] F.A. Khasawneh, B.P. Mann, A spectral element approach for the stability analysis of time-periodic delay equations with multiple delays, Commun. Nonlinear Sci. Numer. Simul. 18 (2013) 2129–2141. https://doi.org/10.1016/j.cnsns.2012.11.030.

[23] Y. Altintas, M. Weck, Chatter stability of metal cutting and grinding, CIRP Ann. - Manuf. Technol. 53 (2004) 619–642. https://doi.org/10.1016/S0007-8506(07)60032-8.

[24] C. Brecher, M. Esser, S. Witt, Simulation of the process stability of HPC milling operations, Mach. Sci. Technol. 13 (2009) 20–35.

[25] P. Rasper, O. Rott, D. Hömberg, E. Uhlmann, Analysis of Uncertainties in the Stability Prediction for Milling Processes, in: CIRP 2nd Int. Conf. Process Mach. Interact., 2010: p. 2010.

[26] H.S. Kim, T.L. Schmitz, Bivariate uncertainty analysis for impact testing, Meas. Sci. Technol. 18 (2007) 3565–3571. https://doi.org/10.1088/0957-0233/18/11/041.

[27] I. Trendafilova, V. Lenaerts, G. Kerschen, J.C. Golinval, H. Van Brussel, W. Heylen, Detection, localisation and identification of nonlinearities in structural dynamics, in: Proc. 25th Int. Conf. Noise Vib. Eng. ISMA, KU Leuven; 1998, 2000: pp. 453–460.

[28] K. De Moerlooze, F. Al-Bender, H. Van Brussel, Modeling of the dynamic behavior of systems with rolling elements, Int. J. Non. Linear. Mech. 46 (2011) 222–233. https://doi.org/10.1016/j.ijnonlinmec.2010.09.003.

[29] I. Trendafilova, H. Van Brussel, Non-linear dynamics tools for the motion analysis and condition monitoring of robot joints, Mech. Syst. Signal Process. 15 (2001) 1141–1164. https://doi.org/10.1006/mssp.2000.1394.

[30] W.G. Halvorsen, D.L. Brown, Impulse technique for structural frequency response testing, S V Sound Vib. 11 (1977) 8–21. https://doi.org/10.1121/1.2016847.

[31] J. Munoa, M. Zatarain, I. Bediaga, Determination of the cutting performance and dynamic behaviour of universal milling machines by means of a stability model, in: Proc. ISMA2006 Int. Conf. Noise Vib. Eng., 2006: pp. 3789–3803.

[32] C. Rebelein, J. Vlacil, M.F. Zaeh, Modeling of the dynamic behavior of machine tools: influences of damping, friction, control and motion, Prod. Eng. 11 (2017)

61–74. https://doi.org/10.1007/s11740-016-0704-5.

[33] T.L. Schmitz, Predicting high-speed machining dynamics by substructure analysis, CIRP Ann. - Manuf. Technol. 49 (2000) 303–308. https://doi.org/10.1016/S0007-8506(07)62951-5.

[34] A. Yadav, D. Talaviya, A. Bansal, M. Law, Design of chatter-resistant damped boring bars using a receptance coupling approach, J. Manuf. Mater. Process. 4 (2020) 53. https://doi.org/10.3390/jmmp4020053.

[35] E. Budak, L.T. Tunç, S. Alan, H.N. Özgüven, Prediction of workpiece dynamics and its effects on chatter stability in milling, CIRP Ann. - Manuf. Technol. 61 (2012) 339–342. https://doi.org/10.1016/j.cirp.2012.03.144.

[36] O.B. Adetoro, P.H. Wen, W.M. Sim, A new damping modelling approach and its application in thin wall machining, Int. J. Adv. Manuf. Technol. 51 (2010) 453–466. https://doi.org/10.1007/s00170-010-2658-7.

[37] W. Ma, J. Yu, Y. Yang, Y. Wang, Optimization and tuning of passive tuned mass damper embedded in milling tool for chatter mitigation, J. Manuf. Mater. Process. 5 (2021) 2. https://doi.org/10.3390/jmmp5010002.

[38] Z. Dombovari, J. Munoa, R. Kuske, G. Stepan, Milling stability for slowly varying parameters, Procedia CIRP. 77 (2018) 110–113. https://doi.org/10.1016/j.procir.2018.08.233.

[39] C. Brecher, H. Altstädter, M. Daniels, Axis position dependent dynamics of multi-axis milling machines, Procedia CIRP. 31 (2015) 508–514. https://doi.org/10.1016/j.procir.2015.03.068.

[40] I. Mancisidor, X. Beudaert, G. Aguirre, R. Barcena, J. Munoa, Development of an active damping system for structural chatter suppression in machining centers, Int. J. Autom. Technol. 12 (2018) 642–649. https://doi.org/10.20965/ijat.2018.p0642.

[41] R. Sagherian, M.A. Elbestawi, A simulation system for improving machining accuracy in milling, Comput. Ind. 14 (1990) 293–305. https://doi.org/10.1016/0166-3615(90)90037-P.

[42] S. Köksal, M.D. Cömert, H.N. Özgüven, Reanalysis of dynamic structures using Successive Matrix Inversion method, in: Conf. Proc. Soc. Exp. Mech. Ser., 2006.

[43] X.M. Zhang, L.M. Zhu, H. Ding, Matrix perturbation method for predicting dynamic modal shapes of the workpiece in high-speed machining, Proc. Inst. Mech. Eng. Part B J. Eng. Manuf. 224 (2010) 177–183. https://doi.org/10.1243/09544054JEM1588SC.

[44] D. Biermann, P. Kersting, T. Surmann, A general approach to simulating workpiece vibrations during five-axis milling of turbine blades, CIRP Ann. - Manuf. Technol. 59 (2010) 125–128. https://doi.org/10.1016/j.cirp.2010.03.057.

[45] P.T. Pedersen, On forward and backward precession of rotors, Ingenieur-Archiv. 42 (1972) 26–41. https://doi.org/10.1007/BF00533283.

[46] J. Tian, S.G. Hutton, Chatter instability in milling systems with flexible rotating spindles-a new theoretical approach, J. Manuf. Sci. Eng. Trans. ASME. 123 (2001) 1–9. https://doi.org/10.1115/1.1285760.

[47] G.L. Xiong, J.M. Yi, C. Zeng, H.K. Guo, L.X. Li, Study of the gyroscopic effect of the spindle on the stability characteristics of the milling system, J. Mater. Process. Technol. 138 (2003) 379–384. https://doi.org/10.1016/S0924-0136(03)00102-X.

[48] M.R. Movahhedy, P. Mosaddegh, Prediction of chatter in high speed milling including gyroscopic effects, Int. J. Mach. Tools Manuf. 46 (2006) 996–1001. https://doi.org/10.1016/j.ijmachtools.2005.07.043.

[49] H. Cao, B. Li, Z. He, Chatter stability of milling with speed-varying dynamics of spindles, Int. J. Mach. Tools Manuf. 52 (2012) 50–58. https://doi.org/10.1016/j.ijmachtools.2011.09.004.

[50] B. Bediz, B. Arda Gozen, E. Korkmaz, O. Burak Ozdoganlar, Dynamics of ultra-high-speed (UHS) spindles used for micromachining, Int. J. Mach. Tools Manuf. 87 (2014) 27–38. https://doi.org/10.1016/j.ijmachtools.2014.07.007.

[51] J. Munoa, I. Etxaniz, M. Zatarain, I. Iturbe, L. Uriarte, Chatter suppression in a high speed magnetic spindle by adding damping, J. Mach. Eng. 14 (2014) 65–74.

[52] O. Özşahin, H.N. Özgüven, E. Budak, Analytical modeling of asymmetric multi-segment rotor - Bearing systems with Timoshenko beam model including gyroscopic moments, Comput. Struct. 144 (2014) 119–126. https://doi.org/10.1016/j.compstruc.2014.08.001.

[53] E. Ozturk, U. Kumar, S. Turner, T. Schmitz, Investigation of spindle bearing preload on dynamics and stability limit in milling, CIRP Ann. - Manuf. Technol. 61 (2012) 343–346. https://doi.org/10.1016/j.cirp.2012.03.134.

[54] C.W. Lin, J.F. Tu, J. Kamman, An integrated thermo-mechanical-dynamic model to characterize motorized machine tool spindles during very high speed rotation, Int. J. Mach. Tools Manuf. 43 (2003) 1035–1050. https://doi.org/10.1016/S0890-6955(03)00091-9.

[55] J.S. Chen, Y.W. Hwang, Centrifugal force induced dynamics of a motorized high-speed spindle, Int. J. Adv. Manuf. Technol. 30 (2006) 10–19.

https://doi.org/10.1007/s00170-005-0032-y.

[56] H. Cao, T. Holkup, Y. Altintas, A comparative study on the dynamics of high speed spindles with respect to different preload mechanisms, Int. J. Adv. Manuf. Technol. 57 (2011) 871–883. https://doi.org/10.1007/s00170-011-3356-9.

[57] M. Postel, N.B. Bugdayci, J. Monnin, F. Kuster, K. Wegener, Improved stability predictions in milling through more realistic load conditions, Procedia CIRP. 77 (2018) 102–105. https://doi.org/10.1016/j.procir.2018.08.231.

[58] E. Abele, U. Fiedler, Creating stability lobe diagrams during milling, CIRP Ann. - Manuf. Technol. 53 (2004) 309–312. https://doi.org/10.1016/S0007-8506(07)60704-5.

[59] R. Florina, C. TUDOSE, L. TUDOSE, A NEW PROOF OF RULE OF THUMB REGARDING CLEARANCE VARIATION WITH TEMPERATURE IN TWO TAPERED ROLLER BEARINGS IN O-ARRANGEMENT, ACTA Tech. NAPOCENSIS-Series Appl. Math. Mech. Eng. 56 (2013).

[60] H. Li, Y.C. Shin, Analysis of bearing configuration effects on high speed spindles using an integrated dynamic thermo-mechanical spindle model, Int. J. Mach. Tools Manuf. 44 (2004) 347–364. https://doi.org/10.1016/j.ijmachtools.2003.10.011.

[61] Y. Altintas, C. Brecher, M. Week, S. Witt, Virtual Machine Tool, CIRP Ann. - Manuf. Technol. 54 (2005) 115–138. https://doi.org/10.1016/s0007-8506(07)60022-5.

[62] M. Wiesauer, C. Habersohn, F. Bleicher, Validation of a Coupled Simulation for Machine Tool Dynamics Using a Linear Drive Actuator, J. Manuf. Mater. Process. 5 (2020) 1.

[63] X. Beudaert, I. Mancisidor, L. Miguel, A. Barrios, K. Erkorkmaz, J. Munoa, Analysis of the feed drives control parameters on structural chatter vibrations, Int. Conf. HIGH SPEED Mach. (2016). https://hal.archives-ouvertes.fr/hal-01484796/.

[64] J. Grau, M. Sulitka, P. Soucek, Influence of linear feed drive controller setting in cnc turning lathe on the stability of machining, J. Mach. Eng. 19 (2019) 18–31. https://doi.org/10.5604/01.3001.0013.2221.

[65] O. Franco, X. Beudaert, K. Erkorkmaz, Effect of rack and pinion feed drive control parameters on machine tool dynamics, J. Manuf. Mater. Process. 4 (2020).

[66] G.P. Zhang, Y.M. Huang, W.H. Shi, W.P. Fu, Predicting dynamic behaviours of a whole machine tool structure based on computer-aided engineering, Int. J. Mach. Tools Manuf. 43 (2003) 699–706.

[67] R.A. Ibrahim, C.L. Pettit, Uncertainties and dynamic problems of bolted joints and other fasteners, J. Sound Vib. 279 (2005) 857–936.

[68] L.T. Tunc, B. Gonul, Effect of quasi-static motion on the dynamics and stability of robotic milling, CIRP Ann. (2021). https://doi.org/10.1016/j.cirp.2021.04.077.

[69] A. Ertürk, H.N. Özgüven, E. Budak, Effect analysis of bearing and interface dynamics on tool point FRF for chatter stability in machine tools by using a new analytical model for spindle-tool assemblies, Int. J. Mach. Tools Manuf. 47 (2007) 23–32. https://doi.org/10.1016/j.ijmachtools.2006.03.001.

[70] D.M. Shamine, Y.C. Shin, Analysis of No. 50 taper joint stiffness under axial and radial loading, J. Manuf. Process. 2 (2000) 167–173. https://doi.org/10.1016/S1526-6125(00)70118-6.

[71] M. Namazi, Y. Altintas, T. Abe, N. Rajapakse, Modeling and identification of tool holder-spindle interface dynamics, Int. J. Mach. Tools Manuf. 47 (2007) 1333–1341. https://doi.org/10.1016/j.ijmachtools.2006.08.003.

[72] T. Aoyama, I. Inasaki, Performances of HSK tool interfaces under high rotational speed, CIRP Ann. - Manuf. Technol. 50 (2001) 281–284. https://doi.org/10.1016/S0007-8506(07)62122-2.

[73] S.A. Jensen, Y.C. Shin, Stability analysis in face milling operations, part 1: Theory of stability lobe prediction, J. Manuf. Sci. Eng. Trans. ASME. 121 (1999) 600–605. https://doi.org/10.1115/1.2833075.

[74] I. Zaghbani, V. Songmene, Estimation of machine-tool dynamic parameters during machining operation through operational modal analysis, Int. J. Mach. Tools Manuf. 49 (2009) 947–957. https://doi.org/10.1016/j.ijmachtools.2009.06.010.

[75] Y. Altintas, M. Eynian, H. Onozuka, Identification of dynamic cutting force coefficients and chatter stability with process damping, CIRP Ann. - Manuf. Technol. 57 (2008) 371–374. https://doi.org/10.1016/j.cirp.2008.03.048.

[76] M. Eynian, Y. Altintas, Chatter stability of general turning operations with process damping, J. Manuf. Sci. Eng. Trans. ASME. 131 (2009) 0410051–04100510. https://doi.org/10.1115/1.3159047.

[77] J. Tlusty, Analysis of the State of Research in Cutting Dynamics., Ann CIRP. 27 (1978) 583–589.

[78] F. Ismail, E. Soliman, A new method for the identification of stability lobes in machining, Int. J. Mach. Tools Manuf. 37 (1997) 763–774.

[79] G. Quintana, J. Ciurana, D. Teixidor, A new experimental methodology for identification of stability lobes diagram in milling operations, Int. J. Mach. Tools

Manuf. 48 (2008) 1637–1645.

[80] N. Grossi, A. Scippa, L. Sallese, R. Sato, G. Campatelli, Spindle speed ramp-up test: A novel experimental approach for chatter stability detection, Int. J. Mach. Tools Manuf. 89 (2015) 221–230.

[81] P. Kruth, J, A.M.M. Liu, P. Vanherck, B. Lauwers, A strategy for selection of optimal cutting parameter in high-speed milling to avoid chatter vibration, Int. J. Prod. Eng. Comput. 4 (2002) 35–42.

[82] N. Grossi, L. Sallese, A. Scippa, G. Campatelli, Improved experimental-analytical approach to compute speed-varying tool-tip FRF, Precis. Eng. 48 (2017) 114–122.

[83] M. Postel, O. Özsahin, Y. Altintas, High speed tooltip FRF predictions of arbitrary tool-holder combinations based on operational spindle identification, Int. J. Mach. Tools Manuf. 129 (2018) 48–60.

[84] N. Suzuki, Y. Kurata, R. Hino, E. Shamoto, Identification of transfer function of mechanical structure by inverse analysis of regenerative chatter vibration in end milling, in: Proc. 3rd Int. CIRP High Perform. Cut. Conf., 2008.

[85] Z.M. Kilic, A. Iglesias, J. Munoa, Y. Altintas, Investigation of tool wear on the stability of milling process using an inverse method, in: CIRP 2nd Int. Conf. Process Mach. Interact. Vancouver, Canada, 2010.

[86] O. Özşahin, E. Budak, H.N. Özgüven, In-process tool point FRF identification under operational conditions using inverse stability solution, Int. J. Mach. Tools Manuf. 89 (2015) 64–73.

[87] M. Eynian, In-process identification of modal parameters using dimensionless relationships in milling chatter, Int. J. Mach. Tools Manuf. 143 (2019) 49–62.

[88] E. Budak, L.T. Tunc, Identification and modeling of process damping in turning and milling using a new approach, J. Manuf. Sci. Eng. Trans. ASME. 135 (2013) 403–408. https://doi.org/10.1115/1.4023708.

[89] L.T. Tunc, E. Budak, Identification and modeling of process damping in milling, J. Manuf. Sci. Eng. Trans. ASME. 135 (2013). https://doi.org/10.1115/1.4023708.

[90] H. Opitz, M. Weck, Determination of the transfer function by means of spectral density measurements and its application to the dynamic investigation of machine tools under machining conditions, in: Adv. Mach. Tool Des. Res. 1969, Elsevier, 1970: pp. 349–378.

[91] I.E. Minis, E.B. Magrab, I.O. Pandelidis, Improved methods for the prediction of chatter in turning, Part 1: Determination of structural response parameters, J.

Manuf. Sci. Eng. Trans. ASME. 112 (1990) 12–20.

[92] X. Liu, K. Cheng, D. Webb, Prediction and simulation on the machining dynamics and instability in peripheral milling, in: ASPE Annu. Meet., 2002: pp. 581–584.

[93] O. Özşahin, E. Budak, H.N. Özgüven, Investigating dynamics of machine tool spindles under operational conditions, Adv. Mater. Res. 223 (2011) 610–621.

[94] B. Li, B. Luo, X. Mao, H. Cai, F. Peng, H. Liu, A new approach to identifying the dynamic behavior of CNC machine tools with respect to different worktable feed speeds, Int. J. Mach. Tools Manuf. 72 (2013) 73–84. https://doi.org/10.1016/j.ijmachtools.2013.06.004.

[95] H. Cai, B. Luo, X. Mao, L. Gui, B. Song, B. Li, F. Peng, A method for identification of machine-tool dynamics under machining, Procedia CIRP. 31 (2015) 502–507. https://doi.org/10.1016/j.procir.2015.03.027.

[96] A. Iglesias, J. Munoa, C. Ramírez, J. Ciurana, Z. Dombovari, FRF Estimation through Sweep Milling Force Excitation (SMFE), Procedia CIRP. 46 (2016) 504–507.

[97] K. Takasugi, T. Fukuda, R. Kito, N. Asakawa, Y. Morimoto, Fast swept sine cutting test for CNC lathes, J. Adv. Mech. Des. Syst. Manuf. 14 (2020) 1–9.

[98] Y. Altintas, A. Verl, C. Brecher, L. Uriarte, G. Pritschow, Machine tool feed drives, CIRP Ann. - Manuf. Technol. 60 (2011) 779–796. https://doi.org/10.1016/j.cirp.2011.05.010.

[99] F. Koenigsberger, J. Tlusty, Machine tool structures, (1970).

[100] G.P. Zhang, Y.M. Huang, W.H. Shi, W.P. Fu, Predicting dynamic behaviours of a whole machine tool structure based on computer-aided engineering, Int. J. Mach. Tools Manuf. 43 (2003) 699–706. https://doi.org/10.1016/S0890-6955(03)00026-9.

[101] B. Armstrong-Hélouvry, P. Dupont, C.C. De Wit, A survey of models, analysis tools and compensation methods for the control of machines with friction, Automatica. 30 (1994) 1083–1138.

[102] R. Stribeck, Kugellager für beliebige Belastungen, Buchdruckerei AW Schade, Berlin N., 1901.

[103] F. Marques, P. Flores, J.C.P. Claro, H.M. Lankarani, Modeling and analysis of friction including rolling effects in multibody dynamics: a review, Multibody Syst. Dyn. 45 (2019) 223–244. https://doi.org/10.1007/s11044-018-09640-6.

[104] F.P. Bowden, L. Leben, Nature of sliding and the analysis of friction [12], Nature. 141 (1938) 691–692. https://doi.org/10.1038/141691b0.

[105] V.I. Johannes, M.A. Green, C.A. Brockley, The role of the rate of application of the tangential force in determining the static friction coefficient, Wear. 24 (1973) 381–385. https://doi.org/10.1016/0043-1648(73)90166-X.

[106] C. Canudas-de-Wit, Comments on “a new model for control of systems with friction,” IEEE Trans. Automat. Contr. 43 (1998) 1189–1190. https://doi.org/10.1109/9.704999.

[107] F. Al-Bender, V. Lampaert, J. Swevers, The generalized Maxwell-slip model: A novel model for friction simulation and compensation, IEEE Trans. Automat. Contr. 50 (2005) 1883–1887. https://doi.org/10.1109/TAC.2005.858676.

[108] L.A. Hagman, Measurement and modelling of microslip for engineering surfaces in contact, (1997).

[109] S. Andersson, A. Söderberg, S. Björklund, Friction models for sliding dry, boundary and mixed lubricated contacts, Tribol. Int. 40 (2007) 580–587. https://doi.org/10.1016/j.triboint.2005.11.014.

[110] P. Brown, J. McPhee, A Continuous Velocity-Based Friction Model for Dynamics and Control with Physically Meaningful Parameters, J. Comput. Nonlinear Dyn. 11 (2016). https://doi.org/10.1115/1.4033658.

[111] T. Specker, M. Buchholz, K. Dietmayer, A new approach of dynamic friction modelling for simulation and observation, IFAC Proc. Vol. 19 (2014) 4523–4528. https://doi.org/10.3182/20140824-6-za-1003.01711.

[112] H. Dankowicz, On the modeling of dynamic friction phenomena, ZAMM Zeitschrift Fur Angew. Math. Und Mech. 79 (1999) 399–409. https://doi.org/10.1002/(SICI)1521-4001(199906)79:6<399::AID-ZAMM399>3.0.CO;2-K.

[113] A. Dumanli, B. Sencer, Pre-compensation of servo tracking errors through data-based reference trajectory modification, CIRP Ann. 68 (2019) 397–400. https://doi.org/10.1016/j.cirp.2019.03.017.

[114] T. Miura, A. Matsubara, I. Yamaji, K. Hoshide, Measurement and analysis of friction fluctuations in linear guideways, CIRP Ann. 67 (2018) 393–396. https://doi.org/10.1016/j.cirp.2018.04.010.

[115] G. Bianchi, S. Cagna, N. Cau, F. Paolucci, Analysis of vibration damping in machine tools, Procedia CIRP. 21 (2014) 367–372. https://doi.org/10.1016/j.procir.2014.03.158.

[116] C. Rebelein, M.F. Zaeh, Friction in feed drives of machine tools: investigation, modeling and validation, Prod. Eng. 10 (2016) 497–507.

https://doi.org/10.1007/s11740-016-0678-3.

[117] M.F. Zaeh, C. Rebelein, T. Semm, Predictive simulation of damping effects in machine tools, CIRP Ann. 68 (2019) 393–396. https://doi.org/10.1016/j.cirp.2019.03.018.

[118] C. Kossack, J. Ziegert, T. Schmitz, The sliding friction contact frequency response function, Procedia Manuf. 34 (2019) 73–82. https://doi.org/10.1016/j.promfg.2019.06.119.

[119] N. Irino, Y. Imabeppu, Y. Higuchi, Y. Shinba, K. Kawai, N. Suzuki, J. Kaneko, Y. Kakinuma, M. Mori, Vibration analysis and cutting simulation of structural nonlinearity for machine tool, CIRP Ann. (2021). https://doi.org/10.1016/j.cirp.2021.04.073.

[120] R. Sato, S. Noguchi, T. Hokazono, I. Nishida, K. Shirase, Time domain coupled simulation of machine tool dynamics and cutting forces considering the influences of nonlinear friction characteristics and process damping, Precis. Eng. 61 (2020) 103–109. https://doi.org/10.1016/j.precisioneng.2019.10.010.

[121] I. Oshita, A. Matsubara, T. Sumida, Evaluation of dynamic characteristics of a hybrid guideway system, Int. J. Autom. Technol. 14 (2020) 274–279. https://doi.org/10.20965/ijat.2020.p0274.

[122] H. Gross, G. Stute, Elektrische Vorschubantriebe für Werkzeugmaschinen, Siemens Aktienges., 1981.

[123] Y. Koren, C.C. Lo, Advanced Controllers for Feed Drives, CIRP Ann. - Manuf. Technol. 41 (1992) 689–698. https://doi.org/10.1016/S0007-8506(07)63255-7.

[124] M.R. Khoshdarregi, S. Tappe, Y. Altintas, Integrated five-axis trajectory shaping and contour error compensation for high-speed CNC machine tools, IEEE/ASME Trans. Mechatronics. 19 (2014) 1859–1871. https://doi.org/10.1109/TMECH.2014.2307473.

[125] K. Erkorkmaz, Y. Altintas, High speed CNC system design. Part I: Jerk limited trajectory generation and quintic spline interpolation, Int. J. Mach. Tools Manuf. 41 (2001) 1323–1345. https://doi.org/10.1016/S0890-6955(01)00002-5.

[126] O. Zirn, Machine Tool Analysis – Modelling , Simulation and Control of Machine Tool Manipulators, Control. (2008).

[127] P. Albertelli, N. Cau, G. Bianchi, M. Monno, The effects of dynamic interaction between machine tool subsystems on cutting process stability, Int. J. Adv. Manuf. Technol. 58 (2012) 923–932. https://doi.org/10.1007/s00170-011-3465-5.

[128] L. Uriarte, M. Zatarain, D. Axinte, J. Yagüe-Fabra, S. Ihlenfeldt, J. Eguia, A. Olarra,

Machine tools for large parts, CIRP Ann. - Manuf. Technol. 62 (2013) 731–750. https://doi.org/10.1016/j.cirp.2013.05.009.

[129] X. Beudaert, I. Mancisidor, L. Miguel, A. Barrios, K. Erkorkmaz, J. Munoa, Analysis of the feed drives control parameters on structural chatter vibrations, in: Int. Conf. HIGH SPEED Mach., 2016. https://hal.archives-ouvertes.fr/hal-01484796/.

[130] D. Lehotzky, T. Insperger, Stability of delayed oscillators subjected to digital PD control, IFAC, 2012. https://doi.org/10.3182/20120622-3-US-4021.00038.

[131] O. Franco, X. Beudaert, K. Erkorkmaz, Effect of rack and pinion feed drive control parameters on machine tool dynamics, J. Manuf. Mater. Process. 4 (2020) 33. https://doi.org/10.3390/jmmp4020033.

[132] S. Futami, N. Kyura, S. Hara, Vibration Absorption Control of Industrial Robots by Acceleration Feedback, IEEE Trans. Ind. Electron. IE-30 (1983) 299–305. https://doi.org/10.1109/TIE.1983.356741.

[133] D.M. Alter, T.C. Tsao, Stability of turning processes with actively controlled linear motor feed drives, J. Manuf. Sci. Eng. Trans. ASME. 116 (1994) 298–307. https://doi.org/10.1115/1.2901945.

[134] Y. che Chen, J. Tlusty, Effect of Low-Friction Guideways and Lead-Screw Flexibility on Dynamics of High-Speed Machines, CIRP Ann. - Manuf. Technol. 44 (1995) 353–356. https://doi.org/10.1016/S0007-8506(07)62341-5.

[135] G. Forster, J. Hamann, D. Stoiber, Method and device for damping a chatter oscillation in a processing machine, Google Patents. (2005). https://doi.org/10.1103/PhysRevE.87.021001.

[136] Siemens, Function Manual Drive Functions, 2009.

[137] Heidenhain, Technical Manual TNC640, 2015.

[138] N. Kerner, Closed-loop control structure for damping low-frequency vibrations, (2015).

[139] Y. Kakinuma, K. Enomoto, T. Hirano, K. Ohnishi, Active chatter suppression in turning by band-limited force control, CIRP Ann. - Manuf. Technol. 63 (2014) 365–368. https://doi.org/10.1016/j.cirp.2014.03.136.

[140] J. Munoa, X. Beudaert, K. Erkorkmaz, A. Iglesias, A. Barrios, M. Zatarain, Active suppression of structural chatter vibrations using machine drives and accelerometers, CIRP Ann. - Manuf. Technol. 64 (2015) 385–388. https://doi.org/10.1016/j.cirp.2015.04.106.

[141] X. Beudaert, A. Barrios, K. Erkorkmaz, J. Munoa, X. Beudaert, A. Barrios, K. Erkorkmaz, J. Munoa, Limiting factors for the active suppression of structural

chatter vibrations using machine ’ s drives To cite this version : HAL Id : hal-01342267, (2016).

[142] O. Franco, X. Beudaert, K. Erkorkmaz, A. Barrios, I. Mancisidor, J. Munoa, Control strategies for structural chatter suppression using a rack and pinion drive, in: 6th Int. Conf. Virtual Mach. Process Technol. (VMPT 2017), 2017.

[143] A. Dumanli, B. Sencer, Active control of high frequency chatter with machine tool feed drives in turning, CIRP Ann. 70 (2021) 309–312. https://doi.org/10.1016/j.cirp.2021.04.060.

[144] K.J. Åström, T. Hägglund, C.C. Hang, W.K. Ho, Automatic tuning and adaptation for PID controllers-a survey, Control Eng. Pract. 1 (1993) 699–714.

[145] D.J. Gordon, K. Erkorkmaz, Accurate control of ball screw drives using pole-placement vibration damping and a novel trajectory prefilter, Precis. Eng. 37 (2013) 308–322.

[146] Y. Altintas, C.E. Okwudire, Dynamic stiffness enhancement of direct-driven machine tools using sliding mode control with disturbance recovery, CIRP Ann. - Manuf. Technol. 58 (2009) 335–338. https://doi.org/10.1016/j.cirp.2009.03.045.

[147] A. Kamalzadeh, K. Erkorkmaz, Compensation of axial vibrations in ball screw drives, CIRP Ann. 56 (2007) 373–378.

[148] K. Erkorkmaz, A. Kamalzadeh, High bandwidth control of ball screw drives, CIRP Ann. - Manuf. Technol. 55 (2006) 393–398. https://doi.org/10.1016/S0007-8506(07)60443-0.

[149] M. Neubauer, F. Brenner, C. Hinze, A. Verl, Cascaded sliding mode position control (SMC-PI) for an improved dynamic behavior of elastic feed drives, Int. J. Mach. Tools Manuf. (2021) 103796.

[150] I.T. Al-Zaharnah, Suppressing vibrations of machining processes in both feed and radial directions using an optimal control strategy: The case of interrupted cutting, J. Mater. Process. Technol. 172 (2006) 305–310. https://doi.org/10.1016/j.jmatprotec.2005.10.008.

[151] H. Van Brussel, P. Van Den Braembussche, Robust control of feed drives with linear motors, CIRP Ann. - Manuf. Technol. 47 (1998) 325–328. https://doi.org/10.1016/s0007-8506(07)62843-1.

[152] D. Dumur, P. Boucher, G. Ramond, Direct adaptive generalized predictive control. Application to motor drives with flexible modes, CIRP Ann. - Manuf. Technol. 49 (2000) 271–274. https://doi.org/10.1016/S0007-8506(07)62944-8.

[153] T. Berners, A. Epple, C. Brecher, Model predictive controller for machine tool feed

drives, in: 2018 4th Int. Conf. Control. Autom. Robot., IEEE, 2018: pp. 136–140.

[154] Z. Sun, G. Pritschow, A. Lechler, Enhancement of feed drive dynamics using additional table speed feedback, CIRP Ann. - Manuf. Technol. 65 (2016) 357–360. https://doi.org/10.1016/j.cirp.2016.04.099.

[155] Z. Sun, G. Pritschow, P. Zahn, A. Lechler, A novel cascade control principle for feed drives of machine tools, CIRP Ann. - Manuf. Technol. 67 (2018) 389–392. https://doi.org/10.1016/j.cirp.2018.03.004.

[156] K. Großmann, Die digitale Simulation für den Entwurf der Werkzeugmaschine, in: Auton. Produktion, Springer, 2004: pp. 457–472. https://doi.org/10.1007/978-3-642-18523-6_32.

[157] B. Denkena, K. Tracht, S. Rehling, Simulationsmodul für Maschinendynamik im Rahmen eines Fertigungssimulationssystems, WT Werkstattstech. Online. 92 (2002) 223–225.

[158] C. Bartelt, V. Böß, J. Brüning, A. Rausch, B. Denkena, J.P. Tatou, A Software Architecture to Synchronize Interactivity of Concurrent Simulations in Systems Engineering., in: ISPE CE, 2013: pp. 19–29.

[159] Matlab, https://www.mathworks.com, (n.d.).

[160] BS Dassault Systemes, https://www.3ds.com/products-services/catia/products/dymola/, (n.d.).

[161] Siemens, https://www.plm.automation.siemens.com/global/en/products/simcenter/simcenter-amesim.html, (n.d.).

[162] A.A. Kadir, X. Xu, E. Hämmerle, Virtual machine tools and virtual machining—a technological review, Robot. Comput. Integr. Manuf. 27 (2011) 494–508.

[163] M.F. Zaeh, T. Oertli, J. Milberg, Finite element modelling of ball screw feed drive systems, CIRP Ann. - Manuf. Technol. 53 (2004) 289–292. https://doi.org/10.1016/s0007-8506(07)60700-8.

[164] J. Vesely, M. Sulitka, Machine tool virtual model, in: Int. Congr. Matar Praha, 2008: pp. 115–122.

[165] R. Neugebauer, C. Scheffler, M. Wabner, C. Zwingenberger, Advanced calculation of static and dynamic stiffness in mechatronic machine tools, Int. J. Mechatronics Manuf. Syst. 4 (2011) 370–384.

[166] M. Law, Y. Altintas, A.S. Phani, Rapid evaluation and optimization of machine tools with position-dependent stability, Int. J. Mach. Tools Manuf. 68 (2013) 81–90.

[167] M. Law, S. Ihlenfeldt, M. Wabner, Y. Altintas, R. Neugebauer, Position-dependent dynamics and stability of serial-parallel kinematic machines, CIRP Ann. - Manuf. Technol. 62 (2013) 375–378. https://doi.org/10.1016/j.cirp.2013.03.134.

[168] M. Law, S. Ihlenfeldt, A frequency-based substructuring approach to efficiently model position-dependent dynamics in machine tools, Proc. Inst. Mech. Eng. Part K J. Multi-Body Dyn. 229 (2015) 304–317.

[169] H.N. Huynh, Y. Altintas, Modeling the Dynamics of Five-Axis Machine Tool Using the Multibody Approach, J. Manuf. Sci. Eng. 143 (2021) 21012.

[170] C.P. Wang, K. Erkorkmaz, J. McPhee, S. Engin, In-process digital twin estimation for high-performance machine tools with coupled multibody dynamics, CIRP Ann. - Manuf. Technol. 69 (2020) 321–324. https://doi.org/10.1016/j.cirp.2020.04.047.

[171] C. Brecher, M. Esser, S. Witt, Interaction of manufacturing process and machine tool, CIRP Ann. - Manuf. Technol. 58 (2009) 588–607. https://doi.org/10.1016/j.cirp.2009.09.005.

[172] T. Schermann, J. Marsolek, C. Schmidt, J. Fleischer, Aspects of the Simulation of a Cutting Process with ABAQUS/Explicit Including the Interaction between the Cutting Process and the Dynamic Behavior of the Machine Tool, 9th CIRP Int. Work. Model. Mach. Oper. Bled, Slowenia. 11 (2006) 12. http://scholar.google.com/scholar?hl=en&btnG=Search&q=intitle:Aspects+of+the+Simulation+of+a+Cutting+Process+with+ABAQUS/Explicit+Including+the+Interaction+between+the+Cutting+Process+and+the+Dynamic+Behavior+of+the+Machine+Tool#0.

[173] S.T. Witt, Integrierte Simulation von Maschine , Werkstück und spanendem Fertigungsprozess, 2007.

[174] R. Neugebauer, S. Ihlenfeldt, U. Frieß, M. Wabner, S. Rauh, New high-speed machine tool structure by holistic mechatronic systems design, Procedia CIRP. 1 (2012) 307–312. https://doi.org/10.1016/j.procir.2012.04.055.

[175] J. Berkemer, Gekoppelte Simulation von Maschinendynamik und Antriebsregelung unter Verwendung linearer Finite Elemente Modelle, (2003).

[176] V. Matyska, P. Kolář, M. Sulitka, P. Fojtů, Optimization of five-axis finish milling using a virtualmachine tool, MM Sci. J. (2019).

[177] M. Armendia, A. Alzaga, F. Peysson, T. Fuertjes, F. Cugnon, E. Ozturk, D. Flum, Machine tool: From the digital twin to the cyber-physical systems, in: Twin-Control, Springer, Cham, 2019: pp. 3–21.

[178] C.A. Sanchez Gomez, L.E. Gil Castiblanco, J.M. Arroyo Osorio, Building a virtual

machine tool in a standard PLM platform, Int. J. Interact. Des. Manuf. 11 (2017) 445–455.

[179] A. Hänel, A. Seidel, U. Frieß, U. Teicher, H. Wiemer, D. Wang, E. Wenkler, L. Penter, A. Hellmich, S. Ihlenfeldt, Digital Twins for High-Tech Machining Applications—A Model-Based Analytics-Ready Approach, J. Manuf. Mater. Process. 5 (2021) 80.

[180] S. Kaneko, R. Sato, M. Tsutsumi, Mathematical model of linear motor stage with non-linear friction characteristics, J. Adv. Mech. Des. Syst. Manuf. 2 (2008) 675–684.

[181] G. Pritschow, A comparison of linear and conventional electromechanical dives, CIRP Ann. - Manuf. Technol. 47 (1998) 541–548. https://doi.org/10.1016/S0007-8506(07)63241-7.

[182] L.N. López De Lacalle, A. Lamikiz, Machine tools for high performance machining, 2009. https://doi.org/10.1007/978-1-84800-380-4.

[183] S. Frey, M. Walther, A. Verl, Periodic variation of preloading in ball screws, Prod. Eng. 4 (2010) 261–267.

[184] A. Verl, S. Frey, T. Heinze, Double nut ball screw with improved operating characteristics, CIRP Ann. - Manuf. Technol. 63 (2014) 361–364. https://doi.org/10.1016/j.cirp.2014.03.128.

[185] C.E. Okwudire, Improved screw-nut interface model for high-performance ball screw drives, J. Mech. Des. Trans. ASME. 133 (2011). https://doi.org/10.1115/1.4004000.

[186] C.E. Okwudire, Y. Altintas, Hybrid modeling of ball screw drives with coupled axial, torsional, and lateral dynamics, J. Mech. Des. Trans. ASME. 131 (2009) 0710021–0710029. https://doi.org/10.1115/1.3125887.

[187] ISO 3408-3:2006, Acceptance conditions and acceptance test., (1989).

[188] A. Verl, S. Frey, Correlation between feed velocity and preloading in ball screw drives, CIRP Ann. - Manuf. Technol. 59 (2010) 429–432. https://doi.org/10.1016/j.cirp.2010.03.136.

[189] C.-G. Zhou, H.-T. Feng, Z.-T. Chen, Y. Ou, Correlation between preload and no-load drag torque of ball screws, Int. J. Mach. Tools Manuf. 102 (2016) 35–40.

[190] G.H. Feng, Y.L. Pan, Investigation of ball screw preload variation based on dynamic modeling of a preload adjustable feed-drive system and spectrum analysis of ball-nuts sensed vibration signals, Int. J. Mach. Tools Manuf. 52 (2012) 85–96. https://doi.org/10.1016/j.ijmachtools.2011.09.008.

[191] W. Zhang, X. Zhang, J. Zhang, W. Zhao, Analysis of lead screw pre-stretching influences on the natural frequency of ball screw feed system, Precis. Eng. 57 (2019) 30–44. https://doi.org/10.1016/j.precisioneng.2019.03.003.

[192] T.L. Nguyen, S.-K. Ro, J.-K. Park, Study of ball screw system preload monitoring during operation based on the motor current and screw-nut vibration, Mech. Syst. Signal Process. 131 (2019) 18–32.

[193] B. Denkena, B. Bergmann, A. Schmidt, Preload monitoring of single nut ball screws based on sensor fusion, CIRP J. Manuf. Sci. Technol. 33 (2021) 63–70. https://doi.org/10.1016/j.cirpj.2021.02.006.

[194] C. Brecher, B. Eßer, J. Falker, F. Kneer, M. Fey, Modelling of ball screw drives rolling element contact characteristics, CIRP Ann. - Manuf. Technol. 67 (2018) 409–412. https://doi.org/10.1016/j.cirp.2018.04.109.

[195] Https://www.elevatorscenestudio.com/, Vessel elevator, (2020).

[196] T. Uchida, A. Ito, T. Oshima, N. Furuya, Positioning system with backlash compensation by twin motor cooperative control, Trans. Japan Soc. Mech. Eng. Ser. C. 77 (2011) 2280–2289.

[197] T. Uchida, A. Ito, T. Kitamura, N. Furuya, Positioning system with backlash compensation by twin motor cooperative control (Evaluation of rectilinear motion mechanism installed planetary gear speed reducer), Trans. JSME (in Japanese). 80 (2014).

[198] A. Verl, T. Engelberth, Adaptive preloading for rack-and-pinion drive systems, CIRP Ann. - Manuf. Technol. 67 (2018) 369–372.

[199] H. Jiang, H. Fu, Z. Han, H. Jin, Elimination of Gear Clearance for the Rotary Table of Ultra Heavy Duty Vertical Milling Lathe Based on Dual Servo Motor Driving System, Appl. Sci. 10 (2020) 4050.

[200] D. Prodan, M. Petre, G. Constantin, A. Bucuresteanu, Eliminating the backlash of circular feed drives of cnc vertical lathes, Proc. Manuf. Syst. 11 (2016) 27.

[201] T. Engelberth, S. Apprich, J. Friedrich, D. Coupek, A. Lechler, Properties of electrically preloaded rack-and-pinion drives, Prod. Eng. 9 (2015) 269–276. https://doi.org/10.1007/s11740-015-0601-3.

[202] Y.H. Choi, E.Y. Choi, S.H. Jang, H.M. Park, J.S. Ha, Vibration analysis and dynamic optimization of a rack and pinion typed feed drive system for a router machine, in: ICMIT 2005 Control Syst. Robot., International Society for Optics and Photonics, 2006: p. 60424I.

[203] F. Brenner, A. Lechler, A. Verl, Acceleration-based disturbance compensation for

elastic rack-and-pinion drives, Prod. Eng. (2021) 1–10.

[204] A. Karim, P. Lindner, A. Verl, Control-based compensation of friction and backlash within rack-and-pinion drives, Prod. Eng. 12 (2018) 589–596.

[205] C. Ehrmann, P. Isabey, J. Fleischer, Condition Monitoring of Rack and Pinion Drive Systems: Necessity and Challenges in Production Environments, Procedia CIRP. 40 (2016) 197–201. https://doi.org/10.1016/j.procir.2016.01.101.

[206] R. Smith, R.K. Mobley, Industrial machinery repair: best maintenance practices pocket guide, Butterworth-Heinemann, 2003.

[207] W.B. Lloyd, J.H. Staehlin, Anti-backlash gear assembly, U.S. Pat. No. 4,072,064, Washington, DC U.S. Pat. Trademark Off. (1978).

[208] L.C. Hale, A.H. Slocum, Design of anti-backlash transmissions for precision position control systems, Precis. Eng. 16 (1994) 244–258.

[209] O'neill Robert F., Anti-backlash gears, U.S. Pat. No. 3,127,784. Washington, DC U.S. Pat. Trademark Off. (1963).

[210] REDEX Rack and Pinions, www.redex-andantex.com, Accessed 23 May. (2021).

[211] Nexen, Zero backlash linear motion, (2010).

[212] Heidenhain, Technical Manual TNC640, Heidenhain Traunreut, Ger. (2015).

[213] T. Engelberth, A. Verl, Adaptive Verspannung von Zahnstagne-Ritzel-Antrieben, Stuttgart: Fraunhofer Verlag, 2019.

[214] J. Margielewicz, D. Gąska, G. Litak, Modelling of the gear backlash, Nonlinear Dyn. 97 (2019) 355–368.

[215] C.G. Cooley, R.G. Parker, A review of planetary and epicyclic gear dynamics and vibrations research, Appl. Mech. Rev. 66 (2014).

[216] Ansol, Calyx www.ansol.us, (2007).

[217] W. Jingyue, G. Lixin, W. Haotion, Analysis of bifurcation and nonlinear control for chaos in gear transmission system, Res. J. Appl. Sci. Eng. Technol. 6 (2013) 1818–1824.

[218] L. Walha, T. Fakhfakh, M. Haddar, Nonlinear dynamics of a two-stage gear system with mesh stiffness fluctuation, bearing flexibility and backlash, Mech. Mach. Theory. 44 (2009) 1058–1069.

[219] G. Litak, M.I. Friswell, Vibration in gear systems, Chaos, Solitons & Fractals. 16 (2003) 795–800.

[220] M.B. Sánchez, M. Pleguezuelos, J.I. Pedrero, Approximate equations for the meshing stiffness and the load sharing ratio of spur gears including hertzian effects, Mech. Mach. Theory. 109 (2017) 231–249.

[221] S.M. Vijayakar, Calyx users manual, Https://Ansol.Us. (2005).

[222] J. Wang, I. Howard, The torsional stiffness of involute spur gears, Proc. Inst. Mech. Eng. Part C J. Mech. Eng. Sci. 218 (2004) 131–142.

[223] T. Kiekbusch, D. Sappok, B. Sauer, I. Howard, Calculation of the combined torsional mesh stiffness of spur gears with two-and three-dimensional parametrical FE models, Strojniški Vestnik-Journal Mech. Eng. 57 (2011) 810–818.

[224] S. Xue, R. Entwistle, I. Mazhar, I. Howard, The spur planetary gear torsional stiffness and its crack sensitivity under quasi-static conditions, Eng. Fail. Anal. 63 (2016) 106–120.

[225] B. Mahr, U. Kissling, Comparison between different commercial gear tooth contact analysis software packages, Www.Kisssoft.Ag. (2017) 1–16.

[226] ISO 6336-1:3, Calculation of load capacity of spur and helical gears, (2006).

[227] SDP/SI, www.sdp-si.com/resources, Accessed 23 May. (2021).

[228] F. Cunliffe, J.D. Smith, D.B. Welbourn, Dynamic Tooth Loads in Epicyclic Gears., J. Eng. Ind. (1973).

[229] J. Lin, R.G. Parker, Analytical characterization of the unique properties of planetary gear free vibration, J. Vib. Acoust. Trans. ASME. 121 (1999) 316–321. https://doi.org/10.1115/1.2893982.

[230] T.M. Ericson, R.G. Parker, Natural frequency clusters in planetary gear vibration, J. Vib. Acoust. 135 (2013).

[231] T.M. Ericson, R.G. Parker, Planetary gear modal vibration experiments and correlation against lumped-parameter and finite element models, J. Sound Vib. 332 (2013) 2350–2375.

[232] E.J.A. Armarego, N.P. Deshpande, Computerized predictive cutting models for forces in end-milling including eccentricity effects, CIRP Ann. 38 (1989) 45–49.

[233] A. Iglesias, J. Munoa, J. Ciurana, Optimisation of face milling operations with structural chatter using a stability model based process planning methodology, Int. J. Adv. Manuf. Technol. 70 (2014) 559–571. https://doi.org/10.1007/s00170-013-5199-z.

[234] P.D. Welch, The Use of Fast Fourier Transform for the Estimation of Power Spectra, Digit. Signal Process. (1967) 70–73.

[235] A. Gómez González, J. Rodríguez, X. Sagartzazu, A. Schuhmacher, I. Isasa, Multiple coherence method in time domain for the analysis of the transmission paths of noise and vibrations with non stationary signals, Proc. ISMA 2010 - Int.

Conf. Noise Vib. Eng. Incl. USD 2010. (2010) 3927–3941.

[236] Siemens, SINUMERIK 840D sl synchronized actions, (2010) 1–114.

[237] Y. Altintas, A. Verl, C. Brecher, L. Uriarte, G. Pritschow, Machine tool feed drives, CIRP Ann. - Manuf. Technol. 60 (2011) 779–796. https://doi.org/10.1016/j.cirp.2011.05.010.

[238] A. Matsubara, K. Nagaoka, T. Fujita, Model-reference feedforward controller design for high-accuracy contouring control of machine tool axes, CIRP Ann. - Manuf. Technol. 60 (2011) 415–418. https://doi.org/10.1016/j.cirp.2011.03.029.

[239] X. Beudaert, I. Mancisidor, L. Miguel, A. Barrios, K. Erkorkmaz, J. Munoa, Analysis of the feed drives control parameters on structural chatter vibrations, Int. Conf. HIGH SPEED Mach. (2016).

[240] M. Zatarain, I. Ruiz de Argandoña, A. Illarramendi, J.L. Azpeitia, R. Bueno, New Control Techniques Based on State Space Observers for Improving the Precision and Dynamic Behaviour of Machine Tools, CIRP Ann. - Manuf. Technol. 54 (2005) 393–396. https://doi.org/10.1016/S0007-8506(07)60130-9.

[241] B. Sencer, A. Dumanli, Optimal control of flexible drives with load side feedback, CIRP Ann. - Manuf. Technol. 66 (2017) 357–360. https://doi.org/10.1016/j.cirp.2017.04.049.

[242] J. Munoa, X. Beudaert, K. Erkorkmaz, A. Iglesias, A. Barrios, M. Zatarain, Active suppression of structural chatter vibrations using machine drives and accelerometers, CIRP Ann. - Manuf. Technol. 64 (2015). https://doi.org/10.1016/j.cirp.2015.04.106.

[243] Z. Sun, G. Pritschow, P. Zahn, A. Lechler, A novel cascade control principle for feed drives of machine tools, CIRP Ann. 67 (2018) 389–392. https://doi.org/10.1016/j.cirp.2018.03.004.

[244] K. Erkorkmaz, Y. Hosseinkhani, Control of ball screw drives based on disturbance response optimization, CIRP Ann. - Manuf. Technol. 62 (2013) 387–390. https://doi.org/10.1016/j.cirp.2013.03.138.

[245] E. Schäfers, J. Hamann, H.P. Tröndle, Mechatronic optimization, analysis and simulation of machines, Praxiswissen Autom. Hüthig, Heidelb. (2001) 618–628.

[246] E. Schäfers, J. Hamann, H.P. Tröndle, Dynamic and robust control of direct drives, SPS/IPC/Drives Exhib. (2003).

[247] K. Lee, S. Ibarakil, A. Matsubara, Y. Kakino, S. Arai, J. Braasch, A Servo Parameter Tuning Method For Highspeed NC Machine Tools Based On Contouring Error Measurement, WIT Trans. Eng. Sci. 44 (2003).

[248] C. Rodríguez de Yurre, J. Zurbitu, A. Lazkano, J.. Azpeitia, I. Ruiz de Argandoña, Nueva utilidad de autoajuste de los lazos de control en CNCs avanzados, 2005.

[249] T. Wakana, Servo gain self-adjustment function in melservo, Mitsubishi Electr. Adv. 129 (2010) 2–4.

[250] Okuma, https://www.okuma.com/servonavi, (2021).

[251] H. Suzuki, M. Yamaguchi, Comparison of FRF Curve Fitting Methods for the Loss Factor Measurement, INTER-NOISE NOISE-CON Congr. Conf. Proc. 2002 (2002) 1060–1065.

[252] Y. Altintaş, E. Budak, Analytical Prediction of Stability Lobes in Milling, CIRP Ann. - Manuf. Technol. 44 (1995) 357–362. https://doi.org/10.1016/S0007-8506(07)62342-7.

[253] E. Pennestrì, V. Rossi, P. Salvini, P.P. Valentini, Review and comparison of dry friction force models, Nonlinear Dyn. 83 (2016) 1785–1801. https://doi.org/10.1007/s11071-015-2485-3.

[254] D. Farago, Z. Dombovari, Experimental study on free vibratory behavior of nonlinear structure, Period. Polytech. Mech. Eng. 63 (2019) 91–99. https://doi.org/10.3311/PPme.12481.

[255] D.J. Ewins, Modal testing: theory and practice, Research studies press Letchworth, 1984.

[256] K. Erkorkmaz, Y. Altintas, High speed CNC system design. Part II: Modeling and identification of feed drives, Int. J. Mach. Tools Manuf. 41 (2001) 1487–1509. https://doi.org/10.1016/S0890-6955(01)00003-7.

[257] H. Moradi, H. Salarieh, Analysis of nonlinear oscillations in spur gear pairs with approximated modelling of backlash nonlinearity, Mech. Mach. Theory. 51 (2012) 14–31. https://doi.org/10.1016/j.mechmachtheory.2011.12.005.